POLITECNICO
MILANO 1863

DEPARTMENT OF PHYSICS
DOCTORAL PROGRAMME IN PHYSICS

Femtosecond laser writing of photonic integrated circuits for quantum technologies

Doctoral dissertation of:
Simone Piacentini
Student ID: 914122

Supervisor:
Prof. Roberto Osellame

Tutor:
Prof. Roberta Ramponi

The Chair of the Doctoral Programme:
Prof. Marco Finazzi

2018 - 2021
XXXIV Cycle

ABSTRACT

The forthcoming second quantum revolution is expected to revolutionize the way in which the information is processed and transmitted. As a matter of fact, by controlling and manipulating purely quantum states we will achieve for instance the realization of fast and efficient quantum computers, capable of solving problems which are now considered intractable. Moreover, the use of quantum carriers will allow us both to communicate in a secure way and to measure the world around us with an enhanced sensitivity. In this regard, quantum photonics could play an important role, thanks to the peculiar properties of photons, which make them perfect candidates for the implementation of quantum systems, and to the recent advances achieved in the realization of compact and stable photonic integrated circuits. Nevertheless, before obtaining useful realizations with relevant effects in our everyday life, several issues should be addressed, first of all the possibility to scale up the complexity of the fabricated quantum devices. For this reason, part of the research in the quantum photonics field is currently focused on providing intermediate results, which can be seen as milestones in the road towards the realization of large-scale, fault-tolerant quantum systems. In this framework, the microfabrication of photonic circuits by femtosecond laser writing is a valuable tool, thanks to its versatility. This platform allows in fact the realization in transparent materials, like glass and crystals, of the main components of a complex photonic circuit, such as optical waveguides, tunable interferometers and integrated polarization optics, without the need of clean-room facilities and lithographic masks, thus providing a fast prototyping of circuits with innovative designs and properties.

In this thesis work we present the femtosecond laser writing of several photonic circuits for different applications in the field of quantum photonics, including the validation of waveguides for space-based optical communications, the realization of scalable photonic processors for quantum computing, and the fabrication of a device for quantum metrology. Despite their diversity, these works share some common features, such as the reconfigurability and the three-dimensionality of the fabricated circuits, both provided by the unique capabilities of femtosecond laser writing, and the effort towards the implementation of experiments employing a large number of photons. In this respect, we also present the optimization of a quantum dot single photon source, which can be interfaced with the circuits fabricated with this technology for further scaling the complexity of the performed experiments.

PUBLICATIONS AND CONFERENCES

PUBLICATIONS

- G. Corrielli, S. Atzeni, S. Piacentini, I. Pitsios, A. Crespi, R. Osellame. "Symmetric polarization-insensitive directional couplers fabricated by femtosecond laser writing." In: *Optics Express* 26.12 (2018)
- S. Piacentini†, T. Vogl†, G. Corrielli, P. K. Lam, R. Osellame. "Space qualification of integrated photonic circuits fabricated by ultrafast laser writing." In: *Laser & Photonics Reviews* 15.2 (2021)
- A. S. Nayak, L. Labadie, T. Kumar Sharma, S. Piacentini, G. Corrielli, R. Osellame, E. Gendron, J.-T. M. Buey, F. Chemla, M. Cohen, N. A. Bharmal, L. F. Bardou, L. Staykov, J. Osborn, T. J. Morris, E. Pedretti, A. N. Dinkelaker, K. V. Madhav, M. M. Roth. "First stellar photons for an integrated optics discrete beam combiner at the William Herschel Telescope." In: *Applied Optics* 60.19 (2021)
- F. Yu, Z.-N. Tian, S. Piacentini, X.-Y. Li, Q.-D. Chen, R. Osellame, H.-B. Sun. "Resetting directional couplers for high-fidelity quantum photonic integrated chips." In: *Optics Letters* 46.20 (2021)
- M. Spagnolo, J. Morris, S. Piacentini, M. Antesberger, F. Massa, F. Ceccarelli, A. Crespi, R. Osellame, P. Walther. "Experimental quantum memristor." In: *arXiv preprint arXiv:2105.04867* (2021). Accepted for publication on Nature Photonics.
- F. Hoch†, S. Piacentini†, T. Giordani, Z.-N. Tian, M. Iuliano, C. Esposito, A. Camillini, G. Carvacho, F. Ceccarelli, N. Spagnolo, A. Crespi, F. Sciarrino, and R. Osellame."Boson Sampling in a reconfigurable continuously-coupled 3D photonic circuit."In: *arXiv preprint arXiv:2106.08260* (2021). In submission.

† equal contribution to the work

CONFERENCE PRESENTATIONS AND PROCEEDINGS

- E. Pedretti, S. Piacentini, G. Corrielli, R. Osellame, S. Minardi. "A six-apertures discrete beam combiners for J-band interferometry." In: *Optical and Infrared Interferometry and Imaging VI.* Vol. 10701. International Society for Optics and Photonics, 2018.

- S. Minardi, M. Diab, E. Pedretti, A. S. Nayak, A. Saviauk, S. Piacentini, G. Corrielli, R. Osellame, R. Diener, J. Tepper, L. Labadie, F. Dreisow, M. Grafe, T. Pertsch, S. Nolte, R. Errmann, D. Stoffel, N. Chakrova. "Discrete beam combiners from astronomy to lasers." In: *Integrated Optics: Devices, Materials, and Technologies XXIII* Vol. 10921. International Society for Optics and Photonics, 2019.

- S. Piacentini*, G. Corrielli, A. S. Nayak, E. Pedretti, S. Minardi, R. Osellame. "Direct Writing of 3D Integrated Photonic Circuits for Astrophotonics." In: *2019 Conference on Lasers and Electro-Optics Europe & European Quantum Electronics Conference (CLEO/Europe-EQEC).* IEEE, 2019.

- A. S. Nayak, S. Piacentini, T. K. Sharma, G. Corrielli, R. Osellame, L. Labadie, S. Minardi, E. Pedretti, K. Madhav, M. M. Roth. "Integrated optics-interferometry using pupil remapping and beam combination at astronomical H-band." In: *Advances in Optical Astronomical Instrumentation 2019.* Vol. 11203. International Society for Optics and Photonics, 2020.

- F. Ceccarelli, S. Atzeni, F. Pellegatta, S. Piacentini, A. Crespi, R. Osellame. "Low-power reconfigurable photonic integrated circuits fabricated by femtosecond laser micromachining (Conference Presentation)." In: *Frontiers in Ultrafast Optics: Biomedical, Scientific, and Industrial Applications XX.* Vol. 112700U. International Society for Optics and Photonics, 2020.

- S. Piacentini*, G. Corrielli, A. S. Nayak, T. K. Sharma, K. V. Madhav, A. Adami, E. Pedretti, S. Minardi, L. Labadie, R. Osellame. "Femtosecond laser writing of 3D polarization insensitive integrated devices for astrophotonics (Conference Presentation)." In: *Frontiers in Ultrafast Optics: Biomedical, Scientific, and Industrial Applications XX.* Vol. 112700S. International Society for Optics and Photonics, 2020.

- S. Piacentini*, G. Corrielli, A. S. Nayak, T. K. Sharma, K. V. Madhav, E. Pedretti, S. Minardi, L. Labadie, R. Osellame. "Integrated discrete beam combiner with a pupil remapper for stellar interferometry (Conference Presentation)." In: *Photonic Instrumentation Engineering VII.* Vol. 112870B. International Society for Optics and Photonics, 2020.

- S. Piacentini*, T. Vogl, G. Corrielli, P. K. Lam, R. Osellame. "Space qualification of integrated photonic circuits fabricated by ultrafast laser writing." In: *Frontiers*

in Ultrafast Optics: Biomedical, Scientific, and Industrial Applications XXI. Vol. 11676. International Society for Optics and Photonics, 2021.

- S. Piacentini⋆, T. Vogl, G. Corrielli, P. K. Lam, R. Osellame. "Qualification of Femtosecond Laser-Written Waveguides for Space Environment." In: *The European Conference on Lasers and Electro-Optics.* Optical Society of America, 2021.
- F. Ceccarelli, C. Pentangelo, S. Piacentini, R. Albiero, E. Urbinati, S. Atzeni, A. Crespi, R. Osellame. "Universal photonic processors in a glass-based femtosecond laser writing platform." In: *Photonics in Switching and Computing.* Optical Society of America, 2021.

⋆ personal oral contribution to the conference

CONTENTS

LIST OF FIGURES

LIST OF TABLES

Part I

BACKGROUND

The first part of this thesis is devoted to give to the reader a general background, useful for a better understanding of the experimental work that will follow. In detail, Chapter 1 will describe the main advances that could be provided by quantum technologies, and quantum photonics in particular, with a focus on the fields of quantum computing, communication and metrology. Chapter 2 will provide instead a description of femtosecond laser waveguide writing, the fabrication technique used in the experimental part of this thesis, with an illustration of its most useful features for the development of photonic integrated quantum devices.

1

PHOTONIC QUANTUM TECHNOLOGIES

1.1 THE SECOND QUANTUM REVOLUTION

The understanding of the nanometric world and its counterintuitive laws was at the basis of some of the most important technological advances occurred in the last century. For instance, the whole field of nanotechnologies and all its products, such as computers and smartphones, originated from the peculiar non classical properties of semiconductors, while the wave-particle duality was at the basis of the invention of the laser and all its applications in the field of photonics. Because of its importance, this tremendous scientific progress is sometimes referred to as *First Quantum Revolution*.

During the XXI century, a further technological improvement is expected to occur, driven by new emerging quantum technologies. This *Second Quantum Revolution* will take advantage of purely quantum phenomena like quantum superposition, entanglement and teleportation, and promises to be as disruptive as the first one if a high efficiency an reliability in the generation and manipulation of quantum states is achieved [1]. Quantum technologies are expected to revolutionize several fields, enabling faster computations [2], secure communications [3] and more sensitive measurements [4]. For achieving this goal, in the recent years several governments and research institutions have funded programs and projects addressing the main technological challenges. For instance, the European Union in 2016 started the Quantum Technologies Flagship, a 1 billion € research program with a duration of 10 years [5], and similar investments have been promoted by US [6], China [7] and also private companies such as Google [8], IBM [9] and Microsoft [10].

There are several problems that researchers need to solve in order to achieve useful implementations. Quantum states are quite fragile, and even the slightest interaction with the environment could destroy their coherence [11]. For this reason, a quantum device should be protected against any possible error, for instance by proper isolation from the surrounding, or by the implementation of error correction techniques [12]. Moreover, to achieve a useful operation, a quantum device should be able to employ thousands or even million of quantum states, therefore scalability is another issue which needs to be addressed.

Among the main platforms [13] that have been proposed for the development of quantum technologies, quantum photonics is one of the most promising. Photons are

indeed robust to noise and unwanted interactions with the surrounding, thus requiring less strict protection techniques. Moreover, they are well-suited for fast and efficient communications, and can be easily manipulated with linear optical elements such as beam splitters and delay lines [14]. With regard to the scalability issue, quantum photonics could benefit from the expertise acquired in the last years in the development of photonic integrated circuits [15], which would provide the miniaturization and stability required in useful quantum devices.

The road for the development of quantum technologies able to outperform classical ones is still long, and it is not clear yet whether only one platform will be able to stand out or hybrid approaches will be preferred. Therefore, for providing a broader background, the following discussion will not be limited to photonic implementations, which are of interest for this thesis, but the other most promising platforms will be considered as well.

1.2 QUANTUM COMPUTING AND SIMULATIONS

1.2.1 *The Qubit*

The basic idea of quantum information is to replace the classical bit with the quantum bit, or *qubit* [16]. While a classical bit can assume only two values, 0 and 1, a qubit lies in a quantum superposition of the two states $|0\rangle$ and $|1\rangle$, with complex amplitudes equal to α and β:

$$|\psi\rangle = \alpha\,|0\rangle + \beta\,|1\rangle = \begin{pmatrix} \alpha \\ \beta \end{pmatrix}, \quad \text{with } \alpha, \beta \in \mathbb{C}. \tag{1.1}$$

As long as the qubit is not measured, and in general does not interact with the environment, the superposition is preserved. However, once measured, the system wavefunction collapses on one of the two eigenstates $|0\rangle$ and $|1\rangle$, respectively with probability $|\alpha|^2$ and $|\beta|^2$.

The superposition state can be graphically visualized as a vector in the Bloch sphere (Fig. 1.1), if we consider without loss of generality $\alpha = \cos(\theta/2)$ and $\beta = e^{i\phi}\sin(\theta/2)$. In this representation, for instance, a state in equal superposition between the two eigenstates lies on the equator, and all the pure states lie on the sphere surface.

As in classical computing, for useful application it is necessary to act on a qubit by means of universal gates [17], which in quantum information are represented by unitary operations. For example, it is possible to define the *NOT* gate as

$$NOT = \begin{pmatrix} 0 & 1 \\ 1 & 0 \end{pmatrix}. \tag{1.2}$$

Its application allows to negate a qubit by switching α with β, thus converting the state $|1\rangle$ to $|0\rangle$ and vice versa. Other notable one-qubit gates are the Z gate, which allows to

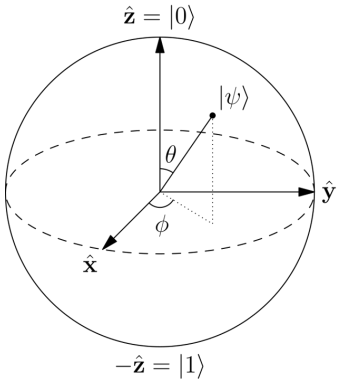

Figure 1.1: Bloch sphere representation of a qubit. θ and ϕ are the polar and azimuthal angles, while $|\psi\rangle$ is the generic qubit. The two eigenstates $|0\rangle$ and $|1\rangle$ are the north and south poles respectively.

flip the phase of the state, and the Hadamard gate, which creates superposition from an eigenstate [18]:

$$H = \frac{1}{\sqrt{2}} \begin{pmatrix} 1 & 1 \\ 1 & -1 \end{pmatrix}. \tag{1.3}$$

In general any one-qubit gate implements a rotation in the Bloch sphere: for instance, the application of H to $|0\rangle$ rotates the state from the north pole to one point of the equator.

For achieving universal computation, conditional gates are necessary as well, in order to change the state of a qubit depending on the state of another one. This can be done by means of two-qubit gates, which enable the interaction between two different qubits. It can be demonstrated that universality can be reached by means of only one two-qubit gate and a complete set of one-qubit gates, i.e. a set allowing an arbitrary state to reach any position in the Bloch sphere [19]. An example of two-qubit operation acting on the state $|\psi_2\rangle = \alpha\,|00\rangle + \beta\,|01\rangle + \gamma\,|10\rangle + \delta\,|11\rangle$ is the controlled-not or $CNOT$ gate:

$$CNOT = \frac{1}{\sqrt{2}} \begin{pmatrix} 1 & 0 & 0 & 0 \\ 0 & 1 & 0 & 0 \\ 0 & 0 & 0 & 1 \\ 0 & 0 & 1 & 0 \end{pmatrix}, \tag{1.4}$$

which flips the state of the second bit if the first one is $|1\rangle$, and leaves it unaltered if the first bit is in $|0\rangle$.

1.2.1.1 *Physical implementations*

Any physical system which can be in a quantum superposition of two levels is in theory a good candidate for the realization of a qubit. However, in order to achieve

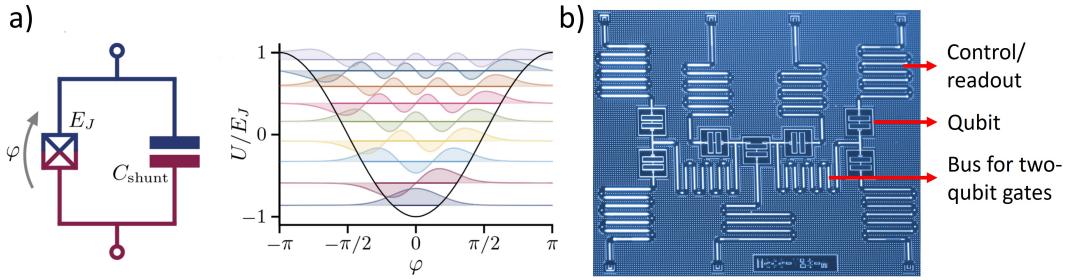

Figure 1.2: Superconducting qubits. a) Representation of the anharmonic potential, energy eigenfunctions and eigenvalues of a superconducting qubit (transmon), composed of a Josephson junction connected to a capacitor. Image taken from [21]. b) Superconducting quantum processor built by IBM and composed of seven supeconducting qubits. The resonators for control/readout and for the interaction between the qubits are highlighted. Adapted from [22].

functioning and useful quantum computers, many other requirements should be satisfied. These are resumed in the DiVincenzo's criteria, proposed in 2000 by David P. DiVincenzo [20]:

1. The physical system should be scalable and based on well-defined qubits, i.e. qubits with only two possible eigenstates;
2. It should be possible to initialize the state of the qubits;
3. The qubit coherence time should be longer than the time required for the gate operation;
4. The physical system should provide a way to implement universal quantum gates;
5. It should be possible to measure the qubit in a reliable way.

It is difficult to find a physical system satisfying all the criteria at the same time in a straightforward way. This is why many technological platforms have been proposed for the implementation of a quantum computer, with their own advantages and disadvantages. In the following paragraphs some of the most advanced and promising are reported.

SUPERCONDUCTING QUBITS The superconducting qubits are based on the idea that the quantum description of an oscillatory LC circuit is formally equivalent to the problem of a mechanical harmonic oscillator, presenting a parabolic potential and quantized energy levels which can be used as eigenstates of a qubit [23]. However, standard LC oscillators would slowly dissipate the stored energy by Joule effect, being the resistance of their elements non negligible. To solve this issue, superconducting materials have been proposed for their realization. Moreover, a harmonic oscillator is not a good candidate for a qubit, since the equal spacing of the energy levels does not allow to clearly address only two of them, thus violating the first DiVincenzo's criterion. In order to add anharmonicity to the potential (Fig. 1.2.a) and obtain unevenly

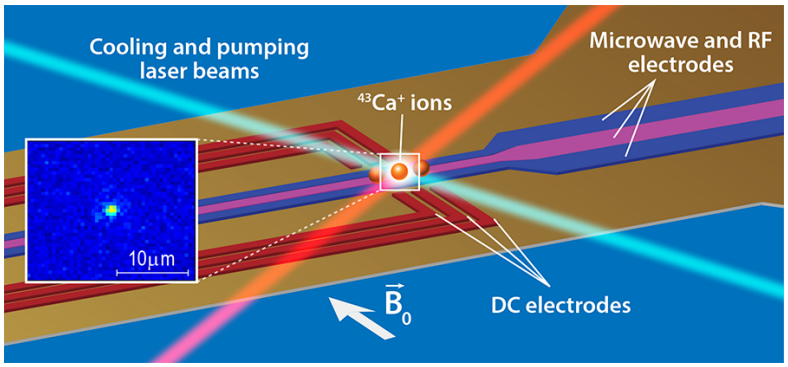

Figure 1.3: Scheme of a qubit based on trapped $^{43}Ca^{+}$ ions. The ions are trapped by a combined action of DC and RF electrodes, and are prepared to the ground state by laser cooling. Microwave electrodes or laser beams are used for control and readout. From [32].

spaced levels, it was proposed to introduce in the circuit one or more Josephson junctions [24], which are thin insulating layers that the flowing Cooper pairs can overcome by quantum tunneling.

Superconducting qubits can be excited and measured by means of microwave resonators working in the GHz regime, and with similar transmission lines it is possible to pairwise connect different qubits (Fig. 1.2.b), thus allowing two-qubit operations in few tens of ns [25]. Moreover, they can take advantage of the existing microfabrication processes, nevertheless the scalability of the number of qubits remains a challenge.

TRAPPED IONS Ions represent good qubit candidates, since they have many unevenly spaced energy states that can be used as $|0\rangle$ and $|1\rangle$. The most used implementations exploit either two hyperfine levels of the ground state (hyperfine qubit), or the ground and one of the excited states (optical qubit) [26]. For providing a stable control of the qubits, the ions are trapped by means of electrical and magnetic fields: in particular, RF electrodes are needed, since DC fields would not be sufficient for the purpose [27]. The qubit preparation is performed with a combination of laser-based Doppler cooling and resolved sideband cooling down to few mK [28], in order to set the ion to the motional ground state, followed by optical pumping. Control and readout can be implemented by resonant microwave excitation in case of hyperfine qubits [29], or laser excitation in case of an optical one [30]. In particular, the readout is performed by measuring the fluorescence emission after resonant excitation, since generally only one of the two states decays radiatively [31]. A typical setup for trapping and controlling ions is represented in Fig. 1.3.

The realization of two or more qubit gates is quite straightforward, since ions collectively interact by Coulomb forces. Therefore, no additional connections are required, moreover the implementable operations are not limited to pairwise interactions. Already in 2003 the physical realization of a *CNOT* gate with this technology was reported [33]. The other advantage of this platform is represented by the long coherence

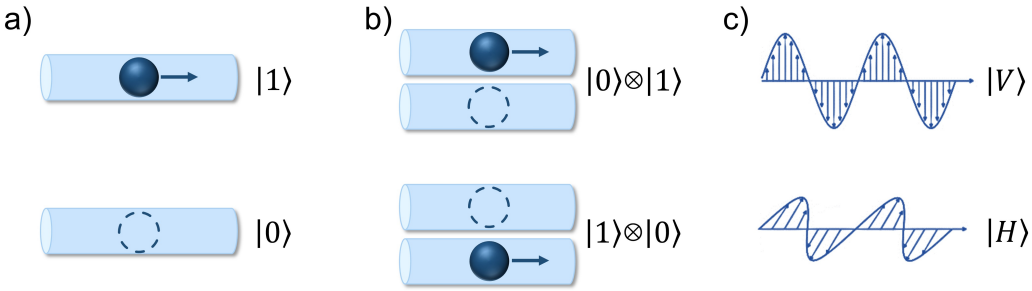

Figure 1.4: Possible encodings for a photonic qubit. a) Single-rail encoding: the photon is present or not present in the spatial mode b) Dual-rail encoding: the photon is either in one or the other spatial mode. c) Polarization encoding: the photon is either horizontally or vertically polarized.

times, which can be of the order of seconds or even more [34] in ultra-high vacuum conditions, thus providing reliable operations. However, also in this case the scalability of the system represents an issue, since it becomes challenging to preserve the high fidelity in many qubits systems [35].

PHOTONS Single photons provide several two-level systems for qubit encoding, with straightforward single-qubit gates and without decoherence problems, due to their weak interaction with the environment [36]. The simplest way to do that is by using the $|0\rangle$ and $|1\rangle$ Fock states [37], which represent the absence or presence of a photon in a spatial mode of a photonic circuit (Fig. 1.4.a). However, this encoding is not robust against photon losses, therefore other approaches are more common. The first one consists in using two different spatial modes or time bins as the two levels of the qubit, choices which are respectively referred to as dual-rail (Fig. 1.4.b) and time-bin encoding [14, 38]. These are good ways of encoding information, since a photon can be transferred in a quantum superposition of the two levels by a beam splitter or a Mach-Zehnder interferometer, whose transformation is equivalent to a Hadamard gate with an additional phase term [39]. Another possibility is to use the polarization encoding, which exploits the two possible orthogonal polarization states that a photon can have, such as $|H\rangle$ and $|V\rangle$ (Fig. 1.4.c) or $|R\rangle$ and $|L\rangle$. In this case, the quantum superposition can be achieved by using half and quarter-waveplates [40]. Other approaches for implementing optical qubits do not involve single photons but other quantum states of light, such as squeezed states [41].

The weak interaction between photons is however one of the main limitation for the realization of two-qubit gates and therefore for universal quantum computation. As a matter of fact, strong nonlinearities would be necessary for making the state of one photon dependent on the state of another one, much stronger than the ones currently available in standard nonlinear materials [42]. This problem was partially solved when in 2000 Knill, Laflamme and Milburn proposed a protocol [43] for the implementation of two-qubit gates without the need of nonlinear elements, but employing

only single-photon sources, linear optical circuits and single-photon detectors. In particular, this scheme involves additional *ancilla* photons and postselection to provide probabilistic gates, thus exploiting projective measurements to induce the nonlinearity which is needed for making the photons interact. After this proposal, two-qubit gates schemes were demonstrated experimentally with good fidelity [44]. The main challenge remains however the probabilistic nature of this protocol, thus making it difficult to scale: nevertheless, efforts are being made in the scientific community to obtain nearly-deterministic operation [45].

1.2.1.2 *Advantages of a quantum computer*

The interest towards the implementation of a quantum computer was born in 1994, when Shor proposed an efficient quantum algorithm to factorize large numbers [46], a problem whose complexity scales exponentially for a classical computer and whose solution can require in some cases a time longer than the age of the universe. From that moment, many applications were identified that would benefit from quantum computing. The main conjecture is that quantum computers will not completely replace their classical counterpart in everyday tasks, but will be mainly used for exponentially hard problems. Moreover, it is still under debate whether they will be able to efficiently solve "very hard" problems, such as NP-complete ones, though they will still be probably faster in finding approximate solutions [47]. Nevertheless, this does not limit the number or the importance of the possible applications of quantum computing. First, all the optimization [48] and research [49] problems would benefit a substantial speed-up. Then, a quantum computer is well-suited for simulating a complex quantum system, such as an ensemble of hundreds of atoms and molecules, whose simulation becomes quickly intractable classically due to the high number of interactions to consider. Quantum simulators would be therefore disruptive for fields like nanotechnologies [50], quantum chemistry [50] and condensed-matter physics [51]. As a final examples we cite quantum machine learning and artificial intelligence [52], which is attracting investments from companies such as Google and Rigetti Computing [53].

1.2.2 *Linear Optical Quantum Computing*

As aforementioned, the development of linear optical quantum computing (LOQC) based on the KLM protocol requires three elements as building blocks: low loss linear optical circuits, deterministic single photon sources and efficient single photon detectors. In the following, we will revise their main requirements and possible implementations.

1.2.2.1 *Universal photonic processors*

The action of any photonic linear circuit can be associated to an operator U, which can be seen as the relation between the creation operators of the M output modes ($\mathbf{a}^\dagger_{out}$) and the ones of the N input modes ($\mathbf{a}^\dagger_{in}$):

$$\mathbf{a}^\dagger_{out} = U \cdot \mathbf{a}^\dagger_{in}. \tag{1.5}$$

The inverse idea, i.e. whether to an arbitrary transformation is always associated an implementable circuit, is not so trivial. The problem was addressed in 1994 by Reck *et al.*, who provided for the first time the proof that a reconfigurable $N \times N$ linear photonic circuit with a suited geometry is able to implement any arbitrary linear unitary $N \times N$ transformation, thus being considerable a universal photonic processor [54]. Such a photonic circuit is based on the repetition of a 2×2 unit cell, that is composed by a phase shift on one of the two spatial modes followed by a lossless beam splitter with a tunable reflectivity (Fig. 1.5.a). This elementary circuit is able to realize any arbitrary transformation of $U(2)$ [55], with matrix

$$U_{2\times 2} = \begin{pmatrix} e^{i\theta}\cos\phi & -\sin\phi \\ e^{i\theta}\sin\phi & \cos\phi \end{pmatrix}, \tag{1.6}$$

where $\cos\phi = r$ and $\sin\phi = t$ are respectively the tunable reflection and transmission coefficients of the beam splitter ($r^2 + t^2 = 1$), and where θ is the phase shift. A universal linear photonic circuit can be then built as a mesh of this $U(2)$ element in such a way that it can be associated to the operator

$$U_{N\times N} = D \cdot \left(\prod_{(m,n)} T_{m,n}(\theta,\phi) \right), \tag{1.7}$$

where D is a diagonal matrix whose elements are global phase shifts, and where the $T_{m,n}(\theta,\phi)$ are the matrices associated to the action of only the (m,n) unit cell, which operates on a 2-dimensional subset of the N-dimensional Hilbert space:

$$T_{m,n}(\theta,\phi) = \begin{pmatrix} 1 & 0 & \dots & \dots & \dots & 0 \\ 0 & \ddots & & & & \vdots \\ \vdots & & e^{i\theta}\cos\phi & -\sin\phi & & \vdots \\ \vdots & & e^{i\theta}\sin\phi & \cos\phi & & \vdots \\ \vdots & & & & \ddots & 0 \\ 0 & \dots & \dots & \dots & 0 & 1 \end{pmatrix}. \tag{1.8}$$

By applying a decomposition method involving a step-by-step nulling of some elements of the matrix in Eq. (1.7), Reck *et al.* were able to demonstrate that the triangular mesh presented in Fig. 1.5.a can act as a universal multiport interferometer, provided

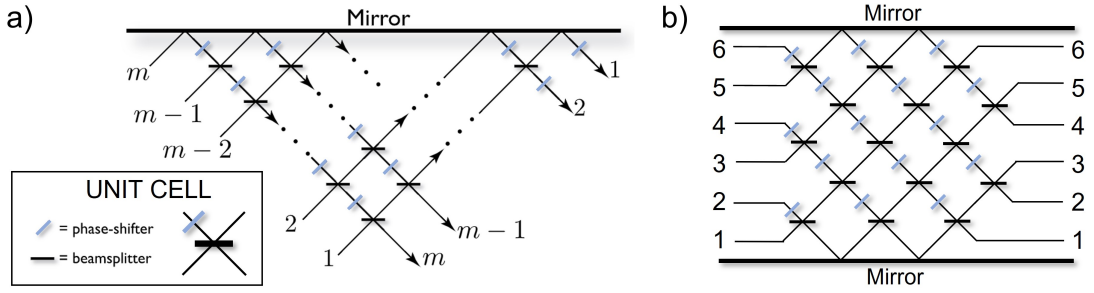

Figure 1.5: a) Reck scheme for a reconfigurable universal photonic processor. The circuit is a mesh of tunable beam splitters and phase shifters, which are arranged in a triangular configuration. b) Example of a six-modes Clements interferometer.

that it is possible to fully reconfigure all the phase shifts and all the splitting ratios of the beam splitters.

In 2016, Clements *et al.* proposed an improved version of the circuit [56], replacing in particular the triangular mesh with a square one (Fig. 1.5.b). This new design provides mainly two advantages over the one proposed by Reck, mostly concerning its experimental realizations. First, it is a symmetric circuit, and this makes it more loss-tolerant, since all the spatial modes are equally affected by possible losses introduced by non-ideal beam splitters. Then, despite using the same $N(N-1)/2$ number of beam splitters, it is more compact, thus providing lower propagation losses and a higher scalability.

Both circuits can be also used to implement $N \times M$ non-unitary transformations, at the cost of increasing their dimensions [57], and can consider realistic lossy circuits as well by adding a scaling factor.

PHYSICAL IMPLEMENTATIONS Both Reck and Clements schemes have been used for experimental demonstrations of universal processing in photonic integrated circuits, which as already stated are preferred to bulk implementations since they provide the scalability needed for the manipulation of many qubits. In particular, the easiest way to implement in integrated optics a tunable beam splitter, required as building block in both configurations, is to exploit a Mach-Zehnder interferometer with two 50:50 directional couplers and a reconfigurable phase shifter ϕ (Fig. 1.6.a), which provides a tunable reflectivity $R = \sin^2(\phi/2)$.

In order to induce a phase shift in the waveguides, thermo-optic [58] and electro-optic [59] phase shifters are widely used, depending on the material. They exploit the dependence of the waveguide refractive index on temperature or applied voltage, respectively, allowing to change the propagation constant β of the guided light [60]. In the recent years, reconfigurable universal photonic circuits were implemented with several technological platforms, such as silicon [61, 62], silica-on-silicon [63], and silicon nitride [64].

The state of the art in this respect is represented by the 12-modes universal quantum photonic processor (Fig. 1.6.c) by the Dutch company QuiX [65]. The device, fabricated in Si_3N_4 and designed to guide light at 1550 nm, is composed by 66 MZIs with 156 thermal phase shifters disposed in the Clements configuration. The circuit proved to be able to implement arbitrary transformations, both with classical and quantum light, with an average fidelity of about 90% (Fig. 1.6.d). Despite the remarkable number of modes achieved, the possibility to further scale the circuit operation is currently affected by two factors. The first is represented by the quite high losses. As a matter of fact, the device shows overall insertion losses of 5 dB, where 0.8 are attributed to propagation losses and the remaining to coupling losses, 2.1 dB per facet. The latter value can in particular be explained by the high confinement of the SiN waveguides, which if on the one hand allows to reduce the radius of curvature and increase the compactness of the circuit, on the other hand causes a large mismatch between the guided mode and the mode of a standard optical fiber. The second issue is represented by the power consumption. In particular, for implementing a π-shift, a voltage of about 10 V should be applied to every phase shifter, with an average dissipated power of 385 mW per element. It is quite understandable therefore that a careful heat dissipation must be considered when the circuit is working with all the shifters actuated.

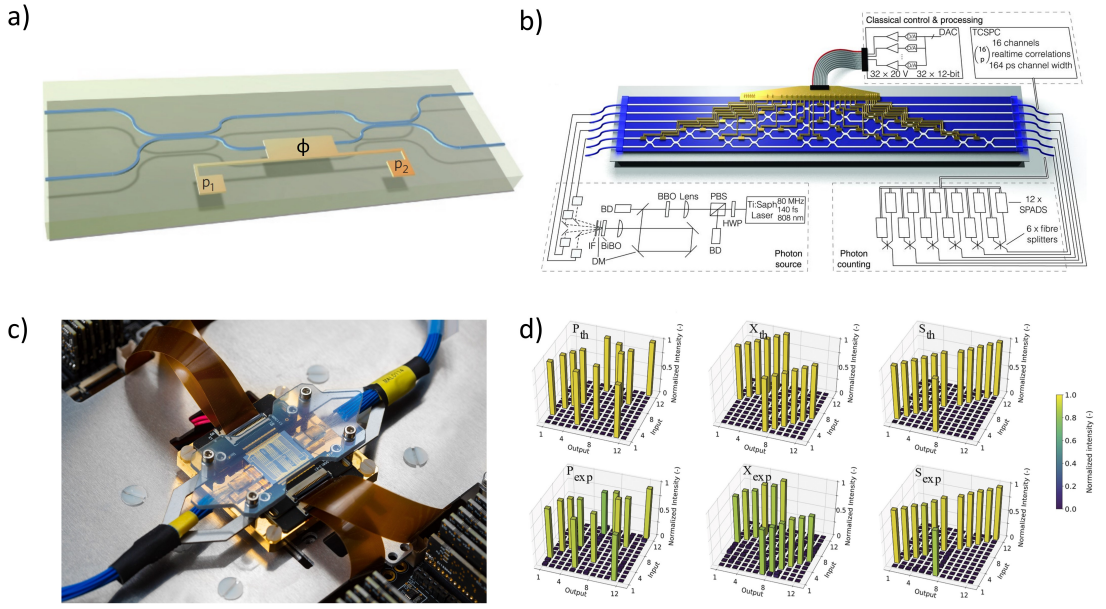

Figure 1.6: Examples of integrated reconfigurable quantum photonic linear circuits. a) A beam splitter with a variable reflectivity can be obtained by an MZI built with two balanced directional couplers and a controllable phase shifter, which is used to tune the power splitting between the two waveguides. Adapted from [58]. b) 6-modes universal linear circuit proposed in [63] based on the Reck scheme. c) Picture showing the optical and electrical connections of the 12-modes photonic processor by QuiX. d) Graphs comparing the theoretical and experimental operations performed by the QuiX processor (random permutation, Pauli X-gate and switching matrix respectively). Both c) and d) are taken from [65].

1.2.2.2 *Single photon sources*

The efficient generation of single photons with high purity and indistinguishability (see Appendix A) is one of the main requirement for the implementation of LOQC. Currently, the most used way to generate them is by spontaneous parametric down-conversion (SPDC) [66]. This process exploits the nonlinear $\chi^{(2)}$ of some crystals, such as β-barium-borate (BBO) and bismuth-borate (BiBO), to convert a pump photon into a pair of signal and idler photons, whose wavelengths and directions satisfy the energy and momentum conservation (Fig. 1.7.a). This technique enables the generation of single photons with very high quality [67], and provides also the possibility to emit pairs of photons entangled in several degrees of freedom, such as polarization [68] and frequency [69]. However, being based on a probabilistic process, it does not allow to generate photons efficiently. Different improvements were proposed in literature, like efficient heralding schemes [70] and the integration of sources directly in optical waveguides [71, 72] to increase the coupling efficiency. Nevertheless, the probabilistic nature of the process remains an issue for the realization of a scalable single photon source, and this is also true for other alternative non-deterministic techniques such as spontaneous four-wave mixing (SFWM) in $\chi^{(3)}$ materials [73].

A way to obtain deterministic on-demand single photon generation is by employing physical systems which naturally act as single photon emitters upon optical or electrical excitation, such as trapped atoms [74], trapped ions [75], and solid-state emitters [76]. Among the latter, semiconductor quantum dots (QDs), which are strain-induced nanometric islands in semiconductor materials like InGaAs [77], provide outstanding performances in terms of brightness, purity and indistinguishability [78], and can be integrated in photonic circuits (Fig. 1.7.b) for increasing the extraction efficiency [79]. The main challenge is however to achieve indistinguishable parallel emissions from different samples, which would allow to implement a scalable source of N photons. Nevertheless some improvements are under investigation, like the possibility to tune their emission properties [80] for increasing their indistinguishability. In alternative, a single source can be used for generating N photons by employing demultiplexing techniques [81], at the cost of reducing the emission rate by at least a factor of N .

1.2.2.3 *Single photon detectors*

A system built with efficient single photon emitters and a lossless optical circuit would not be used to its full potential without efficient photon detectors. In particular, among the main requirements for an ideal detector we list a high detection efficiency η, which is the probability to detect a photon when it impinges on the sensitive area; a low dead time τ_d, i.e. the time the detector needs to recover its original state after a detection; a low time jitter τ_j, which is the width of the output signal; and finally a low dark count rate C_d, i.e the number of false detections per second [82].

Avalanche photodiodes (APDs) working in Geiger mode, also called single-photon avalanche diodes (SPADs), are currently the preferred choice. They exploit avalanche

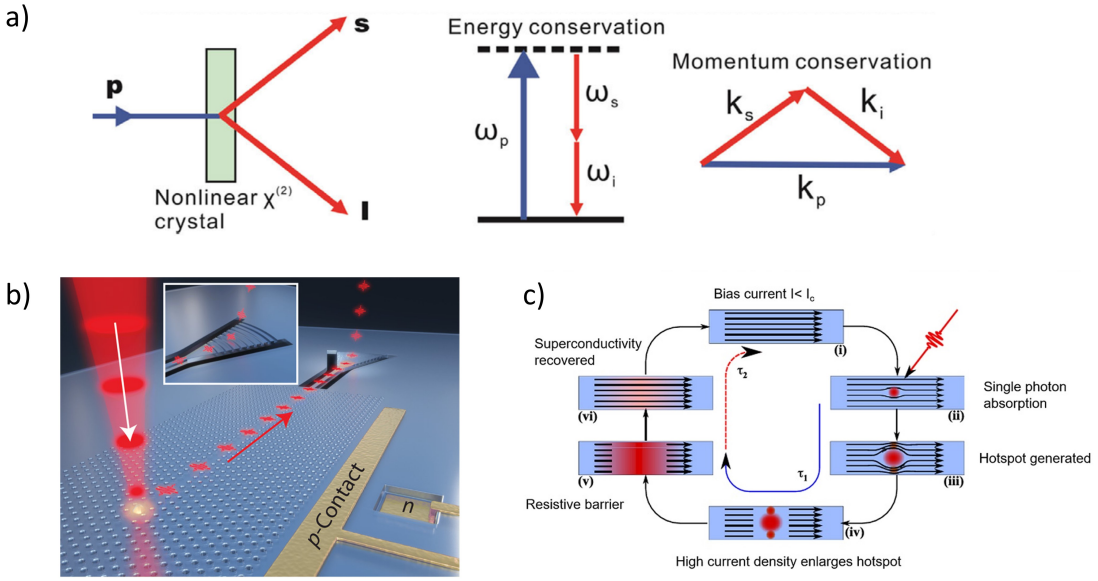

Figure 1.7: Examples of single photon sources and detectors. a) Generation of a single-photon pair by SPDC. A pump photon (p) is converted in a nonlinear crystal in two daughter photons, signal (s) and idler (i). The frequencies and the momenta of the three photons satisfy the conservation laws. From [88]. b) Excitation of a quantum dot coupled to a photonic crystal waveguide for efficient single photon generation. From [89]. c) Working principle of SNSPDs. A bias current slightly lower than the critical one is applied to the superconducting detectors. When a photon is absorbed, a hotspot is generated and the superconductivity is locally broken, causing a sudden increase of the resistance and a detectable voltage spike. From [85].

processes subsequent to the absorption of light to amplify the generated electrical signal, in such a way that the latter can be measured even when triggered by only one photon. They enable detection in both visible and NIR spectra depending on the material (Si and InGaAs respectively), with low time jitters ($\sim$ 50 ps) and good dark counts [83]. However, they are limited in detection efficiency, reaching in the best cases $\eta \sim 65\%$, with lower values for telecom wavelengths. Moreover, their dead time is in the order of tens of ns [84], thus limiting the maximum repetition rates to few MHz.

Better performances in terms of efficiency ($\eta \sim 80 - 90\%$), dead time (few ns) and dark counts (few Hz) are provided by superconducting nanowire single-photon detectors (SNSPSs) [85]. These devices work close to critical conditions, so that even the absorption of the energy carried by one single photon can temporarily destroy their superconductive state (Fig. 1.7.c). However, their main limitation is currently the necessity to operate at cryogenic temperature, which requires complex setups and could be a disadvantage for their integration in reconfigurable photonic circuits, since these mainly use thermal shifters [86]. Nevertheless, there have been promising demonstrations of SNSPDs integrated in passive circuits [87].

1.2.3 *Quantum supremacy in the NISQ era*

In 2018, John Preskill defined the current and the next years as the *noisy intermediate-scale quantum* (NISQ) era [90]. This expression includes the quantum technologies that will be available in the near future, in particular quantum processors that will manipulate up to a few hundreds of qubits with noisy gates and without reliable quantum error correction algorithms, thus not being able to efficiently protect the quantum states from losses and decoherence. In the meanwhile, classical computers will keep improving their performances, both in terms of hardware and efficiency of the implemented algorithms [91]. In this framework, it will be challenging to implement a universal quantum computer capable of outperforming or even being comparable to a classical one.

A more feasible milestone is to prove the so-called *quantum computational supremacy*, i.e. the advantage that a quantum computer would provide in solving specific problems that cannot even be approximated by any classical algorithm [92]. In this respect, the interest towards sampling problems for demonstrating quantum advantage has increased over the years [93]. This kind of problems consists in sampling, exactly or even approximately, a string composed by n qubits from a specific probability distribution. Sampling tasks are preferred to other problems, such as factoring and decision ones, since they can be implemented without the need of a fault-tolerant universal quantum computer [94], thus representing an appropriate choice for NISQ technologies. Moreover, it is strongly believed that classical algorithms able to efficiently solve or even approximate them cannot exist, since this would imply the collapse of the polynomial hierarchy [95].

The first claim of quantum supremacy was reported in 2019 by Google researchers [96]. By using their Sycamore processor (Fig. 1.8.a-b), composed of 53 superconducting transmon qubits, they were able to efficiently take, in about 200 seconds, 1 million samples from the output distribution of a pseudo-random quantum circuit, a task that they claimed to be achievable in about 10,000 years by the most performing classical supercomputer. After some time, however, IBM researchers claimed that the same problem could be solved on a supercomputer in few days by using an optimized classical algorithm [97], thus reducing the advantage achieved by the quantum calculation. This argument shows that it is not so trivial to demonstrate a quantum advantage at the moment, since the quantum computations should be compared with the best classical algorithms for a fair evaluation.

In 2020, quantum supremacy also with photons was reported [98], based still on a sampling problem called gaussian boson sampling (GBS) [99]. In particular, in the experiment the researchers were able to sample the output distribution of an optical bulk interferometer (Fig. 1.8.c-d), fed with 50 single-mode squeezed vacuum states, with a sampling rate they claimed to be 10^{14} times faster than any state-of-the-art supercomputer could achieve. The setup was then improved the following year, ob-

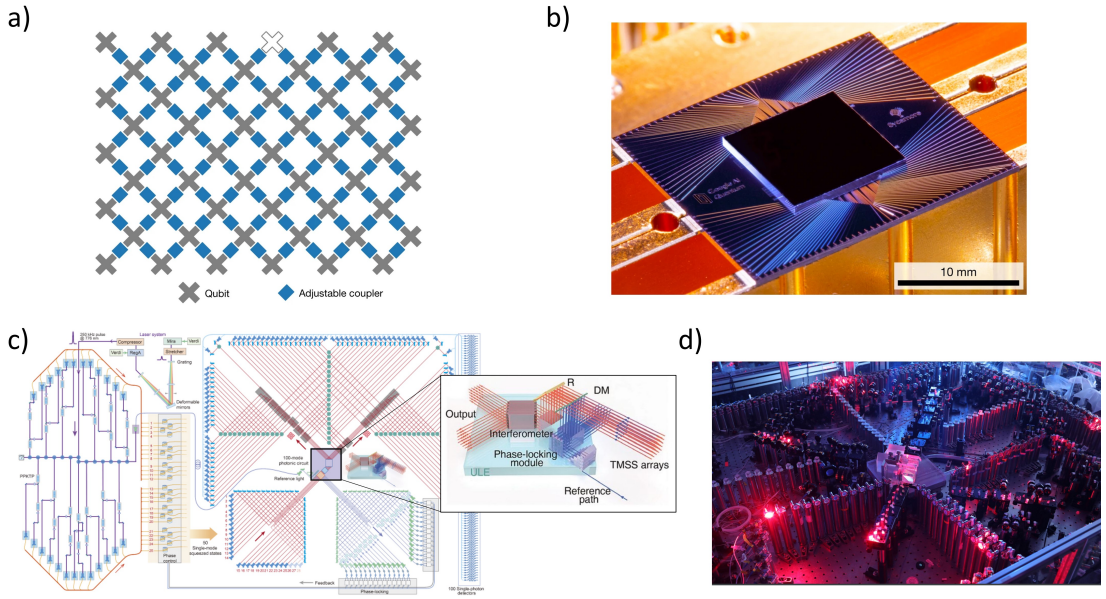

Figure 1.8: Quantum supremacy with superconducting qubits and photons. a) Scheme of the Sycamore quantum processor by Google. The gray crosses represent the 53 working qubits (the white qubit was not operational), while the squares are the couplers used to implement the two-qubits gates. b) Picture of the Sycamore chip. c) Scheme of the GBS setup, where the sources, the optical network and the detectors are represented. The inset shows a sketch of the bulk interferometer, built by gluing together small pieces of glass acting as beam splitters. d) Picture of the GBS setup. Images a) and b) are from [96], c) and d) from [98].

taining samples with up to 113 photons and thus further enlarging the Hilbert space the system operates in [100].

Due to its importance in the field of quantum photonics, the boson sampling problem will be addressed more in detail in the next section, by providing a theoretical background and some additional examples of experimental implementations.

1.2.3.1 *Boson sampling with photons*

Boson sampling (BS) was proposed by Aaronson and Arkhipov as a way to experimentally prove the speed-up provided by quantum computation without the need of a universal, fault-tolerant quantum processor [101]. The problem consists in sampling from the output distribution of n indistinguishable bosons which interfere in a randomly chosen linear network, described by an m-modes unitary U, with $m > n$.

If we define as $|S\rangle = |s_1 s_2 ... s_m\rangle$ the input state vector and as $|T\rangle = |t_1 t_2 ... t_m\rangle$ the output state, we have that the probability of transition from a specific state $|S\rangle$ to $|T\rangle$ is [102]

$$P[S \to T] = \frac{|\text{perm}(U_{S,T})|^2}{s_1! ... s_m! t_1! ... t_m!}, \tag{1.9}$$

with $U_{S,T}$ an n-dimensional submatrix of U, obtained by repeating s_i times its i-th column and t_j times its j-th row, and with $\mathrm{perm}(U_{S,T})$ its permanent [1]. The computation of the permanent of a matrix is known to be not efficient classically, being a #P-hard problem [103]. In fact, the best classical algorithm for its calculation requires $O(n2^n)$ steps, so the boson sampling problem becomes classically intractable for already $n \sim 50 - 100$ [104]. Instead, it can be naturally solved by employing photons that propagate in an optical random linear network. For this purpose, three elements are needed:

- Single photon sources for the generation of the n photons. Each of the m modes should contain either zero or one photon, since having more of them in the same mode could make the permanent computation easier.
- An m-modes photonic interferometer associated to a Haar-random [105] unitary operator U. The randomness is required for avoiding any particular structure that could be exploited by a classical algorithm.
- Single photon detectors at every output of the interferometer to sample the output distribution.

Moreover, since currently the most used detectors do not have photon-counting capabilities [106], it is required $m \sim O(n^2)$: in this particular case the output modes will have indeed a very low probability of containing more than one photon, due to the bosonic birthday paradox in Haar-random unitary matrices [107].

PHYSICAL IMPLEMENTATIONS The first implementations of BS with photons [109–111] exploited SPDC sources pumped with high intensity lasers, since in this way it is possible to generate from a single nonlinear crystal two or more pairs of indistinguishable photons (Fig. 1.9.a). Though with this technique it was possible to obtain quantum interference of up to four photons, this approach is not scalable to higher modes, since it becomes exponentially less efficient. To solve this issue, different improvements were reported, using integrated sources [112] or spatially demultiplexed QD sources [113, 114] to improve the generation probability and the coupling with the interferometer. Moreover, two more efficient variants of the original boson sampling

1 The permanent of a matrix B is defined as [103]

$$\mathrm{perm(B)} = \sum_{\sigma \in S_n} \prod_{i=1}^{n} b_{i,\sigma(i)},$$

and the algorithm for its calculation is basically equivalent to the one used for calculating the determinant, with the difference of replacing the negative signs with the positive ones:

$$\mathrm{perm} \begin{pmatrix} a & b & c \\ d & e & f \\ g & h & i \end{pmatrix} = a \cdot (ei + fh) + b \cdot (di + fg) + c \cdot (dh + eg).$$

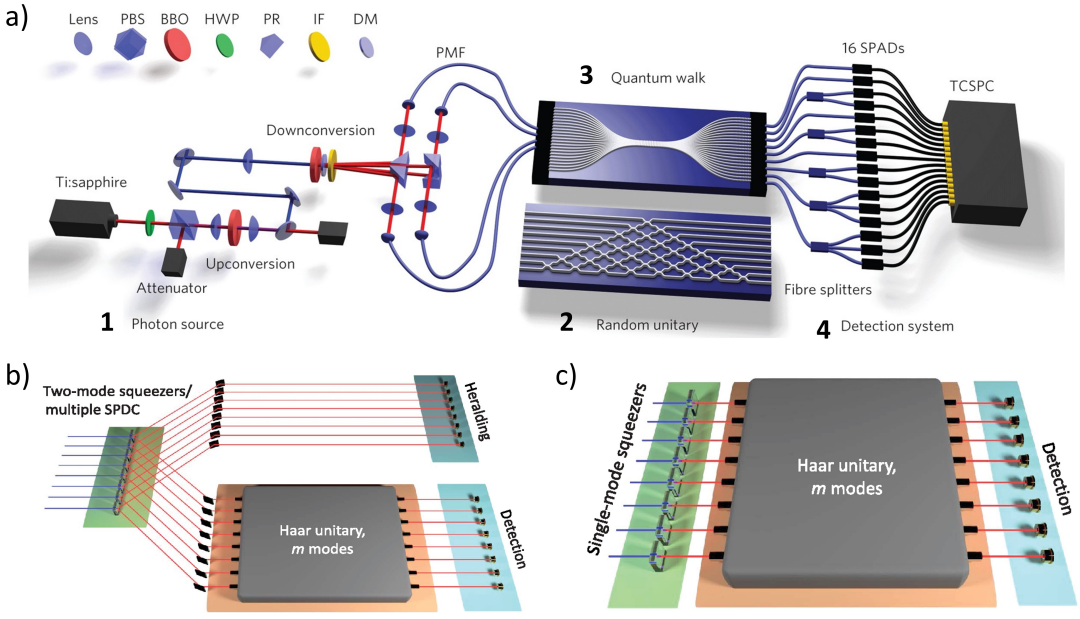

Figure 1.9: Physical implementations of boson sampling with photons. a) Scheme for boson sampling presented in [108]. A single SPDC source is pumped with an intensity suited for the simultaneous emission of two pairs of photons (1). The photons are then injected in an interferometer performing a Haar-random unitary transformation. Two possible implementations are represented: a network of cascaded beam splitters with random reflectivities (2), and random quantum walks based on continuously-coupled waveguide arrays (3). The output distribution is then sampled by using single-photon detectors (4) connected to a coincidence electronics. Adapted from [108]. b) Scheme for scattershot boson sampling experiment. Multiple nonlinear crystal are weakly pumped to generate no more than a photon pair each: one of the photons is used for heralding, the other is injected in the photonic circuit. c) Implementation of gaussian boson sampling. Single-mode squeezed states are generated by nonlinear crystals and used as inputs of the interferometer. Both b) and c) are from [102].

problem were proposed. In the first one, called scattershot boson sampling (SBS) [115], k SPDC sources are used at the same time, pumped with low intensities to have only one pair generation per crystal. Of the two emitted photons, one is used to herald the emission of the other, which is injected in the linear network (Fig. 1.9.b). If $k > n$, this approach provides a higher probability of injecting n photons in the circuit, at the cost of having the inputs chosen uniformly at random. With this approach, up to $n = 12$ photons were reported [116]. The second variant of BS is the aforementioned gaussian boson sampling (GBS), which uses single-mode squeezed states (Fig. 1.9.c) instead of Fock states, with a further advantage in photon generation probability [99].

Despite quantum supremacy with photons was obtained with bulk optical elements, a more scalable approach is for sure represented by employing integrated photonics, which can provide the required miniaturization and reconfigurability. In literature, the majority of the BS implementations used either fiber splitters [113] or integrated circuits fabricated with different platforms, such as femtosecond laser writing [110, 117],

SiO_2 [63], silicon [118] and silicon nitride [108]. To achieve the randomness required in the implementation of the optical network, the main realizations involved the random reconfiguration of a universal circuit based on Reck or Clements schemes, such as [63], or non-universal layouts based either on directional couplers with random reflectivities or on random continuously-coupled waveguide arrays (Fig. 1.9.a). The latter proposals, relaxing the universality requirement, have the advantage of being more compact and requiring easier fabrication processes. However, they enable the implementation of only one Haar-random transformation.

As a final remark, we note that losses of photonic circuits are an issue to address also in this case, since they limit the scalability of the number of photons and modes that can be used in BS. Indeed, if one photon has a probability $p < 1$ of reaching a detector after propagation in a lossy optical network, then the probability of detecting n photons scales as p^n, reaching very low values already for a small value of n if p is not high enough.

1.2.4 *Quantum computing and neural networks*

There are some tasks, such as pattern recognition, decision-making and adaptive control, in which our brains can easily outperform any current supercomputer, with the further advantage of being much more efficient in terms of dimensions and power consumption [119]. After all, despite the non-deterministic nature of the neural links and the lower speed at which the information is transmitted, the biological brains can benefit both from the redundancy and the high parallelization of the connections among neurons, which are continuously rearranged during the learning process [120]. For this reason, the idea of implementing artificial neural networks (ANN) mimicking the biological ones was proposed in the 1940's [121] by McCulloch and Pitts. From that proposal, researchers showed an increasing interest in this field and, thanks to the technological advances achieved in the last two decades, now we can see applications of neural networks in our everyday life [122–124].

In order to perform more complex tasks, further technological advances are needed, enabling the required parallelization of the computations and the close connections among the several "artificial neurons". In this respect, the field could benefit from the improvement provided by quantum computing and the realization of quantum neural networks (QNN), which would exploit the advantages provided by quantum superposition and quantum parallelism for a substantial speed-up both of the learning process and of the performed tasks [125]. If on the one hand the merging of the two fields would allow to obtain quantum-enhanced neural networks, on the other hand it would make it possible to apply the paradigms of artificial intelligence in the simulation and analysis of purely quantum data [126].

1.2.4.1 *Principles of neural networks*

In a biological neural network, the neurons are linked to each other with variable connections, whose strength is weighted by complex chemical processes in the synapses. The plasticity of the connections is actually what gives to the brain the capability of learning, and is therefore at the basis of memory. Moreover, the output of every neuron is related to the input signals it receives from the other ones in a non-linear way, usually involving a threshold [127].

The model proposed in [121] for the realization of an artificial neuron, called *perceptron*, takes into account these aspects. In its simplest form (Fig. 1.10.a), the output y_k of the k-th neuron is the result of a nonlinear function $f(\cdot)$ applied to the sum of a bias b_k and the input signals x_i received from the other neurons, which are weighted with different weights w_{ki}:

$$y_k = f\left(\sum_i w_{ki} x_i + b_k\right), \tag{1.10}$$

with $f(\cdot)$ which is often the step function $f(u) = \theta(u)$ or a sigmoid function such as $f(u) = 1/(1+e^{-au})$. According to this model, the neuron will fire if $\sum_i w_{ki} x_i > \theta_{th}$ and its output will be received by other neurons, otherwise will remain at rest.

The training of the network is based on the adjustment of the weights w_{ki}, in order to strengthen the connections among neurons that were useful during a particular task, and suppress the not used ones. In particular, both supervised and unsupervised learning are possible [128]. In the first case, the network is provided with a series of inputs, and the weights, initially chosen randomly, are adjusted in every iteration in order to make the output of the whole network as close as possible to the desired one:

$$w_{ki}(t+1) = w_{ki}(t) + \eta(d_k - y_k)x_i, \tag{1.11}$$

with η the learning coefficient ($0 < \eta < 1$), and d_k the desired output of the k-th neuron. Unsupervised learning, instead, includes only unlabeled data without suited outputs, and during the training the neural network finds patterns in the data without human intervention.

1.2.4.2 *The idea of a quantum neural network*

The idea behind the implementation of a quantum neural network is to replace the classical signals with quantum states endowed with a modulus and a phase [125]. In this respect, for fully exploiting the enhancement provided by the quantum regime, the neural network should receive quantum signals as input, process them via a combination of linear and nonlinear operations, and provide as well quantum states as output. The *quantum neurons* should be connected among each other by complex weights $\hat{w}_{ki}$, in such a way that the output of the k-th neuron can be expressed, in analogy with Eq. (1.10), as [129]

$$|y_k\rangle = \hat{F}\left(\sum_i \hat{w}_{ki} |k_i\rangle\right). \tag{1.12}$$

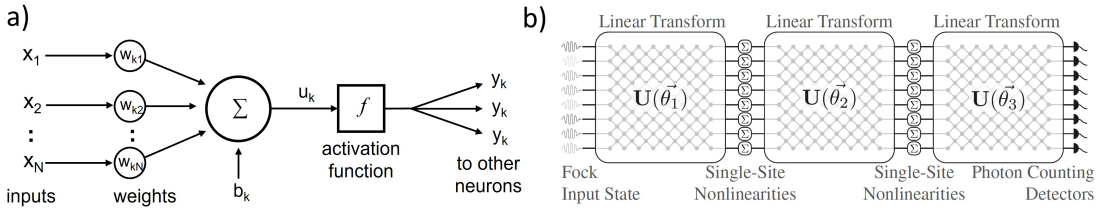

Figure 1.10: a) Scheme of an artificial neuron, which receives weighted input signals x_i by other neurons and, after processing them via an activation function f, provides other neurons with its output. b) Possible implementation of a quantum neural network in a photonic linear circuit accepting Fock states as input It should be noted that in this case the network is composed both by linear and nonlinear elements. From [134].

However, a critical difference between classical and quantum proposals is the training of the network. In fact, every learning procedure, in particular the supervised one, consists in comparing in each iteration the output of the linear network with a suited one, and then adjust the weights accordingly. Therefore, a measurement should be performed on the output state of the neuron, thus destroying the quantum superposition. Moreover, the nonlinear activation of a quantum neuron based on the inputs it receives from the other ones could be challenging to implement experimentally [130]. Though there are several proposals addressing the main issues [131–133], a clear implementation of a quantum neural network has not stood out yet.

PHOTONIC IMPLEMENTATION Since the proposal of quantum neural networks, it was clear that photonics could represent a good platform for their implementation [135], since the same features useful for quantum computation could be exploited also in this field. For instance, it could be possible to use propagating photons as signals between neurons, and encode the quantum information in the polarization or path degrees of freedom, as occurring for a qubit.

In this framework, the weights $\hat{w}_{ki}$ are 2×2 operators in the $(|0\rangle, |1\rangle)$ basis, and they can be physically implemented by means of beam splitters, phase shifters and tunable attenuators, the latter for controlling the strength of the neural connections. For obtaining a trainable quantum photonic neural network (Fig. 1.10.b), however, some nonlinear elements are needed as well [134], and this is the main challenge that the field should overcome, together with the scalability of the system as it is in quantum computing in general.

1.3 QUANTUM COMMUNICATIONS

Quantum technologies are expected to revolutionize the field of communications by increasing both the security and the speed of the transmissions. For instance, by employing dense coding protocols [136], it could be possible to use the transmission of entangled qubits for increasing the capacity of the communication channels, and therefore the bit rate. Moreover, the advanced protocols of quantum cryptography could be used to obtain secure transmissions where an eventual eavesdropping could be clearly detected [137], with possible applications in fields like e-commerce, privacy management and military communications.

The transfer of qubits is important also for quantum computing, since in a complex architecture the several element composing a quantum computer, such as quantum processors, quantum memories and quantum sensors, should be able to interact and exchange information encoded in quantum states [138].

Regardless of their possible application, one of the main requirements of quantum carriers is to transfer information with high fidelity and low decoherence. Therefore, in this regard photons represent probably the most promising implementation, thanks to their long coherence times and negligible interaction with the environment.

1.3.1 *The quest for a secure communication*

The need of encrypting information in order to have secure communications is quite old, and can be dated back to Greeks and Romans. The idea behind almost any implementation of classical cryptography is that the two parts that would like to exchange a private message, called traditionally Alice and Bob, should both cipher and decipher it by using a common key known only by them. In this way, even in the case and external eavesdropper, Eve, is able somehow to obtain the message, she will not be able to understand it.

In principle, a theoretically secure communication could be achieved by using the one-time-pad (OTP) protocol [139], which states that Alice and Bob should use, for every message, a new random key of the same length of the message itself. In this case, however, the speed at which the actual message can be transmitted would be halved, since half of the channel capacity would be dedicated to the distribution of the key. Moreover, it would still be necessary to exchange the key on a secure channel for avoiding any *man-in-the-middle* attack. A secure key distribution, however, is difficult to achieve, and this is an issue for all the protocols implementing a symmetric cryptography, in which the key is the same for encryption and decryption [140]. For this reason, currently the most used and secure protocols are based on asymmetric or public-key cryptography [141], which takes into account the existence of two different keys, one public and one private. In this framework, when Bob wants to receive an encrypted message from Alice, he publishes the public key that she should use to ci-

pher the message. Once the encrypted message is received by Bob, he can decrypt the message by using his private key, which is known to no one, not even to Alice.

Asymmetric cryptography relies on some particular functions [142] whose output is easy to compute once known the input, but which are computationally hard to invert given their output[2]. The most common cryptographic protocols use classically hard problems, such as the factorization of large numbers or the calculation of discrete logarithms, to guarantee their security, since a decryption of the exchanged message without knowing the key would require an exponentially increasing amount of time and resources [143]. In this respect, it was already explained in Sect. 1.2.1.2 that in 1994 Shor proposed an algorithm implementable on a quantum computer for efficiently factorizing large numbers [46], therefore the construction of a large scale quantum computer could put at risk all the current cryptographic protocols.

For overcoming this problem, two main solutions have been proposed. The first one is to improve the public-key protocols for making them unbreakable by a quantum computer, creating an actual *post-quantum cryptography* [144]. This approach would be easily implementable with the current infrastructure, and there have been already some demonstrations in this respect [145]. The second approach would be an improvement of the infrastructure itself based on transmission of quantum states, which would allow for example to safely distribute private keys [146]. It is likely that the two approaches will be combined, in order to take advantages from both of them.

1.3.2 *Quantum key distribution*

Quantum key distribution (QKD) is probably the most known implementation of secure communications based on quantum mechanics. It provides a safe way for Alice and Bob to exchange a common key, in such a way that they can use it both for encryption and decryption without the risk of being eavesdropped [147]. Notably, if the key is composed by a sequence of qubit, also in the event that Eve was able to obtain it, she would not be able to copy it due to the no-cloning theorem, which states that it is impossible to replicate an arbitrarily unknown quantum state [148]. Therefore, the only way Eve can get the key is by measuring the original one, which should then be put back in the communication channel to be received by Bob. In this case, however, if Alice and Bob confront the sent and received keys, they will observe some anomalies and so realize that an eavesdropping has occurred. At this point, they can simply discard the distributed key and perform a second exchange.

In QKD, only the key is encoded in quantum states, since once the key is securely exchanged it is possible to classically transmit the message by using symmetric protocols, like the aforementioned one-time-pad. Moreover, the quantumness of the transmission implies that only real-time eavesdroppings are possible, since the key is destroyed

2 To be more precise, the theoretical existence of the class of one-way functions is still a conjecture, since it is related to the P = NP problem. Therefore, cryptographic protocols can currently employ only problems approximating them.

when Bob measures it. However, for the success of QKD, Eve should not be able to replace one of the two parties, and this can be achieved by authenticated channel, which can also be classical since in this case they can provide already a good level of security [149].

1.3.2.1 *The BB84 protocol*

The most known protocol for QKD was proposed in 1984 by Bennett and Brassard, and goes under the name of BB84 [150]. According to this scheme, Alice can send the common key to Bob in a safe way by using single, indistinguishable photons. In particular, the protocol starts with Alice generating a sequence of N random classical bits. For every bit, she has the possibility to encode it in one of two uncorrelated polarization bases of the corresponding photon, which can be $(|H\rangle, |V\rangle)$ and $(|+\rangle, |-\rangle)$, obtaining the relations in table 1.1. It should be noted that the choice of encoding for every bit should be random as well.

Basis choice	*Bit value*	*Final qubit state*
$(\|H\rangle, \|V\rangle)$	0	$\|H\rangle$
$(\|H\rangle, \|V\rangle)$	1	$\|V\rangle$
$(\|+\rangle, \|-\rangle)$	0	$\|-\rangle$
$(\|+\rangle, \|-\rangle)$	1	$\|+\rangle$

Table 1.1: Correspondence between the bits and their encoding, depending on the chosen basis.

At this point, the photons are sent to Bob, who measures their states without knowing Alice's encoding, so he must choose randomly between the two bases. Therefore, he has a probability of 50% of choosing the same basis as Alice, and in this case he will retrieve the correct bit value, while if he chooses the other basis he will have the same probability of measuring the correct or the wrong bit. This uncertainty is removed when, at the end of the transmission, they publish on a classical channel their bases choices. In this way, they can discard the qubits whose measurement occurred in the wrong basis, while they can keep the others, which will compose the so-called *sifted key*. In order to understand if an eavesdropping occurred, Alice and Bob should publish a portion of the remaining sequence and measure its quantum bit error rate (QBER), which is the rate of qubits received in the wrong state. If the QBER is low and in agreement with the channel noise, no one hacked the transmission and so they can use the remaining bits as their key. However, if Eve broke into the channel and performed some measurements on the key, re-sending it to Bob afterwords, the QBER will be inevitably higher. Indeed, like Bob, Eve has to choose randomly the basis, and this translates in a probability of measuring the wrong state 25% of the times. Therefore, in this case Bob has a significant probability of measuring the wrong bit even when he chooses the correct basis.

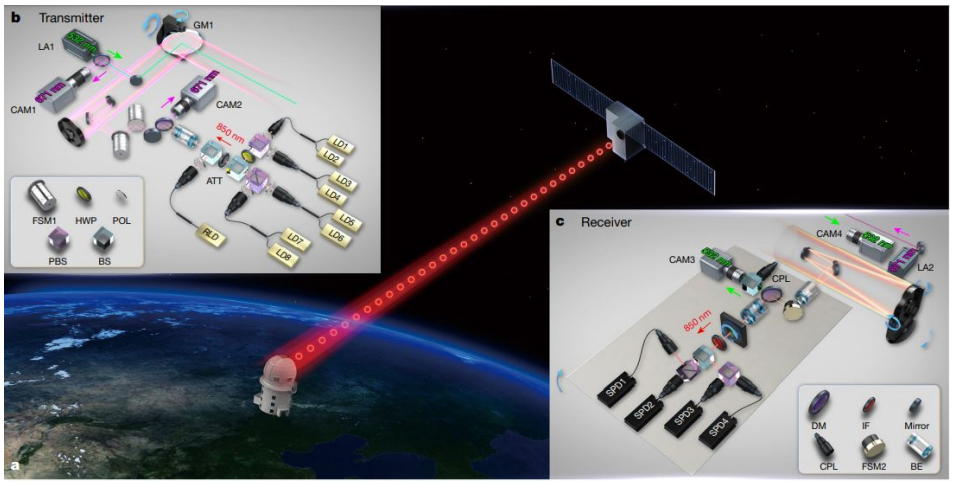

Figure 1.11: Satellite-to-ground quantum key distribution with the Micius satellite [158]. a) The Micius satellite, orbiting ar around 500 km, is able to exchange photons with ground instrumentation by means of optical telescopes. b) Scheme of the decoy-QKD transmitter present in the satellite. In particular, attenuated laser light at 850 nm is injected in a BB84 setup, and then sent out by a Cassegrain telescope. The output beam can be aligned by means of a gimbal mirror. c) Scheme of the receiver in the ground station. The photons collected by the telescope are sent to a BB84 decoder for their projective measurement. From [158].

1.3.2.2 *Experimental implementations*

One of the first experimental demonstrations of QKD was proposed by Bennett himself in 1992 [151] by using attenuated polarized light[3] propagating in free-space for 32.5 cm. From that proposal, several improvements in regard of the length of the channel have been reported [153], mainly by employing optical fibers [154] which allow to scale up the dimensions of the network. For instance, in 2015 a collaboration between the University of Geneva and Corning Inc. enabled the creation of a 307 km long secure channel [155], with demonstration of QKD with a secret key rate of 12.7 kbps over 104 km, which degraded to 3.18 bps over the whole 307 km network. Moreover, QKD has already been used in some selected everyday life applications, as the 2007 Swiss elections [156] or the long-term security of Chinese industries and banks [157], and some commercial solutions are available on the market by companies such as ID Quantique and MagiQ Technologies, Inc.

Despite the remarkable results, however, QKD over fiber networks is not easily scalable, due to the non negligible propagation losses of optical fibers which affect both the bit rate and the length of the secure channel [159]. If in classical communications losses can be compensated with the use of signal amplifiers, this is not the case for quantum ones, due to the no-cloning theorem. Moreover, the technology that would

3 For simplifying the experimental implementation, a common choice is to use faint laser light instead of single photon sources. However, since in this case the communication could be attacked by exploiting the non purity of the states, some improvements have been proposed, like the use of decoy states [152].

allow to have useful quantum repeaters in quantum networks [160] is still in its infancy, with only laboratory realizations. For this reason, a promising way for implementing QKD over long distances is the use of satellites in space. This solution would in fact allow to overcome the propagation losses in optical fibers, since due to the air rarefaction the effective thickness of the atmosphere is of only about 10 km [161], so its absorption is almost negligible. In this respect, the state of the art is represented by the QUESS (Quantum Experiments at Space Scale) project [158], whose main result was the launch in 2016 of the Micius satellite, orbiting at an altitude of around 500 km. With it, researchers were already able to implement decoy-QKD over 1200 km, a value that was further increased to 7600 km the following year, when the satellite was used for exchanging the first quantum secure video call between the Chinese and Austrian Academies of Science [162].

1.4 QUANTUM METROLOGY AND SENSING

The measurement process represents without any doubt one of the most important aspect of science, since it allows to associate a value to the physical quantities in such a way that a comparison among them is possible. Any measurement, however, is affected by an uncertainty [163], caused both by nonidealities of the process itself and by intrinsic limitations given by physical laws, such as the Heisenberg uncertainty principle [164]. In this framework, one of the purposes of the field of metrology is to improve the measurement processes to overcome these limitations and increase its resolution.

Any measurement is performed by using a probe, which should be prepared in the most convenient way for enhancing its interaction with the physical system we would like to measure. In this way, we can retrieve information on the latter by simply looking at the changes occurred to the probe. If we perform only one measurement, its result can be expressed as

$$\phi = \phi_0 \pm \sigma, \tag{1.13}$$

where ϕ_0 is the actual physical quantity and σ is the uncertainty of the estimation. In order to increase the precision, we can perform n measurements on the physical system or, if the process is destructive, one measurement on n systems prepared in the same way. In this case, due to the central limit theorem, the result of the measure will indeed be

$$\phi = \phi_0 \pm \Delta\phi, \tag{1.14}$$

where $\Delta\phi$ is the total uncertainty, which is bounded from below by the value:

$$\Delta\phi \geq \frac{\sigma}{\sqrt{n}}. \tag{1.15}$$

Eq. (1.15), which is usually referred to at Standard Quantum Limit (SQL), shows that the best improvement we can achieve with repeated, classically correlated measurements scales at best with $\sim n^{-1/2}$.

The limitation provided by the SQL, however, is not intrinsic to the measurement process itself, but is related to a non-optimal choice of the probe. In fact, by using particular quantum probes, this bound can be surpassed and a scaling $\sim n^{-1}$ can be achieved, a result known as Heisenberg Limit (HL) [165]. In this way, by using the same number of resources, it is possible to improve the measurement precision of $\sqrt{n}$. The sensitivity enhancement provided by quantum metrology can be beneficial for several applications, like biology [166], lithography [167], general sensing [168] and imaging [169].

1.4.1 *Photonic quantum metrology*

Photons represent probably the most suited platform for several quantum measurements, thanks to their already mentioned peculiar properties, such as the high mobility and low decoherence. In this regard, two main alternatives are possible. The first one exploits the sensitivity enhancement provided by squeezed states, which allow to increase the measurement precision on one physical quantity at the cost of increasing the uncertainty on its complementary (Fig. 1.12.a), in compliance with the Heisenberg uncertainty principle:

$$\Delta\hat{A}\Delta\hat{B} \geq \frac{1}{2}|\langle[\hat{A},\hat{B}]\rangle|, \tag{1.16}$$

where $\Delta\hat{A}$ and $\Delta\hat{B}$ are the uncertainties on two quantities associated to the operators $\hat{A}$ and $\hat{B}$, and $[\hat{A},\hat{B}] = \hat{A}\hat{B} - \hat{B}\hat{A}$ is their commutator. This approach has been used for instance in the detection of gravitational waves [170], where an uncertainty as low as 10^{-18} m was required.

The second alternative, which will be further investigated in the following, is to use entangled photons like the N00N states, which have the form

$$|\psi\rangle = \frac{|N,0\rangle + e^{i\theta}|0,N\rangle}{\sqrt{2}}, \tag{1.17}$$

and represent a balanced superposition of N photons being either in one optical mode or in another one, with a phase shift θ between the two components (Fig. 1.12.b).

1.4.1.1 *Phase estimation with N00N states*

The optical phase encodes information on some important quantities of a physical system, i.e. wavelength, optical path length and refractive index of the material the light is propagating in. For this reason, phase estimation is an interesting problem in photonic quantum metrology, and can find applications in several fields, such as imaging [171, 172], measurement of velocity or lengths [173] and biological systems [174]. Moreover, phase estimation can be a good tool for benchmarking metrological protocols. However, the association of a self-adjoint operator to the optical phase is an open problem [175], therefore its direct measurement is currently not possible. Instead,

a phase difference between two optical paths is easily measurable by looking at the output of an interferometer, and in this regard the Mach-Zehnder interferometer (MZI) represents one of the most common choices.

The MZI was already introduced in Sect. 1.2.2.1 as the basic element of every universal multimode interferometer. If composed by two cascaded balanced beam splitters - or directional couplers in the integrated case - its operation can be described by the matrix

$$U_{MZI} = \begin{pmatrix} e^{i\theta}\cos\frac{\Delta\phi}{2} & -\sin\frac{\Delta\phi}{2} \\ e^{i\theta}\sin\frac{\Delta\phi}{2} & \cos\frac{\Delta\phi}{2} \end{pmatrix}, \tag{1.18}$$

where $\Delta\phi$ is the phase shift among the two optical paths (Fig. 1.12.c).

If we consider the classical case where laser light is injected in only one of the two inputs:

$$E_{in} = \begin{pmatrix} E_0 \\ 0 \end{pmatrix} e^{i(\omega t - kz)} = \begin{pmatrix} \tilde{E}_0 \\ 0 \end{pmatrix}, \tag{1.19}$$

the output intensity distribution of the MZI will be dependent on $\Delta\phi$:

$$\begin{cases} I_{out,1} = I_0 \cdot (1 + \cos\Delta\phi) \\ I_{out,2} = I_0 \cdot (1 - \cos\Delta\phi), \end{cases} \tag{1.20}$$

where $I_0 = |\tilde{E}_0|^2/2$ is the input intensity. In this way, the phase shift can be retrieved from the MZI outputs by inverting the relations in Eq. (1.20).

If now we consider the simplest quantum case, i.e. a single photon injected in one of the two arms, the quantum treatment requires to consider also the vacuum component at the other port [37]:

$$|\psi_{in}\rangle = |1,0\rangle, \tag{1.21}$$

and this leads to the following output state:

$$|\psi_{out}\rangle = \frac{1}{2}\left[i(e^{i\Delta\phi}+1)\,|1,0\rangle + (e^{i\Delta\phi}-1)\,|0,1\rangle\,\right]. \tag{1.22}$$

If we take the probability of finding the system in the state $|1,0\rangle$ or $|0,1\rangle$, we obtain the same relations of Eq. (1.20), since formally the propagation of classical coherent light in an optical network is equivalent to the propagation of the wavefunction of a single photon. Therefore, in this case the quantum measurement does not provide a sensitivity enhancement in the phase estimation with respect to the classical case.

A different result is obtained however if we let propagate in the MZI two photons, one per input port:

$$|\psi_{in}\rangle = |1,1\rangle. \tag{1.23}$$

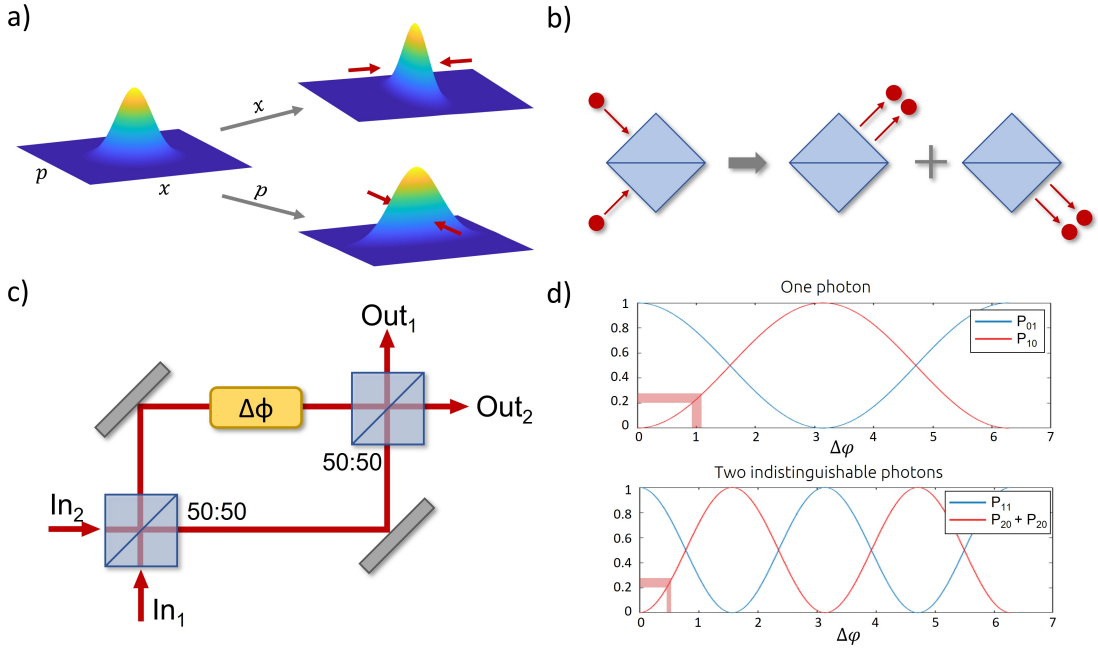

Figure 1.12: Photonic quantum metrology and phase estimation. a) Squeezing operation in the case of position-momentum uncertainty of a photon. The wavefunction can be squeezed for increasing the measurement precision on one of the two quantities, at the cost of increasing the uncertainty on the other. b) Generation of the most trivial N00N state $|\psi\rangle = (|2,0\rangle + |0,2\rangle)/\sqrt{2}$ by exploiting the HOM effect. Two indistinguishable photons injected in the two input ports of a beam splitter have a 0.5 probability of exiting together either from one output or from the other, thus lying in a quantum superposition. c) Mach-Zehnder interferometer composed of two balanced beam splitters. From its output power distribution it is possible to retrieve information on the phase shift $\Delta\phi$. d) Sensitivity of the phase estimation of an MZI with one and two photon states. In particular, if the same uncertainty is present on the measurement of the output probability distribution, when using two photons the uncertainty on the estimated $\Delta\phi$ is reduced.

In this case, we have indeed as output state [176]:

$$|\psi_{out}\rangle = \frac{1}{2\sqrt{2}}(1 - e^{i2\Delta\phi}) \cdot (|2,0\rangle - |0,2\rangle) + \frac{i}{2}(1 + e^{i2\Delta\phi}) \cdot |1,1\rangle\,, \tag{1.24}$$

where it is interesting to observe that now the phase shift $\Delta\phi$ is multiplied by 2. Therefore, if we take the squared moduli of the two components, which represent the probability of having either coincident detections ($|1,1\rangle$) or finding the two photons together in one output ($|2,0\rangle$ or $|0,2\rangle$), we will have as a result an oscillatory dependence on $\Delta\phi$ with doubled frequency. This translates into a higher sensitivity of the measurement (Fig. 1.12.d), and allows to overcome the SQL. This is possible since as a probe

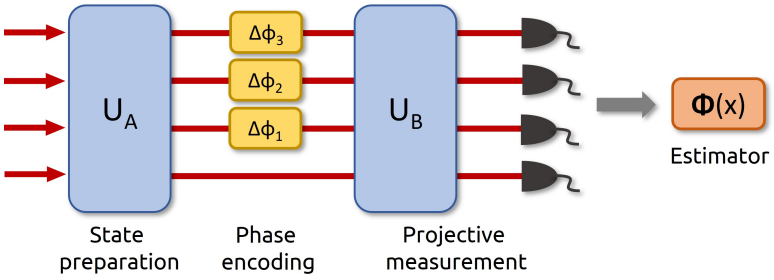

Figure 1.13: Multiphase estimation process. A suitable n-photon input state (in this example $n = 4$) is prepared by the unitary operation U_A, then it interacts with the $n-1$ phase shifts to be estimated, and finally a projective measurement is performed by means of a unitary U_B and single photon detectors.

to measure the phase shift we are using a N00N state with $N = 2$, because after the first beam splitter the state is:

$$|\psi_{BS1}\rangle = \frac{|2,0\rangle + |0,2\rangle}{\sqrt{2}}. \tag{1.25}$$

In particular, it can be demonstrated [177] that the oscillation frequency is linearly dependent on N, and that a N00N state allows to saturate the Heisenberg limit, providing an uncertainty scaling as $\sim N^{-1}$. However, if the generation of the state with $N = 2$ is trivial, this is not true for higher values of N, despite some techniques have been proposed, such as the use of post-selection [178] or the interference at a beam splitter between squeezed and coherent states [179]. Notably, the latter process enabled experimentally the generation of N00N states with N up to 5.

1.4.1.2 *Multiphase estimation*

The process of a single phase estimation can be generalized to the simultaneous estimation of multiple phases by probing them with a suitable n-photon state. This result would allow a further optimization of the measurement process, and for this reason it is widely studied [180, 181].

As for the single phase treatment, we can consider the case of an n-arms interferometer with $n-1$ phase differences to be estimated $\Delta\Phi = \Delta\phi_1, \Delta\phi_2, \ldots \Delta\phi_{n-1}$, defined with respect to the first optical path (Fig. 1.13). The estimation process can be performed by injecting in the interferometer an n-photon state, prepared accordingly by an entangling unitary transformation U_A, in analogy with the operation of the first beam splitter of the MZI. Then, the probe evolves in the interferometer, and the interaction with the phases can be described by the unitary U_ϕ, depending on $\Delta\Phi$. Finally, the modified probe is subjected to another unitary U_B, followed by a projective measurement with single photon detectors at each output. In this way, it is possible to retrieve an estimator $\Phi(x)$ which, if chosen properly, provides a converging estimation of the phase differences in the interferometer.

2

FEMTOSECOND LASER WRITING

In the previous chapter we already discussed the importance of integrated circuits in quantum information processing with photons. With respect to bulk implementations, in fact, the integration of the main functionalities in compact, monolithic devices provides a more stable operation and the possibility of scaling up the number of optical modes. Moreover, the finer control that integrated circuits allow in the manipulation of photonic quantum states enables the implementation of more complex designs and tasks.

In this regard, among the possible fabrication platforms, femtosecond laser writing (FLW) of waveguides in glass substrates represent for sure one of the most versatile [182]. This technique is based on the nonlinear interaction between a focused femtosecond laser and a transparent substrate to induce a localized modification of the bulk material. Depending on the fabrication parameters, e.g. the laser wavelength or the deposited energy, it is possible to obtain different results, such as the creation of voids, the selective removal of material, and the formation of microchannels and optical waveguides [183]. In detail, the possibility of fabricating structures capable of guiding light was reported for the first time in [184] in a fused silica substrate by using an IR laser beam. From that moment, the interest in this platform rapidly increased, and now it is capable of providing complex, reconfigurable photonic circuits for quantum information, with demonstrations of on-chip generation [72], manipulation [117] and detection [185] of quantum states.

With respect to other fabrication platforms, such as lithography on silicon or silica substrates, FLW is a direct writing process which provides fast prototyping capabilities and does not require clean room facilities, being the processing of the bulk substrate less sensitive to its surface cleanliness. Moreover, since the material modification is limited to the focal spot and its immediate surrounding, it is possible to inscribe 3D photonic circuits by simply moving the material in the three dimensions by means of translation stages. Another advantage is its versatility, since it is possible to process any material, as long as it is transparent, due to the nonlinear nature of the interaction. This allows therefore to fabricate waveguides also in crystals or polymers. Its main limitation is however represented by the low induced refractive index contrast, of the order of $10^{-2} - 10^{-3}$, which if on the one hand enables a good coupling with optical fibers, on the other hand reduces the capability of miniaturization, since it is not possible to use radii of curvature lower than few mm without introducing non negligible losses. Moreover, FLW is a sequential technique, and this also reduces the

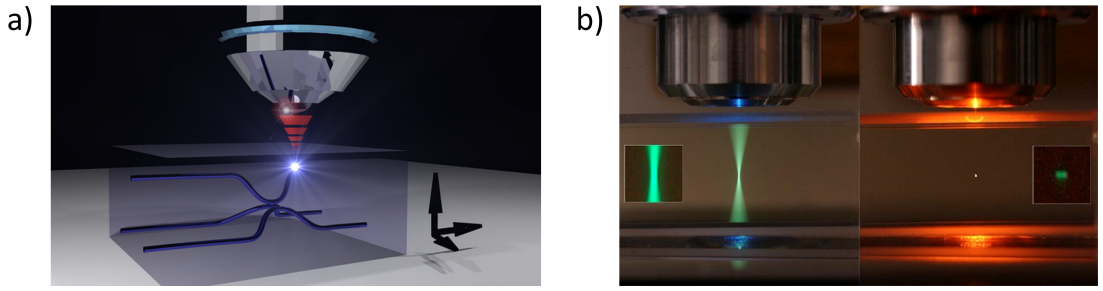

Figure 2.1: Femtosecond laser writing exploiting nonlinear absorption in transparent substrates. a) A fs laser is focused by a microscope objective in a transparent material, thus inducing a permanent modification which can be exploited for fabricating optical waveguides. From [187]. b) Linear versus nonlinear absorption of a focused laser in a fluorescent material. Image from [188].

scalability of the fabrication if compared to parallel processes, despite some advances have been reported in this regard [186]. That being said, if we consider that in the NISQ era the main efforts are being made for obtaining intermediate results and provide proofs-of-concept, we can understand how FLW can nevertheless play an important role in the implementation of photonic quantum technologies.

2.1 LASER-MATERIAL INTERACTION

The process behind the modification of the material induced by its nonlinear interaction with an intense fs laser beam is not completely understood yet [189]. Nevertheless, it is known that the interaction can be divided in two well-defined physical processes, which are the formation of free-electron plasma in the focal volume, followed by a relaxation of the material and a subsequent creation of permanent damages.

2.1.1 *Formation of free-electron plasma*

FLW usually exploits a laser whose photon energy is lower than the energy gap E_g of the material, thus avoiding any possible linear absorption, which could cause larger modifications. In this regime, the promotion of electrons from the valence to the conduction band can occur by two physical processes. The first one, the *multiphoton absorption* (Fig. 2.2.a), consists in the simultaneous absorption of m photons by the same electron, in such a way that if $m\hbar\omega \geq E_g$, the provided energy is sufficient for its promotion. The second one, the *tunneling ionization* (Fig. 2.2.b), occurs when the laser intensity is high enough to distort the energy bands, causing a reduction of the potential barrier and increasing therefore the probability for an electron to move to the conduction band by quantum tunneling. Generally, for low laser intensities and high frequencies the former process is favoured, since the simultaneous absorption of m

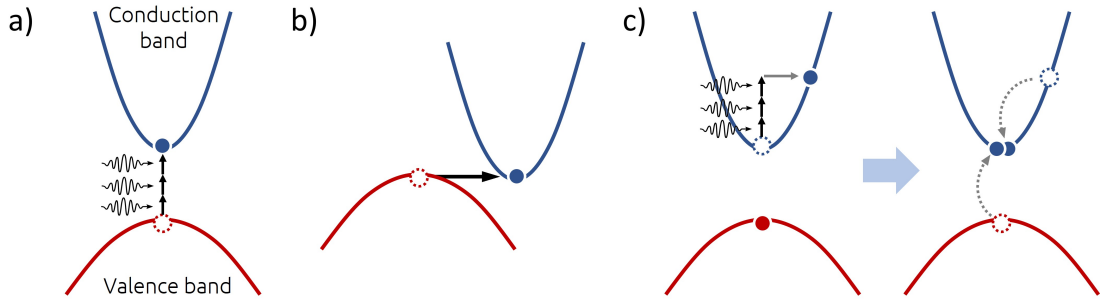

Figure 2.2: Physical processes providing the seed electrons for the plasma generation. An electron in the valence band (in red) can be promoted to the conduction band (in blue) by a) multiphoton absorption, b) tunneling ionization or c) impact ionization, the last one leading to an avalanche process.

photons becomes less probable as m increase, while for high intensities the latter process is predominant. In this regard, the Keldish parameter [190] can be used, defined as

$$\gamma = \frac{\omega}{e}\sqrt{\frac{m_e c n \epsilon_0 E_g}{I}}, \tag{2.1}$$

where ω is the laser frequency, m_e is the electron mass, n is the refractive index of the material, e is the elementary charge and I is the laser intensity. If $\gamma \gg 1.5$, the multiphoton absorption dominates, while tunneling ionization is more favoured for $\gamma \ll 1.5$. Nevertheless, in FLW usually $\gamma \sim 1$, so both processes concur with similar importance.

After its promotion, a free electron can linearly absorb multiple photons without the need to do it simultaneously, therefore it is easier for it to accumulate energy. Notably, once absorbed m photons in such a way that the relation $m\hbar\omega \geq E_g$ is satisfied, an electron in the conduction band can cause the promotion of another valence electron by impact ionization (Fig. 2.2.c). In this way, every promoted electron is the seed for the promotion of an exponentially increasing number of valence electron, thus leading to an *avalanche ionization* process. This regime is what actually makes FLW deterministic and versatile. As a matter of fact, if the modification were caused only by tunneling or multiphoton ionization, the result would be strongly dependent on parameters like laser frequency and energy gap, thus requiring a finer tailoring of the process.

Once the avalanche ionization is started, the density n_e of free electrons greatly increases until it reaches the critical plasma density, defined as

$$n_c = \frac{m_e \epsilon_0 \omega^2}{e^2}. \tag{2.2}$$

From this moment, the plasma, which was previously transparent to the radiation, becomes strongly absorbing [191], so the laser energy is now directly transferred to it and remains localized in the focal spot.

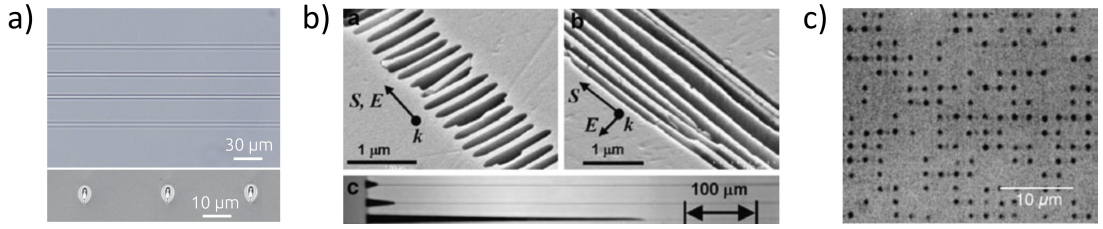

Figure 2.3: Modifications induced by FLW in silicate glasses. a) Generation of a smooth refractive index contrast for fabrication of optical waveguides. b) Birefringent nanogratings which can be selectively etched by HF. From [203]. c) Microvoids. From [201].

2.1.2 *Thermal relaxation and modification*

After the irradiation, the plasma releases the accumulated energy to the surrounding ions by electron-phonon interaction. Since femtosecond laser pulses are used, the generation of plasma is temporally decoupled from the subsequent heat diffusion and relaxation, which require several ps to occur [192]. This allows to maintain the heat confined, and therefore to increase the precision of the process.

Once the energy is released to the lattice, a permanent modification of the material is obtained. Depending on the deposited energy and the used pristine substrate, three main regimes can be defined [193]. Low energies induce a smooth refractive index change, which can be engineered for fabricating integrated waveguides (Fig. 2.3.a). Depending on the material, this change can be explained by different processes, such as the creation of color centers in fused silica [194] or the melting and resolidification of the processed region in the case of borosilicate glasses [195]. By increasing the fabrication energy, in some materials such as fused silica it is possible to obtain the formation of nanogratings (Fig. 2.3.b) with a birefringent refractive index change [196]. Notably, this modification shows a higher sensitivity to etching with hydrofluoric acid [197], and can be exploited for the fabrication of both microfluidic channel [198] and hollow-core waveguides in glass [199] or for nanolithography of crystals [200]. By further increasing the laser energy, it is possible to create voids in the bulk material thanks to the generation of a shock wave (Fig. 2.3.c), a modification which can find application for instance in the storage of photons [201] or in photonic bandgap materials [202].

2.2 WAVEGUIDES FABRICATION

As already mentioned, the fabrication of waveguides by FLW is achieved by exploiting the refractive index modification occurring during the interaction between the substrate and the fs pulses. In particular, the waveguides geometry can be defined by simply moving the material in all the three dimensions by means of precise translation stages with nanometric accuracy. The guiding structures obtained with this technique

are characterized by a fiber-like refractive index contrast, with a guided mode showing a cross section of few μm^2.

The waveguides properties depend non-trivially on the combination of several fabrication parameters, such as the translation speed, the pulse energy, the focusing conditions and the laser repetition rate. Moreover, the inscription process should be tailored on the used substrate and on the desired guided wavelength. In the following sections, an overview of the most important aspects will be presented, with a particular focus on fused silica and borosilicate glasses, which are the most used materials for quantum photonics applications.

2.2.1 *Deposited energy*

The deposited energy per unit length can be controlled by acting on the laser pulse energy and on the scanning speed, since if the translation is slow, the material will interact with the laser for a longer time, thus absorbing more energy. Moreover, several laser scans can be performed on the induced modification for a higher energy deposition [204]. The control on these parameters enables the possibility to slightly act on the refractive index contrast and on the dimension of the modification. In this way, it is possible to achieve optimal guiding conditions in almost the whole transparency window of the material, covering both the VIS and NIR spectra.

2.2.2 *Repetition rate and thermal accumulation*

On the repetition rate it depends the possibility of reaching the heat accumulation regime, which can strongly affect the guiding properties [205, 206]. Notably, for low repetition rates, i.e. < 250 kHz, the laser pulses are separated in time, and this allows the material to thermally relax after every pulse, a process which requires some µs. Therefore, the modification is mainly due to the action of the single pulse, and this generally translates in an elongated cross section of the waveguide, with highly asymmetric modes. Moreover, in this regime low scanning speeds are used, so long fabrication times are required. Low repetition rates are preferred in the inscription of waveguides in fused silica, for which usually Ti:sapphire lasers are used [207].

Higher repetition rate values (> 500 kHz) are instead preferred for the fabrication of waveguides in borosilicate glasses. In this regime, the pulses are closer in time, and so the material does not have enough time to relax after the absorption of a pulse. This causes a heat accumulation, with the modification being dependent on the combined action of the pulse train rather than on the single one. This regime enables more symmetric cross sections and higher scanning speeds, up to $50 - 100$ mm/s, thus reducing the processing time. For achieving this regime, usually Yb-based fs lasers are used, since they provide at the same time high pulse energies and repetition rates up to few MHz [208].

2.2.3 *Focusing conditions*

In order to achieve the peak intensities needed for the process, and for providing a confined modification, the laser beam is focused in the substrate by means of a microscope objective. For obtaining a more efficient focusing, the objective can be equipped with compensation optics reducing chromatic or spherical aberrations.

In fused silica, since the modification is dependent on the single pulse properties, it is possible to engineer the beam shape for changing the waveguide cross section. If we use the approximation of the linear propagation of a gaussian beam in a material with refractive index n [189], we can write the following relations for the waist radius w_0 and the Rayleigh range z_0:

$$w_0 = \frac{M^2 \lambda}{\pi \, \mathrm{NA}}, \qquad z_0 = \frac{M^2 n \lambda}{\pi \, \mathrm{NA}^2}, \tag{2.3}$$

which influence the horizontal and vertical section of the waveguide, respectively. In the formulas, M^2 represents the gaussian beam propagation factor of the beam, λ the laser wavelength and NA the numerical aperture of the objective. Notably, the last parameter can be used to control the shape of the waveguide cross section, since a higher NA can be used to reduce the focus elongation. Nevertheless, high NA objectives are more affected by spherical aberrations. In this respect, oil or water immersion techniques can be used to decrease the refractive index mismatch at the substrate surface [209] and therefore improving the focusing condition.

While in fused silica it is possible to find a correlation between the numerical aperture of the objective and the waveguide shape, in borosilicate glasses this task is not trivial, due to the thermal accumulation process. For this reason, usually it is preferred to act on other fabrication parameters, such as the writing speed and the pulse energy.

2.3 FLW FOR QUANTUM PHOTONICS

The first demonstration of quantum interference in a femtosecond laser-written circuit was reported in 2009 [210], when it was observed the HOM effect (see Appendix A) for two indistinguishable photons injected in a directional coupler fabricated with this technology. From that moment, FLW has shown to be a complete platform for integrated quantum photonics, mostly for what it concerns the fabrication of passive and active circuits for the manipulation of quantum states of light. We already saw how it is possible to combine directional couplers and phase shifters for achieving a universal photonic processor, and FLW can provide these elements with low losses and high fidelity. Moreover, the unique advantages of this technique, such as the low waveguide birefringence or the 3D capability, which are both difficult to achieve with planar lithographic platforms, can be used to exploit the photon polarization degree of freedom or simplify the circuit complexity.

FLW quantum photonic circuits have been used for several applications, such as the generation of Bell states [211], on-chip quantum tomography [212], and photonic quantum metrology [213]. In detail, remarkable results were achieved in the fabrication of multi-port interferometers, used for studying multiphoton interference [214, 215] and for implementing boson sampling experiments [110, 117]. Moreover, by exploiting the formal equivalence between the Schrödinger equation and the propagation of light in a photonic circuit, several FLW simulators of quantum systems or phenomena were reported, e.g. quantum random walks [216, 217], Bloch oscillations [218] and topological insulators [219]. In the following, some of the main examples will be presented, with particular attention in highlighting the peculiar properties of FLW that made them possible.

2.3.1 *3D capability*

FLW enables the implementation of circuits whose geometries cannot be replicated by other platforms, thanks to its 3D capability. The most trivial consequence of this feature is that waveguides can pass one over the other without any intersection [220], a result that in planar lithography would require more complex solutions such as a completely transmissive directional coupler.

Moreover, such a 3D capability can be used to engineer the beam splitting ratio of a directional coupler by rotating the plane on which the two waveguides lie. Indeed, being the guided modes slightly asymmetric, by changing the angle of the interaction plane it is possible to change the overlap integral as well, and without affecting the interaction length. This has been exploited for instance in an interferometer for boson sampling (Fig. 2.4.a), for tuning randomly and independently both the beam splitting ratios of the directional couplers and the phase shifts [110]. As a matter of fact, the rotation of the interaction plane can be also used for obtaining polarization insensitive couplers [221]. By exploiting the different shapes of the H and V polarized modes, it is indeed possible to find the optimal angle at which the overlap integral is the same for both polarizations, thus obtaining the same splitting ratio.

Another peculiar advantage of FLW is related to the inscription of continuously-coupled waveguide arrays [222]. Indeed, while with lithographic platform it is possible to fabricate only arrays with a 1D lattice, where every waveguide interacts only with its nearest neighbour, FLW enables the fabrication of 2D arrays (Fig. 2.4.b), thus providing also a second-order coupling which can be controlled independently of the first-order one [218, 223]. Finally, the three-dimensionality provided by this platform can be used to simplify circuits architectures, for instance it was exploited for obtaining compact tritters [224] or interferometers implementing the quantum fast-Fourier-transform algorithm [225].

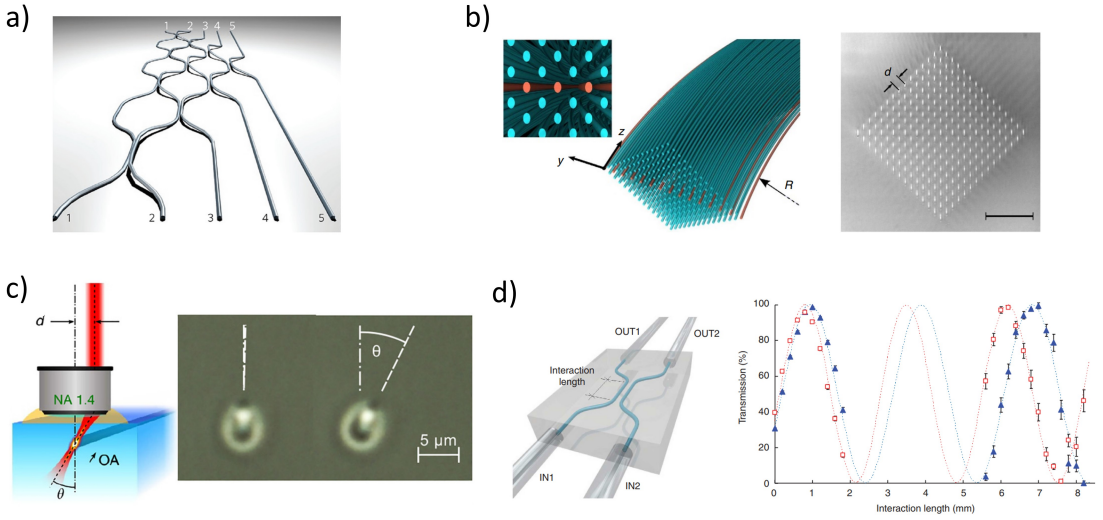

Figure 2.4: 3D capability and polarization processing provided by FLW. a) 5-modes interferometer in the Reck configuration, where the beam splitting ratios of the directional couplers are tuned by tilting the interaction plane. From [110]. b) Scheme and microscope image of the 3D waveguide array used in [218] for the simulation of fractional Bloch oscillations. From [218]. c) Integrated optical waveplate obtained in FLW by tilting the waveguide optical axis. From [226]. d) The behaviour of a typical directional coupler, with polarization dependent splitting ratios, can be exploited to implement a partially polarizing beam splitter. From [227].

2.3.2 *Polarization manipulation*

The low birefringence of femtosecond laser-written circuits makes them suited for experiments where polarization is used to encode information. Already in 2010 [228] it was demonstrated that directional couplers fabricated with this technique preserve the interference of polarization entangled photons, thus enabling the encoding of qubits in the polarization degree of freedom, or even the manipulation of hyperentangled and cluster states [229]. Notably, FLW provides a complete platform for quantum computation in the polarization encoding, a much more challenging result for other fabrication techniques. In this regard, one-qubit gates have been demonstrated with the implementation of integrated waveplates, obtained either by inscribing waveguides with a tilted optical axis [226] (Fig. 2.4.c) or by adding laser-irradiated tracks close to a waveguide to induce a directional stress [40]. Moreover, two-qubit gates are possible by using both partially polarizing and polarizing beam splitters, which can be obtained in FLW by exploiting the fact that horizontally and vertically polarized modes have slightly different coupling coefficients, and therefore different splitting ratios can be achieved by properly choosing the interaction length [227] (Fig. 2.4.d).

Finally, polarization insensitive circuits can be obtained as well. For instance, by adding laser damages at a proper distance from the interaction region, it is possible to compensate for the different coupling strengths of the H and V supported modes,

and therefore obtain polarization transparent directional couplers [204]. In the same work, it was demonstrated how a thermal treatment after irradiation allows to further reduce the waveguides birefringence [230], thus obtaining fully polarization insensitive circuits without the need of ad hoc geometries or post-processing.

2.3.3 *Reconfigurability*

The possibility of dynamically reconfiguring an optical phase in a compact and reliable way is a key advantage of integrated photonics, and one of the main requirement in quantum information processing with photons. In order to achieve a localized and controllable phase shift of the guided light, some physical effects relating the waveguide properties to other external elements can be exploited.

In FLW, the main demonstrations in this respect involved the electro-optic, the elasto-optic, and the thermo-optic effects, i.e. the dependence of the optical properties of a material on electric field, pressure, and temperature, respectively. However, the electro-optic effect is not trivial to exploit in glass materials due to their inversion symmetry, and even when a non-negligible $\chi^{(2)}$ is obtained, high voltages are still required to induce appreciable phase shifts [231]. An elasto-optic modulator has been instead used successfully in a quantum photonic experiment [232], where the birefringence of a shallow waveguide was tuned by actuating a piezo-electric element placed on the substrate surface. Nevertheless, this approach is difficult to scale to larger circuits, where the fabrication of suited microactuators would be necessary. For this reason, practically all the reconfigurable FLW circuits reported in literature exploited thermo-optic phase shifters, whose integration in glass chips is much easier. In particular, these elements are resistive microheaters deposited on top of the glass surface, in such a way that when a voltage is applied to them, heat dissipation by Joule effects occurs, with a local increase of the temperature of the underlying region. Therefore, this induces a variation of the refractive index by thermo-optic effect, which can be exploited for tuning the propagation constant of the guided light if the heater is placed in proximity of the waveguide.

Thermal phase shifters were used for the first time in FLW quantum photonic circuits in two different works [233, 234]. Notably, in the latter, the microheaters were fabricated by depositing a nanometric gold layer on top of a glass substrate, where optical waveguides had been already inscribed. Then, by using the same femtosecond laser used for the optical circuit inscription, after a careful realignment the resistors pattern was defined by selectively ablating the metallic layer (Fig. 2.5.a). In order to have a temperature increase only under the microheaters and not under their electrical connections to the voltage supply, the former were designed with a much lower width. In this way, they showed a higher resistance, albeit having the same resistivity of the remaining gold film, and therefore dissipated most of the electrical power.

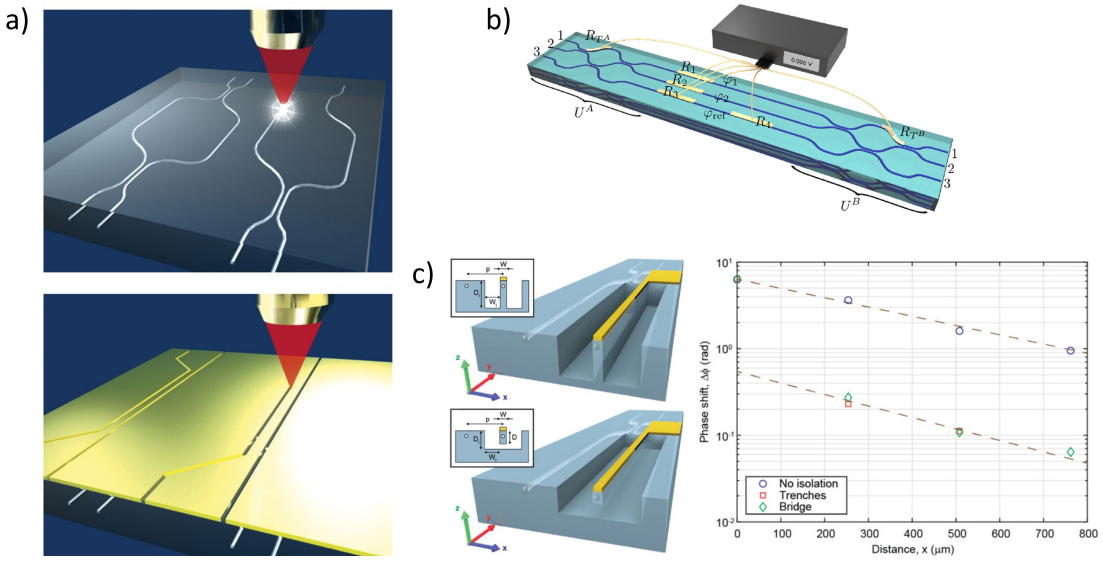

Figure 2.5: Reconfigurable femtosecond laser-written circuits. a) After the inscription of an optical circuit (top image), the thermal phase shifters can be fabricated on the glass surface by depositing a thin layer of gold, which is then patterned with a fs laser for defining the conductive paths (bottom image). From [234]. b). Three-arm interferometer for phase estimation employing thermal phase shifters. Adapted from [235]. c) The fabrication of deep trenches among waveguides, or the inscription of waveguides in bridge structures, allow to reduce both the thermal cross-talk and the required dissipated power, thus making the integration of thermal phase shifters in FLW scalable. In detail, in the graph it is shown the unwanted phase shift induced by a resistor on a far MZI as a function of its distance. The use of insulation trenches or bridges allows to reduce the cross-talk by more than one order of magnitude. From [236].

By using this or similar techniques, several reconfigurable devices were reported, among them a three-arm interferometer for quantum multiphase estimation [235] (Fig. 2.5.b) and a 4-mode universal photonic processor based on the Clements scheme [237]. Nevertheless, in order to increase the circuit complexity, it is necessary to scale up the number of thermal phase shifters that can be placed on a glass chip, and this could be challenging due to the nature of the thermo-optic effect. As a matter of fact, for having an efficient phase shift, the waveguide should be fabricated very close to the surface, and despite some proposals in this regard [238], it is very difficult to achieve distances below few μm. Moreover, glass has a non negligible thermal conductivity coefficient, therefore a heater designed to induce a phase shift on only one waveguide could actually affect also the neighboring ones, thus leading to unavoidable cross-talks [239].

In this respect, a solution is represented by the selective removal of glass between adjacent waveguides by water-assisted laser ablation [240], thus making the heat diffusion less efficient and therefore reducing the cross-talk, as reported in [236]. In the same work it was also shown how, by embedding the waveguide in an insulating suspended bridge with a phase shifter on top, it is possible to obtain similar results (Fig.

2.5.c). The heat confinement in both cases provides also a reduction of more than one order of magnitude of the needed dissipated powers, reaching values down to 20-30 mW, thus making it possible to integrate several phase shifters without needing cumbersome heat sinks. Moreover, the overall performances further improve if the chip is placed in vacuum, thus reaching cross-talk and power values close and even better than other fabrication platforms. Nevertheless, the introduced thermal insulation increases the optical response time, from hundreds of ms to few seconds. However, this is not a critical problem in the majority of experiments in quantum photonics, since longer integration times are usually required.

Part II

EXPERIMENTAL

This part describes the experimental activities at the basis of this thesis work. Chapter 3 will provide a general illustration of the experimental setup and of the main techniques that all the performed activities have in common. Chapter 4 will describe the space qualification of femtosecond laser written photonic circuits, for their use in satellite-based optical transmissions, both in the quantum and the classical regimes. Chapter 5 will be instead devoted to three different activities, all towards a scalable implementation of quantum photonics experiments. In Chapter 6 we will discuss the realization of a quantum photonic memristor, a nonlinear device with possible applications in the field of quantum neural networks. Finally, Chapter 7 will describe the realization of a four-arm interferometer for multiphase estimation.

3

MATERIALS AND METHODS

The purpose of this chapter is to provide an overview of the instrumentation used during the experimental activity described in this thesis. Moreover, all the procedures and the techniques that the different experiments have in common will be presented as well. The chapter flow is organized as a typical fabrication and characterization of an optical sample. Therefore, the first section will describe the inscription of photonic circuits in glass substrates. Then, an overview of the post-fabrication processing performed on the sample will be given. The final section will illustrate instead how to characterize the main components of an integrated optical circuit.

3.1 INSCRIPTION OF THE OPTICAL CIRCUITS

The inscription of the photonic circuits presented in this work has been performed in two different laboratories, CAPABLE and FIRE, belonging to the IFN-CNR and hosted in the spaces of the Physics Department of Politecnico di Milano. Despite having some specific features, which will be described in detail in the following, they share the basic working principle. A pulsed fs laser beam with $\lambda = 1030$ nm emitted by an Yb-based oscillator is sent, by a series of mirror, to a precise, software-controlled motion system, which allows to move the sample with nanometric precision in the three dimensions (Fig. 3.1). The pulse energy of the laser beam can be controlled by rotating a half-waveplate placed before a polarizer, which also sets the polarization used during the inscription. Moreover, a mechanical shutter is placed in the beam line for a fast on-off switching in about 10 ms. The beam is then focused into the sample by a microscope objective. In this regard, both fabrication lines provide a wide range of objectives, with different numerical apertures and working conditions (e.g. dry or water-immersion). The alignment between the sample and the focused beam can be controlled by imaging the back-reflection at the glass surface onto a CCD camera placed behind a partially transmissive mirror in the beam line.

3.1.1 *The laser systems*

FIRE LINE The laser source employed in FIRE line is the result of a collaboration between High Q Laser GmbH and the Max Planck Institute of Heidelberg [241]. The system consists in a cavity-dumped mode-locked oscillator based on a $KY(WO_4)_2$

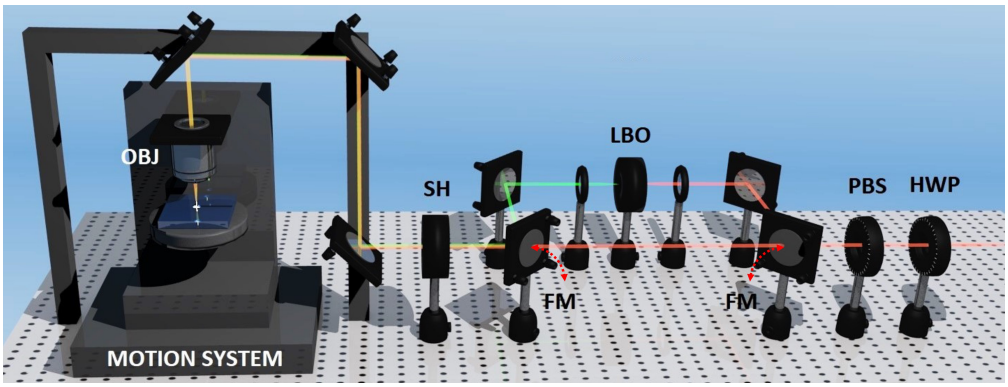

Figure 3.1: Scheme of the FIRE fabrication line. The 1030 nm fs laser passes through a half-waveplate (HWP) and a Glan-Thompson polarizer (PBS) for setting both the power and the polarization used during the inscription process. The beam is then sent to a mechanical shutter (SH) and to the motion system, where is focused by a microscope objective (OBJ). Before the shutter, two flip-mirrors (FM) in the line can redirect the beam to a lithium triborate crystal (LBO) for second-harmonic generation at 515 nm, thus increasing the versatility of the fabrication facility.

(potassium yttrium tungstate) crystal doped with 5% ytterbium. The active medium is pumped by an InGaAs laser diode at 980 nm and is placed in a 8.9 m-long resonant cavity, though a reduced footprint of only 90×50 cm² has been achieved thanks to a proper design of the optical cavity. A SESAM (SEmiconductor Saturable Absorber Mirror) is used as final mirror of the cavity for inducing passive mode-locking with an internal repetition rate of 17 MHz.

The laser pulses are then extracted by a Pockels cell placed before a thin-film polarizer. The former is used to rotate the polarization by applying a high voltage signal, in this way the pulse emission can be quenched or favoured. The resulting laser pulses have a wavelength of 1030 nm, a pulse duration of 300 fs and a maximum energy of 1 µJ, with a repetition rate that can be tuned from few kHz to 1.1 MHz covering the integer submultiples of the internal rate of 17 MHz.

Since the system does not provide any internal second-harmonic generation, in the fabrication line the laser beam can be redirected to a SHG stage by using two flip mirrors, placed before the mechanical shutter (Fig. 3.1). The employed nonlinear medium is a lithium triborate (LBO) crystal, which is preceded by a lens with $f = 15$ mm and followed by another lens of $f = 30$ mm, respectively necessary for focusing the IR beam into the crystal and for collimating the generated VIS radiation.

CAPABLE LINE In this case the fabrication is performed by using the commercial Pharos laser system, provided by Light Conversion (Fig. 3.2.a). The active medium is a Yb:KGW crystal (ytterbium-doped potassium gadolinium tungstate) optically pumped by a laser diode. Mode-locking in the oscillator at 76 MHz is achieved by Kerr lens effect in the active crystal, which is started by a perturbation of the cavity. The emitted

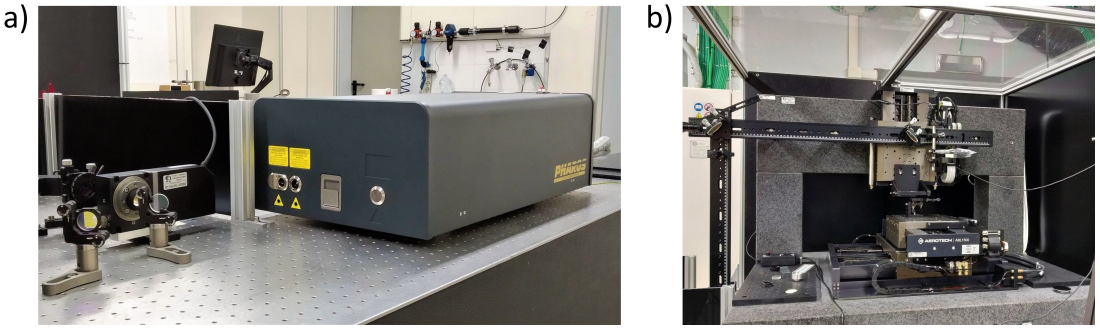

Figure 3.2: Laser source and motion system of CAPABLE line. a) Picture of the Pharos laser and of the waveplate mounted in the Aerotech rotary stage, used in combination with a polarizer for an automatized power control. b) Picture of the Aerotech motion system. The generous dimensions allow both to process long glass samples and to mount directly on the planar stage a custom-made sample holder for water-immersion microfabrications.

laser pulses, with a central wavelength of 1030 nm, a duration of about 70 - 90 fs and a power of 0.6 - 2 W are then amplified by chirped pulse amplification (CPA). The system comprises a pulse stretcher-compressor and a regenerative amplifier (RA) stage, based on a second Yb:KGW crystal. The injection of seed pulses in the RA module and the extraction of the amplified ones is controlled by a Pockels cell. Moreover, after the amplification stage a second Pockels cell, acting as a pulse picker, allows to further choose the repetition rate of the output laser pulses or to completely shut the emission.

The system is characterized by a very high versatility and stability in the emission properties. For instance, by acting on the two Pockels cells it is possible to choose a repetition rate among the submultiples of 1 MHz. Notably, by modifying directly the Pockels cell at the input of the RA, the output power can be preserved since the repetition rate reduction is accompanied by a proper increase of pulse energy. In this way, while at 1 MHz the maximum energy per pulse is 10 µJ, by decreasing the repetition rate at 10 KHz a maximum energy of 1 mJ can be achieved, thus keeping the output power constant at 10 W. Moreover, the pulse duration can be tuned as well by a motorized stage controlling the position of the chirped mirrors in the compressor, allowing duration values from a minimum of 170 fs to a maximum of 12 ps. Finally, the system is equipped with an internal SHG stage, therefore it is possible to have emission also at 515 nm. Concerning the stability of operation, all the main components are water-cooled in order to be insensitive to small variations of the room temperature.

For tuning the output power, beyond the internal laser control it is possible to rotate a half-waveplate before two thin-film Brewster type polarizers. In particular, the waveplate is mounted in a motorized rotary stage (Aerotech MPS75GR), which can be interfaced with the software controlling the translation stages for providing an automatized power control during fabrication.

3.1.2 *The motion systems*

The translation of the sample for the waveguide inscription is achieved in both laboratories by Aerotech state-of-the-art air-bearing linear stages, in particular by a FiberGlide 3D system in the FIRE line and an ABL1500 in the CAPABLE one. Both systems are composed by three independent translation stages, driven by a brushless linear servomotor and controllable via a proprietary software by using the G-code CNC programming language. Both stages enable a smooth, uniform movement in the three dimensions, and provide an accuracy and repeatibility of 100 nm. Moreover, optical encoders continuously monitor the actual position of the stages with a nanometric resolution. The FiberGlide 3D system allows the processing of samples long up to 10 cm with a maximum speed of 300 mm/s, while the ABL1500 system, thanks to its larger dimensions, allows to inscribe waveguides in 20 cm-long samples with a maximum speed of 2 m/s (Fig. 3.2.b). For its dimensions, the latter is also the preferred system when a water-immersion process is required, since it can easily host suitable sample holders.

3.2 POST-INSCRIPTION PROCESSING

After the inscription of optical waveguides, the sample must undergo a series of treatments for improving their performances, for providing a better handling and for exposing the waveguides cross sections for light coupling. Moreover, concerning the circuits that should be reconfigurable, additional steps are required for the fabrication of thermal phase shifters on the glass surface. The main post-inscription treatments are described more in details in the following sections.

3.2.1 *Thermal annealing*

Some thermal treatments can be beneficial for improving the glass properties, and are traditionally used in its manufacturing. In particular, the so called *annealing* process is used to reduce the internal strain which is generated when the glass is cooled down too quickly [242]. This treatment consists in a fast heating of the glass up to a temperature below its melting point but slightly above its annealing point, which is the temperature that enables viscous relaxation of the accumulated strain in few minutes. After that, a slow cooling is required down to room temperature, in this way no additional stresses are induced. The low rate must be kept at least until the strain point is reached, i.e. the temperature below which no strain can be generated by thermal processes.

Thermal annealing can be useful for improving the performances of waveguides inscribed in borosilicate glasses. It has been associated indeed to the creation of a more confined, gaussian-like guided mode, with a consequent reduction of the bend-

ing losses [230], thus enabling radii of curvature down to 20 mm with negligible losses. Moreover, in one of our works [204], we have shown how a three-days thermal annealing can be used to reduce the waveguide birefringence, for achieving a polarization insensitive operation of directional couplers fabricated in borosilicate glass, notably Eagle XG by Corning.

A similar process, but optimized for reducing its duration to only one day, has been used on all the circuits fabricated for this thesis. This annealing procedure consists in a 1-hour heating up to 750 °C, above the annealing point of Eagle XG (722 °C according to its data-sheet). Then, the sample is cooled down to 630 °C, below the strain point (669 °C), with a descending rate of -12°C/h, which is followed by a second cooling down to 500 °C at -24 °C/h. After this step, room temperature is reached by natural cooling. For this process, a muffle furnace provided by Nabertherm GmbH has been used, which can reach temperatures up to 1200 °C and allows a fine control and reproducibility of the heating and cooling rates.

3.2.2 *Cut and polishing*

After fabrication, it is often necessary to cut the glass samples, for instance for removing not irradiated areas and thus providing a better handling of the chip, or for exposing tapered or buried waveguides. For this purpose, the laboratory is equipped with a Well 3241 diamond wire saw, by Well Diamantdrahtsägen GmbH. The machine puts in a continuous motion a stainless-steel wire covered with diamond grains, which is then put in contact with the glass sample to cut it with precision and reliability, with tracks as thin as 300 µm.

After being exposed, the waveguides facets should then be polished to optical quality for providing optimal light injection with negligible losses. In this regard, the sample can be mounted on a FLex Waveguide Polisher by KrellTech, which is a machine that enables the reduction of the glass surface roughness by putting it in contact with a rotating abrasive disk. Several steps using disks with a decreasing grain size should be used for an optimal procedure. Moreover, the machine allows to act on the polishing angle, on the rotation speed of the disk and on the pressure that the sample exerts on it, thus providing a controllable and reliable operation. In alternative, for instance when the sample is too large and cannot be mounted on the automatic polisher, a manual polishing can be performed by employing custom-made holders and by manually moving the sample while applying the proper pressure against the abrasive disks.

3.2.3 *Fabrication of the thermal phase shifters*

The fabrication of the thermal phase shifters on a glass sample is based on the process described in [236] and can be divided in three different steps. The first one consists in the fabrication of insulation trenches between waveguides by water-assisted laser

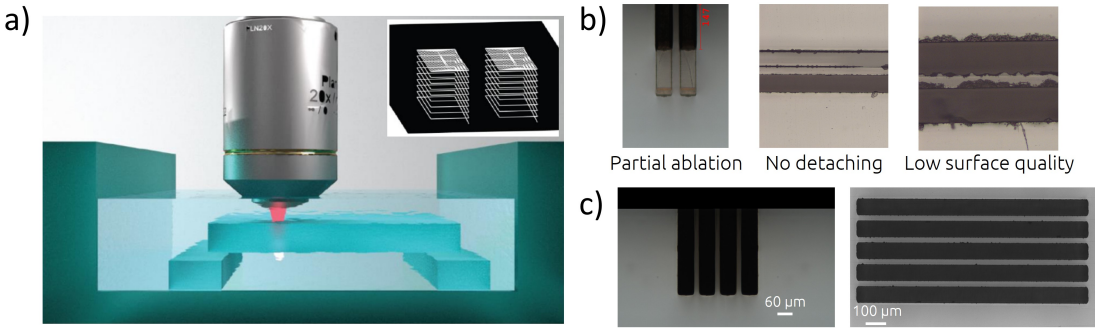

Figure 3.3: Water-assisted laser ablation of insulating trenches. a) Scheme of the inscription process. The bottom surface of the glass sample is suspended in a water environment, and the laser is focused at the glass-water interface for material removal assisted by the liquid vaporization. In the inset, the ablation pattern of two trenches is shown. Adapted from [236]. b) Microscope images showing a failed or non-optimal ablation of the insulation trenches. From left to right: the ablation process was not sustained by water until the end (side view), only one of the trenches is detached (top view), the surface quality of the non-machined glass is not good enough for a successful metal deposition (top view). c) Microscope images of trenches fabricated with the optimized parameters. On the left, side view of four trenches ablated until their bases, on the right, a top view of five trenches with optimal surface quality.

ablation, for enhancing the heat confinement and reducing the cross-talk. Then, the deposition of the gold film is performed, which is followed by the last step, i.e. the patterning of the resistors by selective laser ablation of metal for creating the conductive paths.

3.2.3.1 *Insulating trenches*

The machining process of the insulating trenches has been optimized during this work in the CAPABLE line, for achieving both a high fabrication yield and a good quality of the machined surface. The implemented water-assisted laser ablation process is shown in Fig. 3.3.a. The glass, placed with the already inscribed waveguides at the bottom, is glued to a sample holder, designed for keeping it suspended, and then covered with water. By using a Zeiss 20×, 0.5 NA water-immersion objective, the laser beam is focused 15 - 20 µm below the rear surface. In this way, the machining process starts with the localized vaporization of the water below the substrate, which causes micro-explosions on the glass surface and therefore the selective ablation of material. Moreover, the presence of water favours also the debris removal. The ablated pattern is shown in the inset of the same figure. The walls of the trench are ablated first, from the bottom towards the top for having always the focal spot at the water-glass interface. Then, its base is machined as well, and once the process is finished, the trench detaches from the substrate by gravity.

The optimization of the process has been performed by scanning the main inscription parameters such as the writing speed and the pulses energy, repetition rate and

duration. As a matter of fact, the result of the machining is very sensitive to the fabrication conditions: in Fig. 3.3.b it is possible to see the effects of a non optimal choice of parameters. Indeed, it can happen that the ablation stops before reaching the trench base, for instance if the modification is too small and the water cannot follow the focal spot. Moreover, an already fabricated trench can partially interrupt the laser beam used for the machining of a second one, whose ablation therefore fails. Finally, if a too high energy is used, the surface of the remaining glass can be ruined, and this can prevent a good gold deposition exactly on top of the waveguide between the trenches, where the phase shifter should be fabricated.

The result of the optimization, i.e. well-defined trenches with optimum surface quality, is shown in Fig. 3.3.c. In particular, the structures in the figure were obtained with a laser wavelength of 1030 nm, pulse energy of 1 µJ, duration of 1 ps, repetition rate of 20 kHz and a translation speed equal to 4 mm/s. Moreover, for increasing the success rate, the overall depth of 300 µm was ablated by sequentially detaching four smaller trenches with a depth of 75 µm each, thus slightly increasing the processing time but greatly improving the reliability of the technique.

3.2.3.2 *Gold deposition*

The deposition of the gold film on the glass is performed in Polifab, the clean-room facility of Politecnico di Milano, following the process described in [243]. The first step is the cleaning of the glass surface for increasing the film adhesion. For this purpose, the sample is immersed in a piranha bath, which enables the removal of organic residues. After that, it is placed in a plasma asher (PVA Tepla 300 AL) for 5 minutes, where the interaction with an oxygen plasma, generated by a 500 W microwave power supply, further cleans the substrate surface.

Then, the sample is placed in a magnetron sputtering system (Leybold LH Z400), where energetic ions have enough kinetic energy to sputter atoms from a metallic target, which then redeposit on the sample surface. In particular, with this process 2 nm of chromium, followed by 100 nm of gold, are deposited on the glass. Notably, chromium is necessary for providing an optimum adhesion of the gold layer, which is chosen as conductive layer for its excellent electrical properties and resistance to oxidation.

For improving the stability of the conductive film, an annealing process is required. Indeed, the gold deposited by magnetron sputtering is mainly polycrystalline, which is an energetically less favoured form if compared to the single-crystal state. Therefore, during the normal operation of the phase shifters, their resistance value would not be stable [244] and it would be necessary to frequently characterize their electrical properties. A thermal annealing allows to solve this issue since it induces the immediate formation of single-crystal grains, which then remain stable in time. The treatment consists in a heating ramp of 10 °C/min up to 400 °C, temperature which is maintained for 30 minutes before a cooling down to room temperature with no thermal actuation.

In this regard, a Nabertherm LT 9/11 SKM furnace is used, which provides operation in a controlled N_2 atmosphere. It is worth noting that the maximum temperature of the process is well below the strain point of Eagle XG, therefore no modification is induced on the waveguides.

3.2.3.3 *Resistors patterning*

The last step for the fabrication of the resistors is the definition of the conductive paths, which can be performed both in CAPABLE and FIRE lines. In this regard, a $10\times$, 0.25 NA microscope objective is used to focus on the gold layer the fs laser beam with $\lambda = 1030$ nm, R.R. $= 1$ MHz, $E_P = 200$ nJ, $\Delta t = 170$ fs in CAPABLE line and 300 fs in FIRE one. The lower magnification allows to inscribe tracks with a thickness of 3 - 5 µm, thus increasing their insulating capability. The sample is translated at a speed of 2 mm/s, and the alignment with the already written waveguides can be achieved by using some markers on the sample surface.

As already pointed out, since the resistors have the same resistivity ρ of the pads which are used to contact them to external voltage supplies, their resistance values is increased by acting on their geometry. Indeed, a higher resistance enables the localization of the power dissipation, and therefore of the heating capability, in the phase shifters. In particular, the resistance is defined as

$$R = \rho \frac{l}{wt}, \tag{3.1}$$

where l, t and w are respectively the length, the thickness and the width of the phase shifter. From this relation, since ρ and t are properties of the film, it is possible to understand how to increase the resistance of the phase shifters it is necessary to increase their length and reduce their width. In particular, for inducing appreciable phase shifts with low power dissipation, l should be of the order of some mm, while w of few µm, however the exact values depend on the desired performances and film properties, and are therefore precisely chosen for every circuit.

3.3 DEVICE CHARACTERIZATION

3.3.1 *Microscope inspection*

The visual inspection of the elements of a photonic circuit by means of an optical microscope is a fundamental aspect of their characterization. For instance, by looking the sample from the top it is possible to assess the circuit design, the quality of the induced refractive index contrast and the presence of waveguide interruptions, caused for example by dust particles interrupting the fabrication laser beam. Moreover, the observation of the polished facet can provide information about the waveguide cross

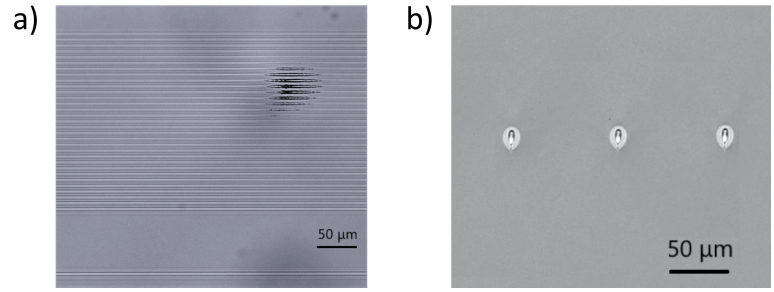

Figure 3.4: Visual inspection of photonic circuits by an optical microscope. a) Top view of damaged waveguides. b) Side view of a sample where three waveguides were inscribed.

section. A microscope inspection can be useful as well in all the steps of the phase shifters fabrication, e.g. to evaluate the detachment of the trenches, the presence of impurities on the gold film or the result of the resistors definition by laser ablation.

For this purpose, in this work a Nikon Eclipse ME600 optical microscope, focusing the magnified image onto a high resolution CCD camera (PixeLINK B871), has been used. The system allows to choose among different magnifications up to 40×, and features both reflected and transmitted illumination. Moreover, it is equipped with a differential interference contrast (DIC) module, which provides the enhanced vision of low refractive index contrasts.

3.3.2 *Laser light coupling*

The coupling of laser light in integrated circuits can be used to characterize their optical properties, such as their transmission, their polarization behaviour and their reconfigurability. For this reason, the characterization laboratory is equipped with several laser sources in both VIS and NIR spectra, such as diodes and solid-state lasers.

Light injection can be achieved in two different configurations. The end-fire one (Fig. 3.5.a) consists in focusing the laser light into the input waveguide facet by using a microscope objective or an aspheric lens, which should be chosen for matching both the size of the guided mode and the waveguide numerical aperture, ~ 0.1 in case of FLW waveguides. The second configuration, called fiber-butt coupling (Fig. 3.5.b), consists instead in injecting light by means of an optical fiber, whose peeled and cleaved tip is brought close to the waveguide input facet. Also in this case, the fiber choice should consider the properties of the guided mode. This configuration is particularly useful when quantitative measurements should be performed, since the fiber mode is a reliable reference for the properties of the injected light.

The precise alignment between objective, fiber and sample can be achieved by submicrometric multi-axis translation stages. In particular, the position of the element used for coupling light in the waveguide is controlled by a three-axis translation stage (Melles Griot NanoMax or the more recent Thorlabs MAX313D). The sample is instead

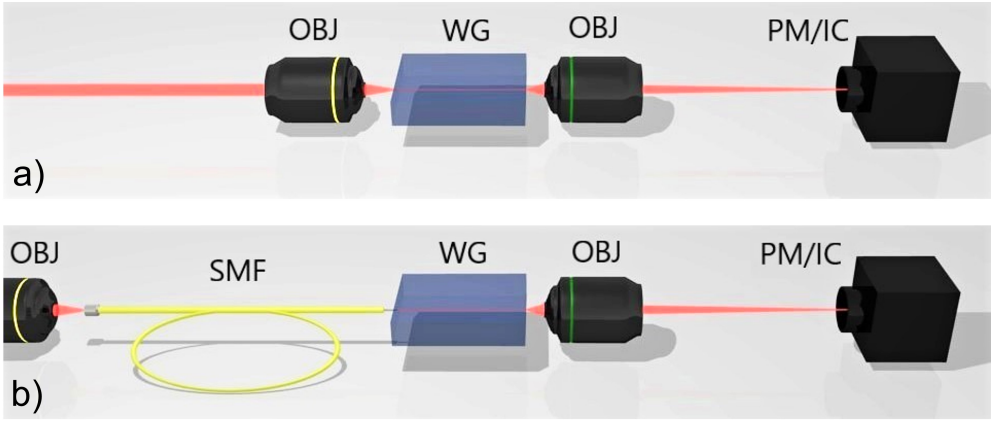

Figure 3.5: Configurations for coupling light in an optical waveguide. a) End-fire coupling, where a microscope objective is used to focus the laser beam into the input facet of the waveguide. b) Fiber-butt coupling, where an optical fiber is brought close to the waveguide input facet. If the laser sources emits in free-space, an end-fire configuration can be used to inject light in the fiber.

mounted on a four-axis micropositioner (Thorlabs MBT402D), with two translation axes enabling the motion in the plane normal to the direction of light propagation, and two rotational axes for tilt adjustment. In the case of coupling with an optical fiber, its distance from the sample facet can be visually controlled by using a Leica M125C bench-top microscope, which provides up to 10× magnification.

For collecting the waveguide output light, the same configurations can be implemented. When using a focusing element, however, a higher NA should be preferred in this case for collecting more light. The output light properties can then be measured by means of a powermeter sensor (Ophir NovaII and Anritsu ML9001A) or an imaging camera, notably an Emdund Optics EO-1312M CCD sensor for $\lambda < 1$ µm, and a Xenics Bobcat-640 InGaAs camera for longer wavelengths.

3.3.3 *Evaluation of the optical properties*

3.3.3.1 *Mode profile*

The measure of the mode profile gives preliminary information about the waveguide properties. From this analysis it is for instance possible to distinguish between single mode and multi-mode waveguides (Fig. 3.6), which is an important information since usually the higher-order modes are more lossy and less controllable. Moreover, from the mode dimension it is possible to retrieve a rough estimation of the waveguide refractive index contrast and on its confinement capabilities, which are related e.g. to the bending losses. The evaluation of the mode profile is also useful when designing directional couplers, since the interaction distance should be low enough for provid-

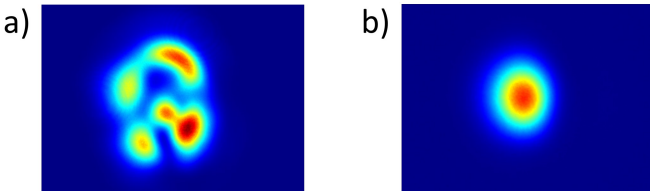

Figure 3.6: Mode profile of a) a multi-mode and b) a single mode waveguide.

ing appreciable overlap integrals but not too low for avoiding reciprocal disturbance between the waveguides.

The mode profile analysis is usually performed by butt-coupling the waveguide with an optical fiber, and by imaging the output intensity distribution by means of a sensitive camera. It is worth noting that, in the case of single mode waveguides, the intensity measurement provides all the necessary information since, due to the absence of sign inversion, the intensity profile is directly related to the electric field: $|\mathbf{E}(x,y)| \propto \sqrt{I(x,y)}$. Moreover, for performing a quantitative measurement, the mode of the fiber can be imaged as well by keeping constant the distance between the collection optics and the camera, and therefore the system magnification. In this way the fiber mode, whose dimension is usually known, can be used as a reference.

3.3.3.2 *Loss analysis*

We already discussed how the losses introduced by integrated optical waveguides are a very important aspect in quantum photonics, since high losses are associated to a degradation of the performances and limit the scalability of the implemented circuits. Nevertheless, we did not discuss yet which are the main sources of losses. For this reason, in the following we will present the main physical phenomena associated to light loss in the circuit, and how we can measure them. For practical reasons, the introduced losses are usually expressed in dB, since in this way their addition is straightforward.

FRESNEL LOSS When injecting light in an optical waveguide, the refractive index mismatch at the environment-substrate interface causes a partial reflection of light, which is therefore not coupled. This kind of loss increases with the refractive index of the material, and can be calculated as

$$FL_{dB} = -10 \cdot \log_{10}\left[1 - \left(\frac{n_2 - n_1}{n_2 + n_1}\right)^2\right], \tag{3.2}$$

where n_1 and n_2 are the environment and substrate refractive indices, respectively. In particular, if we consider an air-glass interface, the Fresnel losses are about 0.18 dB. For reducing this value, ideally to zero, index-matching oils can be used between fiber and glass, thus preventing the Fresnel reflection.

COUPLING LOSS The amount of light that is injected in the waveguide depends on the coupling conditions. In fiber-butt coupling, if the fiber mode E_f and the waveguide one E_{wg} are not perfectly matched, coupling loss arises, which is defined as

$$CL_{dB} = -10 \cdot \log_{10} \left(\frac{|\iint E_{wg}\, E_f \, dx\, dy|^2}{\iint |E_{wg}|^2 \, dx\, dy \cdot \iint |E_f|^2 \, dx\, dy} \right) \tag{3.3}$$

and is dependent on the overlap integral between the two guided modes. In particular, the coupling loss can be estimated once the intensity profiles of the two modes are retrieved with an imaging camera. It is worth noting that Eq. (3.3) provides only a theoretical value, being the actual coupling loss usually higher since other nonidealities also play a role, such as a non perfectly cleaved fiber facet or slight misalignments with the waveguide. Moreover, a similar relation is much more difficult to find in case of end-fire coupling, since the injection efficiency depends not only on the electric field distribution at the focal spot, but also on the lens NA.

PROPAGATION LOSS The unavoidable imperfections of the waveguide profile, such as roughness, inhomogeneities of the refractive index contrast, defects or absorption centers, can cause an exponential attenuation of light as it propagates [245]. In particular, if we define an attenuation coefficient α, which takes into account all the aforementioned causes of loss, after a propagation length l the optical power will be $P(l) = P(0) \cdot e^{-\alpha l}$, with $P(0)$ the initial power. In this framework, the propagation loss, defined as the loss for every cm of propagation, can be retrieved as

$$PL_{dB/cm} = \frac{-10 \cdot \log_{10}[P(l)/P(0)]}{l}, \tag{3.4}$$

and it can be directly related to the attenuation coefficient by considering $PL_{dB/cm} = 10\,\alpha_{cm^{-1}}\,\log_{10} e \simeq 4.3\,\alpha_{cm^{-1}}$.

The propagation loss value can be estimated by the cut-back technique, consisting in measuring the output power of a straight waveguide which undergoes several cuts, gradually reducing its length. In this way, it is possible to retrieve the exponential attenuation coefficient, and from it the propagation loss per cm. This technique can be time consuming, since after every cut the sample facet should be polished, moreover it is destructive for the fabricated circuit. For this reason, an alternative can be the measurement of the total insertion loss of the straight waveguide, defined as

$$IL_{dB} = 2\,FL_{dB} + CL_{dB} + PL_{dB/cm} \cdot l, \tag{3.5}$$

and the retrieval of the propagation loss from it:

$$PL_{dB/cm} = \frac{IL_{dB} - 2\,FL_{dB} - CL_{dB}}{l}, \tag{3.6}$$

once both the Fresnel and coupling losses are known. This method is affected by a non negligible uncertainty for short waveguide, however it becomes more and more

reliable as l increases, since the propagation loss becomes predominant on the other sources of losses.

The insertion loss can be estimated in the fiber-butt coupling configuration by measuring first the waveguide output power P_{out}, and then the input power P_{in} by collecting with the same lens the light coming from the optical fiber:

$$IL_{dB} = -10 \cdot \log_{10}\left(\frac{P_{out}}{P_{in}}\right). \tag{3.7}$$

It is important to use the same collection optics since in this case the loss introduced by it equally affects both the measurements of P_{in} and P_{out}, and therefore its contribution in Eq. (3.7) cancels out.

BENDING LOSS The waveguide curvature introduces an additional source of loss which is not present in a straight one. As a matter of fact, in bending waveguides the guided mode is partially distorted, and for this reason it can couple with radiation modes which are not confined in the core. In particular, the amount of light which is lost in a curved waveguide exponentially increases as the radius of curvature R decreases [246]. In this regard, the bending loss value can be defined as

$$BL_{dB/cm} = c_1\, e^{-c_2\, R}, \tag{3.8}$$

where BL is measured in dB/cm as the PL, and where c_1 and c_2 are two constants depending on the waveguide properties. Notably, a strong confinement, provided by a large refractive index contrast, enables a reduction of both of them, allowing lower radii of curvature with negligible losses. This is why, for instance, the circuits fabricated in silicon can be miniaturized much more than the silica-based ones.

The analysis of the bending loss can be performed by measuring the insertion losses of several curved waveguides, fabricated with different radii of curvature R_i but with the same length l_c of the curved part. In this way, by comparing them with the IL of a straight waveguide inscribed in the same fabrication run and of the same length, the BL for every R_i can be retrieved as:

$$BL_i = \frac{IL_{R_i} - IL_{straight}}{l_c}. \tag{3.9}$$

The values of c_1 and c_2 can then be obtained from a fitting procedure of the experimental data.

3.3.3.3 *Polarization and birefringence*

An important aspect that should be considered when assessing the properties of a waveguide is how it affects the polarization of the guided light. We already discussed that there are some cases, for instance when using polarization as a way to encode a qubit, when the integrated circuit should have a behaviour transparent to polarization.

Moreover, also the polarization of the guided light can have consequences on the circuit operation, for instance on the size of the guided mode and on the splitting ratio of the directional couplers.

In this regard, the polarization state of the guided beam can be fully described by means of the Stokes vector, defined as

$$\mathbf{S} = \begin{pmatrix} S_0 \\ S_1 \\ S_2 \\ S_3 \end{pmatrix} = \begin{pmatrix} 1 \\ (I_H - I_V)/I \\ (I_D - I_A)/I \\ (I_R - I_L)/I, \end{pmatrix} \tag{3.10}$$

where I_i is the intensity retrieved by a projective measurement on the i polarization state (horizontal/vertical, diagonal/antidiagonal, circular right/left-handed respectively), and where I is the total power. In this framework, the action of the waveguide on the guided light can be completely characterized by the so-called Müller matrix M:

$$\mathbf{S}_{out} = M \cdot \mathbf{S}_{in}. \tag{3.11}$$

In particular, for FLW waveguides, the Müller matrix takes the form of the transformation induced by a birefringent medium with a single, fixed optical axis [247]:

$$M = \begin{pmatrix} 1 & 0 & 0 & 0 \\ 0 & \cos^2 2\delta + \sin^2 2\delta \cos\phi & \sin 2\delta \cos 2\phi\,(1 - \cos\phi) & \sin 2\delta \sin\phi \\ 0 & \sin 2\delta \cos 2\phi\,(1 - \cos\phi) & \sin^2 2\delta + \cos^2 2\delta \cos\phi & \cos 2\delta \sin\phi \\ 0 & \sin 2\delta \sin\phi & -\cos 2\delta \sin\phi & \cos\phi \end{pmatrix}, \tag{3.12}$$

being δ the angle between the optical axis and the horizontal direction, and ϕ the phase difference between the light components along the extraordinary and ordinary axes. Notably, ϕ is related to the waveguide birefringence $b = n_e - n_o$ and to its length l by

$$\phi = \frac{2\pi}{\lambda} \cdot b\, l. \tag{3.13}$$

Therefore, by measuring ϕ it is possible to directly retrieve the waveguide birefringence, thus gaining information on the rotation induced on the polarization of the guided light.

The matrix M can be experimentally obtained by using the setup presented in Fig. 3.7. A fixed polarizing beam splitter (PBS), together with a half (HWP) and quarter (QWP) waveplates mounted on two motorized rotation stages (Thorlabs PRM1/MZ8) allow to inject in the waveguide by end-fire coupling any arbitrary polarization state. The output light is then collected by a microscope objective and, after manipulation with the same optical components placed in a reversed order, is focused on a powermeter sensor. In this way, it is possible to perform a tomography of the output polarization state by projective measurements on the three bases involved in the definition of the

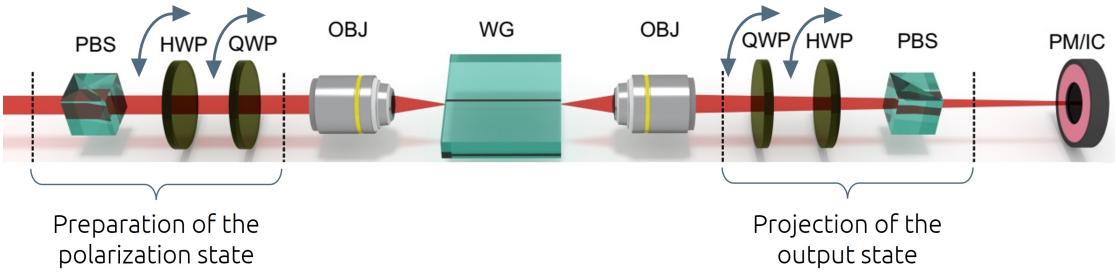

Figure 3.7: Experimental setup for the analysis of the waveguide polarization behaviour. A preparation stage, composed of a polarizing beam splitter, a half and a quarter waveplate, is used to prepare the input light in an arbitrary polarization state. At the waveguide output, the same elements are used to perform a projective measurement and retrieve the Müller matrix. From it, both the birefringence and the orientation of the optical axis can be inferred. Adapted from [247].

Stokes vector (H/V, D/A, R/L), and therefore measure $\mathbf{S}_{out}$. Since $\mathbf{S}_{in}$ is known, a fitting procedure on Eq. (3.11) enables the reconstruction of the Müller matrix, and so the retrieval of both δ and ϕ. It is worth noting that ϕ is measured up to integer multiples of 2π, therefore, for removing any ambiguity on the estimation on the birefringence b, the same measurement should be repeated for waveguides with different lengths.

3.3.3.4 *Evanescent coupling*

We already mentioned that the coupling properties of the optical waveguides depend on the overlap integral, and therefore on the mode profile. In particular, from the coupled-mode theory [248] it is known that two identical waveguides interacting for a length L can exchange light by evanescent coupling. In this framework, the reflectivity R (or equivalently the splitting ratio) can be defined as the fraction of power that remains in the injection waveguide:

$$R(L) = \cos^2(kL + \phi), \tag{3.14}$$

where ϕ is related to the interaction occurring already in the curved regions, and k is the coupling coefficient, proportional to the overlap integral between the two waveguides modes:

$$k \propto \iint E_1(x,y)\, E_2(x,y)\, dx\, dy. \tag{3.15}$$

Notably, k can be expressed in terms of the interaction distance d, since a lower d will cause a higher overlap and therefore a stronger coupling:

$$k(d) = a \cdot e^{-bd}, \tag{3.16}$$

with a and b two constants depending on several parameters such as the refractive index contrast and the light wavelength.

In theory, once all the properties of the system are known, a modelling of the evanescent coupling could be possible. Nevertheless, this task is quite difficult to achieve with

FLW waveguides, due to their low confinement and nontrivial mode profile. Moreover, the coupling occurring already when the waveguide start to interact in the bending regions makes it even more difficult to obtain reliable results. For this reason, the design of the directional couplers for achieving the desired reflectivities is based on an experimental scan of the main geometric parameters, i.e. d and L, while the radius of curvature of the bent parts is usually chosen as a compromise between low losses and a compact circuit. In this regard, the most trivial scanning procedure is the fabrication of directional couplers with an increasing interaction length at a fixed distance. By coupling light in one waveguide, and by measuring the output power of the injection waveguide (P_{bar}) and of the other one (P_{cross}), the reflectivity $R(L)$ can be retrieved as:

$$R(L) = \frac{P_{bar}}{P_{bar} + P_{cross}}, \tag{3.17}$$

from which it is possible to estimate k by a fitting on Eq. (6.17). Moreover, by performing this measurement for different distances d, the exponential dependence of the coupling coefficient on this parameter can be retrieved as well.

In this way, however, for achieving a certain reflectivity with a given distance it could be necessary to use interaction lengths of some mm, thus increasing the length of the circuit. A solution in this respect is to exploit the evanescent coupling occurring in the bending regions for achieving directional coupler with actual interaction length $L = 0$. In this case, the scanning of the parameters is performed by fabricating a series of directional couplers with different interaction distances and zero length, whose reflectivity is then measured. From these data, a fitting procedure on $k(d)$ can be performed, whose results can then be used to choose the exact distance for a desired splitting ratio. As it is possible to understand, not only this technique provides more compact directional couplers, but it is also less time consuming since the number of devices that should be fabricated for deciding the suited geometry is reduced.

Finally, we should note that the characterization of the directional couplers can occur both in the end-fire or fiber-butt coupling configurations. In particular, when the polarization of the guided light should be considered, the former is the preferred choice, while fiber coupling is used when it is necessary to measure the insertion losses of the devices.

3.3.4 *Reconfigurability*

The evaluation of the thermal phase shifters properties is first performed by measuring their resistance R with a digital multimeter. Then, for characterizing the induced phase shifts, light is injected in the circuit and the output power distribution is analyzed while tuning the voltage or the current that is applied to the resistor. As an example, let us consider the simplest case, i.e. a MZI composed of two balanced directional couplers with a heater fabricated on top of one of the two arms (Fig. 3.8.a). The applied phase shift can be retrieved from the measurement of P_{bar} and P_{cross}, since the circuit

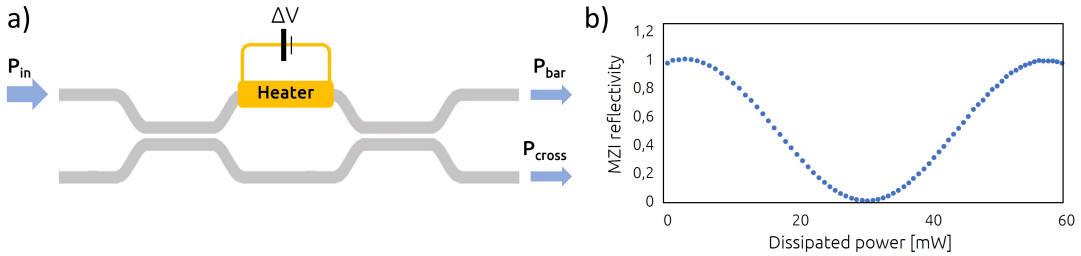

Figure 3.8: Characterization of the optical phase shift induced by a resistive heater. a) The characterization of the reconfigurability of a MZI can be performed by measuring the bar and cross output power, while applying a known voltage (or current) to the resistor. b) Typical experimental dependence of the MZI reflectivity on the induced phase shift.

will show an oscillating reflectivity with a sinusoidal dependence on the dissipated electric power (Fig. 3.8.b). In formulas, $R(\Delta\phi) = \cos^2(\Delta\phi/2)$, where the induced phase shift is linearly dependent on the dissipated power P_{diss}:

$$\Delta\phi = \alpha\, P_{diss} + \Delta\phi_0. \tag{3.18}$$

In this relation, α is a proportionality coefficient which is related to the light wavelength λ, the thermo-optic and thermal conductivity coefficients of glass – $n_T \simeq 10^{-5}\,\mathrm{K^{-1}}$ and $k = 0.9\,\mathrm{W/(m{\cdot}K)}$, respectively – and on the distances r_1 and r_2 between the resistor and the two arms of the MZI [234]:

$$\alpha = \frac{2n_T}{\lambda k}\log\left(\frac{r_1}{r_2}\right). \tag{3.19}$$

By considering that $P_{diss} = V^2/R$ in controlled-voltage operation, and $P_{diss} = RI^2$ in the controlled-current one (where R in this case is the electrical resistance), it is possible to retrieve which values should be used for inducing a desired phase shift.

In the case with more than one heater, Eq. (3.18) assumes a matrix form, since every phase is in principle affected by the action of all the resistors, which sum up linearly. In particular, the off-diagonal elements represent the cross-talk terms, since they describe how a resistor affect the phase of a waveguide not fabricated beneath it. In presence of insulating trenches, these terms are greatly reduced, nevertheless they should be still considered for a good device operation. In this case, the characterization is performed by measuring all the phase shifts induced by every resistor, so that a full knowledge on the linear system can be obtained. It is worth noting that cross-talk does not play in principle a negative role, since, once characterized, its effects can be controlled. However, when the number of resistors is increased, it makes the preliminary characterization of the system more time consuming and, if too high, could cause an increase of the dissipated power necessary for inducing a desired phase shift.

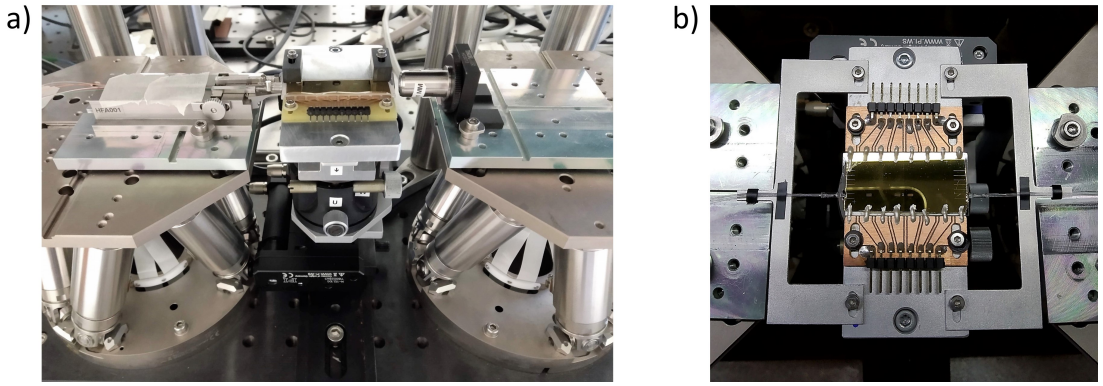

Figure 3.9: Pigtailing setup. a) The two hexapods (at the sides) and the sample holder (in the center) provide a complete control on the alignment between fiber arrays and waveguides. b) Device after pigtailing. For increasing the resistance of the fibers to mechanical stresses, custom-made metallic holders can be used.

3.4 PACKAGING AND PIGTAILING

For providing stable and reliable operation, it is possible to permanently connectorize the inscribed photonic circuits with optical fibers or fiber arrays, both at the input and the output facets. This procedure, called *pigtailing*, is performed by precisely aligning the fibers to the waveguides, and then by gluing them by means of a UV-curing glue, which solidifies when exposed to UV radiation.

The pigtailing setup used in this thesis is shown in Fig. 3.9.a. For the alignment of both the launch and collection fibers, two 6-axis computer-controlled hexapods (H-811.F2 by PI-Physik Instrumente) are used, which enable a precise and repeatable movement in all the six degrees of freedom thanks to brushless DC motors. Notably, the resolution of the three translation axes is 100 nm, while a minimum value of 2 µrad can be achieved for the three rotation ones. The device positioning is instead performed by means of a sample holder that provides a manual control over the three rotation axes, and a motorized one (M-110 by PI) in the plane normal to the direction of propagation of light. The visual inspection of the whole process is enabled by two cameras equipped with a macro objective and placed on the top and on one side of the system.

Once the optimal coupling between fibers and waveguides is achieved, the UV-curing process can be performed. In this regard, the glue is carefully placed on the fiber facet and, once the optimal coupling is restored, it is cured by irradiation with a UV-LED source (L14310 by Hamamatsu) which causes its solidification in few seconds. Moreover, since the glue has the same refractive index of glass, the Fresnel loss is greatly reduced since an index-matching condition is achieved. Finally, some custom-made metallic holders can be used (Fig. 3.9.b) for increasing the mechanical stability of the connectorized fibers.

4

SPACE QUALIFICATION OF FLW WAVEGUIDES

In this chapter we investigate the effects that a space mission in a low Earth orbit environment would have over femtosecond laser-written waveguides in Eagle XG. By proper irradiation with γ-rays and protons, and by performing tests on temperature variations and vacuum conditions, we show that FLW circuits are a valuable tool in the implementation of satellite-based optical communications, both in the classical and quantum regimes. This work has been carried out in collaboration with Prof. Ping Koy Lam and Dr. Tobias Vogl, both affiliated with the Department of Quantum Science of the Australian National University and it has been published in [249]. In this activity I performed the fabrication of all the circuits, their characterization with laser light before and after irradiation, and the comparison of the retrieved data.

4.1 MOTIVATIONS OF THE WORK

In Sect. 1.3.2, we showed that a promising implementation of a global quantum network for secure communications involves relay satellites and ground stations exchanging quantum states of light. This approach would allow to overcome the intrinsic locality of the free-space transmissions without the need of lossy optical fibers. In this respect, it must be mentioned that the footprint of the optical elements placed in a satellite should be as low as possible, considering that both the dimensions and the weight of a satellite are minimized, e.g. for reducing the fuel consumption. Moreover, during a space mission, it would be very challenging to compensate for sudden misalignments, therefore the used instruments should be mechanically stable and resistant to shocks and vibrations. These are the main reasons why in this field an important role could be played by photonic integrated circuits, which on the other hand have already been used in laboratory demonstrations of integrated QKD [250, 251].

However, before being employed in a space mission, the instrumentation should be tested [252] to verify that it will withstand the space environment conditions, which include the presence of high energy radiation, temperature oscillations, high-vacuum, vibrations and mechanical shocks. Despite the functioning of some photonic integrated components, such as single photon detectors [253] and sources [254], has been verified in such harsh conditions, there is little or no knowledge about the space qualification of photonic integrated circuits, mostly because it requires the access to special sites

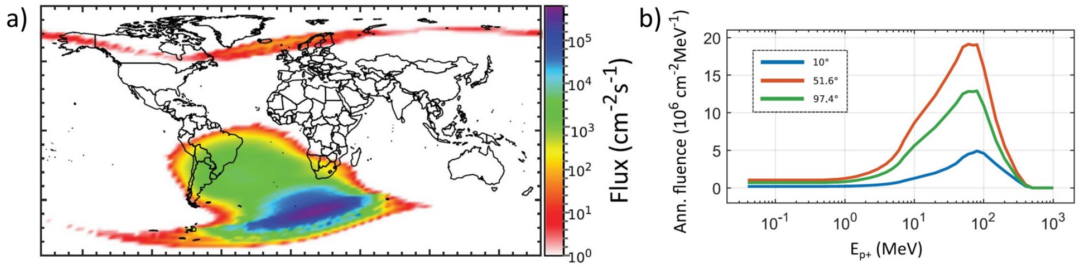

Figure 4.1: SPENVIS simulations of the concentration distribution of protons in the LEO space environment. a) Distribution of the proton flux at an altitude of 700 km, calculated by means of the AP-8 MAX model in SPENVIS. b) Annual proton fluence for different proton energies after a 1.85 mm-thick aluminum shield. Three notable trajectories are highlighted: in red the International Space Station, in green the Micius satellite, and in blue the Van Allen probes. Also in this case, the considered altitude is 700 km. Both images are from [249].

such as particle accelerators and sources of γ radiation. In this regard, in literature some studies have been proposed about FLW waveguides, nevertheless they focus more on the effects of radiation for sensing applications in nuclear facilities [255], or they limit the treatment only to the guiding properties of straight waveguides [256]. For this reason, we decided to further expand our study to the main components of a passive photonic circuit, i.e. straight waveguides, directional couplers (DCs) and Mach-Zehnder interferometers (MZIs). After their fabrication and preliminary characterization, we irradiated them with the proper quantity of protons and γ-rays for simulating a three-years mission in the low Earth orbit (LEO). After this, we measured again their main properties and confronted them with the pre-irradiation characterization. We finally performed also a study on the effects of temperature variations on the inscribed circuits, for addressing the day-night alternation that they would undergo in a satellite orbiting the Earth.

4.2 SPACE ENVIRONMENT

The LEO environment, which is usually where the satellites used in space communications orbit the planet, is characterized by a high concentration of charged particles, mostly protons. Indeed, if on the one hand the geomagnetic field efficiently protects the Earth ground from the energetic charged particles in the solar wind, on the other hand it traps them in the so-called Van Allen belts, which are two toroid regions surrounding our planet. In particular, the inner one is a reason of concern in the telecommunications field, since it extends in the altitude range 200 - 12000 km and thus affects the satellites orbits. Moreover, since the Earth magnetic dipole and rotation axes are not aligned, its distribution is not homogeneous (Fig. 4.1.a), and reaches its maximum in the South Atlantic Anomaly [257]. Therefore, the amount of radiation which a satellite is subjected to during its operation is not constant, and for this reason the properties

of the internal instrumentation should be chosen in function of the predicted mission trajectory (Fig. 4.1.a).

Concerning the energy of such charged particles, we must consider that satellites are usually equipped with protective shields for preserving the operation of the electronic instrumentation. However, these shields are not thick enough for completely stopping the whole impinging radiation since they would be too heavy. They are in fact able to block only the low-energy particles, while the high-energy ones are simply slowed down. This translates therefore in a red-shift of the energy spectrum of the radiation. In particular, by using the SPace ENvironment Information System (SPENVIS) software, provided by the ESA, it can be found that, after a typical shielding enabled by 1.85 mm of aluminum, the radiation arriving in the internal volume of a satellite at an altitude of 700 km is mainly in the range 100 keV - 400 MeV (Fig. 4.1.b). Moreover, the integrated fluence per year is simulated to be about $3 \cdot 10^9$ cm^{-2}.

In space, as we already mentioned, the satellites undergo also a significant exposure to γ-rays, which are mainly generated by the interaction between the cosmic rays and the gases composing the atmosphere [258]. In particular, at an altitude of 700 km, according to the simulations the annual absorbed dose would be of few tens of Gy. As a final consideration, we note that the instrumentation in a satellite should withstand high-vacuum conditions ($\simeq 10^{-7}$ Torr) and temperature fluctuations of the order of $\Delta T \simeq 20$ K [259].

4.2.1 *Interaction between protons and waveguides*

For the simulation of the interaction between the protons and the waveguides, we used the Stopping and Range of Ions in Matter (SRIM) code [260], which allows to calculate the penetration depth of protons and electrons in a material, as long as its chemical composition is known. In this regard, we used the typical composition of borosilicate glasses [261] (55.0% SiO_2, 21.0% CaO, 10.41% Al_2O_3, 7.0% B_2O_3, 5.6% MgO and 1.0% SrO), being the actual Eagle XG one a trade secret. Fig. 4.2.a shows the estimated penetration depth of protons impinging on the substrate surface in function of their energy. As intuitively expected, a particle with a high kinetic energy can propagate longer in the material before being slowed down and then completely stopped.

For our analysis, the most interesting depth range was about $10 - 50$ µm, which is where the FLW waveguides are usually inscribed when thermal phase shifters are used, since in this way they are closer to the corresponding heater. For this reason, we decided to focus our treatment on the energy values of 770 keV, which is related to protons stopping in a depth of about 10 µm (Fig. 4.2), and of 3 MeV, a value enabling the particles propagation up to a depth of 100 µm. Therefore, while in the former case we could analyze the effects of protons stopping in the waveguide core, the latter allowed us to understand the influence on the waveguide performances of the creation of defects caused by the passage of energetic protons. It is worth noting that using pro-

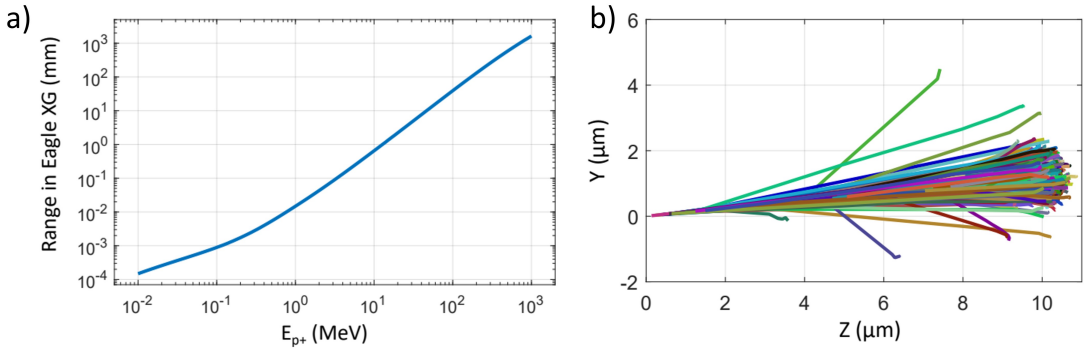

Figure 4.2: Simulations of the penetration of protons in Eagle XG. a) Penetration depth of protons in Eagle XG as a function of their kinetic energy. b) Monte-Carlo simulation of the trajectory of 500 protons with an energy of 770 keV in Eagle XG. It is possible to notice how the trajectories end at a depth of about 10 µm. Both images are from the supplementary information of [249].

tons with even higher energies would only lead to a higher number of defects, mostly vacancies according to our simulations, however the involved physical phenomena would still be the same.

In regard to the γ-rays penetration, we do not expect their energy to be attenuated during the interaction with the glass, thus they completely go through it. For this reason, the previous considerations about the waveguides depth are not necessary in this case.

4.3 FABRICATION AND IRRADIATION

Our simulations allowed us to choose the irradiation parameters to be addressed, which are the proton energy and fluence, and the dose of γ-rays. Moreover, we also showed the importance of the waveguides depth in this treatment. For investigating the main possible combinations, we decided therefore to fabricate seven identical samples, and then expose six of them to different irradiation conditions, while one was kept as control sample.

4.3.1 *Design and fabrication parameters*

The scheme of the seven samples can be found in Fig. 4.3. In each of them, the main building blocks of a passive photonic circuit, i.e. straight waveguides (SWG), directional couplers (DCs) and Mach-Zehnder interferometers (MZIs), were fabricated. Furthermore, we decided to investigate the optical properties of circuits optimized for two different wavelengths, notably 850 nm and 1550 nm, relevant for both classical and quantum telecommunications. For providing statistical significance, in particular

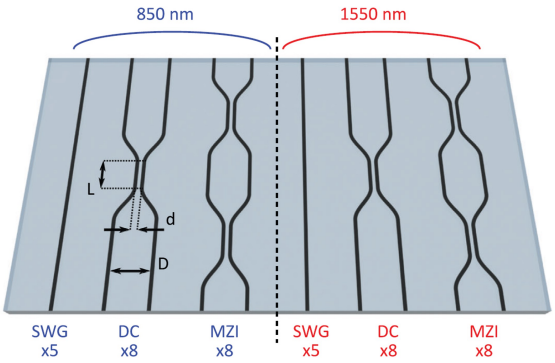

Inscription parameters	850 nm	1550 nm
Laser wavelength	1030 nm	
Focusing objective	50x, 0.6 NA	
Scanning speed	40 mm/s	
Pulse energy	370 nJ	480 nJ
Scans number	5	6
DC distance	8 µm	9 µm
DC length	1:0.5:4.5 mm	0:0.5:3.5 mm

Figure 4.3: Content of the seven samples for space testing. In each of them, two sets of circuits are present, optimized respectively for operation at 850 nm and 1550 nm. Every set is composed by 5 SWGs, 8 DCs and 8 MZIs. From [249]. In the table, the main inscription parameters used for fabricating the circuits are highlighted.

we inscribed 5 SWGs, 8 DCs and 8 MZIs per sample and per wavelength. In this way, we were able to monitor the eventual changes concerning the propagation losses and birefringence of SWGs, the evanescent coupling, and therefore the mode profile properties, of DCs, and finally the optical phase in the MZIs.

The fabrication of all the 7 replicas occurred in the same run and in the same Eagle XG glass sample, which was then cut. This choice was made for providing a fabrication of the seven samples as uniform as possible, for then being able to confront their results. The inscription was performed in the FIRE line with the cavity-dumped Yb:KYW laser, which as explained in Sect. 3.1 emits pulses with $\lambda = 1030$ nm, $\Delta t = 300$ fs, rep. rate $= 1$ MHz. The laser beam was focused by a $50\times$, 0.6 NA microscope objective. After an optimization procedure of the remaining fabrication parameters, i.e. pulse energy E_p, sample translation velocity v and number of laser scans n, the optimal combination was found to be $E_p = 370$ nJ, $v = 40$ mm/s and $n = 5$ for the waveguides at 850 nm, and $E_p = 480$ nJ, $v = 40$ mm/s and $n = 6$ for the ones working at 1550 nm. The processed glass chip was then annealed, polished to optical quality, and cut for separating the seven samples.

4.3.2 *DCs and MZIs design*

After a study of the DCs interaction distance d and length L at the two wavelengths, we chose $d = 8$ µm and L ranging from 1 to 4.5 mm for the DCs at 850 nm, while at 1550 nm we used $d = 9$ µm and L in the range $0 - 3.5$ mm. In both cases, the scan of the interaction length was performed with a spacing of 0.5 mm, and was chosen in such a way to clearly observe the oscillatory dependence of the reflectivity on L. A radius of curvature equal to 50 mm was employed, a quite standard value when the compactness of the circuit is not a strict requirement for the experiment.

Concerning the design of the MZIs, the DCs composing them were fabricated with the same geometry. Notably, one of the two arms of the MZIs was designed slightly longer than the other one, for introducing a passive phase shift of $\pi/2$. We decided to introduce this deformation for obtaining a balanced output distribution between the two waveguides of the MZIs built with balanced DCs, thus enhancing the sensitivity of the measurement of an eventual phase change.

4.3.3 *Waveguides depth*

The desired depth of the inscribed circuits was 10 µm for the first five samples, and 40 µm for the other two. We indeed already explained that shallow waveguides are more interesting than deeper ones since they provide good reconfigurability. However, if the waveguides are directly inscribed so close to the surface, their optical performances are greatly reduced since the fabrication process would be very sensitive to the surface cleanliness, and even the smallest particle of dust could interrupt the focused laser beam and thus increase the waveguide losses. For this reason, we decided to inscribe the circuits deeper in the glass, at 170 µm and 200 µm respectively, and then use a chemical etching for removing the material above them and so reduce their depth. To this purpose, we used a hydrofluoric acid solution with a 10% concentration and a controlled temperature of 35 °C, where the glass sample was immersed for 100 minutes, thus enabling the removal of 160 µm of glass.

4.3.4 *Irradiation with protons and γ-rays*

After a preliminary characterization of their optical properties, which will be discussed in the next section, six among the seven processed samples were irradiated with protons and γ-rays in different conditions, summarized in Tab. 4.1. In particular, two samples (#2 and #3) were irradiated only with γ-rays, three (#4, #6 and #7) only with protons and one (#5) with both for observing eventual combined effects.

Concerning the proton irradiation, as already explained, the kinetic energies of 770 keV and 3 MeV were used. Notably, between the two samples with waveguides at a depth of 10 µm, one was irradiated with the former, and one with the latter. In this way, we could observe both the effects of protons stopping near the waveguides and protons passing through them. The two samples where the waveguides were inscribed at 40 µm below the surface, instead, were both irradiated with the most energetic protons, since the 700 keV ones would not reach them according to our simulation. Moreover, we investigated the effects of fluence values of 10^{10} cm^{-2}, corresponding to a space mission with a duration of three years at an altitude of 700 km, and of 10^{12} cm^{-2}, the amount of protons that would interact with the samples in a mission of 300 years. Of course this value is not realistic, however we decided to implement such a harsh irradiation for enhancing the effects of the interaction. Finally, in respect to the

Sample	Depth [μm]	p^+ energy [MeV]	p^+ fluence [cm^{-2}]	γ-ray dose [Gy]
1	10	-	-	-
2	10	-	-	10
3	10	-	-	100
4	10	0.77	10^{12}	-
5	10	3	10^{12}	50
6	40	3	10^{12}	-
7	40	3	10^{10}	-

Table 4.1: Irradiation conditions of the seven samples.

γ irradiation, we used the doses of 10, 50 and 100 Gy, which are the typical values expected in the LEO space environment for a three-year mission.

The exposure to protons was performed in the Heavy Ion Accelerator Capability, which is a NCRIS facility at the Australian National University. The protons were generated by ion sputtering of a TiH target. The Ti ions were filtered by deflecting them with a 90° magnet, while the protons were accelerated by means of a 1.7 MeV tandem accelerator, which could provide an energy of up to 3.4 MeV per charge. The protons kinetic energy was defined within $\pm$5 keV, while their fluence to the glass sample had an uncertainty of less than $\pm$10%. The irradiation occurred at an angle of 7°, a value which is usually employed in the irradiation of crystals for avoiding ion channeling along the main crystallographic directions. In this case it was not necessary since the glass is amorphous, however we decided to keep the standard alignment anyway. The irradiation occurred at room temperature at a pressure of 10^{-7} Torr.

The γ-irradiation was instead performed in a facility of the Australian Nuclear Science and Technology Organisation. For this purpose, we used a sample of the radioactive Co-60 isotope, emitting two γ-rays with an energy of 1.17 and 1.33 MeV. The dose per minute arriving at the glass samples was 4.329(36) Gy/min.

4.4 POST-IRRADIATION ANALYSIS

4.4.1 *Microscope inspection*

The first characterization that we performed after the irradiation consisted in a microscope visual inspection of the devices. In this regard, Fig. 4.4 shows the lateral facets of the irradiated samples after irradiation, confronted with the not irradiated one (#1). In detail, the facets of samples #2, #3, #4 and #7 were not affected by the irradiation, at least qualitatively. However, an evident change was observed for samples #5 and #6, consisting in a degradation of the waveguides cross-sections and a change of color of the glass, mostly in a superficial region about 100 μm-thick. Notably, these samples

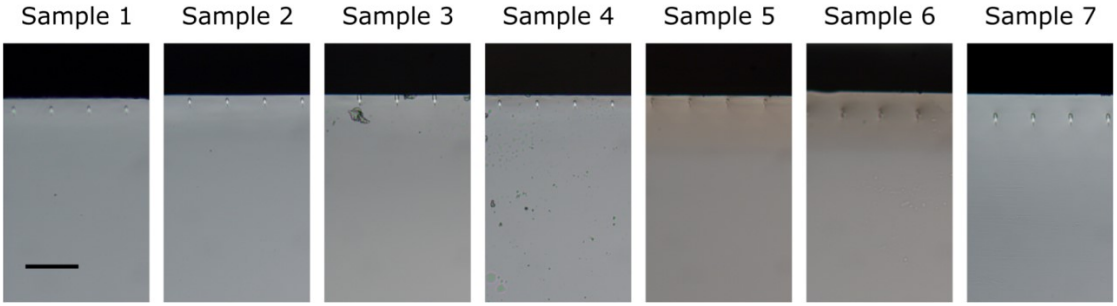

Figure 4.4: Microscope images of the waveguides cross-sections after exposure. Notably, samples #5 and #6, which were irradiated with protons with the highest energy and fluence, show a degradation of the waveguides and a color change of the material. The bar in the first picture corresponds to 100 µm. From [249].

were both irradiated with the highest dose of 3 MeV energetic protons. This result is consistent with our simulations, which predicted a penetration depth of about 100 µm for protons with such kinetic energy. The fact that this degradation did not occur for sample #7, irradiated with protons with the same energy, can be explained by the lower dose, which led to a lower density of generated defects.

4.4.2 *SWGs performances*

4.4.2.1 *Propagation loss*

The measurement of the propagation loss (PL) of the SWGs was performed by coupling them with an optical fiber, in detail an SM800 at 850 nm and an SMF28 at 1550 nm. As explained in Sect. 3.3.3, its value was retrieved by the measurement of the insertion loss (IL), to which the Fresnel (FL) and coupling losses (CL) were subtracted. In particular, the loss occurring at the coupling between fiber and SWGs was estimated by calculating the overlap integral between the two guided modes, which were measured by using an imaging camera. The length of the samples was 2.2 cm.

The results of the analysis are represented in Fig. 4.5.a, which shows the average, for every sample and wavelength, of the PL of the 5 SWGs of every set. It should be noticed that the measurement was affected by some variability, as it is possible to retrieve from the data of sample #1. This was mainly due to the difficulty of obtaining a reproducible fiber coupling, which led to a certain degree of variability on the CL and therefore on the retrieval of the PL from it. As a matter of fact, the more reliable procedure, i.e. the cut-back, could not be implemented in this case since it is destructive for the samples. All this considered, we can anyway conclude that the PLs in samples #2, #3, #4 and #7 did not change, at least in a statistically relevant way. Instead, the samples #5 and #6, whose waveguides cross-sections were qualitatively degraded by the irradiation, also showed a relevant increase of the PL value for both wavelengths, up to 0.5 dB/cm.

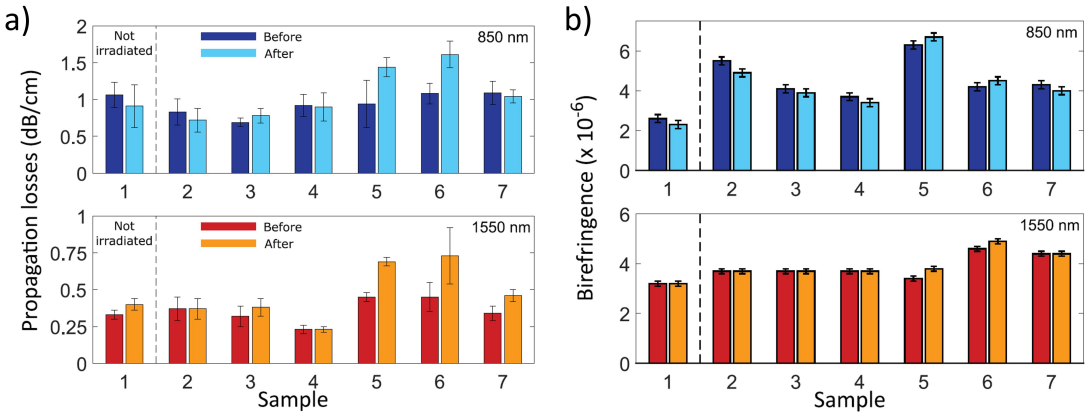

Figure 4.5: Propagation loss and birefringence of the seven samples before and after irradiation. a) Average of the propagation losses of the 5 SWGs in every set sample/wavelength. Except for samples #5 and #6, which shows a relevant increase, the others were not affected by the irradiation. b) Birefringence of one SWG in every set sample/wavelength. In all the cases we did not observe changes within the precision of the measurement. Both from [249].

From this analysis it can be concluded that the waveguides were affected neither by the γ-rays nor by protons with the lowest investigated fluence (10^{10} cm^{-2}), regardless of their energy. These are exactly the conditions which are expected in a standard mission in the LEO environment. The waveguide losses were instead increased by the irradiation with a high fluence (10^{12} cm^{-2}) of more energetic protons, which probably generated a large number of defects in glass while passing through it. However, it should be stressed again that this irradiation condition is not realistic for a standard satellite-based space mission.

4.4.2.2 *Birefringence*

The birefringence of the SWGs was measured by the retrieval of their Müller matrix with the setup presented in Sect. 3.3.3. In particular, the measurement was performed for two SWGs in every sample, one at 850 nm and one at 1550 nm. Moreover, the uncertainty of the procedure was estimated by performing the same measurement without any sample in the setup, thus effectively measuring the residual birefringence related to nonidealities of the optical components, retrieving an uncertainty value of $2 \cdot 10^{-7}$ at 850 nm and $1 \cdot 10^{-7}$ at 1550 nm. The comparison between pre- and post-irradiation measurements is shown in Fig. 4.5.b. In this case, it is possible to observe how all the values are the same within the precision of the measurement. It can be noticed that the birefringence in samples #5 and #6 seems to be affected by a systematic slight increase, however the precision of our setup did not allow to confirm it with a statistical relevance. Nevertheless, even if this was the case, the change would be very small, and would not affect the operation of a circuit.

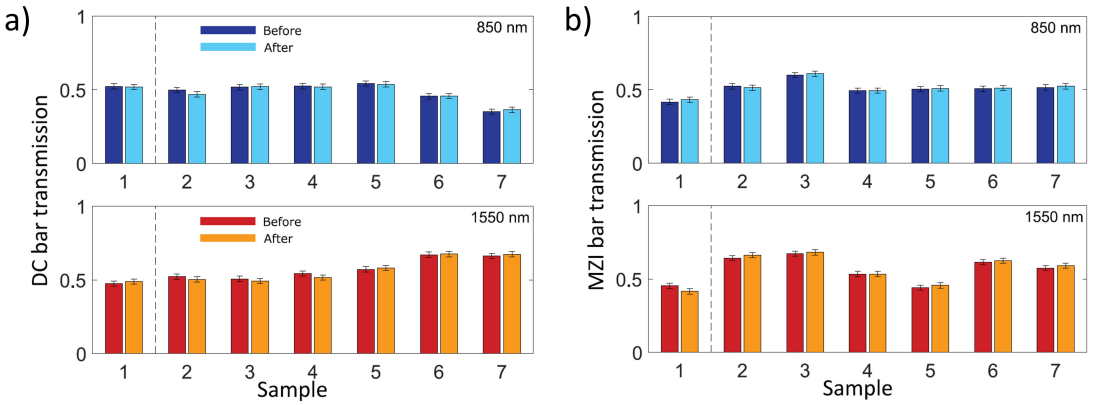

Figure 4.6: Bar transmissions of the most balanced DC and MZI for every sample and wavelength, using V polarized light. All the measured quantities were not significantly affected by the irradiation. Both from [249].

4.4.3 *DCs and MZIs performances*

The characterization of the DCs and MZIs was performed by end-fire coupling of one of their input ports, and then by measuring the bar and cross output powers, thus retrieving their reflectivity, or equivalently their bar transmission. The measurement was carried out for H and V polarizations. Moreover, its uncertainty, mostly attributed to the collection of uncoupled light, was estimated to be about 1%, a value which was retrieved by measuring several times the reflectivity of the same directional coupler in different coupling conditions.

As a result of the characterization, we did not observe any relevant change of the DCs and MZIs reflectivities after irradiation. As an example, we show in Fig. 4.6 the bar transmissions of the most balanced DCs and MZIs for every wavelength and sample, coupled with V polarized light. As a matter of fact, the closer is the splitting ratio to 50%, the higher is the sensitivity on any change of the evanescent coupling properties in the DCs and of the optical phase difference in the MZIs. Moreover, the characterization with H polarization, not shown in the figure, provided the same result, and interestingly the irradiation did not cause any change in samples #5 and #6, as it is represented in detail in Fig. 4.7.

This analysis allows us to conclude that neither the evanescent coupling properties nor the optical path were affected by the exposure. Since both elements are related to the refractive index contrast, at least in the weakly guiding regime as it is for FLW waveguides, we can state that the defects generated by the protons leaved it basically unaltered.

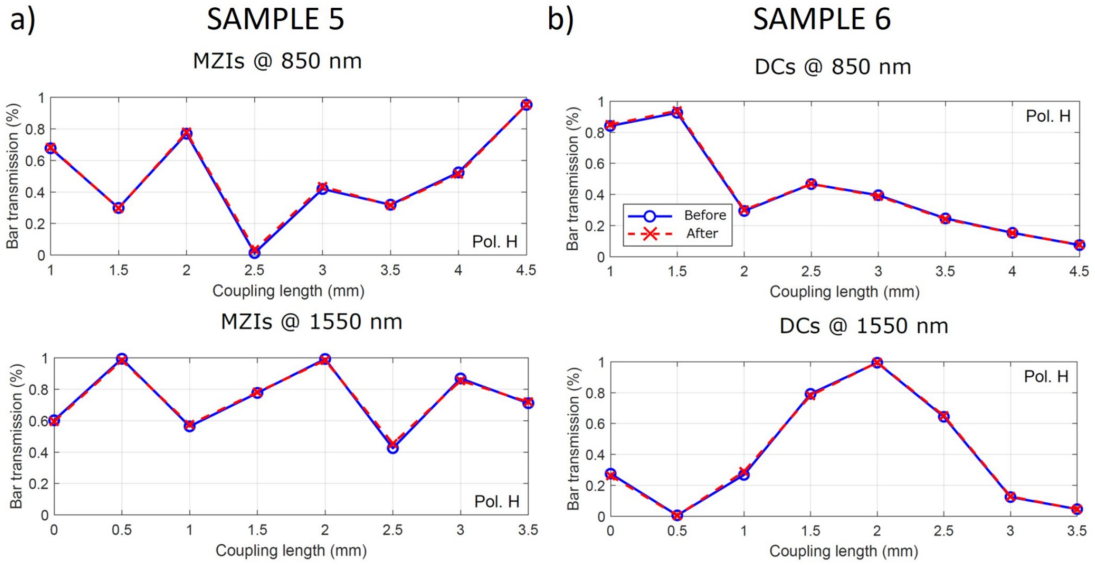

Figure 4.7: Bar transmission of all the MZIs of sample #5 and DCs of sample #6 for H polarization, before and after irradiation. From [249].

4.4.4 *Effects of vacuum and temperature variations*

In a space mission, the instrumentation in a satellite is expected to operate in high vacuum conditions and with temperature fluctuations. Concerning the functioning in vacuum of the FLW waveguides, no further investigations were needed in our analysis, since the irradiation with protons already occurred at a pressure similar to the one expected in LEO, so it was part of the experiment. Moreover, borosilicate glass is known to withstand high-vacuum conditions with negligible outgassing, and as a matter of fact it is often used in the view ports of vacuum chambers.

In regard to the temperature variations, we decided to study their effect on the reflectivity of some MZIs, which among the fabricated circuits are for sure the most sensitive to this parameter. In particular, we investigated a temperature variation of 70°C, which is much higher than the one expected during standard operation in space (about 20°C). For controlling the temperature of the sample we used a Peltier plate, while light was injected in one input of the MZIs by means of a microscope objective. Notably, the sample was mounted in a custom-made copper holder for providing a uniform heating or cooling (Fig. 4.8.a).

Fig. 4.8.b shows the measurements performed on two MZIs, one working at 850 nm in sample #1, thus not irradiated, and one operating at 1550 nm from sample #4. Also in this case, we show the data of the MZIs with the reflectivity as close as possible to 50%. The represented graphs demonstrate that the reflectivity is independent of temperature, this means that a uniform temperature variation, as it would be in a satellite, would not affect the MZIs operation.

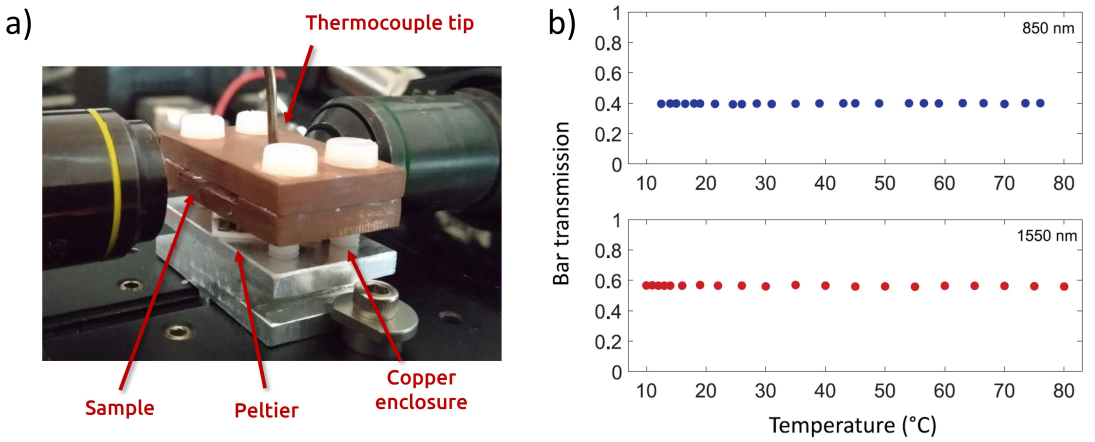

Figure 4.8: Measurement of the temperature sensitivity of MZIs. a) Picture of the used setup. The sample was put in a copper enclosure, which was in contact with a Peltier device for controlling the sample temperature. The MZI input and output ports were coupled by using two microscope objectives. b) Reflectivity of two MZIs from samples #1 and #4, respectively operating at 850 nm and 1550 nm. The temperature ranges from 10°C to 80°C. From [249].

4.5 CONCLUSIONS AND FURTHER DEVELOPMENTS

In this work we showed that FLW waveguides can be a valuable tool in space-based applications, mostly in the field of classical and quantum optical communications. In particular, we addressed the performances of the building blocks of any passive photonic circuit inscribed in the Eagle XG substrate. We demonstrated that the interaction with the protons and γ-rays which are expected in the LEO space environment in a three-years mission would not affect the propagation losses, the birefringence, the evanescent coupling properties and the propagation constant of waveguides. We found that harsher environments, equivalent to a mission with a duration of 300 years, could affect the waveguides losses, nevertheless all the other properties would remain unaltered, thus allowing also in this case a reliable operation. Moreover, we also investigated the effect of high-vacuum and temperature variations of the circuits, finding no relevant changes.

In light of this work, it would be interesting to also test the other fundamental components of FLW circuits. For instance, there is little or no information about the behaviour of thermal phase shifters in vacuum, and it has never been investigated whether they could withstand prolonged exposure to charged particles and energetic radiation without a degradation of their properties. Moreover, if the effect of vibrations was not tested in our work since the waveguides were inscribed in monolithic glass chips, of course the resistance to mechanical shocks of the other components, for instance the pigtailed optical fibers, should be addressed for providing a stable and reliable operation.

5

SCALABLE PHOTONIC PLATFORM FOR QUANTUM INFORMATION PROCESSING

In this chapter we present three different works towards the implementation of a scalable photonic integrated platform for quantum information processing.

The first, carried out in collaboration with Prof. Fabio Sciarrino of La Sapienza University of Rome, consists in the proposal of a new class of photonic circuits for boson sampling. In particular, we show that the unique 3D capability provided by FLW can be exploited for the fabrication of a reconfigurable three-dimensional interferometer, capable of performing unitary Haar-random operations with a reduced length if compared to the standard 2D meshes of MZIs. This work has been published on ArXiv [262] and is currently under the submission process.

The second work consists instead in the fabrication of a six-modes universal photonic processor whose performed unitary operation can be controlled by means of thermal phase shifters with a reduced cross-talk and power dissipation. By characterizing it with classical light, we show that it can be reconfigured for performing several unitary linear transformations, with state-of-the-art fidelities, losses and power consumption.

Finally, we report about the characterization and optimization of the emission of a single photon source based on a semiconductor quantum dot emitter. With our analysis we show that a single photon emission with high brightness, indistinguishability and purity can be achieved, thus paving the way for the use of this kind of sources in the implementation of experiments with a number of photons higher than the one currently provided by SPDC sources.

Concerning my personal contribution, in the first two activities I worked on the optimization of the fabrication process, the design and the inscription of the final circuits, and their characterization with classical light. The last activity was instead performed during a four-months period as a visiting student in the Quantum Optics, Quantum Nanophysics and Quantum Information group of the University of Vienna, led by prof. Philip Walther. Under the supervision of Dr. Juan Loredo, I participated to the collection of the data presented in this work, while also supervising the master student Virginia Oddi.

5.1 RECONFIGURABLE CONTINUOUSLY-COUPLED 3D CIRCUIT FOR BOSON SAMPLING

5.1.1 *Motivations of the work*

We explained in Sect. 1.2.3 that the implementation of the boson sampling problem represents one of the most feasible ways to demonstrate the quantum advantage over classical computation. However, one of the main issues in this respect is represented by the dimensions of the system capable of performing this task with the required complexity. As a matter of fact, we discussed the realization of a gaussian boson sampling (GBS) setup built by bulk components, reported in [98], which allowed to achieve quantum supremacy by sampling up to 76 photons at its output. If on the one hand this is a milestone result, on the other hand the scalability of the presented setup to a higher number of modes is a quite challenging task. Moreover, it does not provide the reconfigurability required for the implementation of arbitrary transformations, since only passive micro-optics elements were used. In this regard, photonic integrated devices could solve these issues, being scalable and fully reconfigurable. The most common choice is to perform boson sampling with circuits based on the universal decomposition schemes proposed by Reck and Clements. However, in this case the number of modes is limited by the propagation losses, since the length of these devices generally scales with the number of modes.

For this reason, in this work we tried to address this issue by proposing a new approach. Instead of using 2D discrete meshes of MZIs, we exploit FLW for fabricating a 3D continuously-coupled waveguide array, and we demonstrate that in this way we can reduce the minimum footprint required for the realization of Haar-random matrices. Moreover, we use thermal phase shifters on top of the waveguides to obtain the possibility to reconfigure the device. This approach, though not providing a universal processing, is suited for boson sampling experiments, where the true randomness of the performed transformation is more necessary than universality.

5.1.2 *Discrete and continuous coupling*

In an integrated interferometer, notable efforts should be dedicated to the reduction of the insertion losses. In particular, in FLW circuits, given the optimum compatibility of the guided mode with the fiber one, the losses mainly arise from the propagation in the waveguides. For this reason, the length of a circuit should be as low as possible. In this discussion, we will consider the length dependence on the number of modes of two different approaches for the implementation of non-universal interferometers, based respectively on discrete and continuous coupling among the waveguides.

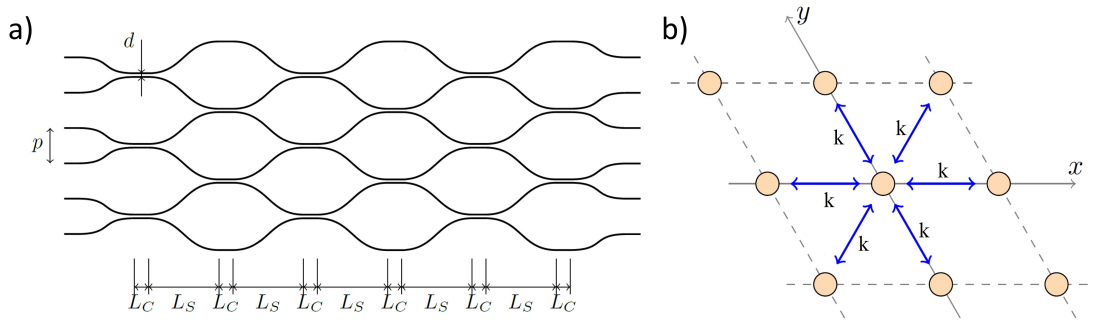

Figure 5.1: Multi-mode interferometers based on discrete and continuous coupling between waveguides. a) Clements configuration for a non-universal 6-ports interferometer built as a mesh of cascaded directional couplers with interaction distance d, coupling length L_C, pitch p and length of the S-bends L_S. b) Cross-section of a continuously-coupled array where the waveguides are arranged in a triangular lattice. The coupling coefficient between the nearest neighbour waveguides is equal to k. Both images are adapted from [262].

CLEMENTS CONFIGURATION Let us consider the Clements scheme for building an integrated multi-mode interferometer with m optical modes, which, as we discussed, is more compact than the proposal by Reck. For the moment, we will limit the discussion to a non-universal realization composed of cascaded directional couplers with static reflectivities in place of reconfigurable MZIs, a configuration which as we already showed is sufficient for boson sampling, as long as both the reflectivities and the phase shifts are random. In this case, the overall length of the circuit, if we exclude the input at output waveguides segments, can be calculated as:

$$L_{Clem} = (m-1) \cdot L_S + m \cdot L_C, \tag{5.1}$$

where L_S is the projection of a DC S-bend on the propagation direction, and L_C is the interaction length of a DC (Fig. 5.1.a), which as a first approximation can be considered the same for all of them. Notably, while L_C is dependent on the design of a DC, and can be even reduced down to 0 if the evanescent coupling in the S-bend region is exploited, the length L_S is instead dependent on the minimum radius of curvature R_{min} that can be employed, and therefore cannot be arbitrarily minimized. As a matter of fact, if we design the bent region with a sinusoidal shape, which is the preferred choice since it provides a continuous second derivative and therefore reduced loss, we have

$$L_S = \frac{\pi}{2}\sqrt{2R_{min}p}, \tag{5.2}$$

where p is the waveguides pitch (with p much greater than the interaction distance d), and where we imposed that the minimum radius of curvature of the S-bend, occurring at its beginning and at its end, is exactly equal to R_{min}.

Therefore, in the approximation of reaching the desired splitting ratio with $L_C = 0$ by a proper choice of d, we can write the whole length of the circuit as:

$$L_{Clem} = (m-1) \cdot \frac{\pi}{2}\sqrt{2R_{min}p}, \tag{5.3}$$

where a scaling law proportional to the number of modes m is evident. In particular, if we consider the typical values of $R_{min} = 30$ mm and $p = 80$ µm for FLW circuits, we have that the footprint of the device increases of about 4 mm per mode. Moreover, if a certain degree of reconfiguration of the circuit is necessary, we should introduce additional straigth regions for placing the thermal phase shifters, and replace the DCs with MZIs. In this case, as a rule of thumb we can say that the dependence found in Eq. (5.3) would be at least doubled, further increasing the circuit length.

3D CONTINUOUS COUPLING Let us consider now a continuously-coupled interferometer where waveguides are arranged in a triangular lattice configuration (Fig. 5.1.b). As opposed to discretely-coupled ones, in this case it is not possible to implement a decomposition method enabling universality. Nevertheless, intuitively we can state that, for good operation, a continuously-coupled array should be long enough to enable interference among all the propagating photons, regardless of their input port. For this reason, we can take as L_{min} the length that allows the photon wavefunction injected at port 1 to spread until the mode m, which is the farthest one.

The propagation of a photon wavefunction in a continuously-coupled waveguide array [263] can be described by a set of differential equations for the destruction operators $\hat{a}_i$, with i the waveguide index:

$$-i\,\frac{d\hat{a}_i}{dz} = \sum_{j\neq i} k_{ij}\,\hat{a}_j, \tag{5.4}$$

where z is the light propagation direction and k_{ij} is the coupling coefficient between modes i and j. This set of equations has as a solution a plane-wave of the kind:

$$\hat{a}_i = \hat{A}\,e^{i\,(\beta_z z+\beta_x x+\beta_y y)}, \tag{5.5}$$

where β_z, β_x and β_y are the components of the wavevector respectively on the propagation direction and on the two axes of the 2D Bravais lattice.

If now we consider coupling only with the nearest neighbour waveguides, and that in a triangular lattice the coupling coefficients are all equal to k, we can obtain the following dispersion relation

$$\beta_z = 2k\left(\cos\beta_x + \cos\beta_y + \cos\big(\beta_x + \beta_y\big)\right) \tag{5.6}$$

by using in Eq. (5.4) the plane-wave solution. Moreover, we can retrieve the group velocities in the two directions x and y as:

$$v_{x,y} = \frac{\partial\beta_z}{\partial\beta_{x,y}} = -4k\,\sin\beta_{x,y}, \tag{5.7}$$

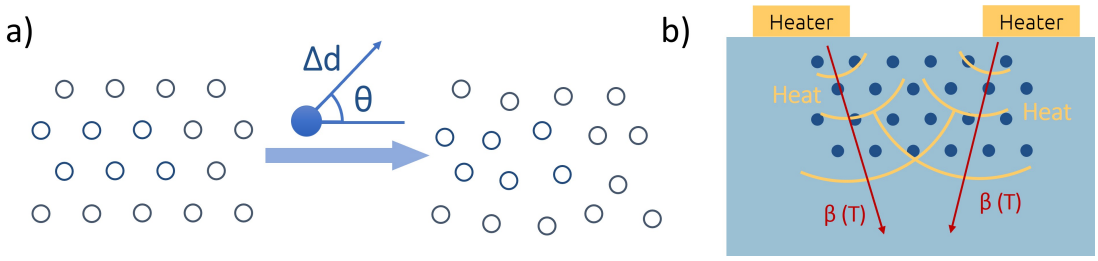

Figure 5.2: Achieving random transformation with continuously-coupled waveguide arrays. a) By randomly displacing the waveguides with respect to their ideal position in a triangular lattice, it is possible to obtain a random modulation of the coupling coefficients. b) By inducing a temperature gradient in the array, it is possible to obtain a non-uniform distribution of the waveguides propagation constants.

which govern the spreading of the wavefunction in the Bravais lattice. In particular, being the photon spatially point-like, it will contain all the transverse components, therefore also the one spreading with the maximum velocity $|v_x|_{max} = |v_y|_{max} = 4k$. Now, if we consider that the maximum number of modes in x and y that the wavefunction should travel across is $\sqrt{m}$, we have that the minimum length of the array enabling a spreading of the wavefunction in the whole lattice is

$$L_{min} = \frac{\sqrt{m}}{|v_{x,y}|_{max}} = \frac{\sqrt{m}}{4k}. \tag{5.8}$$

Therefore, as opposed to planar interferometers, the 3D disposition of the waveguides enables a faster spreading of the wavefunction in the extreme sites of the arrays, since it can travel in both x and y directions at the same time.

Of course this treatment considers the most favorable case, in which the maximum velocity in x and y is achieved. Moreover, it could be necessary to propagate longer for implementing useful transformations. Nevertheless, these nonidealities can be addressed by increasing the length of the device by a proper factor $B > 1$ in such a way that $L = BL_{min}$, and the scaling law retrieved in Eq. (5.8) would still be valid.

5.1.3 *Implementation of random transformations*

Until now, we have considered the propagation of light in a homogeneous waveguide array. However, this kind of devices is not suited for a boson sampling experiment, since they provide highly symmetric transformations which could be easy to simulate classically. For this reason, we decided to introduce the randomness required for the experiment by randomizing the coupling coefficients k_{ij} and the propagation constants $(\beta_z)_i$ of the waveguides, which in some ways replace the random reflectivities and phase shifts of the Clements configuration.

Notably, we achieved a random distribution of the coupling coefficients k_{ij} by randomly displacing the position of every waveguides by a distance Δd and an angle

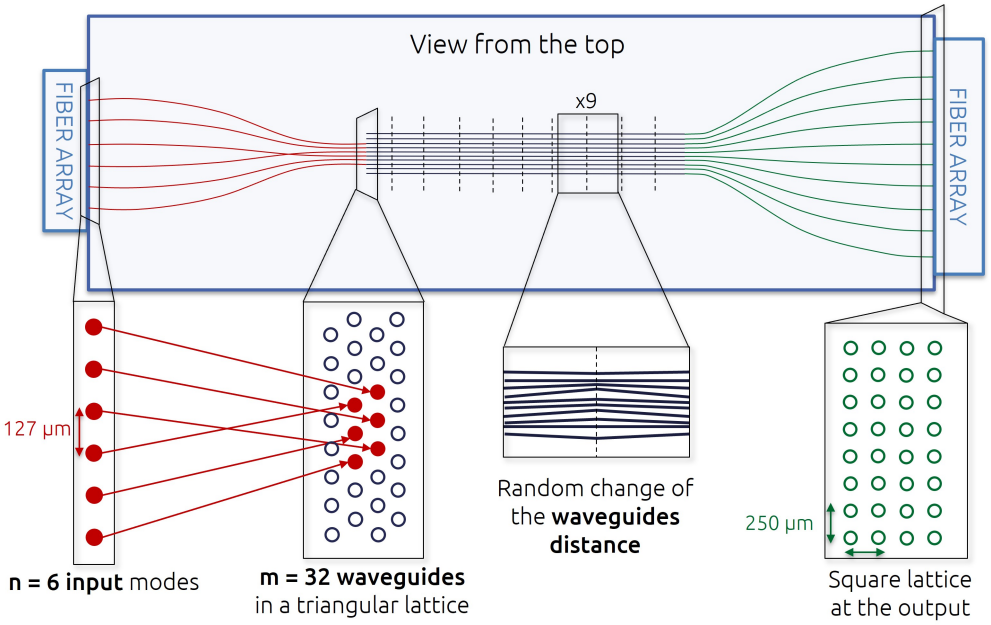

Figure 5.3: Scheme of the 3D photonic circuit.

θ with respect to the ideal triangular arrangement (Fig. 5.2.a). This modulation was performed several times along the propagation direction for increasing the achieved randomness.

Concerning the modification of the propagation constant of every waveguide, we decided to fabricate some thermal phase shifters at the two sides of the array for inducing thermal gradients in the interferometer. By exploiting the thermo-optic effect, in this way we induced a non-uniform distribution in the transverse plane of the $(\beta_z)_i$ (Fig. 5.2.b). Moreover, the introduced reconfigurability, despite not providing universality, enables the implementation of a larger number of random transformations, which is for sure an added value if compared to a static passive device.

5.1.4 *Design and fabrication of the optical circuit*

5.1.4.1 *Design*

The design of the optical circuit is shown in Fig. 5.3. It includes:

- $n = 6$ input modes, spaced by a pitch of 127 µm for coupling with standard fiber arrays;
- a continuously-coupled interferometer composed by $m = 32$ waveguides placed in a 8×4 triangular lattice. The waveguides distances are randomly modulated 9 times along the propagation;

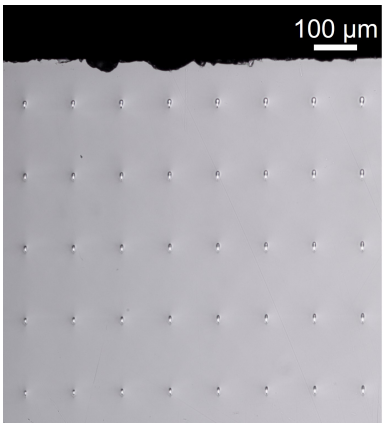

Inscription parameters	
Laser system	Pharos
Laser wavelength	1030 nm
Repetition rate	1 MHz
Focusing objective	20x WI, 0.5 NA
Scanning speed	20 mm/s
Pulse energy	290 nJ
Scans number	6

Figure 5.4: Fabrication of waveguides with uniform properties in a depth interval of 750 µm. The microscope image shows the cross-sections of some waveguides inscribed at different depths for some combinations of the inscription parameters. In the table, the optimal parameters resulting from the optimization procedure are shown.

- an output distribution of the waveguides matching an 8×4 commercial fiber array, with a square arrangement and a pitch of 250 µm.

Moreover, cosinusoidal fan-in and a fan-out regions enable the waveguides remapping, to connect respectively the input and output ports with the waveguides of the interferometer. It should be noted that the depth interval of the circuit is equal to 750 µm, as required by the output fiber array. The choice of using a 2D fiber array for collecting the output light instead of a 1D, thus increasing the complexity of the fan-out region, has the purpose of reducing the footprint of the device. As a matter of fact, a linear fan-out would place less strict requirements on the fabrication of the circuit, since the output waveguides would be on the same plane. Nevertheless, it would require a longer propagation for remapping them, thus introducing additional losses.

5.1.4.2 *Optimization of the waveguide performances*

The first step of the fabrication of the interferometer was the optimization of the inscription parameters for obtaining a waveguide guiding light at 785 nm with low losses and a good mode profile in the required depth range. The chosen wavelength corresponds to the single photon emission of the SPDC source used for the boson sampling experiment.

The fabrication was performed in the CAPABLE line, with the standard emission of the Pharos laser ($\lambda = 1030$ nm, rep. rate $= 1$ MHz, $\Delta t = 170$ fs). For reducing the spherical aberrations, and so the sensitivity of the focal spot properties to the focusing depth, a water-immersion objective was used, with a $20\times$ magnification and 0.5 NA. The optimization was performed on the pulse energy E_p, the translation velocity v, and the number of scans n, obtaining the optimal values $E_p = 290$ nJ, $v = 20$ mm/s and $n = 6$. The choice was made for obtaining as uniform as possible guiding properties in

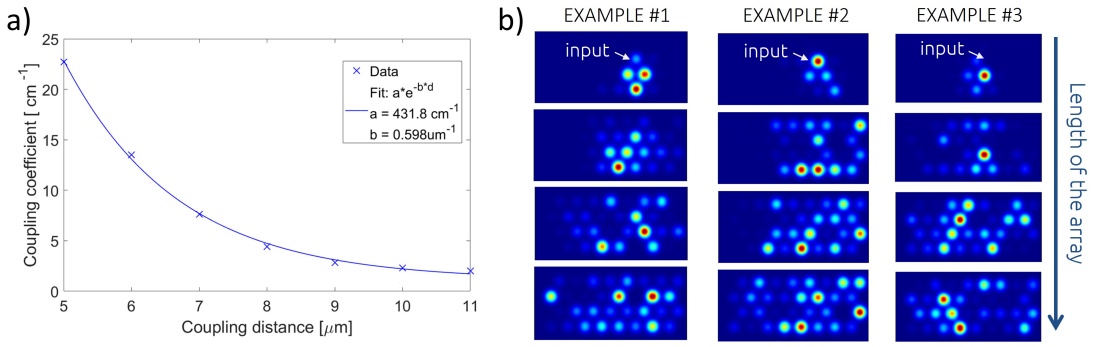

Figure 5.5: Engineering of the waveguides distance for achieving the required randomness. a) Dependence of the coupling coefficient on the interaction distance. b) Three simulations where light, injected in the same input, propagates in interferometers with different random modulations of the interaction distances. As it is possible to see, the three modulations lead to significantly different output distributions, thus strongly affecting the light propagation.

the depth range $300 - 1070$ µm (Fig. 5.4). In particular, the mean measured propagation loss was of 0.25 dB/cm, with a maximum value of 0.4 dB/cm 300 µm below the glass surface, and a minimum of 0.1 dB/cm for the waveguide fabricated at a depth of 1070 µm (or equivalently, fabricated 30 µm above the bottom surface). The mode size ranged from of 4.1×4.3 µm² to 4.6×4.9 µm² as the inscription depth increased. It should be noted that, despite some variability is present, the achieved level of reproducibility and quality of the guiding properties in such a large inscription depth range is quite a remarkable result, enabled as already explained by the immersion in water of the sample.

After inscription, the waveguides were subjected to the thermal annealing presented in Sect. 3.2 for reducing their birefringence and bending loss. Concerning the latter, these fabrication parameters enabled the used of a minimum radius of curvature of 30 mm with negligible additional losses.

5.1.4.3 *Study of the evanescent coupling*

We studied the evanescent coupling properties of the waveguides by fabricating directional couplers with zero interaction length and different interaction distances d. The fabrication occurred 30 µm above the bottom surface, since this was the planned depth of the final interferometer, chosen for providing a good reconfigurability by means of the thermal phase shifters. By a fitting procedure on the reflectivities of the directional couplers we were able to estimate the curve $k = k(d)$, as shown in Fig. 5.5.a.

We then used the retrieved curve for estimating the degree of randomness introduced by the modulation of the waveguides positions in the lattice. For this purpose, we performed some simulations of the behaviour of the interferometer. In particular, we split it in a series of shorter arrays, each one characterized by a fixed, random distribution of the waveguides positions, which was obtained by applying to every

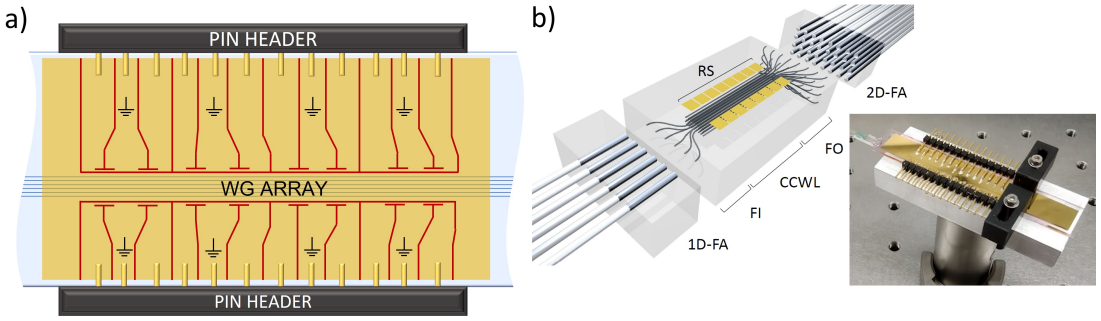

Figure 5.6: Fabrication of the final circuit. a) Ablation pattern of the resistors necessary for inducing thermal gradients along the array. In particular, the 16 resistors can be controlled individually by 24 contact pads, 8 of which provide connection to ground. b) Scheme of the final device, including the input fiber array (1D-FA), the fan-in (FI), the continuously-coupled waveguide lattice (CCWL), the fan-out (FO) and the 2D fiber array used for collection (2D-FA). In the inset, a picture of the assembled device is shown. Adapted from [262].

waveguide a displacement with modulus Δd and angle ranging in the whole transverse plane. In particular, Δd could not be completely arbitrary, for avoiding excessive overlaps of the guided modes. Considering that the mode diameter was about 5 µm, we chose the value $d = 11$ µm as the pitch of the ideal triangular lattice, and fixed the maximum displacement to $\Delta d_{max} = 2$ µm. In this way, the distance between two neighbouring waveguides could not be lower than $d_{min} = d - 2\Delta d_{max} = 7$ µm, which is a safe value for avoiding any disturbance between them. With these parameters, we performed some simulations of the propagation of light in the array (Fig. 5.5). This analysis showed that it was possible to obtain a good degree of randomness with a 36 mm-long interferometer, with a modulation of the waveguides positions occurring every 4 mm, thus 9 times along the array.

It should be noted that, considering $k \simeq 0.2$ mm^{-1} as it is for $d_{avg} = 11$ µm, and due to the fact that the two lattice sizes are not the same ($\Delta x = 8,\ \Delta y = 4$), the minimum length calculated in Eq. (5.8) should be roughly modified in

$$L_{min} \simeq \frac{max\{\Delta x, \Delta y\}}{4k} = 10 \text{ mm}, \tag{5.9}$$

since the light must travel across more waveguides in the x direction than y. With a length $L = 36$ mm we are therefore sure that the light is interfering in all the modes of the arrays. If now we consider a Clements interferometer, and we use the scaling law of 4 mm per added mode, the total length becomes $L_{Clem} \simeq 13$ cm. It is therefore clear that the continuously-coupled approach provides a much higher compactness.

5.1.4.4 *Fabrication of the final circuit*

After the optimization procedure and the choice of all the parameters, we fabricated the optical circuit in a 1.1 mm-thick Eagle XG sample by using the scheme in Fig.

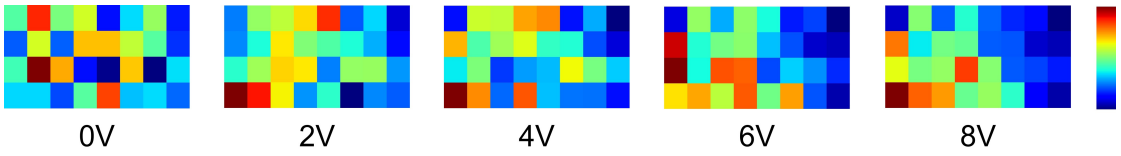

Figure 5.7: Reconfiguration of the output power distribution by applying an increasing voltage on a phase shifter.

5.3. In detail, the final length of the circuit was 8 cm, including the 3.6 cm of the interferometer and the footprint of both the fan-in and fan-out regions.

After the inscription of the waveguides, 16 thermal phase shifters, 8 per side, were fabricated on the glass surface by using the process described in Sect. 3.1. In particular, after deposition of 2 nm of chromium and 100 nm of gold, the conductive paths were defined by using the Pharos laser, with an energy per pulse of 200 nJ and a translation speed of 2 mm/s. A 10×, 0.25 NA microscope objective was used for obtaining 5 µm-thick tracks. It should be noted that no insulating trenches were fabricated since the heat was supposed to be distributed in the whole array, rather than localized on specific waveguides. The ablation pattern and the arrangement of the resistors are shown in Fig. 5.6.a. In particular, the phase shifters were designed with a width $w = 20$ µm and a length $L = 3$ mm, with a resistance value of $R = 70 \pm 13\ \Omega$. For their control, the phase shifters were connected to two pin headers, which were glued at the two sides of the glass sample.

Finally, the sample was pigtailed to an input fiber array, including six 780-HP fibers linearly arranged with a pitch of 127 µm. Moreover, for providing both thermal dissipation and mechanical stability, the device was mounted on an aluminum heat sink. The result of the fabrication process is presented in Fig. 5.6.b.

5.1.4.5 *Characterization with classical light*

Before using the device with single photons, we performed a characterization with classical light addressing the insertion losses and the capability of reconfiguring the output distribution by acting on the phase shifters.

The insertion loss was measured after pigtailing, by injecting in the six input fibers laser light at 785 nm. The 32 output modes were collected by a 25× microscope objective, and their output power measured singularly with a powermeter. Notably, the used magnification was high enough for clearly separating the output modes on the sensor head. The measured insertion losses were in the interval $3.2 - 3.6$ dB depending on the chosen input, corresponding to a transmission of the input light between 43% and 48%.

As a final analysis, we measured the output power distribution for different voltages applied to different resistors, while coupling light in one of the six inputs. As shown in Fig. 5.7, by acting on the phase shifters it was actually possible to change the output distribution of the array.

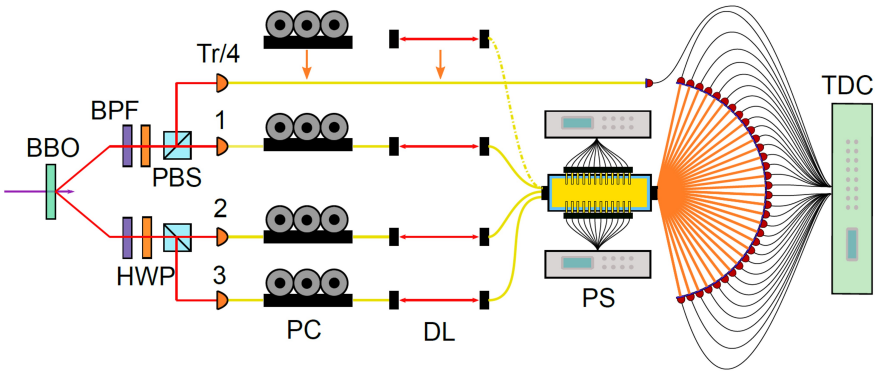

Figure 5.8: Experimental setup for the generation, manipulation and detection of the single photons interfering in the circuit. Legend: BBO = beta-barium borate, HWP = half-wave plate, BPF = band-pass filter, PBS = polarizing beam splitter, PC = polarization controller, DL = delay line, PS = power supply, TDC = time-to-digital converter. From [262].

5.1.5 *The boson sampling experiment*

Here we present the measurements performed with the device at the Quantum Information Lab of La Sapienza University of Rome. After a brief description of the experimental setup, we will discuss the preliminary characterization of the circuit with quantum states of light, followed by the actual boson sampling experiment.

5.1.5.1 *Experimental setup*

The setup used in the experiment is shown in Fig. 5.8. The single photons were generated by an SPDC source, based on a BBO (beta-barium borate) crystal pumped with the second harmonic of a Ti:sapphire laser for having emission of photons at 785 nm. Depending on the laser intensity, the crystal could emit either one or two pairs of photons. The former regime was useful for the preliminary characterization of the circuit, while the latter was necessary for injecting more photons in the device during the boson sampling experiment. After generation, the photons were split in four different spatial modes by means of half-wave plates and polarizing beam splitters. Moreover, 3 nm band-pass filters were used for increasing their indistinguishability. Polarization controllers and delay stages provided the possibility to manipulate the polarization and the time of arrival of the photons before coupling with the circuit, thus controlling their indistinguishability. At this point, the four photons were injected into the input fibers of the device. In alternative, one of the photons could be coupled into a fiber that was directly connected to one detector, thus heralding the arrival of the other three, at the cost however of reducing the number of photons useful for the experiment. After propagation in the circuit, the four (or three) photons could be collected by the output fiber array and detected by 32 SPADs, which were connected to a time-to-digital converter for identifying the coincident detections.

5.1.5.2 *Preliminary analysis with single photons*

The full characterization of the unitary operation U of a continuously-coupled interferometer is more difficult to perform if compared to the discrete ones, since it is not possible to directly associate an element of the matrix to a component of the circuit. For this reason, the characterization started by assuming the most general form of an unitary transformation composed of complex elements:

$$U = \{U_{lm}\} = \{\rho_{lm} \cdot e^{i\phi_{lm}}\}, \tag{5.10}$$

where the moduli ρ_{lm} and the phases ϕ_{lm} can be retrieved by a proper measurement.

In particular, the moduli are associated to the probability a_{ij}^{hk} of finding two distinguishable photons in the output modes i, j when injected in the inputs h, k:

$$a_{ij}^{hk} = \rho_{ih}^2 \rho_{jk}^2 + \rho_{jh}^2 \rho_{ik}^2. \tag{5.11}$$

This quantity can be retrieved from the output probability distribution of heralded distinguishable photons injected in inputs h and k, or in alternative from the output power distribution of laser light injected in the same inputs.

Concerning the phases, they are associated to the visibility of the Hong-Ou-Mandel (HOM) dip, defined as the normalized difference between a_{ij}^{hk} and the same probability when the two photons are indistinguishable:

$$V_{ij}^{hk} = \frac{a_{ij}^{hk} - |U_{ih}U_{jk} + U_{jh}U_{ik}|}{a_{ij}^{hk}} = -\frac{2\rho_{ih}\rho_{jk}\rho_{jh}\rho_{ik}}{a_{ij}^{hk}} \cdot \cos\left(\phi_{ih} + \phi_{jk} - \phi_{jh} - \phi_{ik}\right). \tag{5.12}$$

This value can be retrieved from the measurement of the output probability distribution while scanning the difference in time of arrival between the input photons, thus switching from the distinguishable to the indistinguishable case.

By implementing this reconstruction procedure, it was possible to characterize the unitary operation of the circuit for several configurations of the phase shifters. As an example, we show in Fig. 5.9.a one of the 4×32 reconstructed matrix, being 4 the number of used input ports and 32 the number of the modes in the interferometer. In this way, it was possible to understand whether the realized transformations could be considered random. For this purpose, by changing the currents applied to the 16 resistors, 15 different transformations were implemented for retrieving the frequencies of the phases and the moduli of the corresponding matrix elements. The resulting distributions were then compared to the ones expected for a set of Haar-random unitaries, obtaining a good agreement (Fig. 5.9.b and 5.9.c).

Finally, the reproducibility of the phase shifters was addressed by injecting a single heralded photon in one of the input ports and by measuring the probability distribution at the output of the circuit. The measurement was performed in three different days, while keeping the same configuration of the applied currents. As shown in Fig. 5.9.d, the three measured distributions are basically the same, with a similarity equal to 99.8%.

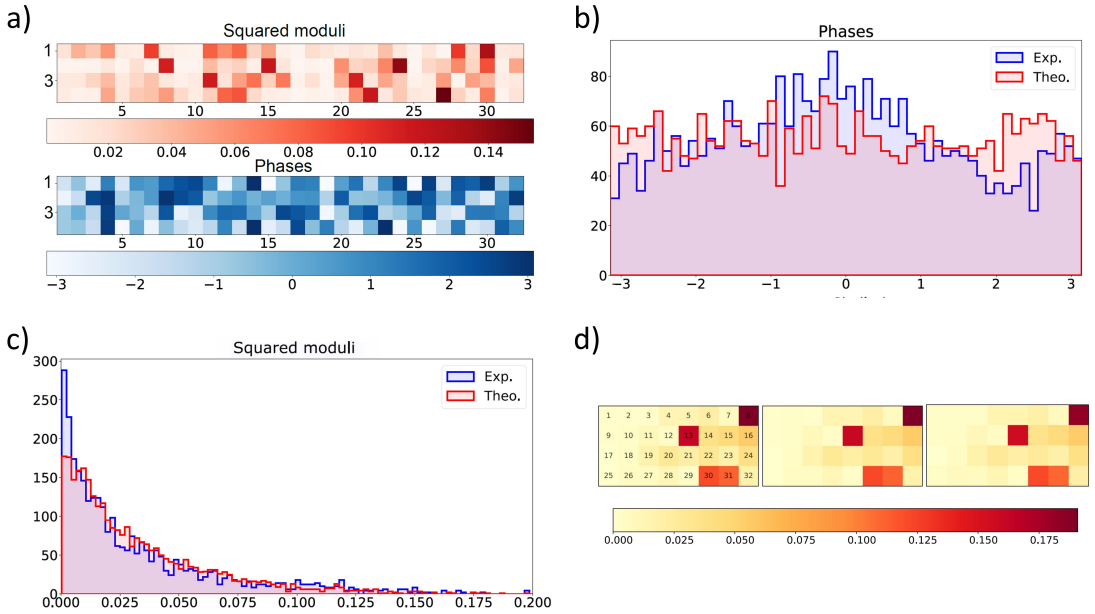

Figure 5.9: Reconstruction of the unitaries and implementation of random transformations. a) Reconstructed moduli and phases of an 8×4 sub-matrix of the unitary U for a fixed combination of currents applied to the resistors. b-c) Comparison of the frequency distributions of the phases (b) and squared moduli (c) between 15 experimental 3×32 sub-matrices and 15 sub-matrices sampled from a Haar measure. d) Reproducibility of the output probability distribution measured in three different days by using the same applied currents. All the images are from [262].

5.1.5.3 *Boson sampling with 3 and 4 photons*

Once performed the preliminary characterization of the circuit with quantum light, the boson sampling experiment with 3 and 4 photons was implemented. As previously explained, the SPDC source could provide the injection in the circuit of either 3 photons, with the fourth one used for heralding, or all the 4 photons without heralding. Moreover, since the used SPADs could not distinguish between the arrival of one or more photons, only collision-free events could be recorded. Nevertheless, we already explained that if $m \sim n^2$ this is not an issue, since, due to the bosonic birthday paradox, the case of two or more photons exiting from the same output mode has a very low probability.

The output distribution was sampled with rates of ~ 300 and ~ 60 events per hour in the case of three- and four-fold coincident detections, respectively. To understand whether the sampling was occurring from a truly random distribution rather than a trivial one, some validation techniques were implemented. The validation of a boson sampling experiment it is indeed not straightforward since it cannot be simulated classically. In this regard, the performed tests allowed us to validate the experiment against the uniform distribution and the distinguishable sampler hypotheses. Notably,

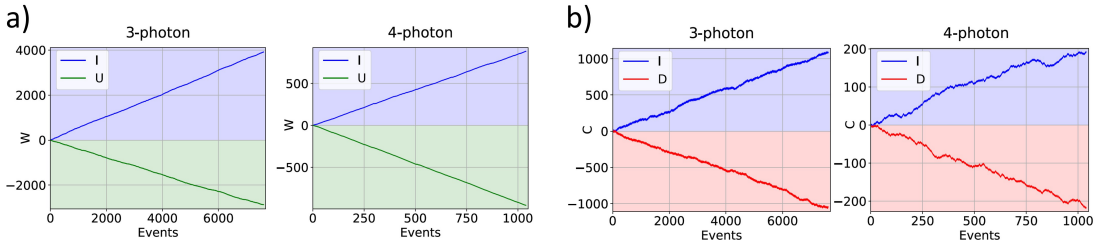

Figure 5.10: Boson sampling validation against the uniform distribution (a) and distinguishable sampler hypotheses. From [262].

this analysis includes the calculation of two counters, C in the former case and W in the latter, which are decreased when the measurement is sampling respectively from a uniform distribution or from the distribution of distinguishable particles, while are increased in the opposite case, i.e. when the experiment has been performed successfully. As an example, we show in Fig. 5.10.a and 5.10.b the result of the measurement. In particular, it is possible to see that when the boson sampling is performed correctly (blue curve) the experimentally retrieved counters increase, while if the photons are made distinguishable (green curve) or the distribution is made uniform (red curve) they decrease, thus validating the correctness of the experiment. The definition of the counters W and C goes beyond the scope of this thesis, and can be found in [262].

5.1.6 *Conclusions and future perspectives*

This work showed that continuously-coupled waveguide arrays can be used as an alternative to discrete interferometers for the realization of boson sampling experiments, with the advantage of being much more compact when the number of modes is increased. As a matter of fact, this approach allowed us to fabricate the integrated interferometer for boson sampling with the highest number of modes ever reported in literature. Moreover, thermal phase shifters fabricated at the side of the array can be used to induce thermal gradients and therefore provide randomness and reconfiguration capabilities.

Despite being a non universal approach, we believe that this scheme can be used to greatly scale the complexity of the realized experiments. In this respect, we are planning a new circuit with at least 64 modes and 40 phase shifters with comparable length and loss, and with low additional efforts in terms of fabrication. However, the main limitation in this work was not the circuit performance, but rather the emission rate of the SPDC single photon source. In this regard, an advance could be achieved by using much more powerful sources such as quantum dot emitters, which provide higher emission efficiencies, as it will be explained in Sect. 5.3.

5.2 LOW-POWER RECONFIGURABLE SIX-MODE PHOTONIC PROCESSOR

5.2.1 *Motivations of the work*

In Sect. 1.2.2 we discussed the importance of reconfigurable photonic circuits for achieving a universal quantum processing. A quantum photonic processor can be built by means of a multi-mode interferometer, either bulk or integrated, realizing any arbitrary linear transformation on a quantum state of light. For achieving this result, both the Clements and Reck schemes can be used. In integrated photonics, both implementations include cascaded reconfigurable MZIs preceded by reconfigurable phases, arranged in such a way to allow any injected photon to interfere with all the others.

The largest universal photonic processor ever reported in literature [65] is a SiN Clements interferometer enabling the manipulation of 12 optical modes with fidelities higher than 90%. As we discussed, however, that circuit is affected by two important issues: the insertion losses and the high power dissipation. As a matter of fact, the high confinement provided by SiN waveguides causes a poor coupling efficiency with optical fibers, thus resulting in an insertion loss higher than 5 dB, corresponding to a transmission of about 20%. This quite low value does not allow to perform 12-photons experiments with high rates, in particular when combined to the low emission efficiency of the SPDC sources, which currently are the most used ones. Moreover, for achieving a π phase shift on a single MZI, the needed power dissipation on the corresponding heater is reported to be about 385 mW. It is clear that this high value places strict requirements on the heat dissipation of the chip when several phase shifters are used, and further limits the scalability.

In this regard, we can exploit femtosecond laser writing for addressing and solve these issues. It has already been explained that this fabrication platform enables high coupling efficiency with optical fibers, and very low power dissipation of the phase shifters thanks to the micromachining of insulating structures in glass. Moreover, this is also accompanied by the reduction of the thermal cross-talk, in particular when operating in vacuum, as described in [236]. However, the possibility of fabricating several phase shifters with such a high quality has never been addressed in literature, therefore the realization of a complex FLW circuit with low power dissipation is not straightforward. Moreover, the low confinement has the negative effect of limiting the miniaturization of the circuit, and so the number of modes. For this reason, as a first study, we decided to fabricate a smaller device, i.e. a 6-modes universal photonic processor, to test whether FLW could be suited for the integration of such a high number of components on the same device.

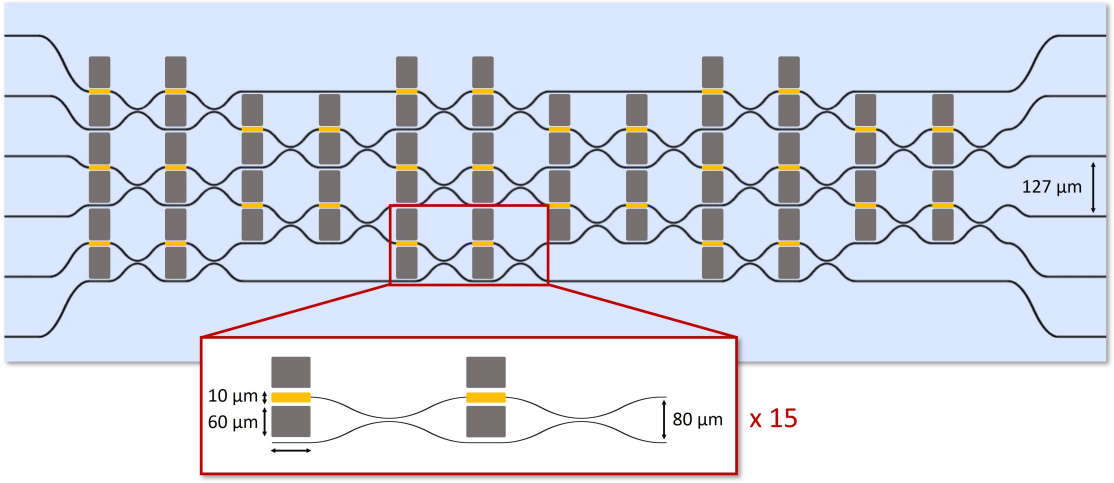

Figure 5.11: Scheme of the 6-mode photonic processor fabricated by FLW. The inset shows the unit cell, composed of a MZI which can be fully reconfigured by controlling two phase shifters.

5.2.2 *Design and fabrication*

5.2.2.1 *Scheme of the device*

The preliminary design of the 6-mode interferometer is represented in Fig. 5.11. The unit cell of the device is composed by a MZI whose internal and external phases can be controlled by means of two resistors, each with a length $L_R = 1.5$ mm and a width $w_R = 10$ µm, and delimited by two 300 µm-deep insulation trenches with the same length and width $w_T = 60$ µm. The unit cell is repeated 15 times according to the Clements scheme, which has been preferred to the Reck one since it is more compact. This results in the fabrication of 30 phase shifters and 60 trenches. Concerning the optical circuit, the design wavelength is set to 785 nm as in the previously described experiment, and the inscription depth is 30 µm for providing an optimal reconfigurability. Moreover, the input and output ports are spaced by 127 µm for coupling them with standard fiber arrays, while the pitch of the MZIs is set to 80 µm for reducing the footprint of the device. Therefore, a fan-in and a fan-out region are necessary for remapping the waveguides from the larger pitch to the smaller one. Finally, the minimum radius of curvature is fixed to 30 mm as a compromise between compactness and reduced bending loss. With these parameters, and overall length of the whole circuit of about 8 cm is obtained.

5.2.2.2 *Optimization of the inscription parameters*

The optimization of the fabrication consisted in a scan of the parameters for finding the combination reducing the loss of the circuit. In particular, the geometry of the inscribed waveguides resembled the one of the first spatial mode of the final device, thus directly measuring its expected insertion losses, which after all is the most important

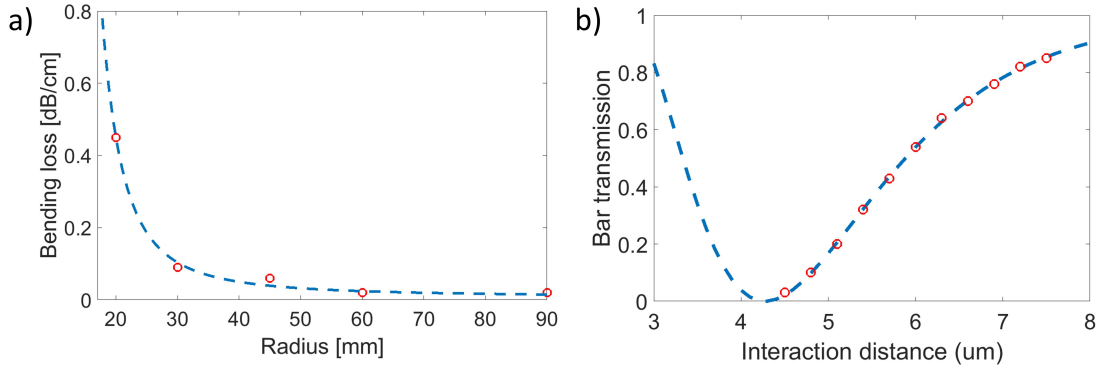

Figure 5.12: Bending loss and directional couplers. a) Bending loss for different radii of curvature. In red the measured data, in blue the exponential fit. b) Reflectivity of directional couplers with zero length and different interaction distances. In red the measured data, in blue the fit used to retrieve the distance guaranteeing a balanced splitting.

parameter. The fabrication was performed in the CAPABLE line, with the Pharos laser ($\lambda = 1030$ nm, rep. rate $= 1$ MHz, $\Delta t = 170$ fs), and 1.1 mm-thick Eagle XG glass samples were used. Since the waveguides were supposed to be at 30 µm from one of the two surfaces of the glass, a 20×, 0.5 NA was used to focus the laser 30 µm above the bottom surface. This side of the sample was chosen because, when the waveguides are fabricated close to the upper surface, they are generally of lower quality, while the water immersion was implemented for reducing the spherical aberrations when focusing in such a thick portion of material. The resulting parameters from the optimization procedure, i.e. energy per pulse of 330 nJ, translation speed of 25 mm/s and 6 scans, provided a waveguide with $IL \simeq 2.5$ dB for a length of 8 cm, and a mode size of 4.5×4.7 µm². Also in this case the waveguides underwent the thermal annealing described in Sect. 3.1.

Moreover, to make sure that the chosen radius of curvature was not too low, we studied the bending loss of the waveguide for different radii of curvature, as explained in Sec. 3.3.3, finding an almost negligible value of 0.1 dB/cm for $R = 30$ mm (Fig. 5.12.a).

5.2.2.3 *Balanced directional couplers*

We studied the evanescent coupling between waveguides to find the optimal geometry of directional couplers providing a splitting ratio as close as possible to 50%, which is the condition for achieving fully reconfigurable MZIs. For reducing the footprint of the circuit, we limited our study to couplers with $L_C = 0$, thus exploiting the evanescent coupling occurring in the S-bends. To find the distance guaranteeing a balanced splitting, we fabricated several directional couplers with different interaction lengths, and then we characterized their reflectivities (Fig. 5.12.b). By performing a fit procedure, the optimal distance was estimated to be equal to $d = 5.9$ µm.

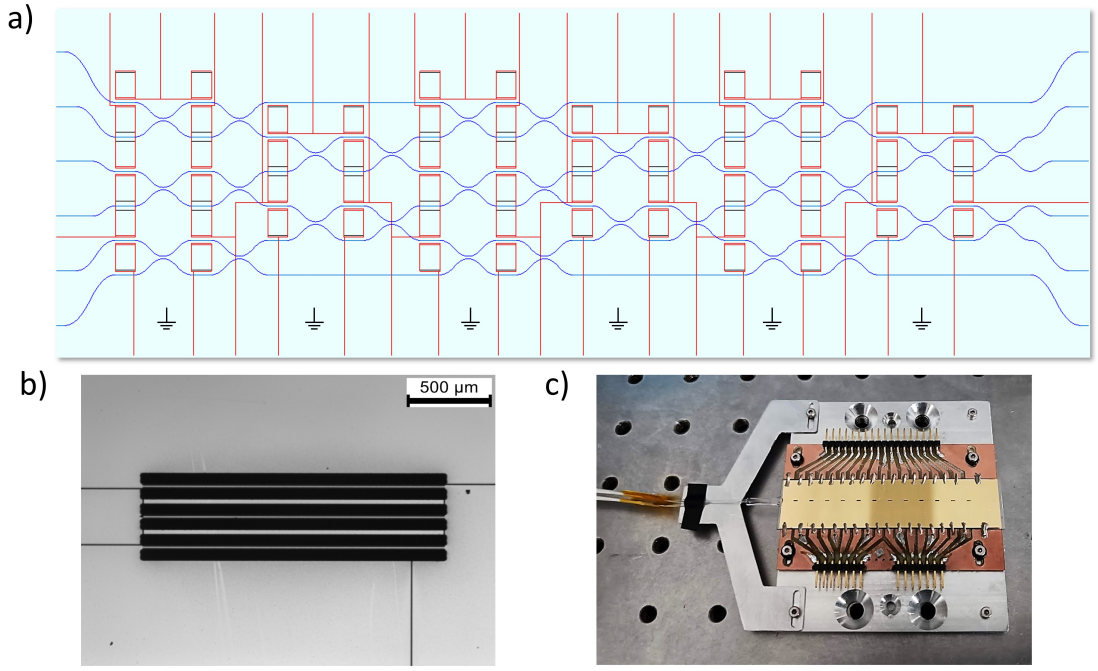

Figure 5.13: Fabrication of the resistors and final packaging. a) Ablation pattern (in red) of the phase shifters on the optical circuit (in blue). Notably, the 30 resistors can be controlled by means of 36 electrodes, 6 of which provide connection to ground. The latter were designed slightly wider than the others, since more current is expected to pass through them. b) Microscope image showing the laser ablations near a group of six trenches. c) Picture showing the final packaging of the device.

5.2.2.4 *Fabrication of the final circuit*

After finding the optimal design and inscription parameters, the optical circuit was inscribed on the basis of the scheme in Fig. 5.11, then annealed and its facets polished to optical quality. After a preliminary characterization to check whether all the optical performances were as expected, the insulation trenches were fabricated by using the procedure in Sect. 3.1, which, as already explained, was the result of an optimization process performed as a part of this thesis. Notably, of 60 trenches, 59 completely detached from the bulk glass, while one was removed only partially, up to a depth of 225 µm. Nevertheless, this was not a problem while operating the circuit since the defective trench was deep enough to provide a sufficient heat confinement.

Then, the chromium-gold film was deposited on the glass surface, and patterned (Fig. 5.13.a-b) in the CAPABLE line by means of the fs laser, with an energy per pulse equal to 200 nJ and a translation speed of 2 mm/s. A 10×, 0.25 NA microscope objective was used, thus obtaining 5 µm-thick ablations. The pattern was carefully optimized for concentrating the heat dissipation on the resistors, rather than on their electrodes. As a matter of fact, while the heaters had a size of 10 µm × 1.5 mm, showing an aspect ratio of 150, their connections were designed to have an aspect ratio

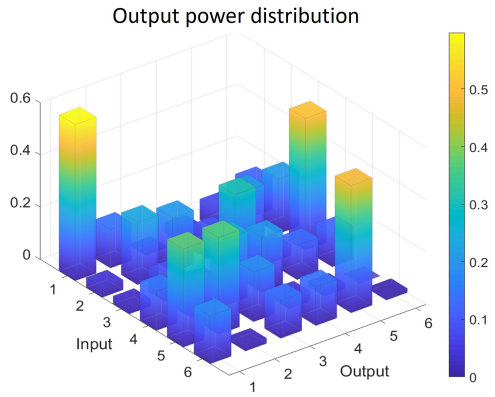

Input	Insertion Loss [dB]
1	2.68
2	2.67
3	2.6
4	2.66
5	2.67
6	2.71

Figure 5.14: Output power distribution and insertion losses of the passive optical circuit.

lower than 2. In this way, their parasitic resistance in series to the one of the actual resistors was lower than 1.3%, thus leading to a negligible power dissipation.

Finally, the sample was pigtailed to an input fiber array for a stable coupling, and the electrodes were connected by a conductive glue to two printed circuit boards (PCBs) for providing the electrical connections with the external power supply. Moreover, the sample was put in contact with an aluminum heat sink for stable operation. The final packaging of the device can be found in Fig 5.13.c.

5.2.3 *Characterization*

5.2.3.1 *Performances of the passive circuit*

The optical performances of the passive photonic circuit were assessed at first by sequentially coupling its six inputs with laser light, and by measuring the output power distribution for each input (Fig. 5.14). In particular, we measured an insertion loss value of about 2.7 dB for each input, thus providing more than 50% of transmitted light. Moreover, in the image we present also the light power distribution from the six output waveguides for each input. It is possible to see that, without any reconfiguration, the resulting output distribution is quite random. This is mainly caused by the poor control that we have on the passive phase shift of the MZIs, which is very sensitive to any variability of the fabrication process, such as nanometric positioning errors of the translation stages or laser fluctuations. Nevertheless, this is not an issue, since this phase shift can be characterized and compensated when operating the phase shifters.

5.2.3.2 *Performances of the phase shifters*

The resistance value of a phase shifter is generally dependent on the current or voltage applied to it, since if the dissipated electrical power increases, the temperature of the

resistor increases as well, thus causing a change of the resistance, which is mostly positive for metals. For this reason, the resistance of the 30 phase shifters was measured both in the low and high voltage regimes. Moreover, every data was taken after a waiting time of about 2 minutes, for allowing thermal stabilization of the phase shifters. The measured resistances in the low-voltage regime were in the range $118 - 132\ \Omega$, with an average value of 124.5 Ω, while in the high voltage regime they increased to $132 - 146\ \Omega$, with an average of 139.6 Ω. It should be noted that the retrieved resistances are all compatible with the Qontrol Q8IV controller which were later used for controlling all of them at the same time. This device is able indeed to provide up to 24 mA of current per channel, thus with these resistance values up to 75 mW per phase shifter could be dissipated, which is much higher than the power dissipation $P_{2\pi}$ needed for inducing a 2π shift.

Then, the electrical stability of the resistors was studied. As a matter of fact, the stability of the circuits is a crucial parameter in quantum photonics experiments, since usually long integration times are required and so the operation of the devices should not change. For this purpose, some resistors were controlled for 12 hours with a voltage slightly higher than $V_{2\pi}$, for simulating a typical operation. The measurement was performed both in room pressure and medium vacuum ($2.7 \cdot 10^{-3}$), finding respectively a change of 0.73% and 0.14%, corresponding to variations in optical phase of 0.05 rad and 0.009 rad. It should be noted moreover that these measurement were performed without a control of the room temperature, therefore they take into account also temperature fluctuation occurring for instance between day and night. Nevertheless, the retrieved values are negligible and allow therefore a reliable and stable operation of the device.

5.2.4 *Reconfigurability and arbitrary transformations*

5.2.4.1 *Calibration of the induced phase shift*

For achieving the capability of implementing arbitrary transformations, the dependence of the induced phase shift on the dissipated power should be retrieved for every resistor. However, given the complexity of the interferometer, this task is not trivial, since only for some particular configurations it is possible to find a unique correspondence between the output of the circuit and the power dissipated by a single phase shifter. As a matter of fact, for the characterization of the processor it is necessary to use the decomposition method which can be found in [56].

The first step of this procedure is the characterization of the phase shifters controlling the internal phases of the MZIs. Let us start by considering the MZIs placed on the diagonal of the circuit (Fig. 5.15.a). If we inject light in mode 1, the output of mode 6 will depend only on their internal phases (highlighted in gold in the figure), since the light that eventually enters in the other MZIs cannot spread until the last output waveguide. Moreover, the output light power is not affected by the external phases

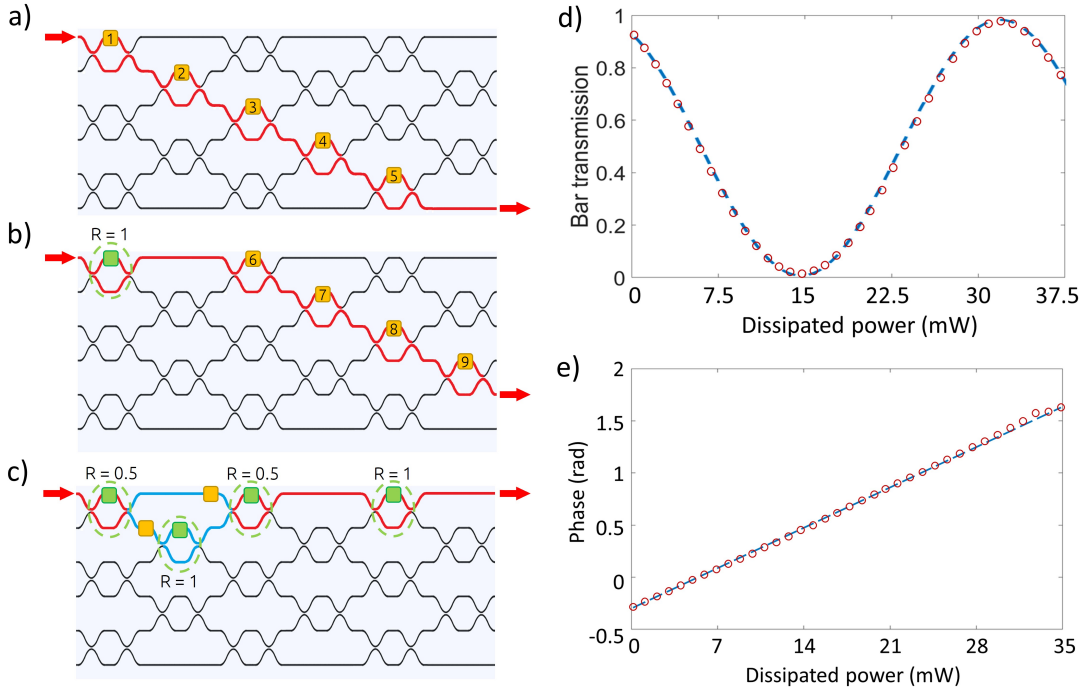

Figure 5.15: Calibration of the phase shifters. a) The diagonal MZIs can be characterized by injecting light in the first input an by measuring the output of the last one. The MZIs are labelled according to the order in which they should be calibrated. b) The upper sub-diagonal can be analyzed by setting the MZI with $R = 1$, thus simulating the case in a) with a 5×5 triangular sub-circuit. c) The external phases of the MZIs can be calibrated by individuating proper interferometric rings (in light blue) containing them. The MZIs delimiting these rings should be set accordingly to simulate a larger MZI. e) Curve of the bar transmission of MZI 5 as a function of the dissipated electrical power, when light is injected in input 1 and all the MZIs in the diagonal are set in transmission mode. e) Phase shift induced on MZI 5 when controlling the upper resistor in the same column.

either, since they only contribute to a global phase term which does not influence the output power of mode 6. Therefore, if for instance we control only the resistor labelled as 1, we can retrieve the induced phase shift by measuring the oscillations in the output power of mode 6. Once the resistor is characterized, then it can be set in transmission mode, in this way all the light enters the second MZI of the diagonal, labelled as 2. At this point, this element can be characterized as well, and the procedure goes on until the last MZI of the diagonal, labelled as 5, is set to be fully transmittive, and all the light injected in the circuit exits from output 6. Then, the MZIs belonging to the upper sub-diagonal (Fig. 5.15.b) can be analysed by setting the MZI 1 in reflection mode for injecting all the light in the MZI 6. This configuration is the same as before, with the difference that the 5×5 sub-circuit delimited by the sub-diagonal should be considered. By reiterating this procedure, it is possible to characterize all the MZIs present in the upper triangular matrix. Then, by injecting light in the mode 6, and

by measuring the light coming from waveguide 1, it is possible to perform the same process and characterize the lower triangular mesh. The MZI not belonging to any of the two meshes, which is the one placed in the first column and combining modes 3 and 4, can be straightforwardly characterized by injecting light in one of its two input ports, and by setting the other MZIs in such a way that the output power distribution depends only in it.

The analysis of the external phase shifters of the MZIs is more complicated. In this case it is indeed necessary to find some large interferometric rings (Fig. 5.15.c) in the circuit, and to set their input and output MZIs to a balanced operation, while the MZIs belonging to one of the two interferometric arms should be set with reflectivity equal to 1. In this way, the external phase shifters of the MZIs act as internal shifters of these large interferometers, and therefore their action can be measured by looking at the output power distribution of the circuit. However, since more than one resistor share the same ring, for unequivocally retrieving their phase shift more than one ring per resistor should be considered.

By performing this calibration procedure, it was possible to find the relation between the applied current and the induced phase shift for each heater (Fig. 5.15.d). In particular, we found that a 2π shift can be obtained by dissipating only 30 mW, thus confirming our preliminary hypothesis. Moreover, we analyzed also the thermal cross-talk by measuring the phase induced on a MZI by a far phase shifter. The analysis in this case was limited to the elements of the same column, since in the propagation direction the MZIs are too far for having cross-talk effects. We found that the application on a resistor of the current needed for a 2π shift induces a phase shift on the neighboring MZI of about $1 - 1.5$ rad, which corresponds to a cross-talk of about $15 - 20\%$ (Fig. 5.15.e).

Finally, we performed also some preliminary tests in vacuum, in detail at a pressure equal to $3 \cdot 10^{-3}$ mbar. In this case, as expected both the power dissipation and the thermal cross-talk values drop, respectively to 10 mW and 2%.

5.2.4.2 *Implementation of arbitrary operations*

After the full calibration of the phase shifters, we tested with classical light the processor performances when implementing arbitrary unitary matrices. In Fig. 5.16 we show the measured output distribution of the circuit for some particular transformations, such as the identity (a), the X-Pauli (b) and the antidiagonal (c) matrices. As it is possible to notice from the figure, the obtained transformations are almost indistinguishable from the theoretical ones. For estimating the goodness of the implemented matrices, we used the fidelity value, defined as:

$$F = \frac{1}{6} \cdot \mathrm{Tr}\left(|U_{th}^{\dagger}| \cdot |U_{exp}| \right), \tag{5.13}$$

where U_{th} and U_{exp} are respectively the ideal and the experimental transformations. In all the cases, we found very good fidelities, with values higher than 99%.

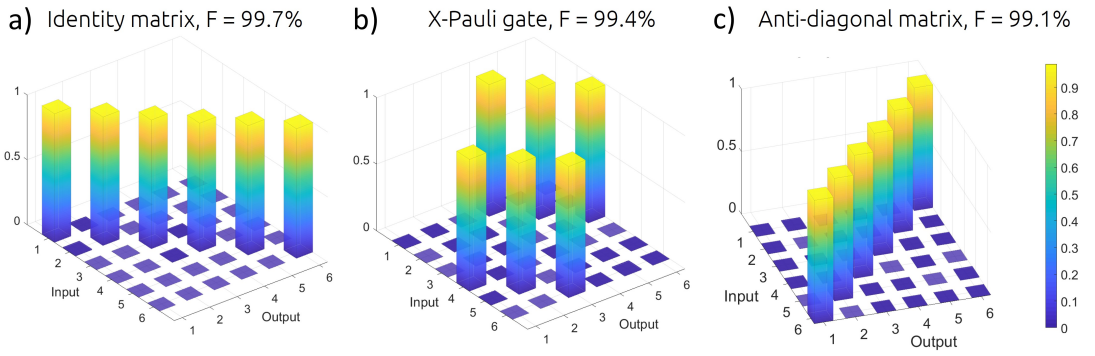

Figure 5.16: Implementation of arbitrary transformations. Every graph shows how the light is distributed in the output waveguides when injected in one input port. a) Identity operation b) X-Pauli gate. c) Anti-diagonal matrix. It should be noted that the fidelity of the obtained distributions with respect to the theoretical ones is higher than 99%.

Further investigations are in progress about the possibility to implement Haar random matrices, which need also the control of the external phase shifters of the MZIs. This kind of transformations would indeed allow a full characterization of the performances of the circuit, since they uniformly cover the space of all the possible unitary matrices.

5.2.5 *Conclusions and future perspectives*

In this work we showed that femtosecond laser writing can be used for the fabrication of a low-loss and low-power photonic processor, able to implement 6×6 arbitrary transformations with very high fidelity. In particular, the low power dissipation is enabled by a novel ablation process which allows the fabrication with an almost 100% yield of insulating structures between the phase shifters. For achieving a 2π shift, we showed that in average 30 mW should be dissipated on every resistor, thus obtaining a fully operational circuit with an overall maximum power dissipation of about 500 mW. This is for sure a remarkable result, if we consider that in the Quix processor a similar amount of power is required by a single resistor for inducing a 2π shift.

Despite the outstanding fidelities achieved on the presented transformations, we are planning to implement a large set of Haar matrices with the circuit, since as already discussed this would enable a more complete characterization of its universality. Moreover, also the quantum response should be addresses, and this is why we have in program to characterize the processor with single photons.

Concerning the possibility to increase the number of modes, some problems should be addressed first. While we showed that the power dissipation is not a problem, some efforts should be dedicated to the further reduction of the propagation losses of the circuit. Moreover, a higher miniaturization of all the components should be achieved

as well, for reducing the length of the circuit, or equivalently for arranging a higher number of MZIs in the same footprint. In this regard, we are studying the possibility to fabricate the phase shifters on the S-bends of the directional couplers, which would allow us to avoid the fabrication of the straight arms of the MZIs. Moreover, we are also investigating the possibility to use different borosilicate glasses for reducing the propagation and bending losses: in particular, we are finding promising results in Borofloat 33 by Schott, however further studies are still needed. On another topic, concerning the quantum experiment, a low-loss circuit with a high number of modes would be useless if probabilistic single photon sources are used. For this reason, our idea is to interface the new versions of the photonic processor with more efficient deterministic sources, for instance quantum dots.

5.3 STUDY OF A BRIGHT QUANTUM DOT SINGLE PHOTON SOURCE

5.3.1 *Motivations of the work*

Probabilistic single photon sources, based on SPDC or SFWM processes, have allowed the research in quantum photonics to achieve interesting and useful results. Nevertheless, now they are among the elements that are currently limiting further advances in terms of complexity and scalability of the quantum photonic implementations. As a matter of fact, this kind of sources has a very low probability of emitting a photon upon excitation, and this greatly affects the maximum number of photons that can be used in an experiment. For this reason, some alternatives have been proposed towards a deterministic emission.

In this regard, semiconductor quantum dots are among the most promising platforms. They consist in strain-induced defects with nanometric dimensions which effectively act as artificial atoms with discretized levels, in such a way that they can be pumped either electrically or optically to obtain the nearly on-demand emission of a photon. Due to their high quality, single photon sources based on quantum dots are attracting interest in the community, and the number of laboratories where they are being installed is increasing. Nevertheless, being the field still in its infancy, plug-and-play sources are not available yet. Therefore, before using them for actual experiments, a careful optimization of their emission properties should be carried out for finding the best working conditions.

For this reason, in this section we describe the characterization and optimization of the emission of a commercial InGaAs quantum dot, developed by the French company Quandela, a spin-off of the CNRS group led by Prof. Pascale Senellart. As already mentioned, this activity was performed during a secondment at the University of Vienna, in a laboratory led by Prof. Philip Walther, where the source had just been installed.

5.3.2 *Quantum dots as single photon emitters*

This section will describe the main characteristics of quantum dots, ranging from their growth process to their optical performances. In particular, the discussion will be limited to InGaAs QDs, since not only they are of interest for this thesis, but they are also among the most studied in this field thanks to their large emission spectrum, in the range $850 - 1400$ nm.

5.3.2.1 *Fabrication*

The growth process of self-assembled semiconductor QDs is usually performed by molecular beam epitaxy (MBE) or metal-organic vapor phase epitaxy (MOVPE) in the Stranski-Krastanov mode [264]. For InGaAs QDs, the process starts by depositing a layer of InAs on a GaAs substrate. At the beginning, a thin 2D wetting layer is created. However, due to the lattice mismatch of about 7%, if the deposition continues a considerable strain is induced, thus causing the creation of nanometric InAs islands in random positions (Fig. 5.17.a), which is the energetically most favoured configuration [265]. At this point, for avoiding the oxidation of the grown QDs, a capping GaAs layer is deposited (Fig. 5.17.b). The result is therefore the fabrication of three-dimensionally confined QDs with typical in-plane size of $10 - 30$ nm, and thickness equal to $2 - 5$ nm [266]. It should be noted that the capping layer affects the optical properties of the dots, since intermixing of GaAs in InAs can occur: in particular, it causes a shift of the lowest optical transition to a wavelength in the range $900 - 1000$ nm. Moreover, the randomness of the process leads to a very low indistinguishability of photons emitted by different quantum dots, even if grown in the same sample. To partially overcome this problem, at least concerning the emission wavelength, it is possible to exploit strain or electric field for achieving the same emission spectrum for all the dots [267].

5.3.2.2 *Energy levels and pumping schemes*

Due to their strong confinement, QDs are characterized by discrete shell-like energy levels [268]. In the case of InGaAs QDs, the confinement is enhanced by the large difference between the energy gaps of InAs and GaAs, respectively equal to 0.422 eV and 1.522 eV. In Fig. 5.17.c it is shown a typical band structure, with the GaAs and the wetting layers presenting continuous energy levels, while the QD shows p- and s-shells with lower energy gap.

The excitation of the QD can occur by shining it with laser light, both in continuous or pulsed regime. As a matter of fact, the optical pumping causes the promotion of an electron in the conduction band, with the creation of a hole in the valence band. Regardless of the pump energy, the created electron and hole eventually get trapped in the quantum dot and form an excitonic state by Coulomb interaction. At this point, the generated exciton can radiatively recombine with the emission of a single photon. Depending on the spin of the involved particles, only the transitions with projection

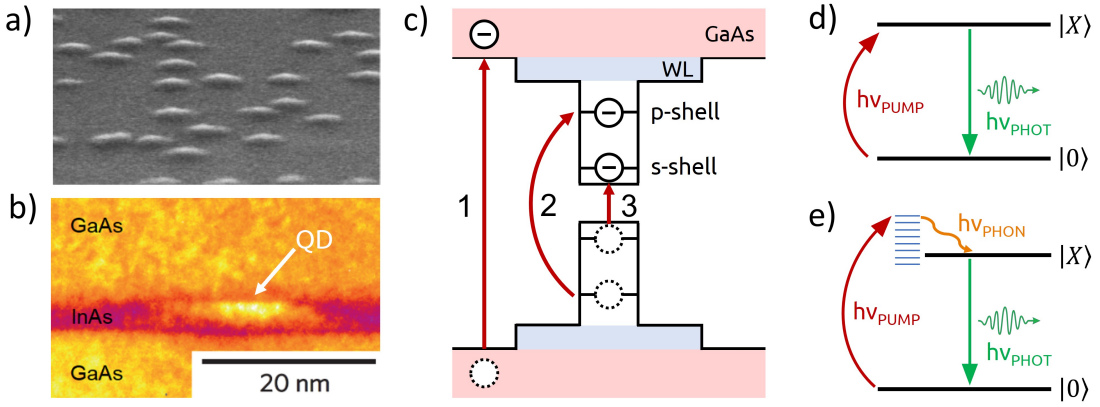

Figure 5.17: QD growth, energy levels and pumping schemes. a-b) Transmission electron microscopy of InGaAs QDs, obtained by a random growth of InAs islands on a GaAs substrate. From [264] and [266] respectively. c) Discrete energy levels and pumping schemes of a InGaAs quantum dot. 1: non-resonant excitation, leading to the generation of an electron-hole pair in either the GaAs or the wetting layers. 2: quasi-resonant p-shell pumping. 3: resonant s-shell pumping. In all the three cases, the emission occurs when the electron and the hole are trapped in the s-shell: while in 3 this happens immediately after pumping, in 1 and 2 this is possible after collisions and emission of optical phonons. d) Resonant s-shell pumping, with $\nu_{pump} = \nu_{phot}$. e) Off-resonant s-shell pumping assisted by longitudinal-acoustic phonons, with $\nu_{pump} + \nu_{phon} \simeq \nu_{phot}$, where $\nu_{phon} \ll \nu_{phot}, \nu_{pump}$.

of the angular momentum $J_z = \pm 1$ are optically allowed, usually referred to as bright excitons. Moreover, if two electron-hole pairs are trapped in the dot, a biexciton is formed, thus leading to the emission of two single photons with slightly different wavelengths due to Coulomb interaction. Beyond these neutral states, also charged excitons known as trions can be formed, if for instance one electron or one hole is trapped in addition to the electron-hole pair.

The optical pumping can occur in three different regimes. If a non-resonant process is used, i.e. if the employed energy is much higher than the s-shell gap, the electron-hole pair is generated from the GaAs or the wetting layers and then trapped in the QD states by carrier collisions and emission of optical phonon. This pumping scheme is the most trivial one, since it does not require a careful tuning of the laser wavelength. Moreover, spectral filtering can be used to separate the single photon emission from the excitation laser reflected by the dot surface. Nevertheless, the emitted photons in this case have very low indstinguishability, in terms of both time of arrival, due to the introduced time jitter, and wavelength, since the pair can be trapped in other defects with different energy gap [269].

The other two choices consist in the direct excitation of either the p- or the s-shell by quasi-resonant and resonant processes, respectively. In particular, the resonant scheme (Fig. 5.17.d) allows to obtain an emission with higher quality, since it does not require the interaction with the solid state environment. In this case, however, it becomes impossible to separate the laser from the emission of the dot by simply using spectral

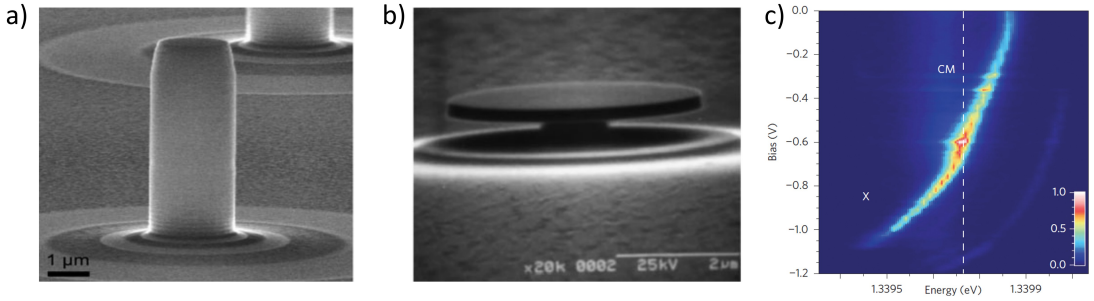

Figure 5.18: Quantum dots in micro-cavities. SEM images of a) a micropillar cavity and b) a microdisk cavity. Both from [272]. c) The application of a bias voltage allows to control the emission wavelength of a QD by Stark effect. This can be exploited to achieve a resonance condition among the excitonic transition (X) and the cavity mode (CM), thus enhancing the emission efficiency. From [78].

filtering. Therefore, either the pumping should occur in a different direction than the emission, or a cross-polarization setup should be used, which consists in the collection of photons whose polarization is orthogonal to the pump one.

In alternative, an off-resonant pumping of the s-shell can be achieved by exploiting the interaction with longitudinal-acoustic (LA) phonons (Fig. 5.17.e). In this scheme, an intense detuned laser pulse is able to cause the dressing of the ground and the excited states, which is then followed by a relaxation of the system into the excited state through the emission of LA phonons, and then by the radiative decay to the ground state. With this technique it is possible to achieve photons with high purity and indistinguishability [270], moreover it enables the spectral filtering in collection of the pump. However, this process leads to a slightly lower brightness if compared to the resonant one, and requires much higher intensities [271].

5.3.2.3 *Purcell-enhanced emission*

In order to improve both the brightness and the indistinguishability of the emitted single photons, quantum dots can be coupled to a single cavity mode. In absence of any external factor, a dot in fact spontaneously emits photons in all the directions, therefore their collection with objectives or optical fibers becomes challenging. Moreover, the high refractive index mismatch between the semiconductor and its environment, usually vacuum, further reduces the efficiency of the system, because of the total internal reflections occurring at the material surface. However, by embedding the QD in a cavity, which can be a micropillar (Fig. 5.18.a), a microdisk (Fig. 5.18.b) or in general a structure providing a strong confinement, it is possible to increase the collection efficiency β [272], defined as the ratio between the collected photons and the emitted ones. Moreover, the coupling with an optical cavity mode also causes a reduction of the QD lifetime by the Purcell effect, thus leading to higher emission rates and lower time jitters [273].

In detail, if we express as Q the quality factor of the cavity, and as V its volume, we can define the Purcell factor as [274]

$$F_p = \frac{3}{4\pi^2}\left(\frac{\lambda}{n}\right)^3 \frac{Q}{V}, \tag{5.14}$$

where λ/n is the wavelength of the cavity mode, being n the refractive index of the material. A high F_p leads to an efficient collection of the emitted photons, which can be estimated as

$$\beta = \frac{F_p}{F_p + \gamma}, \tag{5.15}$$

where $\gamma \simeq 1$ is a parameter related to the spontaneous emission of photons coupled to the leaky modes of the cavity. Concerning the emission rate of photons in the cavity mode, it can be expressed as

$$\frac{1}{\tau} = \frac{F_p}{\tau_{free}}, \tag{5.16}$$

thus obtaining an increase by a factor F_p with respect to the free case $1/\tau_{free}$. It is therefore clear that the Purcell effect allows an improvement of the dot emission if the cavity has a high Q and low V. Moreover, the cavity mode energy and profile should be matched to the QD emission wavelength and position. In this regard, the resonance condition can be obtained by a temperature tuning or by quantum confined Stark effect (Fig. 5.18.c), while the position of the cavity can be chosen after the random growth of the QDs, thus effectively fabricating it around the emitter [275].

Among the possible implementations, micropillar cavities provide very high brightness and reduced lifetimes thanks to their low volume, which can be of the order of few λ^3 [276], and high quality factors, up to $2.5 \cdot 10^5$ [277]. Micropillar cavities can be obtained by growing the dot between two distributed Bragg reflectors (DBR), composed of several alternating $\lambda/4$ layers of two materials with different refractive index, such as GaAs and AlGaAs in the case of InGaAs QDs [78].

5.3.3 *Experimental setup*

5.3.3.1 *The Quandela source*

The source studied during this activity was a chip containing 35 InGaAs QDs, embedded in GaAs/$Al_{0.9}Ga_{0.1}As$ DBR micropillar cavities (Fig. 5.19.a) and emitting single photons with a wavelength of around 928 nm. The cavities were fabricated after the QDs growth by an advanced in situ lithography technique, with a precision on their positioning of about 50 nm [78]. Moreover, the micropillars were doped to obtain n-i-p diode structures, which were then put in contact with a large mesa (Fig. 5.19.b) for providing electrical connection with the surrounding and enabling a slight tuning of the wavelength by Stark effect.

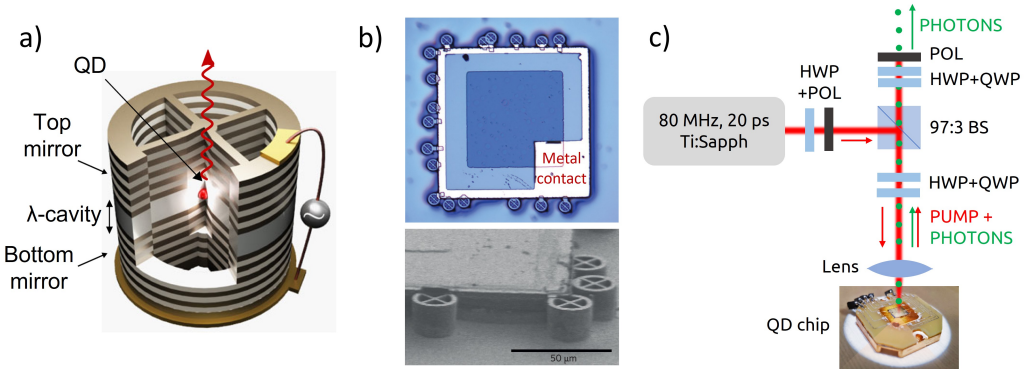

Figure 5.19: The Quandela source characterized in this thesis. a) The InGaAs QD is placed at the center of a DBR micropillar λ-cavity. From [271]. b) Microscope images showing the micropillars connected to metal pads for providing electrical control. Top image from [78], bottom from [266]. c) Cross-polarization setup enabling the filtering of the reflected laser pump, thus leading to the collection of only the single photons emitted by the source.

The sample was kept at 4 K and at a pressure of $1 \cdot 10^{-6}$ mbar in an attoDRY800 cryostat system. Its alignment with respect to the pump laser could be controlled by means of a 3-axis piezo nanopositioner, which provided also the necessary equipment for connecting the diode structure to a voltage supply external to the vacuum chamber.

5.3.3.2 *Pump and collection*

The scheme of the cross-polarization setup used for pump and collection can be found in Fig. 5.19.c. For pumping the dot, a Tsunami Ti:sapphire laser by Spectra Physics was used, emitting laser pulses with tunable duration ($2 - 100$ ps) and wavelength ($690 - 1080$ nm) at a repetition rate of 80 MHz, a value which could be slightly modified by an active control of the cavity length. The laser beam passed through a half-waveplate (HWP) and a polarizer (POL) for fixing its polarization and controlling the pulse energy. A fraction equal to 3% of the laser light was reflected by a 97:3 beam splitter (BS) into the vacuum chamber, after a further manipulation by a set of a half- and a quarter-waveplate (QWP) to align the pump polarization in between the two orthogonal modes of the cavity, in order to excite both of them. A lens inside the chamber was used both to focus the laser beam on the QD sample and to collect the emitted photons. In a collinear configuration, however, the collected beam contains also a fraction of the reflected pump laser, detrimental for the purity and indistinguishability of the source output. For this reason, the polarization of the collected beam was controlled after the BS by a set of QWP+HWP+POL for letting through only the polarization orthogonal to the one of the reflected pump. In this way only the single photons could pass, being originally in a mixture of both parallel and orthogonal polarizations. This choice allowed therefore to obtain high quality single photon states, however at the cost of introducing losses of about 50%. Nevertheless, this is currently the only possibility

when collecting the resonance fluorescence of the QDs whose emission is collinear to the pump path.

5.3.3.3 *Emission analysis and coincidence electronics*

For measuring the rate of emission of the source, at the beginning some Excelitas Si SPADs were used, which provided a detection efficiency of 20-30%, a time jitter of about 300 ps and a dead time in the range 30-40 ns. However, during the activity a Single Quantum system based on 8 SNSPDs was installed in the laboratory, thus enabling much better performances in the spectral window of the dot emission. In particular, this new system was characterized by a detection efficiency higher than 80%, a time jitter as low as 17 ps and a dead time lower than 15 ns.

The output signals of the single photon detectors were sent to a coincidence electronics (Time Tagger by Swabian Instruments) for the analysis of the coincident detections. Notably, this device allowed the measurement of the count rates, and could show the time correlations between two or more detectors with a time jitter of 9 ps and a dead time of 2 ns.

Concerning the analysis of the emission spectrum, a SpectraPro HRS-750 spectrometer by Princeton Instruments was used, providing a resolution of 17 pm.

5.3.4 *Characterization of the source*

5.3.4.1 *Determining the best QD by non-resonance fluorescence*

As previously explained, the studied chip contained 35 quantum dots. Therefore, the first analysis was devoted to find the best dot among the fabricated ones, focusing in particular our attention on the spectral distance between the emission of the dot and the cavity mode. In fact, if the two central wavelengths are too far, for instance because of fabrication uncertainties, the tuning enabled by the control on the diode voltage is not enough to achieve a resonance condition, thus leading to a low brightness.

The characterization of the dots was performed by exciting them one by one via a non-resonant process enabled by two pulsed fiber-coupled diode lasers (Thorlabs MCLS1) at 780 nm and 850 nm. A non-resonant excitation was preferred at this stage since it is generally easier to implement, and allows the population of both the quantum dot states and the cavity mode. After proper pump extinction by a cross-polarization scheme, the output of the QDs was then sent to the spectrometer and the spectral distance with respect to the cavity mode was evaluated. By this analysis we determined the dots that were more in resonance with the cavity, and that for this reason were worthy to be characterized with resonant pumping, which as anticipated provides single photons with higher quality.

5.3.4.2 *Characterization of the resonance fluorescence*

BRIGHTNESS The characterization of the resonance fluorescence of the QDs was performed by exciting the samples with the Ti:sapphire laser, emitting pulses with duration fixed at $\Delta t = 20$ ps and a central wavelength matching every time the dot emission.

Since they are two-level systems, the quantum dots show Rabi oscillations if excited with a resonant pulse. This means that the occupation probability of the excited state

$$P_{|X\rangle}(t) = \sin^2\left(\frac{\Phi(t)}{2}\right) \tag{5.17}$$

has a sinusoidal dependence on the area $\Phi(t)$ of the pulse that has interacted with the system until time t:

$$\Phi(t) = \frac{\boldsymbol{\mu}_{eg} \cdot \hat{\boldsymbol{\epsilon}}}{\hbar} \int_{-\infty}^{t} E(\tau)\, d\tau, \tag{5.18}$$

where $\boldsymbol{\mu}_{eg}$ is the electric dipole moment of the transition and $E(t)$ the electric field [278]. Moreover, if the pulse duration is much smaller than the lifetime of the excited state, as it occurs for QDs in microcavities, the temporal dependence of $\Phi(t)$ can be removed, and so the whole area of the pulse can be considered. Eq. (5.18) notably shows that if the area is increased, either by modifying Δt or $E(t)$, the system coherently oscillates between the excited and the ground state. In particular, for low pulse areas, the dot absorbs a photon from the cavity mode with a probability which increases with the area, thus leading to a more and more probable spontaneous emission of a single photon until a pulse area equal to π is reached. However, if the area is further increased, the system is driven back to the ground state by stimulated emission of a photon that, having the same properties of the pump, is filtered in collection, thus leading to a reduction of the detected count rate. For achieving an optimal operation, the occupation probability of the excited state must be therefore maximized.

For this purpose, we performed a scan of the pump pulse area while measuring the rate of emission of the excited dot. In particular, we modified the pulse area by rotating the half-waveplate placed before the input polarizer, thus controlling the attenuation of the laser beam. In Fig. 5.20.a we show the measurement performed on the dot that presented the highest emission rate for a π-pulse, equal to 10.5 MHz. From this value, the brightness of the setup could be calculated as:

$$B = \frac{C}{R \cdot \eta} \simeq 0.16, \tag{5.19}$$

where C is the measured count, $R = 80$ MHz is the laser repetition rate and $\eta \simeq 80\%$ is the efficiency of the SNSPD used as a detector.

The retrieved brightness is quite good, considering that it is measured at the end of all the collection setup, thus includes all the losses introduced by the cross-polarization setup and by the fiber coupling. This means that the brightness of the source alone

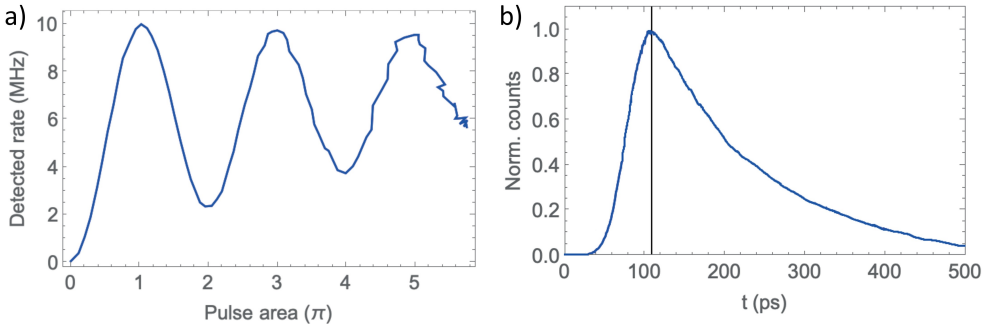

Figure 5.20: Measured Rabi oscillations and lifetime of the brightest QD. a) Emission rate of the source versus pulse area. A maximum rate of 10.5 MHz was reached for a π-pulse excitation. The measurement becomes noisy for large pulse areas for two reasons: the collected excitation laser is increased, and in this region the angles of the HWP used for controlling the pump power are the ones maximizing the effects of any rotation uncertainty. b) Lifetime measurement of the QD. The time when the maximum emission occurs is highlighted, for making it easier the localization of the beginning of the exponential decay.

would be at least doubled, thus achieving an emission of a photon every three excitation pulses. Unfortunately, the collinear resonant pumping requires the filtering of the emitted photons having the same polarization of the reflected laser, however as we discussed different configurations can be used to overcome this limitation, for instance a pumping occurring in a different direction than the one of the emitted beam. Nevertheless, this brightness value is for sure an improvement with respect to SPDC sources, with emission efficiencies which are hardly higher than 1%.

As a final remark, the wavelengths of the dot emission and the cavity mode were measured equal to 928.14 nm and 928.055 nm respectively.

LIFETIME We already discussed that the lifetime of the excited state is an important parameter when evaluating the performances of a quantum dot, since faster decays provide the possibility to use higher repetition rates. For this reason, we measured the time evolution of the emission of the most efficient QD of the chip. The measurement was performed by synchronizing the SNSPD to the clock signal of the pump laser, thus having an exact indication of when the excitation of the dot occurred. We show in Fig. 5.20.b the resulting graph, where in particular the y axis reports the normalized number of emissions occurring at a time t after excitation. The count rate exhibits an exponential decay, with a $1/e$ time constant estimated to be equal to $\tau \simeq 140$ ps. This means that after $t = 1$ ns the system provides already the 99.99% probability of having emitted a photon, thus repetition rates up to 1 GHz could be used without the risk of pumping the dot when it is still in the excited state. From this measurement it was also possible to conclude that the characterized dot was a trion, or charged exciton, since this kind of sources present an exponential decay, while neutral ones show a more peculiar behaviour, with the presence of revivals [279].

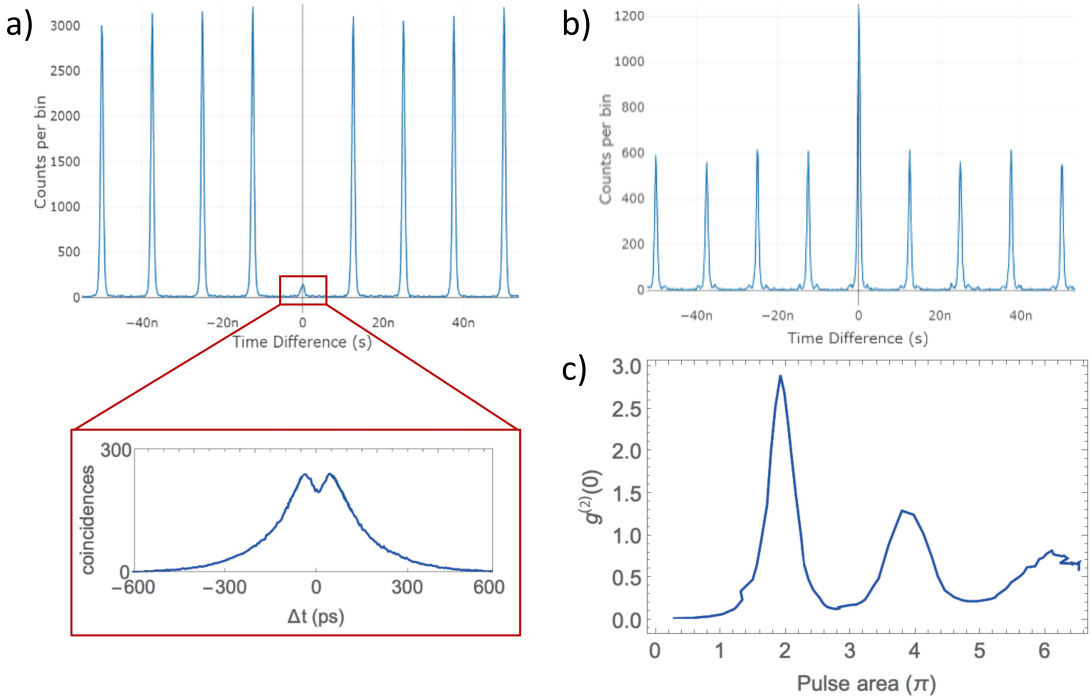

Figure 5.21: Measurements of the source purity. a) Coincident detections versus time delay at π-pulse excitation, measured by performing an HBT experiment. In particular, the lower peak in the center shows a photon anti-bunching, though with low purity. In the inset, the dip present at the center of the zero-delay peak is highlighted, thus showing that the low purity is mainly caused by re-excitation of the dot within the same laser pulse. b) Coincident detections versus time delay at 2π-pulse. In this case, a photon bunching can be observed. c) $g^{(2)}(0)$ for different pulse areas, showing minima for the odd multiples of π, and maxima for the even ones.

PURITY The purity of the source emission under π-pulse excitation was analyzed by measuring its second-order autocorrelation function $g^{(2)}(t)$ through a Hanbury Brown and Twiss experiment (see Appendix A). In detail, the photons coming from the source were sent to a balanced beam splitter, whose outputs were collected by two optical fibers and measured by two SNSPDs. The detectors were connected to the time tagger for the analysis of their temporal correlation, in this way the coincident detections could be recorded. The result of the measurement is the graph shown in Fig. 5.21.a. From it, it was possible to retrieve the $g^{(2)}(0)$ as:

$$g^{(2)}(0) = \frac{\int_{\Delta\tau} C(0)}{\langle \int_{\Delta\tau} C(\tau) \rangle} \simeq 0.06, \tag{5.20}$$

where $C(0)$ and $C(\tau)$ are the coincident detections at zero delay and at delay $\tau = n/80$ MHz^{-1} (side-band peaks) respectively. Both peaks were integrated over a time interval

$\Delta\tau = 3$ ns for a better estimation. From the $g^{(2)}(0)$ value, the probability of emitting more than one photon was estimated to be equal to

$$p(n > 1) = \frac{g^{(2)}(0)}{2}\langle n\rangle^2 \simeq 3\%, \tag{5.21}$$

where we used the approximation $\langle n\rangle^2 \simeq 1$ since the source emits single photons most of the time. Despite showing a clear anti-bunching of photons with a sub-Poissonian statistics, this value is quite high for providing reliable operation.

We tried to investigate the reasons of this low purity value. From literature [279] it is known that charged excitons (or trions) systematically show lower purity than neutral ones. This is due to the different excitation mechanism occurring in the two cases. In particular, while in neutral excitons a spin rotation is involved, which delays the population of the excited state, in the case of trions this rotation does not occur, and the excited state starts to get populated as soon as the laser pulse arrives. This leads therefore to an emission of a photon when the quantum dot is still interacting with the pump pulse. When this happens, the dot can be re-excited by the remaining fraction of the pulse, and thus it can emit a second photon in the same time-bin. This was confirmed experimentally in our case by a more detailed analysis of the central peak of the $g^{(2)}(0)$, shown in the inset of Fig. 5.21.a. By increasing the temporal resolution, i.e. by reducing the time-bin width of the detection, a dip in the center of the peak was clearly visible. This means that if we consider very short time interval, the quantum dot was still emitting only one photon at a time. Therefore, in resonant excitation the purity of our trion source was limited by the non-negligible probability of re-exciting the dot within the same pulse. For overcoming this problem, a delay between the excitation and the emission should be introduced, as we will show in the following when discussing the off-resonant excitation of the source assisted by LA phonons.

We conclude the analysis of the purity of the source by addressing the $g^{(2)}(0)$ value for different pulse areas. Interestingly, for a 2π-pulse excitation, we have that $g^{(2)}(0) > g^{(2)}(\tau)$, showing thus a clear bunching behaviour (Fig. 5.21.b). This can be explained if we consider that the area of a 2π-pulse is equal to the sum of the areas of two subsequent π-pulses, and that during the interaction with the pulse some decoherence could affect the system. In this framework, once the first half of the pulse has interacted with the dot, which is now in the maximum population of the excited state, an emission of a photon can occur, accompanied by the de-excitation of the system. At this point, the dot can be pumped again by the second half of the pulse, thus emitting another photon. It is therefore clear that the dot emission will contain vacuum component most of the time, as it is possible to see from the Rabi oscillation, however, due to decoherence, there is still a certain probability of emitting one photon, immediately followed with a high probability by a second emission. This behaviour occurs for all the even multiple of π, while for the odd ones we obtain again a photon anti-bunching, though with a higher $g^{(2)}(0)$ (Fig. 5.21.c).

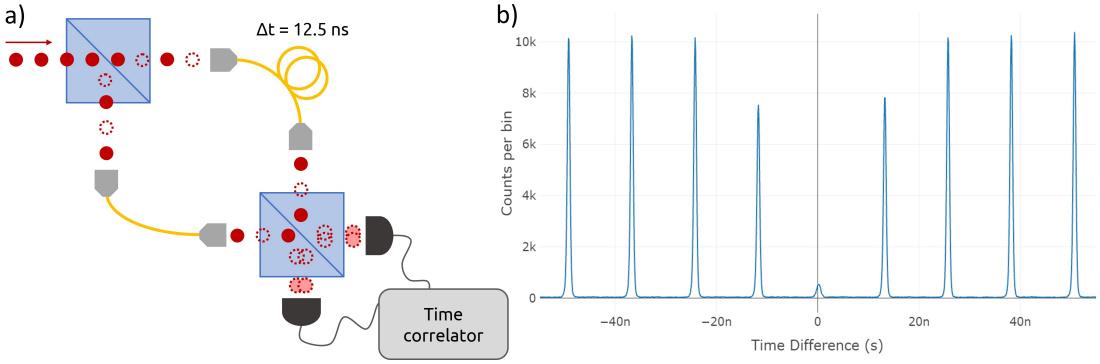

Figure 5.22: Indistinguishability measurement. a) The stream of emitted photons is sent through a path-unbalanced MZI in such a way that photons initially beloning to two subsequent time-bins have the same time of arrival at the second BS, thus interfering. The coincident detections are then recorded. b) Coincident detections for different time delays. The indistinguishability can be retrieved from the central peak: the lower it is, the more identical are the two photons.

INDISTINGUISHABILITY As a final analysis of the source performances, we show the measurement of the indistinguishability of the emitted photons. For the purpose, we used the setup presented in Fig. 5.22.a, which allowed us to perform an HOM experiment between two subsequent photons. In detail, one of the two was delayed by means of a fiber loop matching the laser repetition rate, and then both were sent to a balanced beam splitter, where quantum interference could occur. As in the HBT setup, the outputs of the BS were measured by single photon detectors for retrieving the coincidence events. The result is shown in Fig. 5.22.b. Being the beam splitter balanced, the indistinguishability could be directly estimated from the visibility of the central peak

$$M = V_{HOM} = \frac{\int_{\Delta\tau} C(0) - \langle \int_{\Delta\tau} C(\tau) \rangle}{\langle \int_{\Delta\tau} C(\tau) \rangle} \simeq 0.87, \tag{5.22}$$

where the peaks were integrated for $\Delta\tau = 3$ nm as in the purity measurement. However, for taking into account also the high $g^{(2)}(0)$, which could lead to coincident detections even in the case of identical photons, we calculated also the corrected indistinguishability [280], finding a very good result:

$$M^* = \frac{M + g^{(2)}(0)}{1 - g^{(2)}(0)} \simeq 99\%. \tag{5.23}$$

5.3.4.3 *Off-resonant excitation assisted by LA phonons*

From the analysis of the resonance fluorescence, we obtained a source with high brightness and indistinguishability, but quite low purity. As explained, this was mainly due to the fact that the characterized dot was a trion, and in this case the population of

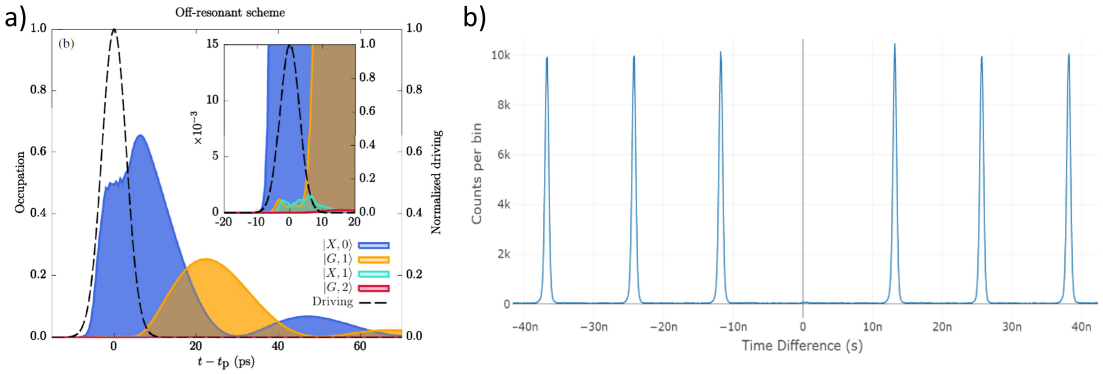

Figure 5.23: Off-resonant excitation mediated by LA phonons. a) The interaction with LA phonons provides a delay between the arrival of the pump pulse (dashed line) and the maximum occupation of the excitonic state (in blue), thus reducing the probability of re-excitation (in light green) and consequent re-emission (in red). From [270]. b) $g^{(2)}(t)$ measurement retrieved by an HBT experiment in the case of LA phonon-assisted pumping. The central peak is much lower than the one obtained in resonance fluorescence, with a $g^{(2)}(0) < 0.01$.

the excited state starts as soon as the pump laser pulse arrives, thus leading to a non-negligible probability of re-excitation within the same time-bin. For this reason, we further analyzed the source emission also by pumping it with an off-resonant process which exploits the interaction with longitudinal-acoustic phonons for populating the excited state. It is in fact known [270] that this additional step introduces a delay between the arrival of the excitation pulse and the increase of the occupation probability of the excited state (Fig. 5.23.a). In this way, the system is maximally excited, and thus has the maximum probability of emission of a photon in the cavity, only after the pulse is gone, and this leads to a much lower probability of re-excitation.

In detail, the dot was pumped with a laser detuned by $\Delta\lambda$ with respect to its emission. Since the brightness of the source is dependent on this parameter, we performed an optimization which provided the best value $\Delta\lambda = 0.5$ nm. Moreover, since it is important not to have laser component in the spectral window of the dot emission, which would lead to a residual resonance fluorescence, we used a band-pass filter for further suppressing the pulse tails. For comparing the results to the ones obtained in resonance fluorescence, we decided to keep the cross-polarization setup in collection, even though the detuning between laser and dot emission allowed a spectral filtering. The maximum obtained count rate was equal to 7.3 MHz, about 70% of the value obtained in resonance fluorescence. As a matter of fact, this process provides lower brightness, which in general does not go beyond the 80% of the value obtained with resonant pumping [271]. In our setup, we achieved a lower value since this excitation scheme also requires $10 - 20$ times higher energies than the resonant case, which we could not obtain with our pumping setup. Nevertheless, despite the lower efficiency, it should be considered that employing the spectral filtering instead of the cross-polarization setup

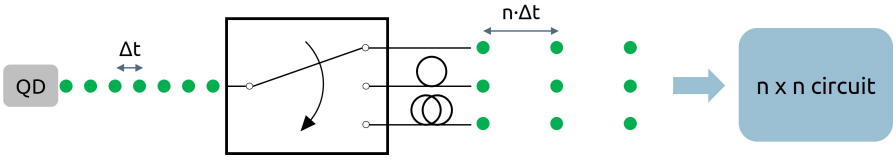

Figure 5.24: Active demultiplexing of the emission of a quantum dot source. The photons are rerouted in n spatial modes by a demultiplexer, and synchronized by using fibers with different lengths. The result of this setup is a train with spacing equal to $n \cdot \Delta t$ of n photons propagating in different spatial modes within the same time-bin.

would allow the collection of all the emitted photons, therefore it would still provide an advantage.

Concerning the purity of the emitted states, we were actually able to obtain much better results, shown in Fig. 5.23.b. From the graph, it is possible to see how the central peak related to coincident detections at zero delay almost disappeared, providing a $g^{(2)}(0) < 0.01$, with $p(n > 1) < 0.5\%$. We then addressed the photon indistinguishability. It is known that the introduced delay can slightly increase the time jitter of the emission, thus leading to a higher uncertainty in the emission time. By an HOM measurement, we retrieved a corrected indistinguishability value equal to $M^* = 97\%$, which is indeed lower than the one obtained with resonant pumping, but still high enough for having good quantum interference.

5.3.5 *Conclusions and further perspectives*

In this work we showed the optimization of the emission of a trion InGaAs quantum dot fabricated by the company Quandela. By pumping it in resonance with the excitonic transition, we were able to obtain a brightness at the output fiber equal to 0.16 with a corrected purity equal to $M^* = 99\%$. However, we also found that, because of a non-negligible probability of double excitation of the dot in the same time-bin, the purity of the source was limited to $P = 94\%$, which is a quite low value for many quantum protocols, such as boson sampling and QKD. In this regard we showed that a LA phonon-assisted off-resonant pumping allowed to increase the purity of our trion source by adding a delay between excitation and emission. With this scheme, we were notably able to obtain a brightness of 0.11, with a purity higher than 99% and an indistinguishability equal to 97%. Moreover, it should be noted that the brightness was the result of the filtering of the photons with the same cross-polarization setup used in resonance fluorescence, which is not needed in LA excitation since spectral filtering can be used. In this case the brightness could be almost doubled, reaching at least a value of 0.2.

The LA excitation provides therefore a high quality and high brightness source which can be used to scale the number of photons in a quantum photonics experiment. Since the quantum dot is a sequential emitter, a demultiplexing setup would be needed

(Fig. 5.24) for obtaining n photons in the same time-bin but different spatial modes, as it is required for instance at the input of a n-mode interferometer. The demultiplexing stage, which can be both active or passive, allows the rerouting of the photons to the different spatial modes, while optical fibers with different lengths would introduce proper delays for achieving their synchronization in the same time-bin. It should be noted that the most trivial implementation, i.e. the use of n quantum dots pumped by the same laser, cannot be considered due to the low indistinguishability of photons emitted by different quantum dots.

We conclude this discussion by providing some numerical examples about the probability of emitting n photons in n spatial modes both with a typical probabilistic source and with the quantum dot analyzed in this work. The main limitation of SPDC sources is the compromise between brightness and purity. As a matter of fact, increasing the former leads to a decrease of the latter, for this reason for having a $g^{(2)}(0) < 0.02$ usually $B < 0.01$ is required [78]. Therefore, if we consider the most efficient way of implementing an n-photon source by SPDC, which is the use of n heralded crystals pumped by the same pulse, we have that the rate of emission of n photons scales as $C_n \sim B^n R$, where R is the pump repetition rate. This relation is valid in the approximation of having a 100% heralding efficiency, thus it is an upper bound. If now we consider for instance $n = 8$ and $R = 80$ MHz, which is the typical rate of a Ti:sapphire laser, by using $B = 0.01$ we have $C_8 \simeq 1 \cdot 10^{-8}$ Hz, which corresponds more or less to a coincidence every 3 years. If instead we use the quantum dot source of this work in LA excitation, followed by an active demultiplexer, the rate of emission of n photons in all the n spatial mode will scale as $C_n \sim B^n \cdot R/n$, where the rate is reduced by n since we are using only one source. Therefore, if we consider a brightness $B = 0.2$, which as we said can be easily reached in our case by slightly modifying the setup, we obtain that 8 photons will be emitted with a rate equal to $C_8 \simeq 25$ Hz, with a clear advantage with respect to the SPDC source.

6

PHOTONIC INTEGRATED QUANTUM MEMRISTOR

In this work we present for the first time the realization by FLW of a photonic integrated quantum memristor, a device whose operation depends on the mean number of photons it has processed until that moment. This feature is notably provided by a Mach-Zehnder interferometer with an internal phase shifter, controlled by a feedback loop which is based on the measurement of the previous output states. By characterizing the memristor with Fock states encoded in the path degree of freedom, we demonstrate that it presents a hysteresis behaviour and preserves the quantum coherence. Thanks to their "memory", this new class of devices could provide the variable connections among photonic neurons in a quantum neuromorphic network, for application in the quantum artificial intelligence field. This activity has been carried out in collaboration with the group of Prof. Philip Walther, which provided the design of the circuit and performed its characterization with quantum states of light, while my contribution regarded the fabrication of the circuit and its characterization with classical light. The work has been published on ArXiv [281], moreover at the time of writing it has been accepted for publication on Nature Photonics.

6.1 MOTIVATIONS

In Sect. 1.2.4 we mentioned that classical computers based on a von Neumann architecture are inefficient in some peculiarly human tasks, such as speech or image recognition, in which the biological brain is way more performing with a much lower power consumption. For this reason, the field of neural network has raised, with the purpose of building artificial networks mimicking the brain structure. In this regard, if the most successful results have been obtained so far by neural networks based on algorithms still executed on digital von Neumann machines, a further advance would be the actual physical realization of such networks with a dedicated hardware, enabling the storage of data in the same elements that process it, an approach known as neuromorphic computing [282, 283]. This remarkable result would be a step forward the realization of a quantum artificial neural network, as long as all the used elements preserve the quantum coherence of the processed states.

In this framework, one of the most promising approaches is represented by the use of analog silicon devices, which would allow for instance the simulation of the spiking

neuron activity by means of properly designed circuits [284], with the advantage of exploiting the scalability provided by the VLSI technology. However, one of the main challenges is represented by the realization of the variable non-linear connections with memory capability, necessary for the simulation of the synapses between neurons. For this purpose, electrical memristive devices based on ion transport in nanometric junctions have been proposed [285, 286], despite no quantum implementation has been demonstrated so far.

A valid alternative would be the implementation of a photonic neuromorphic network [287], which not only could take advantage of the already existing technology for the fabrication of photonic integrated circuits, but would provide also a substantial reduction of the computation times, thanks to the higher speed of optical signals with respect to electrical ones. In this regard, there have been some proposals for the realization of spiking photonic neurons in the classical regime [288]. However, this feature is much more difficult to achieve in a quantum network, despite some preliminary results have been achieved with solid-state quantum dots in waveguides [289]. Therefore, a photonic element behaving like an electrical memristor but still able to preserve quantum coherence would be a remarkable result in the field, enabling an advancement towards the realization of more complex architectures.

6.1.1 *Features of a memristive device*

The idea of a memristor, or memory-resistor, has been introduced for the first time in [290]. In that paper, this device was theoretically postulated as the missing fundamental circuital element together with the resistor, the inductor and the capacitor. In fact, it relates the magnetic flux ϕ and the charge q passing in it by means of the memristance M:

$$d\phi = M\, dq. \tag{6.1}$$

If M is constant, we retrieve the usual resistive behaviour, however if a dependence on the charge itself is introduced, we obtain a non-linear relation between voltage and current, characterized by a hysteresis loop pinched in the origin which shrinks as the driving frequency increases (Fig. 6.1.a).

Beyond the electrical definition, a memristive device can be generally defined as an element whose input $u(t)$ and output $y(t)$ satisfy the following relations [291]:

$$\begin{aligned} y &= f(s,u,t)\, u, \\ \dot{s} &= g(s,u,t), \end{aligned} \tag{6.2}$$

with $s(t)$ a state variable whose choice depends on the considered system. As a matter of fact, these relations provide a figure-of-eight hysteresis loop which always crosses the origin, a feature caused by the fact that u directly multiplies $f(\cdot)$ in Eq. (6.2).

The memristive model was used in [285] for explaining the behaviour of nanometric junctions, which are known to show hysteresis. It is possible to consider as an example

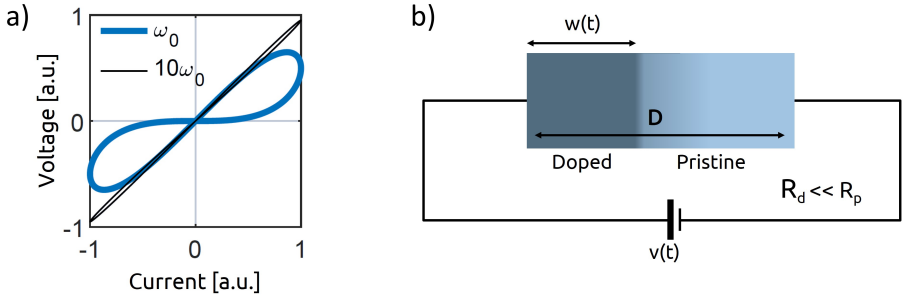

Figure 6.1: Implementation of an electronic memristor. a) Hysteresis loop presented by a memristive device driven by an alternating current with frequency ω_0. As ω increases, the loop shrinks leading to a more resistive behaviour. b) If driven by an alternating electric field, the position of the junction between a doped and an undoped semiconductor will oscillate because of the migration of ions at the interface, thus leading to a memristive behaviour.

a junction between two regions of a semiconductor (Fig. 6.1.b), one pristine and the other doped, characterized by resistance values respectively equal to R_p and R_d, with $R_p \gg R_d$ due to the different dopant concentrations. Therefore, in absence of a driving electric field the overall resistance of the element can be computed as $R_{tot} = R_d\, w/D + R_p\,(D-w)/D$, where D is its total thickness and w is the thickness of only the doped region. However, when an alternating voltage $v(t)$ is applied to the junction, the ions in the doped region will drift in the undoped one, thus effectively changing in time the thickness of the material with the lower resistivity value $w = w(t)$, and therefore the overall resistance $R_{tot} = R_{tot}(t)$. This leads to a set of two equations for voltage and current which are formally equivalent to Eq. (6.2):

$$\begin{aligned} v(t) &= \left[R_d \frac{w(t)}{D} + R_p\left(1 - \frac{w(t)}{D}\right)\right] \cdot i(t), \\ \dot{w}(t) &= \mu \frac{R_p}{D} \cdot i(t), \end{aligned} \tag{6.3}$$

where μ is the ion mobility. As it is possible to notice, the width, and thus the resistance, is dependent on the integral of the current, which is the charge accumulated in the element. In particular, in the approximation of $R_p \gg R_d$, we can express the resistance, which now we can call memristance M, as

$$R(t,q) = M(t,q) = R_p\left(1 - \mu \frac{R_d}{D^2} \cdot q(t)\right). \tag{6.4}$$

We showed how this model allows to explain the hysteresis found in already existing nanometric elements, which can now be considered as classical memristors [292].

However, if we want to realize a quantum meristor, such a component is required to show an additional feature beyond the hysteresis loop, which is the coherent processing of quantum information. However, these two properties are somehow in contradiction, since the presence of the memristivity would require a non-Markovian behaviour

in the interaction of the quantum system with the environment [293], a feature leading however to decoherence. Therefore, a careful engineering of this interaction is necessary, for providing memristivity while preserving quantum coherence, and in fact this is very hard to achieve [294].

6.2 TOWARDS A PHOTONIC QUANTUM MEMRISTOR

The model explaining the hysteresis of a memristive device was applied in [295] for the theoretical proposal of a photonic implementation, achieving a memristive behaviour when using coherent states and quadrature operators of the electric fields. Nevertheless, when processing Fock states, which are among the most interesting ones in quantum photonics, the proposed element presented a hysteresis loop not pinched in the origin, thus not satisfying one of the requirements for a memristive device. Moreover, the proposed implementation was quite challenging to achieve experimentally, due to the difficulty of tuning and measuring quadrature operators.

In this regard, we propose an improvement of this scheme for obtaining a proper memristive behaviour in the processing of Fock states. Moreover, we switch from single-rail to dual-rail encoding, which is a more common choice. If we consider the beam splitter with a tunable reflectivity $R(t)$ shown in Fig. 6.2.a, we have that the photon number expectation value $\langle n_{out}(t)\rangle$ at its output C will be equal to

$$\langle n_{out}(t)\rangle = [1 - R(t)]\langle n_{in}(t)\rangle, \tag{6.5}$$

where $\langle n_{in}(t)\rangle$ is the expectation value of the number of input photons at time t. This relation is remarkably equivalent to the one presented in Eq. (6.3) for the voltage $v(t)$: if we consider $R_d \simeq 0$, which is a reasonable approximation since the resistance of doped semiconductors is usually very low, we have in fact:

$$v(t) \simeq R_p\left(1 - \frac{w(t)}{D}\right) \cdot i(t). \tag{6.6}$$

Thus, in this framework the beam splitter will provide a hysteresis loop between $\langle n_{out}(t)\rangle$ and $\langle n_{in}(t)\rangle$ if

$$\dot{R}(t) = \alpha \langle n_{in}(t)\rangle, \tag{6.7}$$

where α is a constant and $R(t)$ plays now the role of $w(t)$, i.e. the state variable of the system. Therefore, if we are able to update the reflectivity value based on a measurement of $\langle n_{in}\rangle$, then we obtain a complete formal equivalence. This is possible to achieve by simply measuring $\langle n_{out}(t)\rangle$ at the output port D, from which we can immediately retrieve $\langle n_{in}(t)\rangle$ once $R(t)$ is known, which is generally true since we are actively controlling it. Moreover, in Eq. (6.7) we can choose α equal to 1 without loss of generality, since this will only cause a rescaling of the hysteresis loop. However, if we use $\dot{R}(t) = \langle n_{in}(t)\rangle$, the reflectivity will keep increasing and eventually will assume

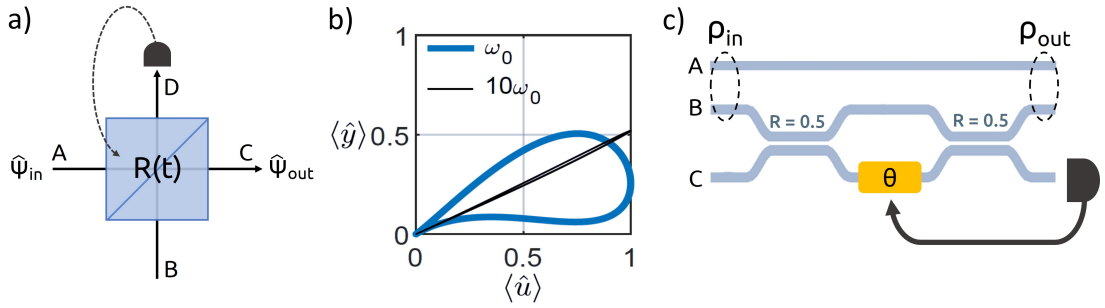

Figure 6.2: Realization of a photonic quantum memristor. a) A beam splitter whose reflectivity is updated depending on the measurement performed on its output is formally described by the same equations of a memristive device, thus being considerable as a photonic memristor. Moreover, this element is able to preserve quantum coherence, as opposed to the electronic realization. b) Hysteresis loop obtained for the mean number of input and output photons of the proposed photonic quantum memristor. As opposed to the electronic one, in this case the loop extends only in the positive quadrant. c) Photonic quantum memristor in dual-rail encoding. The input state is in a superposition of $|1\rangle_A$ and $|1\rangle_B$: the former state will propagate in the straight waveguide, thus providing the same output $|1\rangle_A$, while the latter one will enter in the variable beam splitter.

values higher than 1, which is obviously not physically acceptable. Therefore, $\dot{R}(t)$ should also take negative values, and this is provided by a simple shift:

$$\dot{R}(t) = \langle n_{in}(t) \rangle - 0.5 \langle n_{max} \rangle, \tag{6.8}$$

where $\langle n_{max} \rangle$ is the maximum value that $\langle n_{in}(t) \rangle$ can achieve in time. By using this relation, our simulations show a hysteresis loop pinched at the origin (Fig. 6.2.b). However, since the number of input and output photons can only be positive, it will be limited to the positive quadrant, as opposed to the electronic memristor which showed a figure-of-eight loop extending also in the negative one. As a final remark, the memristive behaviour of the presented device is also achieved in the classical regime, since the equations governing the beam splitter operation are the same.

Let us now address the issue of the preservation of the quantum coherence when the input state at port A is in a quantum superposition of the $|0\rangle_A$ and $|1\rangle_A$ Fock states, whose projections depend on t:

$$|\psi_{in}(t)\rangle = \alpha(t) |0\rangle_A + \beta(t) |1\rangle_A . \tag{6.9}$$

This result can be achieved for instance by a modulation of the mean number of photon $\langle n_{in}(t) \rangle = |\beta(t)|^2$, bounded by $\langle n_{max} \rangle = 1$. If now we perform a measurement on port D, which as we said is necessary for knowing $\langle n_{in}(t) \rangle$ and thus update $R(t)$, we have that if a photon is detected, then the output state at port C will be equal to vacuum $|0\rangle_C$. However, if no photon is detected in D, then at port C we have again a quantum superposition:

$$|\psi_{out,C}(t)\rangle = \frac{\alpha(t)}{\sqrt{N}} |0\rangle_C + \frac{\beta(t)\sqrt{1 - R(t)}}{\sqrt{N}} |1\rangle_C , \tag{6.10}$$

with N a normalization factor, thus preserving the quantum coherence of the input state.

6.2.1 *From single-rail to dual-rail encoding*

Up to now we presented a scheme for single-rail encoding of Fock states. Nevertheless, this configuration is quite difficult to implement experimentally in a reliable way, due to the presence of losses. For this reason, we switched to a similar scheme, but in dual-rail encoding, which is represented in Fig. 6.2.c. In particular, instead of the $|0\rangle$ and $|1\rangle$ states in the same input, the basis is represented by a photon injected either in waveguide A or in waveguide B, in such a way that the input is a superposition state of the two cases:

$$|\psi_{in}(t)\rangle = \alpha(t)\,|1\rangle_A\,|0\rangle_B + \beta(t)\,|0\rangle_A\,|1\rangle_B\,, \tag{6.11}$$

with $|\alpha(t)|^2 + |\beta(t)|^2 = 1$. While waveguide A is straight, B is the input of a beam splitter with reflectivity $R(t)$[1]. In this framework, we have that the output of the circuit is:

$$\begin{aligned}|\psi_{out}(t)\rangle = \alpha(t)\,|1\rangle_A\,|0\rangle_B\,|0\rangle_C + \beta(t)\sqrt{1-R(t)}\,|0\rangle_A\,|1\rangle_B\,|0\rangle_C + \\ + i\beta(t)\sqrt{R(t)}\,|0\rangle_A\,|0\rangle_B\,|1\rangle_C\,.\end{aligned} \tag{6.12}$$

Therefore, if we consider as output of the memristor the waveguides A and B, while we use a measurement of output C to update $R(t)$, we have again two possibilities. If a photon is detected in output C, the output state of the memristor will be

$$|\psi_{out}(t)\rangle = |0\rangle_A\,|0\rangle_B\,, \tag{6.13}$$

while if no photon is detected in C, then the photon will remain in a superposition dependent on $R(t)$:

$$|\psi_{out}(t)\rangle = \frac{\alpha(t)}{\sqrt{N}}|1\rangle_A\,|0\rangle_B + \frac{\beta(t)}{\sqrt{N}}\sqrt{1-R(t)}\,|0\rangle_A\,|1\rangle_B\,. \tag{6.14}$$

As it is possible to see by a comparison with Eq. (6.10), this result is formally equivalent to the one obtained for a photonic memristor in single-rail encoding, thus is expected to show hysteresis in both classical and quantum regimes.

Concerning the modulation of $\alpha(t)$ and $\beta(t)$, it can be easily achieved by placing before the A and B input ports of the memristor a tunable MZI fed with the $|1\rangle_A$ Fock state, whose output is indeed a superposition between $|1\rangle_A$ and $|1\rangle_B$, with projections dependent on the imposed phase shift.

1 For being consistent with the published paper, in the following part of the chapter we will use as definition of reflectivity $R = P_{cross}/(P_{bar} + P_{cross})$, a convention different than the one used in the rest of the thesis, but still widely accepted in literature.

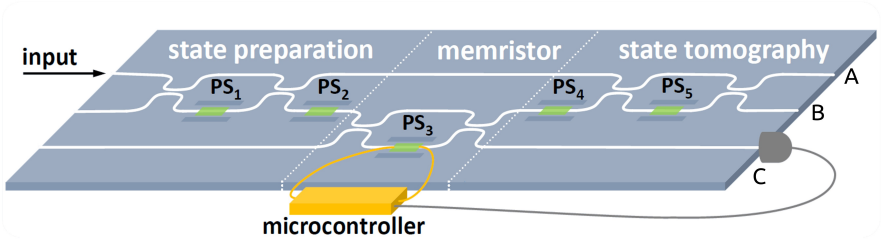

Figure 6.3: Scheme of the device. The actual memristor is preceded by an MZI preparing the input superposition state, and is followed by a tomography stage in the dual-rail encoding. The actual output ports of the device are A and B, while the signal from C is measured and used to update the state of PS_3. Adapted from [281].

6.3 DESIGN AND FABRICATION OF THE DEVICE

6.3.1 *Scheme*

Based on the previous considerations, in Fig. 6.3 we show the final scheme of the device. As it is possible to see, it can be divided in three stages:

- Input and state preparation. The $|1\rangle_A$ Fock state is injected in a tunable MZI for generating the superposition state

$$|\psi_{in}(t)\rangle = \alpha(t)\,|1\rangle_A\,|0\rangle_B + \beta(t)\,e^{i\phi(t)}\,|0\rangle_A\,|1\rangle_B\,, \tag{6.15}$$

  where $\alpha(t)$ and $\beta(t)$ can be controlled by acting on the phase shifter PS_1, while PS_2 is used to modify $\phi(t)$.

- Actual memristor, implemented with the already presented scheme, i.e. a straight waveguide and a tunable MZI with reflectivity $R(t)$, which can be controlled by means of phase shifter PS_3.

- State tomography and output. While the output C of the memristor is directly sent to a detector for updating $R(t)$ by means of a feedback loop, the outputs A and B are the input ports of another MZI, with external and internal phases controlled by the phase shifters PS_4 and PS_5 respectively. This element allows the characterization of the output state by performing a tomography in the path degree of freedom.

6.3.2 *Fabrication by fs-laser writing*

The fabrication process started as usual with a scan of the inscription parameters for minimizing the propagation losses at 1550 nm, which was the wavelength chosen for the quantum experiment. The optimization was performed in the FIRE line, by using

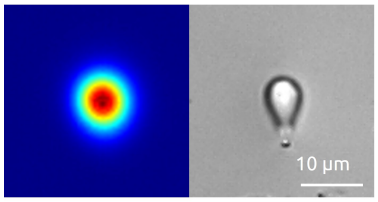

Inscription parameters	
Laser system	Yb:KYW cavity dumped
Laser wavelength	1030 nm
Repetition rate	1 MHz
Focusing objective	50x, 0.65 NA
Scanning speed	40 mm/s
Pulse energy	520 nJ
Scans number	6

Figure 6.4: Inscription parameters for achieving the best guiding properties at 1550 nm. The figures show the guided mode (left) and the waveguide cross-section (right).

the cavity-dumped Yb:KYW laser, with the standard emission properties (rep. rate = 1 MHz, $\lambda = 1030$ nm, 300 fs pulse duration). A 50×, 0.65 NA microscope objective was used for focusing the beam 25 µm above the lower surface in a 1.1 mm-thick Eagle XG sample. Notably, the objective was equipped with a correction collar for reducing the spherical aberrations, a choice which is equivalent to using oil or water immersion techniques, but which requires a simpler setup. The optimization was performed on the remaining parameters, obtaining a minimum propagation loss equal to 0.15 dB/cm when using a pulse energy of 520 nJ, a translation speed of 40 mm/s and 6 scans (Fig. 6.4). The resulting waveguide presented a mode size of 8×8.5 µm², providing a 96% overlap with the mode of a SMF-28 fiber and negligible bending losses (< 0.1 dB/cm) for a radius of 30 mm. It should be noted that also in this case the thermal annealing described in Sect. 3.1 was performed on all the inscribed waveguides.

The geometry of the directional couplers was then optimized for achieving a balanced splitting. In particular, while the interaction length was kept equal to zero, the distance and the radius of curvature of the S-bends were studied, obtaining the desired splitting ratio for $R = 40$ mm and $d = 7.5$ µm. It should be noted that a radius of 30 mm could not provide a balanced operation without an excessive overlap of the two guiding regions, thus it was not used.

After this optimization, the final optical circuit was inscribed, with input and output pitchs equal to 127 µm for optimal coupling with standard fiber arrays. Then, the phase shifters were fabricated with the technique reported in Sect. 3.1 for providing the possibility to tune the MZIs reflectivity. First, the insulation trenches were ablated between the waveguides (Fig. 6.5.a), a step that was then followed by the deposition of the chromium-gold layer and the definition of the conductive paths by a fs-laser ablation, which was performed in the CAPABLE line. At the end of this process, resistors with a width $w_r = 30$ µm and length $L = 2$ mm were obtained, corresponding to an average resistance of 38 Ω and $P_{2\pi} = 55$ mW (Fig. 6.5.b). It should be noted that, if compared to the other works presented in this thesis, a higher dissipation was required due to the employed larger wavelength, which reduced the achieved phase shift under the same dissipated power. For the same reason, longer resistors were re-

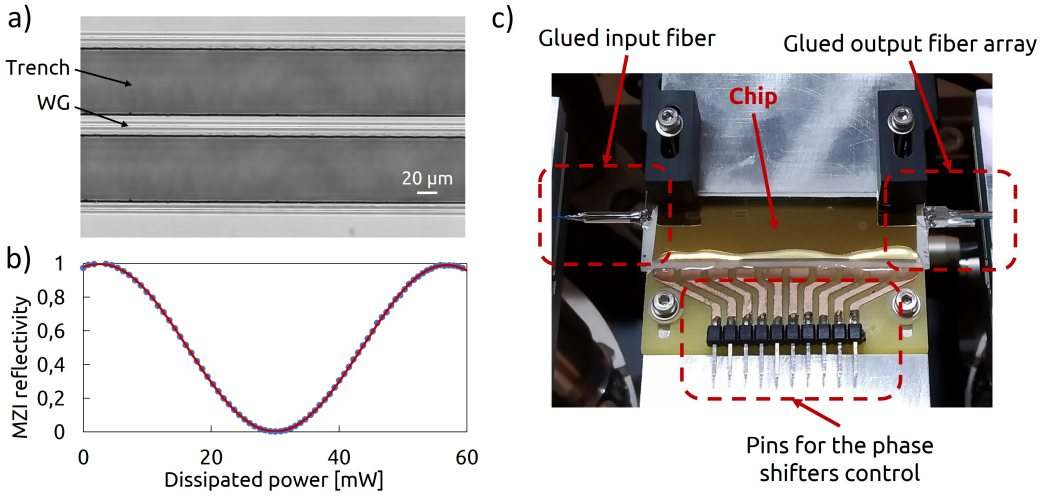

Figure 6.5: Thermal phase shifters and final packaging. a) Microscope top image showing the two trenches ablated around the waveguide of PS_1 before the gold deposition. b) Reflectivity of the MZI of the tomography stage with respect to the power dissipated on PS_5. In particular, a dissipation of 55 mW is required for obtaining a 2π phase shift. c) Final packaging of the device after connection to a PCB and pigtailing.

quired as well. Concerning the dimensions of the trenches, they were designed with a width equal to $w_t = 97$ µm, thus having $w_r + w_t = 127$ µm, a depth of 300 µm and a length of 2 mm.

At the end of the fabrication process, the sample was wire-bonded to a printed circuit board (PCB) for providing the external electrical connections, and pigtailed to input and output SMF-28 fibers (Fig. 6.5.c). The overall insertion loss from connector to connector was measured to 2 dB, corresponding to a transmission of 63%.

6.4 CHARACTERIZATION WITH SINGLE PHOTONS

6.4.1 *Experimental setup*

The setup used for the generation of single photons, the implementation of the feedback loop and the measurement of the memristor output can be found in Fig. 6.6. A collinear type II SPDC source based on a periodically-poled KTP crystal was used to generate two identical photons at 1550 nm, upon pumping by a CW diode laser emitting a beam at 775 nm with an average power of 80 mW. Of the two generated photons, one was used to herald the emission of the other, which was injected in the input fiber of the memristor, after passing a half- and quarter-waveplate for the adjustment of its polarization. The output A and C of the circuit were then measured by two SNSPDs with an efficiency higher than 95% at 1550 nm.

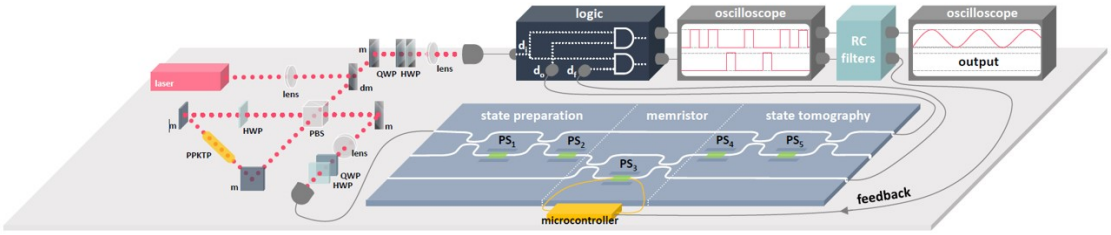

Figure 6.6: Experimental setup for the quantum experiment. An SPDC source is used to generate an heralded photon, which is injected into the input port of the memristor. The phase shifter controlling its operation is actuated by a microcontroller, which computes the necessary phase shift for properly updating $R(t)$. The calculation is based on the mean number of photons measured at output C in the time interval T. From [281].

The signals coming from the three detectors (heralding + two outputs) were then sent to a logic unit, with the purpose of analyzing their coincident detections and choose the voltage to apply on PS_3. In detail, the mean number of input photons could be estimated by a microcontroller from the counts of detector C as

$$\langle n_{in}(t)\rangle = \frac{\langle n_{out,C}(t)\rangle}{R(t)}, \tag{6.16}$$

and used in the feedback loop for updating the new value $R(t+\Delta t)$:

$$R(t+\Delta t) = 0.5 + \frac{1}{T}\sum_{\tau=t-T}^{t}\left(\frac{\langle n_{out,C}(\tau)\rangle}{R(\tau)} - 0.5\right)\Delta t, \tag{6.17}$$

which is the discretized solution of Eq. (6.8). A summation over a sliding time window T was required for avoiding the divergence of the sum in case of constant or slowly varying input signal. The logic unit was then followed by an RC low-pass filter with $RC = 100$ ms, for converting the coincidence spikes into a continuous voltage signal. Moreover, it should be noted that $\Delta t = 50$ µs since the microcontroller updated R with a rate of 20 kSa/s. As a final remark, we point out that the SPDC source provided single photons at 30 kHz, while the mean of the input number of photons was integrated over a time interval equal to RC. This means that $\langle n_{in}(t)\rangle$ was calculated over about 3000 events, thus providing an actual average.

6.4.2 *Experimental demonstration of the memristive behaviour*

The phase shifter PS_1 of the preparation stage was actuated with a sinusoidal voltage of period T_{osc} for obtaining at the input of the memristor the superposition state:

$$|\psi_{in}(t)\rangle = \cos\left(\frac{\pi}{T_{osc}}\cdot t\right)|1\rangle_A|0\rangle_B + \sin\left(\frac{\pi}{T_{osc}}\cdot t\right)|0\rangle_A|1\rangle_B, \tag{6.18}$$

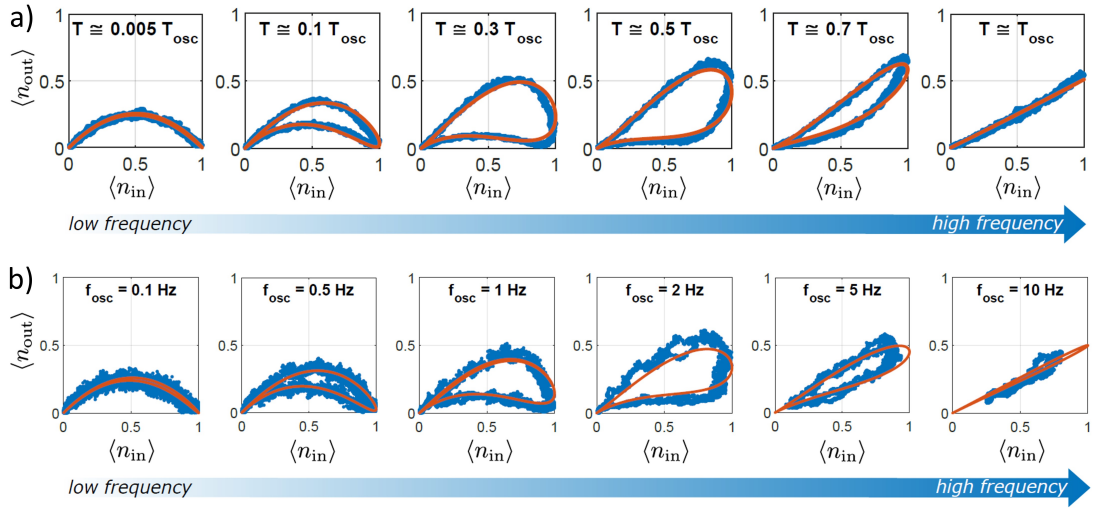

Figure 6.7: Results of the quantum operation of the photonic memristor. a) Dependence between $\langle n_{in}(t)\rangle$ and $\langle n_{out}(t)\rangle$ for different driving frequencies. As the ratio T/T_{osc} increases, three different behaviours can be observed: first, a strong non-linear dependence without hysteresis, then a hysteresis loop, and finally a linear behaviour. b) The same behaviour is obtained when the frequency of oscillation approaches the cutoff of the resistors. In the last graph, the average input number of photons does not span the whole $[0,1]$ interval since the PS_1 used to control the superposition state is operating as well above its cutoff. Both from [281].

with mean number of photons entering the MZI of the memristor equal to $\langle n_{in}(t)\rangle = |\beta(t)|^2 = \sin^2(\pi\, t/T_{osc})$. At this point we measured $\langle n_{out}(t)\rangle$ for different ratios T/T_{osc}, obtaining the behaviours shown in Fig. 6.7.a .

When $T \ll T_{osc}$, corresponding to very slow oscillations, a non-linear behaviour without hysteresis was observed. It is possible to explain this result by looking at Eq. (6.17). For almost constant values of $\langle n_{in}(t)\rangle$, the averaged summation will give as result its input variables, thus leading to a reflectivity value equal to $R(t+\Delta t) \simeq \langle n_{in}(t)\rangle$ and an average number of output photon equal to $\langle n_{out,A}(t)\rangle = \langle n_{in}(t)\rangle - \langle n_{in}(t)\rangle^2$. This relation is the one describing a parabola crossing the x axis at 0 and 1, and presenting a maximum value of 0.25, which is exactly what we observed experimentally.

When increasing T/T_{osc}, as expected the device showed a memristive behaviour with a hysteresis loop pinched in the origin, which shrinks as the ratio further increases, i.e. when the oscillations become faster. Finally, for T/T_{osc} approaching 1, the summation in Eq. (6.17) goes to 0, therefore the reflectivity tends to the constant value of 0.5 and a linear dependence is observed. We point out that integrating for a time interval higher than the period would lead to the same results, therefore we did not analyze larger ratios. Moreover, the scan was performed on T while keeping T_{osc} constant at about 10 s. This choice was made for operating well below the cutoff frequency of the resistors, which was of about $f_{cut} = 5$ Hz, corresponding to a minimum integration period of $T_{cut} = 0.2$ s. Interestingly, when a frequency higher than f_{cut} is used, a memristive behaviour can be obtained as well from the phase shifters, since they act

as low-pass filters, as it is possible to see in Fig. 6.7.b. In particular, these results were obtained by implementing a feedback loop imposing $R(t) = \langle n_{in}(t) \rangle$, thus making it evident the sole hysteresis effect given by the shifters.

For confirming the preservation of the quantum coherence, we performed a tomography of the output state by using the integrated stage. As an example, when imposing $|\beta|^2 = 0.3$ and $R = 0.7$, the measured output density matrix provided a fidelity of 99.7% with respect to the theoretical one, with a purity $\mathrm{Tr}(\rho_{exp}) = 0.66 \simeq \mathrm{Tr}(\rho_{th}) = 0.67$. In general, by performing a tomography for several values of $|\beta|^2$ and R an average fidelity of 98.7% was achieved.

6.5 CONCLUSIONS AND FURTHER DEVELOPMENTS

In this work we showed the implementation of the first quantum memristive device. First, we theoretically demonstrated that a simple beam splitter can present a memristive behaviour for quantum states of light encoded in the path degree of freedom if its reflectivity is updated depending on the average number of output photons. Then, we exploited femtosecond laser writing for the actual fabrication of the circuit. Notably, the tunable reflectivity was enabled by a phase shifter controlled by a feedback loop, and the device was equipped also with input preparation and output tomography stages, both integrated. By performing a measurement with single photons, we showed that the device behaved as expected, satisfying the definition of a memristive device [291] in both the classical and quantum regime.

Despite the achieved results, of course the presented implementation is affected by some limitations. First, the speed of operation could not be increased to few Hz due to the slow response of the thermal phase shifters. However, in current quantum experiments this is not a critical issue, since in any case long integration times are required when using sources with low emission efficiency. However, if one wants to increase the speed of operation, for instance when using deterministic sources, the proposed scheme is easily transferable to other fabrication platforms providing fast phase shifts in the GHz regime thanks to the electro-optic effect [296]. Another advance would be the integration of all the components, both electronic and photonic, in the same device, thus enabling a scalable implementation. Once this improvements are achieved, the proposed scheme could play an important role in the implementation of photonic quantum neural networks, providing the required non-linearity.

7

FOUR-ARM INTERFEROMETER FOR MULTIPHASE ESTIMATION

In this final chapter we present the fabrication and characterization with classical light of a four-arm interferometer, with application in the field of quantum metrology. In particular, by interfacing two quarters, i.e. the four-mode equivalent of two balanced beam splitters, this device would allow the contemporary estimation of the three phase differences between three of its arms and the fourth one, taken as reference. This work is part of a collaboration with the Quantum Information Lab of La Sapienza University of Rome, led by Prof. Fabio Sciarrino, which proposed the experiment. In this regard, my activity was devoted to the design of the circuit, its fabrication by FLW, and its characterization with laser light. The photonic chip is currently in Rome for its characterization with quantum states of light and for the implementation of the metrology experiment.

7.1 MOTIVATIONS

We discussed in Sect. 1.4 that by using a properly prepared probe it is possible to increase the sensitivity of a measurement, saturating the Heisenberg limit. In photonic quantum metrology, an interesting and useful problem is the simultaneous estimation of n phases in an interferometer, which can be achieved with a reduced number of resources if multiphoton states are used, rather than classical or one-photon states.

This improvement was for instance demonstrated in [235], where a three-arm interferometer was realized by FLW and then used for the estimation of two phases. In the circuit, a first tritter allowed the preparation of the probe by a balanced splitting in three different spatial modes. Then, the resulting state interacted with the three optical phases of the three waveguides, and then another balanced tritter followed by a projective measurement allowed the estimation of the phases, to be more precise of the difference of two phases with respect to the third one. In this work we make a further step towards scalability, by realizing an interferometer with four arms, thus enabling the estimation of a third phase difference.

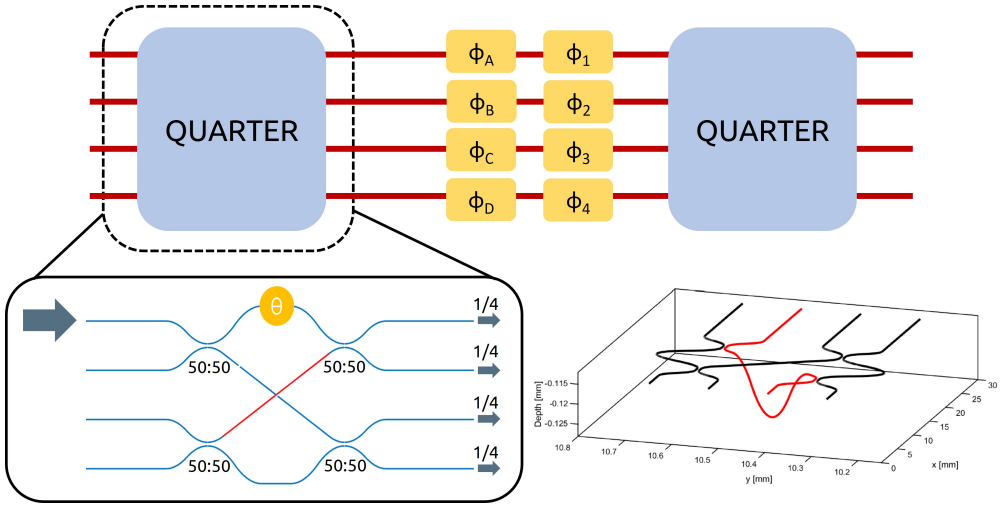

Figure 7.1: Scheme of the proposed four-arm interferometer. A quarter followed by four phase shifters $\phi_A \dots \phi_D$ enables the preparation of the probe. In particular (inset) the quarter is composed of four balanced directional couplers, a phase shifter and a waveguide crossing (in red), and allows the interaction of all the four spatial modes with the others. After preparation, the probe interact with the four phase shifts induced by other four resistors $\phi_1 \dots \phi_4$, which simulate the physical quantities to be estimated in an actual metrology experiment. Then, another quarter allows the projective measurement of the probe.

7.2 DESIGN OF THE FOUR-ARM INTERFEROMETER

The proposed scheme for the realization of the four-arm interferometer is presented in Fig. 7.1. In the following, we will analyze more in detail how a balanced splitting among four spatial modes can be achieved by using a quarter, and how two quarters can be used to realize the equivalent of a four-mode MZI.

7.2.1 *Quarter*

The quarter is a 4×4 device which equally splits into its four outputs the light injected in any of its inputs. Its operation can be described by the matrix [297]:

$$U_{4\times4}(\theta) = \frac{1}{2}\begin{pmatrix} e^{i\theta} & e^{i\theta} & 1 & 1 \\ -e^{i\theta} & -e^{i\theta} & 1 & 1 \\ -1 & 1 & -1 & 1 \\ 1 & -1 & -1 & 1 \end{pmatrix}, \tag{7.1}$$

where θ is a phase shift which can be induced without altering the splitting properties of the device, thus defining an equivalence class of infinite quarters with θ in $[0, \pi]$, a feature arising only for $n \geq 4$.

Concerning its implementation, of course it would be possible to use a Clements or Reck scheme. However, here we propose a more compact design enabled by the 3D capability of FLW, represented in the inset of Fig. 7.1. In particular, a quarter can be implemented by using only four balanced directional couplers and a waveguide crossing, which allows one waveguide to pass above the other without intersection. In this way, while two DCs enable the interaction between modes $1-2$ and $3-4$, after the crossing a further interaction between modes $1-3$ and $2-4$ occurs at two other DCs. This results in a balanced splitting of the input light, regardless of which is the injection port. Moreover, on one of the two external arms a phase shifter can be fabricated for controlling θ and thus achieving the realization of an arbitrary quarter transformation in the whole equivalence class.

7.2.2 *The interferometer*

At this point, as two DCs are used to form an MZI, two quarters can be put together to realize a four-arm interferometer. For the quantum experiment, eight phase shifters should be fabricated on the four arms, two per spatial mode. As a matter of fact, while four of them (labeled as $\phi_1 ... \phi_4$ in the figure) are used to impose the actual phase shifts that should be estimated, the other four ($\phi_A ... \phi_D$) allow the optimal preparation of the probe by an adaptive protocol that maximizes the measurement sensitivity.

The resulting operation can be calculated therefore as:

$$U_{4arm} = U_{4\times4}(\theta_2) \cdot U_{[1...4]} \cdot U_{[A...D]} \cdot U_{4\times4}(\theta_1), \tag{7.2}$$

where $U_{4\times4}(\theta_1)$ and $U_{4\times4}(\theta_2)$ are the matrices of the first and second quarter respectively, and where $U_{[1...4]}$ and $U_{[A...D]}$ are the matrices related to the phase shifts, defined as:

$$U_{[1...4]} = \begin{pmatrix} e^{i\phi_1} & 0 & 0 & 0 \\ 0 & e^{i\phi_2} & 0 & 0 \\ 0 & 0 & e^{i\phi_3} & 0 \\ 0 & 0 & 0 & e^{i\phi_4} \end{pmatrix} = e^{i\phi_4} \begin{pmatrix} e^{i\Delta\phi_1} & 0 & 0 & 0 \\ 0 & e^{i\Delta\phi_2} & 0 & 0 \\ 0 & 0 & e^{i\Delta\phi_3} & 0 \\ 0 & 0 & 0 & 1 \end{pmatrix}, \tag{7.3}$$

where ϕ_4 has been taken outside the matrix as a global phase. Interestingly, when all the phase shifts $\Delta\phi$ and θ are set to zero, the device shows a symmetric behaviour if light is injected in only one input: for instance, if only input 1 is coupled, then light will come only from output 4, while if injected in 2, it will exit only from 3, and so on.

7.3 FABRICATION OF THE CIRCUIT

The fabrication recipe used for the realization of this circuit was the one described in Sect. 5.2 when treating the implementation of the six-mode photonic processor. As a matter of fact, both devices shared the same design wavelength, equal to 785 nm, the

Fabrication parameters	*Value*
Laser system	Pharos (1030 nm, 1 MHz, 170 fs)
Objective	20×, 0.5 NA, WI
Pulse energy	330 nJ
Translation speed	25 mm/s
Number of scans	6
DC distance for 50:50	5.9 µm
S-bend radius	30 mm

Table 7.1: Fabrication parameters for straight waveguides and balanced directional couplers.

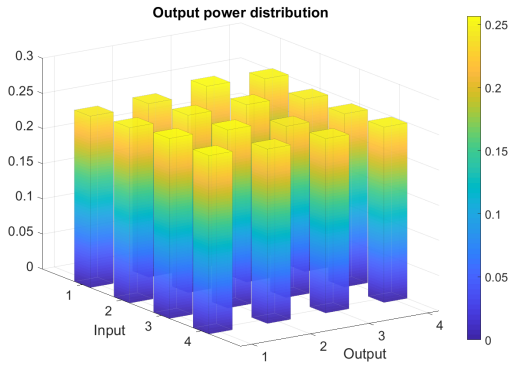

Figure 7.2: Normalized output power distribution of the fabricated quarter, showing a fidelity of 99.99% with respect to the ideal case.

same substrate (Eagle XG) and the same inscription depth (30 µm above the bottom surface). The main inscription parameters are summarized in Table 7.1. In particular, the optimization of the fabrication process resulted in waveguides with propagation loss of 0.1 dB/cm, mode size of 4.5×4.7 µm², bending loss of 0.1 dB/cm for a radius of 30 mm, and balanced zero-length directional couplers for an interaction distance equal to 5.9 µm.

Concerning the crossing at the center of each quarter, one of the two waveguides was fabricated in the plane, while the other was designed to pass 20 µm above the other, thus avoiding any unwanted coupling among the two. Moreover, the depth change was designed to be smooth enough not to introduce additional losses. For balancing the optical paths, the lengths of the three in-plane waveguides were matched to the one of the bridge by a tuning of their radii of curvature.

With these parameters we fabricated a preliminary quarter device for controlling that it was actually able to equally split the input light among the four modes. In fact this characterization would have been less straightforward in a full interferometer, since in this case a control of the thermal phase shifters would have been required.

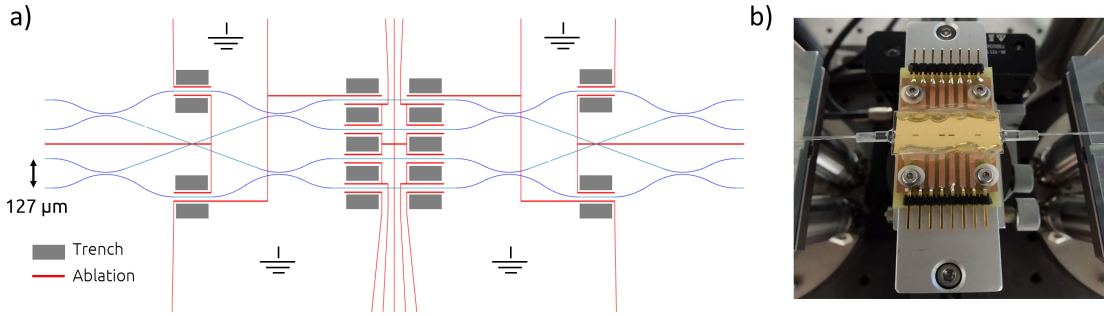

Figure 7.3: Scheme and picture of the fabricated four-arm interferometer. a) Scheme of the optical circuit (in blue), of the insulation trenches (in grey) and the laser ablation of the gold layer (in red). Concerning the phase shifters, a total of 16 pads are used, 4 of which provide connection to ground. b) Picture showing the final packaging of the device, mounted on the pigtailing setup at the end of the gluing process.

Notably, the fabricated quarter showed a balanced splitting of all its inputs, with a measured fidelity with respect to the ideal operation of 99.99% (Fig. 7.2).

The final circuit was then fabricated with the scheme presented in Fig. 7.3.a. In particular, after the inscription of the optical waveguides, deep trenches were water-ablated for thermally insulating the phase shifters, which were fabricated by depositing a chromium-gold layer and then patterned by the process presented in Sect. 3.1. In this case, the resistors were designed with a width of 5 µm and a length of 1.5 mm for having a resistance of about 120 Ω, a choice made after the measurement of the sheet resistance of the deposited layer for being compatible with the output of the Qontrol Q8IV controller. In the figure, the laser ablations are highlighted in red, the insulation trenches in grey, while the optical waveguides in blue. Finally, the sample was glued to two PCBs, providing the electrical connections of the phase shifters, and then pigtailed to both input and output fiber arrays, with an overall insertion loss of 2.2 dB (Fig. 7.3.b).

7.4 PRELIMINARY CHARACTERIZATION

7.4.1 *Phase shifters operation*

A characterization of the phase shifters was performed for evaluating both their stability and the dissipated power needed for inducing a 2π shift. Moreover, we also studied whether the induced phase shift was dependent on the polarization of the guided light, which could happen since the propagation constants of the two orthogonally polarized mode H and V are in general different. This study was made necessary since the input and output fibers cause a change of polarization, therefore in this situation it is no more possible to know which polarization state enters the circuit. This

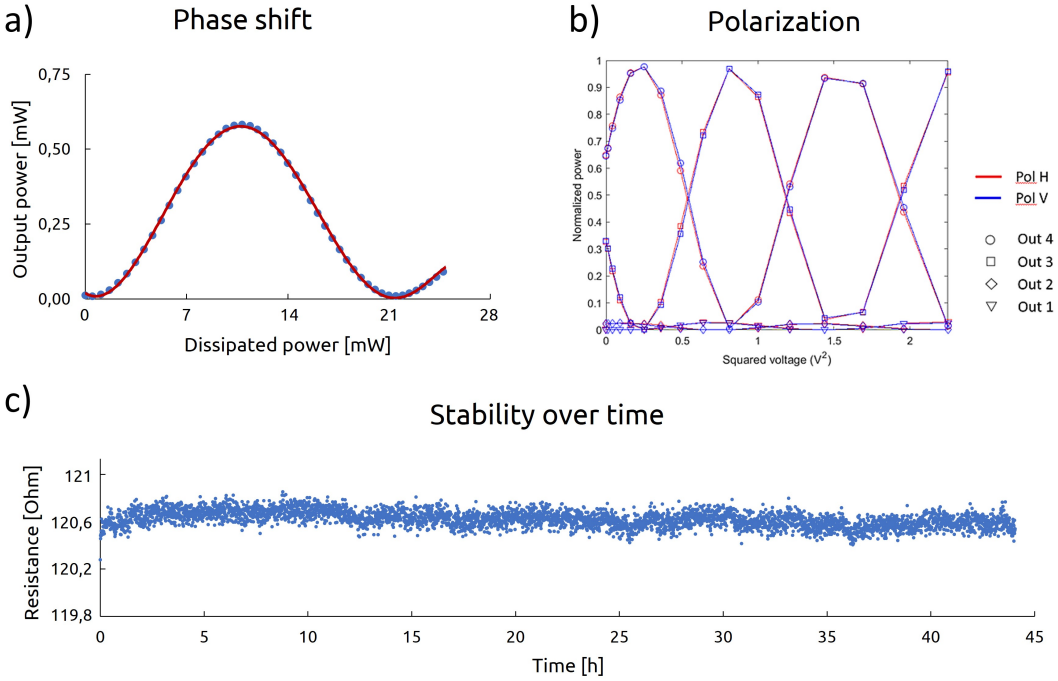

Figure 7.4: Characterization of the phase shifters. a) A dissipated power equal to 22 mW is needed for inducing a 2π phase shift. b) Polarization dependence of the output power distribution when applying an increasing voltage on a resistor. As it is possible to see, no relevant changes are observed between H and V. c) Stability measurement of the resistance value over 45 hours.

is in general not a problem if the whole device has the same operation regardless of the polarization of the guided photons, since they can be set to the same (unknown) polarization by looking at their quantum interference, which occurs only if they are indistinguishable.

Some of the results we obtained are presented in Fig. 7.4. Concerning the needed power dissipation, we retrieved an average value of $P_{2\pi} = 22$ mW. The resistance values also proved to be quite stable in time, since by continuously measuring it over about 45 hours we found a variation lower than 0.4%. Finally, concerning the polarization dependence, we injected either H or V polarized light in one input, and measured all the four outputs while increasing the applied voltage on a resistor, finding no relevant differences between the two distributions, thus validating the polarization insensitive operation of the phase shifters.

7.4.2 *Study of the induced phase shifts*

As a final analysis, we show some examples of the phase shifts induced by the resistors. The purpose of this characterization was not the retrieval of the full transfer matrix of

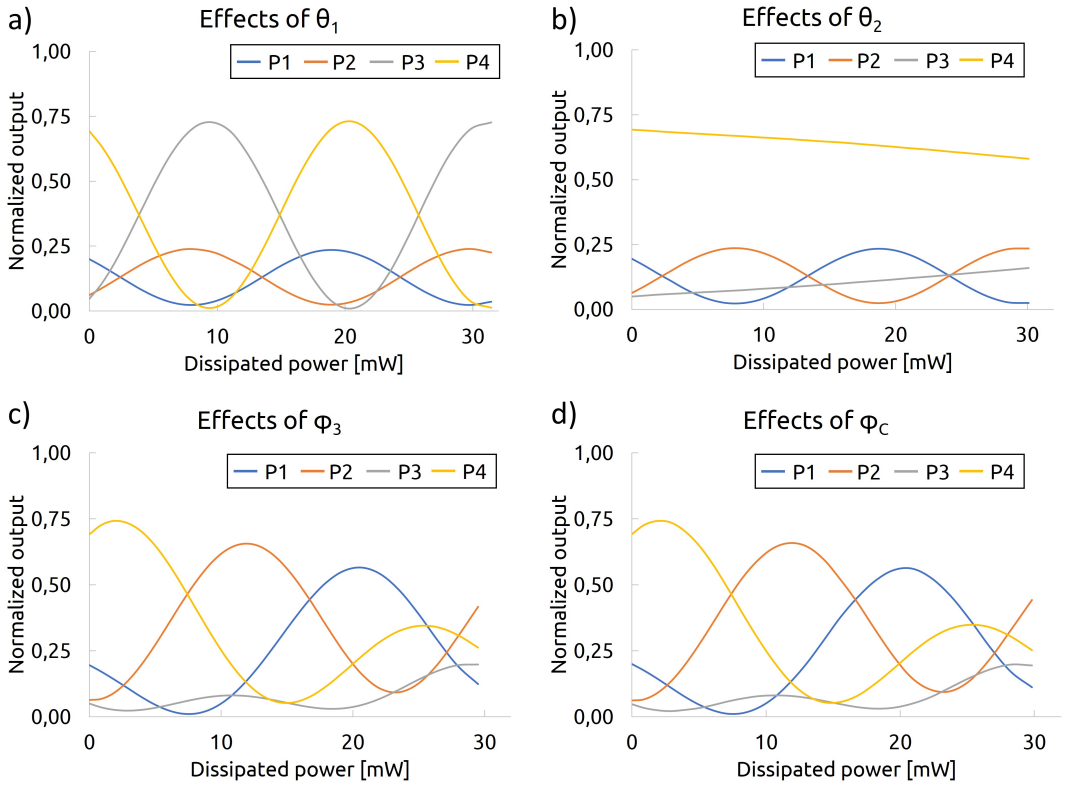

Figure 7.5: Measurement of the output power distributions when acting on some phase shifts. a) Effect of θ_1, the internal phase of the first quarter. b) Effect of θ_2, the internal phase of the last quarter. This is the most trivial behaviour to explain, since no other interferometric rings are present after the shifter. From the output of modes 3 and 4, which in theory should be unaltered, it is possible to notice the effect of thermal cross-talk. c) Effect of ϕ_3 and d) effect of ϕ_C, which are both fabricated on top of the third arm of the interferometer. Their equal effect means that their fabrication process is highly reproducible.

device, since this will be performed with single photons before the quantum metrology experiment, but to control whether the output distributions changed in a reasonable way when applying a voltage on the resistors. In detail, in Fig. 7.5 we show the result obtained when injecting light in mode 1 and controlling separately the phase shifts θ_1, θ_2, ϕ_3 and ϕ_C. Concerning the phase θ_2, which is the one internal to the last quarter, its effect is easier to explain since it basically acts only on the phase difference between modes 3 and 4. As expected, the power coming from these two spatial modes showed two opposed sinusoidal behaviours, i.e. when one reached its maximum, the other was minimized and vice versa. However, from Fig. 7.5.b it is possible to see that also modes 1 and 2 were slightly affected by the power dissipated on this resistor. This was due to the presence of cross-talk, which from this measurement can be estimated of about 10%. As already explained, this residual value, remaining despite the fabrication of the insulation trenches, can be further reduced by operating in vacuum. Nevertheless, it usually does not represent a problem, as long as it is fully characterized.

In Fig. 7.5.c-d we show instead the results for two internal phase shifters, namely ϕ_3 and ϕ_C. In this case the interpretation is more difficult since the output power distribution is changed in a non trivial way. Nevertheless, from this preliminary characterization it is possible to show that the two resistors, which are fabricated on the same waveguide, present very similar behaviours, and this confirms the reproducibility of their deposition and ablation processes.

7.5 CONCLUSIONS AND FURTHER PERSPECTIVES

In this activity we showed the fabrication of a four-arm interferometer, whose realization is beneficial for the simultaneous estimation of multiple phases on the same chip. By characterizing it with laser light, we showed that the optical circuit presented low insertion losses, and that the fabricated quarters were able to perform the balanced splitting in the four optical modes with very high fidelity with respect to the ideal case. Moreover, the characterization of the resistors provided very good results in terms of stability, reproducibility and low power dissipation, enabling the complete manipulation of the operation implemented by the circuit.

The device is currently in the Quantum Information Lab at La Sapienza University, where by using single photons a more detailed characterization is being performed. After the preliminary results presented in this thesis are confirmed, the circuit will be used with 3 and 4 photons for the estimation of the internal phase shifts by means of adaptive protocols enabling the saturation of the Heisenberg limit.

CONCLUSIONS

In this thesis work we demonstrated that femtosecond laser writing can be a valuable tool in the realization of scalable, reconfigurable photonic circuits. For this purpose, we exploited here all the main features that distinguish this fabrication platform from the others, like the possibility to realize three-dimensional circuits, the low birefringence of the inscribed waveguides, and the low power dissipation enabled by efficient thermal phase shifters.

First, we showed that passive femtosecond laser written circuits could be used in the implementation of satellite-based optical quantum communications. In particular, by replicating the typical conditions experienced by the instrumentation of a satellite, including the exposure to charged particles and high-energy radiation, high vacuum and temperature variations, we demonstrated that the inscribed devices could withstand such a harsh environment without any degradation of their operation during a three-year mission.

Then, we discussed three different activities towards the implementation of a photonic platform for quantum information processing. In detail, in the first work we showed that the unique 3D capability of FLW can be used to realize interferometers based on continuously coupled 3D waveguide arrays, with a clear advantage in terms of compactness and losses if compared to discrete implementations. In particular, we presented the realization of a 32-mode continuously coupled interferometer that, by means of 16 phase shifters, allowed the implementation of a large number of Haar-random transformations in a boson sampling experiment involving up to four photons. In the second work we showed instead the realization of a low-loss and low-power six-modes universal photonic processor. The reconfigurability required for its universality was achieved by means of a mesh of 15 MZIs, whose internal and external phases could be controlled by 30 thermal phase shifters, fabricated between isolation structures for reducing both their thermal crosstalk and their power consumption. After a proper characterization with classical light, we showed that the inscribed circuit could implement arbitrary unitary transformations with state-of-the-art fidelity and losses. The last activity, carried out at the University of Vienna, involved instead the optimization of the emission of a semiconductor quantum dot single photon source for achieving high brightness, purity, and indistinguishability, thus enabling the efficient generation of multi-photon states which can be then injected in a multi-mode interferometer.

The following work involved the femtosecond laser writing of the first quantum photonic memristor, a device composed by an MZI whose internal phase is controlled

by a feedback loop based on the measurement of its output. By injecting in the device an arbitrary superposition state with an oscillating average number of photons, we showed that the MZI output presents a hysteresis curve pinched at the origin, thus satisfying the requirement of a memristive device. In addition, by performing a tomography of the output state, we also showed that our photonic implementation preserves the coherence of the processed quantum states, and therefore could be useful in the realization of quantum photonic circuits requiring nonlinear sites, like quantum neuromorphic networks.

Finally, we presented the inscription and the characterization with classical light of a four-arm interferometer, the four-modes equivalent of an MZI. Notably, this device would enable the simultaneous quantum estimation of three optical phases with an enhanced sensitivity if compared to a classical measurement, thus finding applications in the field of photonic quantum metrology.

A

PROPERTIES OF SINGLE PHOTON SOURCES

A.1 BRIGHTNESS

Any single photon source, both deterministic and probabilistic, can emit photons only upon proper excitation. In this respect, the brightness B is defined as the probability of triggering the emission of a single photon, and in the ideal case it is equal to 1. The stream of photons coming from a source with $B < 1$ will contain some vacuum component $|0\rangle$, and this limits the scalability of a quantum system in the same way as photon losses or non-efficient detectors do.

Since there are several kinds of sources, a unique operative definition of the brightness cannot be expressed. For quantum dots, in particular, the brightness depends on the position where it is measured, for instance at the first lens (B_{lens}) or at the output of the collection fiber (B_{SMF}). In general, for deterministic sources B can be retrieved from the measured count rates, since it is directly related to the probability of having one photon per pulse:

$$B = p(1), \tag{A.1}$$

which is valid if $p(1) \gg p(n > 1)$. Operationally, the relation

$$B_{SMF} = \frac{C}{R \cdot \eta} \tag{A.2}$$

can be used, where C is the detected count rate at the output of the collection fiber, R is the repetition rate of the excitation pulses, and η is the detection efficiency of the detector used to measure C.

A.2 PURITY

For several applications, it is necessary that the source truly emits only $|1\rangle$ Fock states after every excitation. For instance, if more than one photon is used in the QKD protocol, an eavesdropping could occur by simply "stealing" the additional photon, while in boson sampling two photons in the same spatial mode could lead to wrong samplings events.

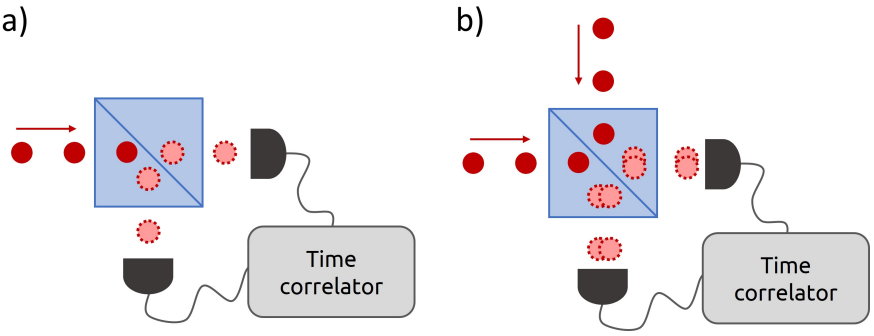

Figure A.1: Purity and indistinguishability measurements of single photon sources. a) Hanbury Brown and Twiss experiment for measuring the $g^{(2)}(0)$ of a stream of photons. b) Houng-Ou-Mandel experiment for the measurement of the indistinguishability of two single photons.

The capability of a source of emitting a stream of only single photons can be evaluated by measuring its purity, which is defined as

$$P = 1 - g^{(2)}(0). \tag{A.3}$$

In Eq. (A.3), $g^{(2)}(0)$ is the value at zero delay of the second order autocorrelation function $g^{(2)}(t,\tau)$, defined as

$$g^{(2)}(t, t+\tau) = \frac{\langle \hat{a}^\dagger(t)\, \hat{a}^\dagger(t+\tau)\, \hat{a}(t)\, \hat{a}(t+\tau)\rangle}{\langle \hat{a}^\dagger(t)\, \hat{a}(t)\rangle}, \tag{A.4}$$

where $\hat{a}^\dagger$ and $\hat{a}$ are respectively the creation and annihilation operators, and τ is the time difference at which the autocorrelation is evaluated. It is worth noting that for sources whose operation is stable in time, the dependence on t can be removed.

The value of $g^{(2)}(0)$ can be experimentally measured by performing the Hanbury Brown and Twiss (HBT) experiment [298]. The emitted stream of photons is split by a balanced beam splitter in two different spatial modes, which are sent to two single photon detectors (Fig. A.1.a). These are then connected to a coincidence electronics, which records the correlation at different delays of the detection events. In particular, a $g^{(2)}(0) > 0$ implies that for some events both detectors revealed a photon at the same time, which means that in the source output some pulses contained at least two photons.

From the $g^{(2)}(0)$ value, it is possible to retrieve the probability of emitting at least two photons as:

$$p(n \geq 2) = p(1) \cdot \frac{g^{(2)}(0)}{2}, \tag{A.5}$$

which is equal to zero for an ideal source. It should be noted that $p(1)$ can be retrieved from the brightness measurement.

A.3 INDISTINGUISHABILITY

For having quantum interference, the photons should be identical in all their properties, such as wavelength, polarization and time of arrival, in a way that they cannot be distinguished by any measurement. For an estimation of their indistinguishability, an Hong-Ou-Mandel (HOM) experiment can be performed [299] by using the setup in Fig. A.1.b. If two identical photons are sent to the two input ports of a balanced beam splitter, quantum interference occurs. In particular, the cases where one photon per output is present interfere destructively, and therefore only the bunching of both photons in one of the two outputs is possible, with a 50% probability each. Instead, if the photons are made distinguishable, for instance by tuning their polarization or time of arrival, then the probability of having coincident detections at the two output increases.

In this framework, the indistinguishability M can be measured by looking at the visibility V_{HOM} of the quantum interference, defined as

$$V_{HOM} = \left| \frac{C_{dist} - C_{ind}}{C_{dist}} \right|, \tag{A.6}$$

where C_{dist} and C_{ind} are the rates of coincident detections in the distinguishable and indistinguishable cases, respectively. Ideally, it should be $V_{HOM} = 1$. If the beam splitter is balanced, then the indistinguishability M is exactly equal to V_{HOM}, otherwise M is defined as:

$$M = V_{HOM} \frac{R^2 + (1-R)^2}{2R(1-R)}, \tag{A.7}$$

for taking into account the different reflectivity R of the beam splitter.

If the photon emission is not pure, the retrieval of the indistinguishability from the HOM setup could be spoiled by the coincident detections caused by the presence of more than one photon per input port, thus leading to low M values even when the photons are actually identical. For this reason, the corrected indistinguishability can be defined as

$$M^* = \frac{M + g^{(2)}(0)}{1 - g^{(2)}(0)}, \tag{A.8}$$

which however provides reasonable results only when $g^{(2)}(0) \ll 1$ [280]. This definition makes sense for quantum dots, since the indistinguishability and the purity are depending on different physical processes, thus it is reasonable to consider them separately.

BIBLIOGRAPHY

[1] J. P. Dowling and G. J. Milburn. "Quantum technology: the second quantum revolution." In: *Philosophical Transactions of the Royal Society of London. Series A: Mathematical, Physical and Engineering Sciences* 361.1809 (2003), pp. 1655–1674 (cit. on p. 3).

[2] A. Steane. "Quantum computing." In: *Reports on Progress in Physics* 61.2 (1998), p. 117 (cit. on p. 3).

[3] N. Gisin and R. Thew. "Quantum communication." In: *Nature Photonics* 1.3 (2007), pp. 165–171 (cit. on p. 3).

[4] V. Giovannetti, S. Lloyd, and L. Maccone. "Quantum metrology." In: *Physical Review Letters* 96.1 (2006), p. 010401 (cit. on p. 3).

[5] M. F. Riedel, D. Binosi, R. Thew, and T. Calarco. "The European quantum technologies flagship programme." In: *Quantum Science and Technology* 2.3 (2017), p. 030501 (cit. on p. 3).

[6] M. G. Raymer and C. Monroe. "The US national quantum initiative." In: *Quantum Science and Technology* 4.2 (2019), p. 020504 (cit. on p. 3).

[7] Q. Zhang, F. Xu, L. Li, N.-L. Liu, and J.-W. Pan. "Quantum information research in China." In: *Quantum Science and Technology* 4.4 (2019), p. 040503 (cit. on p. 3).

[8] M. Mohseni, P. Read, H. Neven, S. Boixo, V. Denchev, R. Babbush, A. Fowler, V. Smelyanskiy, and J. Martinis. "Commercialize quantum technologies in five years." In: *Nature News* 543.7644 (2017), p. 171 (cit. on p. 3).

[9] U. Alvarez-Rodriguez, M. Sanz, L. Lamata, and E. Solano. "Quantum artificial life in an IBM quantum computer." In: *Scientific Reports* 8.1 (2018), pp. 1–9 (cit. on p. 3).

[10] D. Castelvecchi. "Quantum computers ready to leap out of the lab in 2017." In: *Nature News* 541.7635 (2017), p. 9 (cit. on p. 3).

[11] M. Schlosshauer. "Quantum decoherence." In: *Physics Reports* 831 (2019), pp. 1–57 (cit. on p. 3).

[12] D. A. Lidar and T. A. Brun. *Quantum Error Correction*. Cambridge University Press, 2013 (cit. on p. 3).

[13] A. Acín, I. Bloch, H. Buhrman, T. Calarco, C. Eichler, J. Eisert, D. Esteve, N. Gisin, S. J. Glaser, F. Jelezko, et al. "The quantum technologies roadmap: a European community view." In: *New Journal of Physics* 20.8 (2018), p. 080201 (cit. on p. 3).

[14] J. L. O'brien. "Optical quantum computing." In: *Science* 318.5856 (2007), pp. 1567–1570 (cit. on pp. 4, 8).

[15] A. Politi, J. C. Matthews, M. G. Thompson, and J. L. O'Brien. "Integrated quantum photonics." In: *IEEE Journal of Selected Topics in Quantum Electronics* 15.6 (2009), pp. 1673–1684 (cit. on p. 4).

[16] F. Jazaeri, A. Beckers, A. Tajalli, and J.-M. Sallese. "A review on quantum computing: From qubits to front-end electronics and cryogenic MOSFET physics." In: *2019 MIXDES-26th International Conference" Mixed Design of Integrated Circuits and Systems"*. IEEE. 2019, pp. 15–25 (cit. on p. 4).

[17] D. Deutsch. "Quantum theory, the Church–Turing principle and the universal quantum computer." In: *Proceedings of the Royal Society of London. A. Mathematical and Physical Sciences* 400.1818 (1985), pp. 97–117 (cit. on p. 4).

[18] D. P. DiVincenzo. "Quantum gates and circuits." In: *Proceedings of the Royal Society of London. Series A: Mathematical, Physical and Engineering Sciences* 454.1969 (1998), pp. 261–276 (cit. on p. 5).

[19] M. A. Nielsen and I. Chuang. *Quantum computation and quantum information*. 2002 (cit. on p. 5).

[20] D. P. DiVincenzo. "The physical implementation of quantum computation." In: *Fortschritte der Physik: Progress of Physics* 48.9-11 (2000), pp. 771–783 (cit. on p. 6).

[21] W. Smith, A Kou, X Xiao, U Vool, and M. Devoret. "Superconducting circuit protected by two-Cooper-pair tunneling." In: *npj Quantum Information* 6.1 (2020), pp. 1–9 (cit. on p. 6).

[22] A. Kandala, A. Mezzacapo, K. Temme, M. Takita, M. Brink, J. M. Chow, and J. M. Gambetta. "Hardware-efficient variational quantum eigensolver for small molecules and quantum magnets." In: *Nature* 549.7671 (2017), pp. 242–246 (cit. on p. 6).

[23] A. Blais, A. L. Grimsmo, S. Girvin, and A. Wallraff. "Circuit quantum electrodynamics." In: *Reviews of Modern Physics* 93.2 (2021), p. 025005 (cit. on p. 6).

[24] Y. Makhlin, G. Schön, and A. Shnirman. "Quantum-state engineering with Josephson-junction devices." In: *Reviews of Modern Physics* 73.2 (2001), p. 357 (cit. on p. 7).

[25] L. DiCarlo, J. M. Chow, J. M. Gambetta, L. S. Bishop, B. R. Johnson, D. Schuster, J Majer, A. Blais, L. Frunzio, S. Girvin, et al. "Demonstration of two-qubit algorithms with a superconducting quantum processor." In: *Nature* 460.7252 (2009), pp. 240–244 (cit. on p. 7).

[26] H. Häffner, C. F. Roos, and R. Blatt. "Quantum computing with trapped ions." In: *Physics Reports* 469.4 (2008), pp. 155–203 (cit. on p. 7).

[27] C. D. Bruzewicz, J. Chiaverini, R. McConnell, and J. M. Sage. "Trapped-ion quantum computing: Progress and challenges." In: *Applied Physics Reviews* 6.2 (2019), p. 021314 (cit. on p. 7).

[28] W. M. Itano, J. C. Bergquist, J. J. Bollinger, and D. J. Wineland. "Cooling methods in ion traps." In: *Physica Scripta* 1995.T59 (1995), p. 106 (cit. on p. 7).

[29] B. B. Blinov, D. Leibfried, C Monroe, and D. J. Wineland. "Quantum computing with trapped ion hyperfine qubits." In: *Quantum Information Processing* 3.1 (2004), pp. 45–59 (cit. on p. 7).

[30] K. K. Mehta, C. D. Bruzewicz, R. McConnell, R. J. Ram, J. M. Sage, and J. Chiaverini. "Integrated optical addressing of an ion qubit." In: *Nature Nanotechnology* 11.12 (2016), pp. 1066–1070 (cit. on p. 7).

[31] A. Myerson, D. Szwer, S. Webster, D. Allcock, M. Curtis, G Imreh, J. Sherman, D. Stacey, A. Steane, and D. Lucas. "High-fidelity readout of trapped-ion qubits." In: *Physical Review Letters* 100.20 (2008), p. 200502 (cit. on p. 7).

[32] J. Kim. "Trapped ions make impeccable qubits." In: *Physics* 7 (2014), p. 119 (cit. on p. 7).

[33] F. Schmidt-Kaler, H. Häffner, M. Riebe, S. Gulde, G. P. Lancaster, T. Deuschle, C. Becher, C. F. Roos, J. Eschner, and R. Blatt. "Realization of the Cirac–Zoller controlled-NOT quantum gate." In: *Nature* 422.6930 (2003), pp. 408–411 (cit. on p. 7).

[34] C Langer, R Ozeri, J. D. Jost, J Chiaverini, B DeMarco, A Ben-Kish, R. Blakestad, J. Britton, D. Hume, W. M. Itano, et al. "Long-lived qubit memory using atomic ions." In: *Physical Review Letters* 95.6 (2005), p. 060502 (cit. on p. 8).

[35] I. Pogorelov, T. Feldker, C. D. Marciniak, L. Postler, G. Jacob, O. Krieglsteiner, V. Podlesnic, M. Meth, V. Negnevitsky, M. Stadler, et al. "Compact Ion-Trap Quantum Computing Demonstrator." In: *PRX Quantum* 2.2 (2021), p. 020343 (cit. on p. 8).

[36] T. D. Ladd, F. Jelezko, R. Laflamme, Y. Nakamura, C. Monroe, and J. L. O'Brien. "Quantum computers." In: *Nature* 464.7285 (2010), pp. 45–53 (cit. on p. 8).

[37] C. Gerry, P. Knight, and P. L. Knight. *Introductory Quantum Optics*. Cambridge University Press, 2005 (cit. on pp. 8, 28).

[38] K. R. Motes, A. Gilchrist, J. P. Dowling, and P. P. Rohde. "Scalable boson sampling with time-bin encoding using a loop-based architecture." In: *Physical Review Letters* 113.12 (2014), p. 120501 (cit. on p. 8).

[39] N. J. Cerf, C. Adami, and P. G. Kwiat. "Optical simulation of quantum logic." In: *Physical Review A* 57.3 (1998), R1477 (cit. on p. 8).

[40] R. Heilmann, M. Gräfe, S. Nolte, and A. Szameit. "Arbitrary photonic wave plate operations on chip: realizing Hadamard, Pauli-X and rotation gates for polarisation qubits." In: *Scientific Reports* 4.1 (2014), pp. 1–5 (cit. on pp. 8, 38).

[41] S. L. Braunstein and P. Van Loock. "Quantum information with continuous variables." In: *Reviews of Modern Physics* 77.2 (2005), p. 513 (cit. on p. 8).

[42] L.-M. Duan and H. Kimble. "Scalable photonic quantum computation through cavity-assisted interactions." In: *Physical Review Letters* 92.12 (2004), p. 127902 (cit. on p. 8).

[43] E. Knill, R. Laflamme, and G. J. Milburn. "A scheme for efficient quantum computation with linear optics." In: *Nature* 409.6816 (2001), pp. 46–52 (cit. on p. 8).

[44] K. Nemoto and W. J. Munro. "Nearly deterministic linear optical controlled-NOT gate." In: *Physical Review Letters* 93.25 (2004), p. 250502 (cit. on p. 9).

[45] P. Kok, W. J. Munro, K. Nemoto, T. C. Ralph, J. P. Dowling, and G. J. Milburn. "Linear optical quantum computing with photonic qubits." In: *Reviews of Modern Physics* 79.1 (2007), p. 135 (cit. on p. 9).

[46] P. W. Shor. "Algorithms for quantum computation: discrete logarithms and factoring." In: *Proceedings 35th annual symposium on foundations of computer science*. Ieee. 1994, pp. 124–134 (cit. on pp. 9, 23).

[47] S. Aaronson. "The limits of quantum." In: *Scientific American* 298.3 (2008), pp. 62–69 (cit. on p. 9).

[48] N. Moll, P. Barkoutsos, L. S. Bishop, J. M. Chow, A. Cross, D. J. Egger, S. Filipp, A. Fuhrer, J. M. Gambetta, M. Ganzhorn, et al. "Quantum optimization using variational algorithms on near-term quantum devices." In: *Quantum Science and Technology* 3.3 (2018), p. 030503 (cit. on p. 9).

[49] L. K. Grover. "A fast quantum mechanical algorithm for database search." In: *Proceedings of the twenty-eighth annual ACM symposium on Theory of computing*. 1996, pp. 212–219 (cit. on p. 9).

[50] J. I. Cirac and P. Zoller. "Goals and opportunities in quantum simulation." In: *Nature Physics* 8.4 (2012), pp. 264–266 (cit. on p. 9).

[51] I. M. Georgescu, S. Ashhab, and F. Nori. "Quantum simulation." In: *Reviews of Modern Physics* 86.1 (2014), p. 153 (cit. on p. 9).

[52] V. Dunjko and H. J. Briegel. "Machine learning & artificial intelligence in the quantum domain: a review of recent progress." In: *Reports on Progress in Physics* 81.7 (2018), p. 074001 (cit. on p. 9).

[53] J. Otterbach, R Manenti, N Alidoust, A Bestwick, M Block, B Bloom, S Caldwell, N Didier, E. S. Fried, S Hong, et al. "Unsupervised machine learning on a hybrid quantum computer." In: *arXiv preprint arXiv:1712.05771* (2017) (cit. on p. 9).

[54] M. Reck, A. Zeilinger, H. J. Bernstein, and P. Bertani. "Experimental realization of any discrete unitary operator." In: *Physical Review Letters* 73.1 (1994), p. 58 (cit. on p. 10).

[55] B. Yurke, S. L. McCall, and J. R. Klauder. "SU (2) and SU (1, 1) interferometers." In: *Physical Review A* 33.6 (1986), p. 4033 (cit. on p. 10).

[56] W. R. Clements, P. C. Humphreys, B. J. Metcalf, W. S. Kolthammer, and I. A. Walmsley. "Optimal design for universal multiport interferometers." In: *Optica* 3.12 (2016), pp. 1460–1465 (cit. on pp. 11, 94).

[57] D. A. Miller. "Self-configuring universal linear optical component." In: *Photonics Research* 1.1 (2013), pp. 1–15 (cit. on p. 11).

[58] J. C. Matthews, A. Politi, A. Stefanov, and J. L. O'brien. "Manipulation of multiphoton entanglement in waveguide quantum circuits." In: *Nature Photonics* 3.6 (2009), pp. 346–350 (cit. on pp. 11, 12).

[59] E. L. Wooten, K. M. Kissa, A. Yi-Yan, E. J. Murphy, D. A. Lafaw, P. F. Hallemeier, D. Maack, D. V. Attanasio, D. J. Fritz, G. J. McBrien, et al. "A review of lithium niobate modulators for fiber-optic communications systems." In: *IEEE Journal of selected topics in Quantum Electronics* 6.1 (2000), pp. 69–82 (cit. on p. 11).

[60] G. P. Agrawal. *Fiber-optic communication systems*. Vol. 222. John Wiley & Sons, 2012 (cit. on p. 11).

[61] N. C. Harris, G. R. Steinbrecher, M. Prabhu, Y. Lahini, J. Mower, D. Bunandar, C. Chen, F. N. Wong, T. Baehr-Jones, M. Hochberg, et al. "Quantum transport simulations in a programmable nanophotonic processor." In: *Nature Photonics* 11.7 (2017), pp. 447–452 (cit. on p. 11).

[62] X. Qiang, X. Zhou, J. Wang, C. M. Wilkes, T. Loke, S. O'Gara, L. Kling, G. D. Marshall, R. Santagati, T. C. Ralph, et al. "Large-scale silicon quantum photonics implementing arbitrary two-qubit processing." In: *Nature Photonics* 12.9 (2018), pp. 534–539 (cit. on p. 11).

[63] J. Carolan, C. Harrold, C. Sparrow, E. Martín-López, N. J. Russell, J. W. Silverstone, P. J. Shadbolt, N. Matsuda, M. Oguma, M. Itoh, et al. "Universal linear optics." In: *Science* 349.6249 (2015), pp. 711–716 (cit. on pp. 11, 12, 19).

[64] C. Taballione, T. A. Wolterink, J. Lugani, A. Eckstein, B. A. Bell, R. Grootjans, I. Visscher, D. Geskus, C. G. Roeloffzen, J. J. Renema, et al. "8× 8 reconfigurable quantum photonic processor based on silicon nitride waveguides." In: *Optics Express* 27.19 (2019), pp. 26842–26857 (cit. on p. 11).

[65] C. Taballione, R. van der Meer, H. J. Snijders, P. Hooijschuur, J. P. Epping, M. de Goede, B. Kassenberg, P. Venderbosch, C. Toebes, H. van den Vlekkert, et al. "A universal fully reconfigurable 12-mode quantum photonic processor." In: *Materials for Quantum Technology* 1.3 (2021), p. 035002 (cit. on pp. 12, 89).

[66] D. C. Burnham and D. L. Weinberg. "Observation of simultaneity in parametric production of optical photon pairs." In: *Physical Review Letters* 25.2 (1970), p. 84 (cit. on p. 13).

[67] C. Osorio, N Sangouard, and R. T. Thew. "On the purity and indistinguishability of down-converted photons." In: *Journal of Physics B: Atomic, Molecular and Optical Physics* 46.5 (2013), p. 055501 (cit. on p. 13).

[68] P. G. Kwiat, K. Mattle, H. Weinfurter, A. Zeilinger, A. V. Sergienko, and Y. Shih. "New high-intensity source of polarization-entangled photon pairs." In: *Physical Review Letters* 75.24 (1995), p. 4337 (cit. on p. 13).

[69] V. Giovannetti, L. Maccone, J. H. Shapiro, and F. N. Wong. "Generating entangled two-photon states with coincident frequencies." In: *Physical Review Letters* 88.18 (2002), p. 183602 (cit. on p. 13).

[70] R. García-Patrón, J. J. Renema, and V. Shchesnovich. "Simulating boson sampling in lossy architectures." In: *Quantum* 3 (2019), p. 169 (cit. on p. 13).

[71] X. Guo, C.-l. Zou, C. Schuck, H. Jung, R. Cheng, and H. X. Tang. "Parametric down-conversion photon-pair source on a nanophotonic chip." In: *Light: Science & Applications* 6.5 (2017), e16249–e16249 (cit. on p. 13).

[72] S. Atzeni, A. S. Rab, G. Corrielli, E. Polino, M. Valeri, P. Mataloni, N. Spagnolo, A. Crespi, F. Sciarrino, and R. Osellame. "Integrated sources of entangled photons at the telecom wavelength in femtosecond-laser-written circuits." In: *Optica* 5.3 (2018), pp. 311–314 (cit. on pp. 13, 31).

[73] A. C. Turner, M. A. Foster, A. L. Gaeta, and M. Lipson. "Ultra-low power parametric frequency conversion in a silicon microring resonator." In: *Optics Express* 16.7 (2008), pp. 4881–4887 (cit. on p. 13).

[74] B. Darquié, M. P. Jones, J. Dingjan, J. Beugnon, S. Bergamini, Y. Sortais, G. Messin, A. Browaeys, and P. Grangier. "Controlled single-photon emission from a single trapped two-level atom." In: *Science* 309.5733 (2005), pp. 454–456 (cit. on p. 13).

[75] C. Maurer, C. Becher, C. Russo, J. Eschner, and R. Blatt. "A single-photon source based on a single Ca+ ion." In: *New Journal of Physics* 6.1 (2004), p. 94 (cit. on p. 13).

[76] T. Schröder, F. Gädeke, M. J. Banholzer, and O. Benson. "Ultrabright and efficient single-photon generation based on nitrogen-vacancy centres in nanodiamonds on a solid immersion lens." In: *New Journal of Physics* 13.5 (2011), p. 055017 (cit. on p. 13).

[77] S. Hepp, M. Jetter, S. L. Portalupi, and P. Michler. "Semiconductor quantum dots for integrated quantum photonics." In: *Advanced Quantum Technologies* 2.9 (2019), p. 1900020 (cit. on p. 13).

[78] N. Somaschi, V. Giesz, L. De Santis, J. Loredo, M. P. Almeida, G. Hornecker, S. L. Portalupi, T. Grange, C. Anton, J. Demory, et al. "Near-optimal single-photon sources in the solid state." In: *Nature Photonics* 10.5 (2016), pp. 340–345 (cit. on pp. 13, 101–103, 112).

[79] M. Arcari, I. Söllner, A. Javadi, S. L. Hansen, S. Mahmoodian, J. Liu, H. Thyrrestrup, E. H. Lee, J. D. Song, S. Stobbe, et al. "Near-unity coupling efficiency of a quantum emitter to a photonic crystal waveguide." In: *Physical Review Letters* 113.9 (2014), p. 093603 (cit. on p. 13).

[80] R. B. Patel, A. J. Bennett, I. Farrer, C. A. Nicoll, D. A. Ritchie, and A. J. Shields. "Two-photon interference of the emission from electrically tunable remote quantum dots." In: *Nature Photonics* 4.9 (2010), pp. 632–635 (cit. on p. 13).

[81] C Antón, J. C. Loredo, G. Coppola, H. Ollivier, N. Viggianiello, A. Harouri, N. Somaschi, A. Crespi, I. Sagnes, A. Lemaitre, et al. "Interfacing scalable photonic platforms: solid-state based multi-photon interference in a reconfigurable glass chip." In: *Optica* 6.12 (2019), pp. 1471–1477 (cit. on p. 13).

[82] R. H. Hadfield. "Single-photon detectors for optical quantum information applications." In: *Nature Photonics* 3.12 (2009), pp. 696–705 (cit. on p. 13).

[83] D. Bronzi, F. Villa, S. Tisa, A. Tosi, and F. Zappa. "SPAD figures of merit for photon-counting, photon-timing, and imaging applications: a review." In: *IEEE Sensors Journal* 16.1 (2015), pp. 3–12 (cit. on p. 14).

[84] S. Slussarenko and G. J. Pryde. "Photonic quantum information processing: A concise review." In: *Applied Physics Reviews* 6.4 (2019), p. 041303 (cit. on p. 14).

[85] C. M. Natarajan, M. G. Tanner, and R. H. Hadfield. "Superconducting nanowire single-photon detectors: physics and applications." In: *Superconductor Science and Technology* 25.6 (2012), p. 063001 (cit. on p. 14).

[86] F. Ceccarelli, G. Acconcia, A. Gulinatti, M. Ghioni, I. Rech, and R. Osellame. "Recent Advances and Future Perspectives of Single-Photon Avalanche Diodes for Quantum Photonics Applications." In: *Advanced Quantum Technologies* 4.2 (2021), p. 2000102 (cit. on p. 14).

[87] F. Najafi, J. Mower, N. C. Harris, F. Bellei, A. Dane, C. Lee, X. Hu, P. Kharel, F. Marsili, S. Assefa, et al. "On-chip detection of non-classical light by scalable integration of single-photon detectors." In: *Nature Communications* 6.1 (2015), pp. 1–8 (cit. on p. 14).

[88] C. Zhang, Y.-F. Huang, B.-H. Liu, C.-F. Li, and G.-C. Guo. "Spontaneous Parametric Down-Conversion Sources for Multiphoton Experiments." In: *Advanced Quantum Technologies* 4.5 (2021), p. 2000132 (cit. on p. 14).

[89] R. Uppu, F. T. Pedersen, Y. Wang, C. T. Olesen, C. Papon, X. Zhou, L. Midolo, S. Scholz, A. D. Wieck, A. Ludwig, et al. "Scalable integrated single-photon source." In: *Science Advances* 6.50 (2020), eabc8268 (cit. on p. 14).

[90] J. Preskill. "Quantum computing in the NISQ era and beyond." In: *Quantum* 2 (2018), p. 79 (cit. on p. 15).

[91] D. Qian. "High performance computing: a brief review and prospects." In: *National Science Review* 3.1 (2016), p. 16 (cit. on p. 15).

[92] A. W. Harrow and A. Montanaro. "Quantum computational supremacy." In: *Nature* 549.7671 (2017), pp. 203–209 (cit. on p. 15).

[93] S. Aaronson and L. Chen. "Complexity-theoretic foundations of quantum supremacy experiments." In: *arXiv preprint arXiv:1612.05903* (2016) (cit. on p. 15).

[94] E. Farhi and A. W. Harrow. "Quantum supremacy through the quantum approximate optimization algorithm." In: *arXiv preprint arXiv:1602.07674* (2016) (cit. on p. 15).

[95] M. J. Bremner, R. Jozsa, and D. J. Shepherd. "Classical simulation of commuting quantum computations implies collapse of the polynomial hierarchy." In: *Proceedings of the Royal Society A: Mathematical, Physical and Engineering Sciences* 467.2126 (2011), pp. 459–472 (cit. on p. 15).

[96] F. Arute, K. Arya, R. Babbush, D. Bacon, J. C. Bardin, R. Barends, R. Biswas, S. Boixo, F. G. Brandao, D. A. Buell, et al. "Quantum supremacy using a programmable superconducting processor." In: *Nature* 574.7779 (2019), pp. 505–510 (cit. on pp. 15, 16).

[97] E. Pednault, J. Gunnels, D. Maslov, and J. Gambetta. *On "Quantum Supremacy"*. 2019. URL: https://www.ibm.com/blogs/research/2019/10/on-quantum-supremacy/ (visited on 04/11/2021) (cit. on p. 15).

[98] H.-S. Zhong, H. Wang, Y.-H. Deng, M.-C. Chen, L.-C. Peng, Y.-H. Luo, J. Qin, D. Wu, X. Ding, Y. Hu, et al. "Quantum computational advantage using photons." In: *Science* 370.6523 (2020), pp. 1460–1463 (cit. on pp. 15, 16, 76).

[99] C. S. Hamilton, R. Kruse, L. Sansoni, S. Barkhofen, C. Silberhorn, and I. Jex. "Gaussian boson sampling." In: *Physical Review Letters* 119.17 (2017), p. 170501 (cit. on pp. 15, 18).

[100] H.-S. Zhong, Y.-H. Deng, J. Qin, H. Wang, M.-C. Chen, L.-C. Peng, Y.-H. Luo, D. Wu, S.-Q. Gong, H. Su, et al. "Phase-programmable Gaussian boson sampling using stimulated squeezed light." In: *Physical Review Letters* 127.18 (2021), p. 180502 (cit. on p. 16).

[101] S. Aaronson and A. Arkhipov. "The computational complexity of linear optics." In: *Proceedings of the forty-third annual ACM symposium on Theory of computing*. 2011, pp. 333–342 (cit. on p. 16).

[102] D. J. Brod, E. F. Galvão, A. Crespi, R. Osellame, N. Spagnolo, and F. Sciarrino. "Photonic implementation of boson sampling: a review." In: *Advanced Photonics* 1.3 (2019), p. 034001 (cit. on pp. 16, 18).

[103] L. G. Valiant. "The complexity of computing the permanent." In: *Theoretical Computer Science* 8.2 (1979), pp. 189–201 (cit. on p. 17).

[104] A. Neville, C. Sparrow, R. Clifford, E. Johnston, P. M. Birchall, A. Montanaro, and A. Laing. "Classical boson sampling algorithms with superior performance to near-term experiments." In: *Nature Physics* 13.12 (2017), pp. 1153–1157 (cit. on p. 17).

[105] K. Zyczkowski and M. Kus. "Random unitary matrices." In: *Journal of Physics A: Mathematical and General* 27.12 (1994), p. 4235 (cit. on p. 17).

[106] F. Mattioli, Z. Zhou, A. Gaggero, R. Gaudio, S. Jahanmirinejad, D. Sahin, F. Marsili, R. Leoni, and A. Fiore. "Photon-number-resolving superconducting nanowire detectors." In: *Superconductor Science and Technology* 28.10 (2015), p. 104001 (cit. on p. 17).

[107] A. Arkhipov and G. Kuperberg. "The bosonic birthday paradox." In: *Geometry & Topology Monographs* 18.1 (2012), pp. 10–2140 (cit. on p. 17).

[108] J. Carolan, J. D. Meinecke, P. J. Shadbolt, N. J. Russell, N. Ismail, K. Wörhoff, T. Rudolph, M. G. Thompson, J. L. O'brien, J. C. Matthews, et al. "On the experimental verification of quantum complexity in linear optics." In: *Nature Photonics* 8.8 (2014), pp. 621–626 (cit. on pp. 18, 19).

[109] M. A. Broome, A. Fedrizzi, S. Rahimi-Keshari, J. Dove, S. Aaronson, T. C. Ralph, and A. G. White. "Photonic boson sampling in a tunable circuit." In: *Science* 339.6121 (2013), pp. 794–798 (cit. on p. 17).

[110] A. Crespi, R. Osellame, R. Ramponi, D. J. Brod, E. F. Galvao, N. Spagnolo, C. Vitelli, E. Maiorino, P. Mataloni, and F. Sciarrino. "Integrated multimode interferometers with arbitrary designs for photonic boson sampling." In: *Nature Photonics* 7.7 (2013), pp. 545–549 (cit. on pp. 17, 18, 37, 38).

[111] J. B. Spring, B. J. Metcalf, P. C. Humphreys, W. S. Kolthammer, X.-M. Jin, M. Barbieri, A. Datta, N. Thomas-Peter, N. K. Langford, D. Kundys, et al. "Boson sampling on a photonic chip." In: *Science* 339.6121 (2013), pp. 798–801 (cit. on p. 17).

[112] J. Wang, S. Paesani, Y. Ding, R. Santagati, P. Skrzypczyk, A. Salavrakos, J. Tura, R. Augusiak, L. Mančinska, D. Bacco, et al. "Multidimensional quantum entanglement with large-scale integrated optics." In: *Science* 360.6386 (2018), pp. 285–291 (cit. on p. 17).

[113] J. Loredo, M. Broome, P Hilaire, O Gazzano, I Sagnes, A Lemaitre, M. Almeida, P Senellart, and A. White. "Boson sampling with single-photon fock states from a bright solid-state source." In: *Physical review letters* 118.13 (2017), p. 130503 (cit. on pp. 17, 18).

[114] H. Wang, W. Li, X. Jiang, Y.-M. He, Y.-H. Li, X. Ding, M.-C. Chen, J. Qin, C.-Z. Peng, C. Schneider, et al. "Toward scalable boson sampling with photon loss." In: *Physical Review Letters* 120.23 (2018), p. 230502 (cit. on p. 17).

[115] A. P. Lund, A. Laing, S. Rahimi-Keshari, T. Rudolph, J. L. O'Brien, and T. C. Ralph. "Boson sampling from a Gaussian state." In: *Physical Review Letters* 113.10 (2014), p. 100502 (cit. on p. 18).

[116] H.-S. Zhong, Y. Li, W. Li, L.-C. Peng, Z.-E. Su, Y. Hu, Y.-M. He, X. Ding, W. Zhang, H. Li, et al. "12-photon entanglement and scalable scattershot boson sampling with optimal entangled-photon pairs from parametric down-conversion." In: *Physical review letters* 121.25 (2018), p. 250505 (cit. on p. 18).

[117] M. Tillmann, B. Dakić, R. Heilmann, S. Nolte, A. Szameit, and P. Walther. "Experimental boson sampling." In: *Nature Photonics* 7.7 (2013), pp. 540–544 (cit. on pp. 18, 31, 37).

[118] S. Paesani, Y. Ding, R. Santagati, L. Chakhmakhchyan, C. Vigliar, K. Rottwitt, L. K. Oxenløwe, J. Wang, M. G. Thompson, and A. Laing. "Generation and sampling of quantum states of light in a silicon chip." In: *Nature Physics* 15.9 (2019), pp. 925–929 (cit. on p. 19).

[119] J. J. Hopfield. "Neural networks and physical systems with emergent collective computational abilities." In: *Proceedings of the National Academy of Sciences* 79.8 (1982), pp. 2554–2558 (cit. on p. 19).

[120] B. Müller, J. Reinhardt, and M. T. Strickland. *Neural networks: an introduction*. Springer Science & Business Media, 1995 (cit. on p. 19).

[121] W. S. McCulloch and W. Pitts. "A logical calculus of the ideas immanent in nervous activity." In: *The bulletin of mathematical biophysics* 5.4 (1943), pp. 115–133 (cit. on pp. 19, 20).

[122] D. Silver, A. Huang, C. J. Maddison, A. Guez, L. Sifre, G. Van Den Driessche, J. Schrittwieser, I. Antonoglou, V. Panneershelvam, M. Lanctot, et al. "Mastering the game of Go with deep neural networks and tree search." In: *Nature* 529.7587 (2016), pp. 484–489 (cit. on p. 19).

[123] D. S. Maitra, U. Bhattacharya, and S. K. Parui. "CNN based common approach to handwritten character recognition of multiple scripts." In: *2015 13th International Conference on Document Analysis and Recognition (ICDAR)*. IEEE. 2015, pp. 1021–1025 (cit. on p. 19).

[124] W. Chan, N. Jaitly, Q. Le, and O. Vinyals. "Listen, attend and spell: A neural network for large vocabulary conversational speech recognition." In: *2016 IEEE International Conference on Acoustics, Speech and Signal Processing (ICASSP)*. IEEE. 2016, pp. 4960–4964 (cit. on p. 19).

[125] S. C. Kak. "Quantum neural computing." In: *Advances in Imaging and Electron Physics* 94 (1995), pp. 259–313 (cit. on pp. 19, 20).

[126] J. Biamonte, P. Wittek, N. Pancotti, P. Rebentrost, N. Wiebe, and S. Lloyd. "Quantum machine learning." In: *Nature* 549.7671 (2017), pp. 195–202 (cit. on p. 19).

[127] D. Kriesel. *A Brief Introduction to Neural Networks*. 2005. URL: `https://www.dkriesel.com/_media/science/neuronalenetze-en-zeta2-2col-dkrieselcom.pdf` (cit. on p. 20).

[128] R. Sathya, A. Abraham, et al. "Comparison of supervised and unsupervised learning algorithms for pattern classification." In: *International Journal of Advanced Research in Artificial Intelligence* 2.2 (2013), pp. 34–38 (cit. on p. 20).

[129] M. V. Altaisky, N. E. Kaputkina, and V. Krylov. "Quantum neural networks: Current status and prospects for development." In: *Physics of Particles and Nuclei* 45.6 (2014), pp. 1013–1032 (cit. on p. 20).

[130] M. Schuld, I. Sinayskiy, and F. Petruccione. "The quest for a quantum neural network." In: *Quantum Information Processing* 13.11 (2014), pp. 2567–2586 (cit. on p. 21).

[131] M. Peruš. "Neural networks as a basis for quantum associative networks." In: *Neural Network World* 10.6 (2000), pp. 1001–1013 (cit. on p. 21).

[132] M. Siomau. "A quantum model for autonomous learning automata." In: *Quantum Information Processing* 13.5 (2014), pp. 1211–1221 (cit. on p. 21).

[133] C. P. Gonçalves. "Quantum cybernetics and complex quantum systems science-A quantum connectionist exploration." In: *arXiv preprint arXiv:1402.1141* (2014) (cit. on p. 21).

[134] G. R. Steinbrecher, J. P. Olson, D. Englund, and J. Carolan. "Quantum optical neural networks." In: *npj Quantum Information* 5.1 (2019), pp. 1–9 (cit. on p. 21).

[135] M. Altaisky. "Quantum neural network." In: *arXiv preprint quant-ph/0107012* (2001) (cit. on p. 21).

[136] K. Mattle, H. Weinfurter, P. G. Kwiat, and A. Zeilinger. "Dense coding in experimental quantum communication." In: *Physical Review Letters* 76.25 (1996), p. 4656 (cit. on p. 22).

[137] N. Gisin, G. Ribordy, W. Tittel, and H. Zbinden. "Quantum cryptography." In: *Reviews of Modern Physics* 74.1 (2002), p. 145 (cit. on p. 22).

[138] D. Kielpinski, C. Monroe, and D. J. Wineland. "Architecture for a large-scale ion-trap quantum computer." In: *Nature* 417.6890 (2002), pp. 709–711 (cit. on p. 22).

[139] G. S. Vernam. "Cipher printing telegraph systems: For secret wire and radio telegraphic communications." In: *Journal of the AIEE* 45.2 (1926), pp. 109–115 (cit. on p. 22).

[140] H. Delfs and H. Knebl. "Symmetric-key encryption." In: *Introduction to Cryptography*. Springer, 2007, pp. 11–31 (cit. on p. 22).

[141] W. Stallings, L. Brown, M. D. Bauer, and A. K. Bhattacharjee. *Computer security: principles and practice*. Pearson Education Upper Saddle River, NJ, USA, 2012 (cit. on p. 22).

[142] O. Goldreich. *Foundations of cryptography: volume 2, basic applications*. Cambridge University Press, 2009 (cit. on p. 23).

[143] R. L. Rivest, A. Shamir, and L. Adleman. "A method for obtaining digital signatures and public-key cryptosystems." In: *Communications of the ACM* 21.2 (1978), pp. 120–126 (cit. on p. 23).

[144] D. J. Bernstein. "Introduction to post-quantum cryptography." In: *Post-quantum cryptography*. Springer, 2009, pp. 1–14 (cit. on p. 23).

[145] C. Paquin, D. Stebila, and G. Tamvada. "Benchmarking Post-Quantum Cryptography in TLS." In: *PQCrypto*. 2020, pp. 72–91 (cit. on p. 23).

[146] F. Xu, X. Ma, Q. Zhang, H.-K. Lo, and J.-W. Pan. "Secure quantum key distribution with realistic devices." In: *Reviews of Modern Physics* 92.2 (2020), p. 025002 (cit. on p. 23).

[147] R. Renner. "Security of quantum key distribution." In: *International Journal of Quantum Information* 6.01 (2008), pp. 1–127 (cit. on p. 23).

[148] W. K. Wootters and W. H. Zurek. "A single quantum cannot be cloned." In: *Nature* 299.5886 (1982), pp. 802–803 (cit. on p. 23).

[149] S. Vaudenay. "Secure communications over insecure channels based on short authenticated strings." In: *Annual International Cryptology Conference*. Springer. 2005, pp. 309–326 (cit. on p. 24).

[150] C. Bennett and G Brassard. "Quantum crytography: Public key distribution and coin tossing." In: *Proceedings of IEEE International Conference on Computers, Systems, and Signal Processing*. 1984, pp. 175–179 (cit. on p. 24).

[151] C. H. Bennett, F. Bessette, G. Brassard, L. Salvail, and J. Smolin. "Experimental quantum cryptography." In: *Journal of Cryptology* 5.1 (1992), pp. 3–28 (cit. on p. 25).

[152] H.-K. Lo, X. Ma, and K. Chen. "Decoy state quantum key distribution." In: *Physical Review Letters* 94.23 (2005), p. 230504 (cit. on p. 25).

[153] V. Scarani, H. Bechmann-Pasquinucci, N. J. Cerf, M. Dušek, N. Lütkenhaus, and M. Peev. "The security of practical quantum key distribution." In: *Reviews of Modern Physics* 81.3 (2009), p. 1301 (cit. on p. 25).

[154] P. A. Hiskett, D. Rosenberg, C. G. Peterson, R. J. Hughes, S Nam, A. Lita, A. Miller, and J. Nordholt. "Long-distance quantum key distribution in optical fibre." In: *New Journal of Physics* 8.9 (2006), p. 193 (cit. on p. 25).

[155] B. Korzh, C. C. W. Lim, R. Houlmann, N. Gisin, M. J. Li, D. Nolan, B. Sanguinetti, R. Thew, and H. Zbinden. "Provably secure and practical quantum key distribution over 307 km of optical fibre." In: *Nature Photonics* 9.3 (2015), pp. 163–168 (cit. on p. 25).

[156] *IDQ Celebrates 10-Year Anniversary of the World's First Real-Life Quantum Cryptography Installation*. 2017. URL: https://www.idquantique.com/idq-celebrates-10-year-anniversary-of-the-worlds-first-real-life-quantum-cryptography-installation/ (cit. on p. 25).

[157] Y.-A. Chen, Q. Zhang, T.-Y. Chen, W.-Q. Cai, S.-K. Liao, J. Zhang, K. Chen, J. Yin, J.-G. Ren, Z. Chen, et al. "An integrated space-to-ground quantum communication network over 4,600 kilometres." In: *Nature* 589.7841 (2021), pp. 214–219 (cit. on p. 25).

[158] S.-K. Liao, W.-Q. Cai, W.-Y. Liu, L. Zhang, Y. Li, J.-G. Ren, J. Yin, Q. Shen, Y. Cao, Z.-P. Li, et al. "Satellite-to-ground quantum key distribution." In: *Nature* 549.7670 (2017), pp. 43–47 (cit. on pp. 25, 26).

[159] H.-L. Yin, T.-Y. Chen, Z.-W. Yu, H. Liu, L.-X. You, Y.-H. Zhou, S.-J. Chen, Y. Mao, M.-Q. Huang, W.-J. Zhang, et al. "Measurement-device-independent quantum key distribution over a 404 km optical fiber." In: *Physical Review Letters* 117.19 (2016), p. 190501 (cit. on p. 25).

[160] H.-J. Briegel, W. Dür, J. I. Cirac, and P. Zoller. "Quantum repeaters: the role of imperfect local operations in quantum communication." In: *Physical Review Letters* 81.26 (1998), p. 5932 (cit. on p. 26).

[161] J. G. Rarity, P. Tapster, P. Gorman, and P. Knight. "Ground to satellite secure key exchange using quantum cryptography." In: *New Journal of Physics* 4.1 (2002), p. 82 (cit. on p. 26).

[162] S.-K. Liao, W.-Q. Cai, J. Handsteiner, B. Liu, J. Yin, L. Zhang, D. Rauch, M. Fink, J.-G. Ren, W.-Y. Liu, et al. "Satellite-relayed intercontinental quantum network." In: *Physical Review Letters* 120.3 (2018), p. 030501 (cit. on p. 26).

[163] International Organization for Standardization (ISO). *Guide to the Expression of Uncertainty in Measurement*. ISO, Geneva, 1993 (cit. on p. 26).

[164] W. Heisenberg. "Über den anschaulichen Inhalt der quantentheoretischen Kinematik und Mechanik." In: *Original Scientific Papers Wissenschaftliche Originalarbeiten*. Springer, 1985, pp. 478–504 (cit. on p. 26).

[165] M. Holland and K Burnett. "Interferometric detection of optical phase shifts at the Heisenberg limit." In: *Physical Review Letters* 71.9 (1993), p. 1355 (cit. on p. 27).

[166] M. A. Taylor and W. P. Bowen. "Quantum metrology and its application in biology." In: *Physics Reports* 615 (2016), pp. 1–59 (cit. on p. 27).

[167] A. N. Boto, P. Kok, D. S. Abrams, S. L. Braunstein, C. P. Williams, and J. P. Dowling. "Quantum interferometric optical lithography: exploiting entanglement to beat the diffraction limit." In: *Physical Review Letters* 85.13 (2000), p. 2733 (cit. on p. 27).

[168] C. L. Degen, F Reinhard, and P. Cappellaro. "Quantum sensing." In: *Reviews of Modern Physics* 89.3 (2017), p. 035002 (cit. on p. 27).

[169] P.-A. Moreau, E. Toninelli, T. Gregory, and M. J. Padgett. "Imaging with quantum states of light." In: *Nature Reviews Physics* 1.6 (2019), pp. 367–380 (cit. on p. 27).

[170] B. P. Abbott, R. Abbott, T. Abbott, M. Abernathy, F. Acernese, K. Ackley, C. Adams, T. Adams, P. Addesso, R. Adhikari, et al. "Observation of gravitational waves from a binary black hole merger." In: *Physical Review Letters* 116.6 (2016), p. 061102 (cit. on p. 27).

[171] I. R. Berchera and I. P. Degiovanni. "Quantum imaging with sub-Poissonian light: challenges and perspectives in optical metrology." In: *Metrologia* 56.2 (2019), p. 024001 (cit. on p. 27).

[172] T. Ono, R. Okamoto, and S. Takeuchi. "An entanglement-enhanced microscope." In: *Nature Communications* 4.1 (2013), pp. 1–7 (cit. on p. 27).

[173] V. Giovannetti, S. Lloyd, and L. Maccone. "Advances in quantum metrology." In: *Nature Photonics* 5.4 (2011), pp. 222–229 (cit. on p. 27).

[174] A. Crespi, Y. Gu, B. Ngamsom, H. J. Hoekstra, C. Dongre, M. Pollnau, R. Ramponi, H. H. van den Vlekkert, P. Watts, G. Cerullo, et al. "Three-dimensional Mach-Zehnder interferometer in a microfluidic chip for spatially-resolved label-free detection." In: *Lab on a Chip* 10.9 (2010), pp. 1167–1173 (cit. on p. 27).

[175] R. Lynch. "The quantum phase problem: a critical review." In: *Physics Reports* 256.6 (1995), pp. 367–436 (cit. on p. 27).

[176] J. J. Bollinger, W. M. Itano, D. J. Wineland, and D. J. Heinzen. "Optimal frequency measurements with maximally correlated states." In: *Physical Review A* 54.6 (1996), R4649 (cit. on p. 29).

[177] J. P. Dowling. "Quantum optical metrology–the lowdown on high-N00N states." In: *Contemporary Physics* 49.2 (2008), pp. 125–143 (cit. on p. 30).

[178] P. Kok, H. Lee, and J. P. Dowling. "Creation of large-photon-number path entanglement conditioned on photodetection." In: *Physical Review A* 65.5 (2002), p. 052104 (cit. on p. 30).

[179] I. Afek, O. Ambar, and Y. Silberberg. "High-NOON states by mixing quantum and classical light." In: *Science* 328.5980 (2010), pp. 879–881 (cit. on p. 30).

[180] M. Gessner, L. Pezzè, and A. Smerzi. "Sensitivity bounds for multiparameter quantum metrology." In: *Physical Review Letters* 121.13 (2018), p. 130503 (cit. on p. 30).

[181] E. Polino, M. Valeri, N. Spagnolo, and F. Sciarrino. "Photonic quantum metrology." In: *AVS Quantum Science* 2.2 (2020), p. 024703 (cit. on p. 30).

[182] G. Corrielli, A. Crespi, and R. Osellame. "Femtosecond laser micromachining for integrated quantum photonics." In: *Nanophotonics* (2021) (cit. on p. 31).

[183] R. R. Gattass and E. Mazur. "Femtosecond laser micromachining in transparent materials." In: *Nature Photonics* 2.4 (2008), pp. 219–225 (cit. on p. 31).

[184] K. M. Davis, K. Miura, N. Sugimoto, and K. Hirao. "Writing waveguides in glass with a femtosecond laser." In: *Optics Letters* 21.21 (1996), pp. 1729–1731 (cit. on p. 31).

[185] X. Hou, X.-Y. Xu, G. Xu, L. You, X.-M. Jin, H. Li, W. Zhang, R.-J. Ren, X.-L. Huang, and Z. Wang. "Waveguide-coupled superconducting nanowire single-photon detectors based on femtosecond laser direct writing." In: *Optics Express* 29.5 (2021), pp. 7746–7756 (cit. on p. 31).

[186] B. Xu, W.-Q. Du, J.-W. Li, Y.-L. Hu, L. Yang, C.-C. Zhang, G.-Q. Li, Z.-X. Lao, J.-C. Ni, J.-R. Chu, et al. "High efficiency integration of three-dimensional functional microdevices inside a microfluidic chip by using femtosecond laser multifoci parallel microfabrication." In: *Scientific Reports* 6.1 (2016), pp. 1–9 (cit. on p. 32).

[187] T. Meany, M. Gräfe, R. Heilmann, A. Perez-Leija, S. Gross, M. J. Steel, M. J. Withford, and A. Szameit. "Laser written circuits for quantum photonics." In: *Laser & Photonics Reviews* 9.4 (2015), pp. 363–384 (cit. on p. 32).

[188] *Two-photon fluorescence microscopy*. URL: `https://microscopy.berkeley.edu/courses/TLM/2P/index.html` (visited on 01/12/2021) (cit. on p. 32).

[189] R. Osellame, G. Cerullo, and R. Ramponi. *Femtosecond laser micromachining: photonic and microfluidic devices in transparent materials*. Vol. 123. Springer Science & Business Media, 2012 (cit. on pp. 32, 36).

[190] L. Keldysh et al. "Ionization in the field of a strong electromagnetic wave." In: *Sov. Phys. JETP* 20.5 (1965), pp. 1307–1314 (cit. on p. 33).

[191] C. B. Schaffer, A. Brodeur, and E. Mazur. "Laser-induced breakdown and damage in bulk transparent materials induced by tightly focused femtosecond laser pulses." In: *Measurement Science and Technology* 12.11 (2001), p. 1784 (cit. on p. 33).

[192] M. Shimizu, M. Sakakura, M. Ohnishi, Y. Shimotsuma, T. Nakaya, K. Miura, and K. Hirao. "Mechanism of heat-modification inside a glass after irradiation with high-repetition rate femtosecond laser pulses." In: *Journal of Applied Physics* 108.7 (2010), p. 073533 (cit. on p. 34).

[193] J. W. Chan, T. Huser, S Risbud, and D. Krol. "Structural changes in fused silica after exposure to focused femtosecond laser pulses." In: *Optics Letters* 26.21 (2001), pp. 1726–1728 (cit. on p. 34).

[194] A. M. Streltsov and N. F. Borrelli. "Study of femtosecond-laser-written waveguides in glasses." In: *JOSA B* 19.10 (2002), pp. 2496–2504 (cit. on p. 34).

[195] C. B. Schaffer, A. Brodeur, J. F. García, and E. Mazur. "Micromachining bulk glass by use of femtosecond laser pulses with nanojoule energy." In: *Optics Letters* 26.2 (2001), pp. 93–95 (cit. on p. 34).

[196] L. Sudrie, M. Franco, B. Prade, and A. Mysyrowicz. "Writing of permanent birefringent microlayers in bulk fused silica with femtosecond laser pulses." In: *Optics Communications* 171.4-6 (1999), pp. 279–284 (cit. on p. 34).

[197] C Hnatovsky, R. Taylor, E Simova, V. Bhardwaj, D. Rayner, and P. Corkum. "Polarization-selective etching in femtosecond laser-assisted microfluidic channel fabrication in fused silica." In: *Optics Letters* 30.14 (2005), pp. 1867–1869 (cit. on p. 34).

[198] P. Paiè, F. Bragheri, R. M. Vazquez, and R. Osellame. "Straightforward 3D hydrodynamic focusing in femtosecond laser fabricated microfluidic channels." In: *Lab on a Chip* 14.11 (2014), pp. 1826–1833 (cit. on p. 34).

[199] A. Ciriolo, R. M. Vázquez, V Tosa, A Frezzotti, G Crippa, M Devetta, D Faccialá, F Frassetto, L Poletto, A Pusala, et al. "High-order harmonic generation in a microfluidic glass device." In: *Journal of Physics: Photonics* 2.2 (2020), p. 024005 (cit. on p. 34).

[200] A. Ródenas, M. Gu, G. Corrielli, P. Paiè, S. John, A. K. Kar, and R. Osellame. "Three-dimensional femtosecond laser nanolithography of crystals." In: *Nature Photonics* 13.2 (2019), pp. 105–109 (cit. on p. 34).

[201] E. Glezer, M Milosavljevic, L Huang, R. Finlay, T.-H. Her, J. P. Callan, and E. Mazur. "Three-dimensional optical storage inside transparent materials." In: *Optics Letters* 21.24 (1996), pp. 2023–2025 (cit. on p. 34).

[202] S Juodkazis, S Matsuo, H Misawa, V Mizeikis, A Marcinkevicius, H.-B. Sun, Y Tokuda, M Takahashi, T Yoko, and J Nishii. "Application of femtosecond laser pulses for microfabrication of transparent media." In: *Applied Surface Science* 197 (2002), pp. 705–709 (cit. on p. 34).

[203] C. Hnatovsky, R. Taylor, E Simova, P. Rajeev, D. Rayner, V. Bhardwaj, and P. Corkum. "Fabrication of microchannels in glass using focused femtosecond laser radiation and selective chemical etching." In: *Applied Physics A* 84.1 (2006), pp. 47–61 (cit. on p. 34).

[204] G. Corrielli, S. Atzeni, S. Piacentini, I. Pitsios, A. Crespi, and R. Osellame. "Symmetric polarization-insensitive directional couplers fabricated by femtosecond laser writing." In: *Optics Express* 26.12 (2018), pp. 15101–15109 (cit. on pp. 35, 39, 49).

[205] S. M. Eaton, H. Zhang, M. L. Ng, J. Li, W.-J. Chen, S. Ho, and P. R. Herman. "Transition from thermal diffusion to heat accumulation in high repetition rate femtosecond laser writing of buried optical waveguides." In: *Optics Express* 16.13 (2008), pp. 9443–9458 (cit. on p. 35).

[206] S. M. Eaton, H. Zhang, P. R. Herman, F. Yoshino, L. Shah, J. Bovatsek, and A. Y. Arai. "Heat accumulation effects in femtosecond laser-written waveguides with variable repetition rate." In: *Optics Express* 13.12 (2005), pp. 4708–4716 (cit. on p. 35).

[207] M. Will, S. Nolte, B. N. Chichkov, and A. Tünnermann. "Optical properties of waveguides fabricated in fused silica by femtosecond laser pulses." In: *Applied Optics* 41.21 (2002), pp. 4360–4364 (cit. on p. 35).

[208] R. Osellame, N. Chiodo, G. Della Valle, S. Taccheo, R. Ramponi, G. Cerullo, A. Killi, U. Morgner, M. Lederer, and D. Kopf. "Optical waveguide writing with a diode-pumped femtosecond oscillator." In: *Optics letters* 29.16 (2004), pp. 1900–1902 (cit. on p. 35).

[209] A Marcinkevičius, V. Mizeikis, S Juodkazis, S Matsuo, and H. Misawa. "Effect of refractive index-mismatch on laser microfabrication in silica glass." In: *Applied Physics A* 76.2 (2003), pp. 257–260 (cit. on p. 36).

[210] G. D. Marshall, A. Politi, J. C. Matthews, P. Dekker, M. Ams, M. J. Withford, and J. L. O'Brien. "Laser written waveguide photonic quantum circuits." In: *Optics Express* 17.15 (2009), pp. 12546–12554 (cit. on p. 36).

[211] M. Li, Q. Zhang, Y. Chen, X. Ren, Q. Gong, and Y. Li. "Femtosecond Laser Direct Writing of Integrated Photonic Quantum Chips for Generating Path-Encoded Bell States." In: *Micromachines* 11.12 (2020), p. 1111 (cit. on p. 37).

[212] J. G. Titchener, M. Gräfe, R. Heilmann, A. S. Solntsev, A. Szameit, and A. A. Sukhorukov. "Scalable on-chip quantum state tomography." In: *npj Quantum Information* 4.1 (2018), pp. 1–6 (cit. on p. 37).

[213] A. Crespi, M. Lobino, J. C. Matthews, A. Politi, C. R. Neal, R. Ramponi, R. Osellame, and J. L. O'Brien. "Measuring protein concentration with entangled photons." In: *Applied Physics Letters* 100.23 (2012), p. 233704 (cit. on p. 37).

[214] N. Spagnolo, C. Vitelli, L. Sansoni, E. Maiorino, P. Mataloni, F. Sciarrino, D. J. Brod, E. F. Galvao, A. Crespi, R. Ramponi, et al. "General rules for bosonic bunching in multimode interferometers." In: *Physical Review Letters* 111.13 (2013), p. 130503 (cit. on p. 37).

[215] M. Tillmann, S.-H. Tan, S. E. Stoeckl, B. C. Sanders, H. De Guise, R. Heilmann, S. Nolte, A. Szameit, and P. Walther. "Generalized multiphoton quantum interference." In: *Physical Review X* 5.4 (2015), p. 041015 (cit. on p. 37).

[216] A. Crespi, R. Osellame, R. Ramponi, V. Giovannetti, R. Fazio, L. Sansoni, F. De Nicola, F. Sciarrino, and P. Mataloni. "Anderson localization of entangled photons in an integrated quantum walk." In: *Nature Photonics* 7.4 (2013), pp. 322–328 (cit. on p. 37).

[217] J. O. Owens, M. A. Broome, D. N. Biggerstaff, M. E. Goggin, A. Fedrizzi, T. Linjordet, M. Ams, G. D. Marshall, J. Twamley, M. J. Withford, et al. "Two-photon quantum walks in an elliptical direct-write waveguide array." In: *New Journal of Physics* 13.7 (2011), p. 075003 (cit. on p. 37).

[218] G. Corrielli, A. Crespi, G. Della Valle, S. Longhi, and R. Osellame. "Fractional Bloch oscillations in photonic lattices." In: *Nature Communications* 4.1 (2013), pp. 1–6 (cit. on pp. 37, 38).

[219] Y. Wang, X.-L. Pang, Y.-H. Lu, J. Gao, Y.-J. Chang, L.-F. Qiao, Z.-Q. Jiao, H. Tang, and X.-M. Jin. "Topological protection of two-photon quantum correlation on a photonic chip." In: *Optica* 6.8 (2019), pp. 955–960 (cit. on p. 37).

[220] T. Meany, D. N. Biggerstaff, M. A. Broome, A. Fedrizzi, M. Delanty, M. Steel, A. Gilchrist, G. D. Marshall, A. G. White, and M. J. Withford. "Engineering integrated photonics for heralded quantum gates." In: *Scientific Reports* 6.1 (2016), pp. 1–8 (cit. on p. 37).

[221] I. Pitsios, F. Samara, G. Corrielli, A. Crespi, and R. Osellame. "Geometrically-controlled polarisation processing in femtosecond-laser-written photonic circuits." In: *Scientific Reports* 7.1 (2017), pp. 1–10 (cit. on p. 37).

[222] M. Gräfe, R. Heilmann, A. Perez-Leija, R. Keil, F. Dreisow, M. Heinrich, H. Moya-Cessa, S. Nolte, D. N. Christodoulides, and A. Szameit. "On-chip generation of high-order single-photon W-states." In: *Nature Photonics* 8.10 (2014), pp. 791–795 (cit. on p. 37).

[223] K. Poulios, R. Keil, D. Fry, J. D. Meinecke, J. C. Matthews, A. Politi, M. Lobino, M. Gräfe, M. Heinrich, S. Nolte, et al. "Quantum walks of correlated photon pairs in two-dimensional waveguide arrays." In: *Physical Review Letters* 112.14 (2014), p. 143604 (cit. on p. 37).

[224] N. Spagnolo, C. Vitelli, L. Aparo, P. Mataloni, F. Sciarrino, A. Crespi, R. Ramponi, and R. Osellame. "Three-photon bosonic coalescence in an integrated tritter." In: *Nature Communications* 4.1 (2013), pp. 1–6 (cit. on p. 37).

[225] A. Crespi, R. Osellame, R. Ramponi, M. Bentivegna, F. Flamini, N. Spagnolo, N. Viggianiello, L. Innocenti, P. Mataloni, and F. Sciarrino. "Suppression law of quantum states in a 3D photonic fast Fourier transform chip." In: *Nature Communications* 7.1 (2016), pp. 1–8 (cit. on p. 37).

[226] G. Corrielli, A. Crespi, R. Geremia, R. Ramponi, L. Sansoni, A. Santinelli, P. Mataloni, F. Sciarrino, and R. Osellame. "Rotated waveplates in integrated waveguide optics." In: *Nature Communications* 5.1 (2014), pp. 1–6 (cit. on p. 38).

[227] A. Crespi, R. Ramponi, R. Osellame, L. Sansoni, I. Bongioanni, F. Sciarrino, G. Vallone, and P. Mataloni. "Integrated photonic quantum gates for polarization qubits." In: *Nature Communications* 2.1 (2011), pp. 1–6 (cit. on p. 38).

[228] L. Sansoni, F. Sciarrino, G. Vallone, P. Mataloni, A. Crespi, R. Ramponi, and R. Osellame. "Polarization entangled state measurement on a chip." In: *Physical Review Letters* 105.20 (2010), p. 200503 (cit. on p. 38).

[229] M. A. Ciampini, A. Orieux, S. Paesani, F. Sciarrino, G. Corrielli, A. Crespi, R. Ramponi, R. Osellame, and P. Mataloni. "Path-polarization hyperentangled and cluster states of photons on a chip." In: *Light: Science & Applications* 5.4 (2016), e16064–e16064 (cit. on p. 38).

[230] A. Arriola, S. Gross, N. Jovanovic, N. Charles, P. G. Tuthill, S. M. Olaizola, A. Fuerbach, and M. J. Withford. "Low bend loss waveguides enable compact, efficient 3D photonic chips." In: *Optics Express* 21.3 (2013), pp. 2978–2986 (cit. on pp. 39, 49).

[231] G. Li, K. A. Winick, A. A. Said, M. Dugan, and P. Bado. "Waveguide electro-optic modulator in fused silica fabricated by femtosecond laser direct writing and thermal poling." In: *Optics Letters* 31.6 (2006), pp. 739–741 (cit. on p. 39).

[232] P. C. Humphreys, B. J. Metcalf, J. B. Spring, M. Moore, P. S. Salter, M. J. Booth, W. S. Kolthammer, and I. A. Walmsley. "Strain-optic active control for quantum integrated photonics." In: *Optics Express* 22.18 (2014), pp. 21719–21726 (cit. on p. 39).

[233] Z. Chaboyer, T. Meany, L. Helt, M. J. Withford, and M. Steel. "Tunable quantum interference in a 3D integrated circuit." In: *Scientific Reports* 5.1 (2015), pp. 1–5 (cit. on p. 39).

[234] F. Flamini, L. Magrini, A. S. Rab, N. Spagnolo, V. D'ambrosio, P. Mataloni, F. Sciarrino, T. Zandrini, A. Crespi, R. Ramponi, et al. "Thermally reconfigurable quantum photonic circuits at telecom wavelength by femtosecond laser micromachining." In: *Light: Science & Applications* 4.11 (2015), e354–e354 (cit. on pp. 39, 40, 61).

[235] E. Polino, M. Riva, M. Valeri, R. Silvestri, G. Corrielli, A. Crespi, N. Spagnolo, R. Osellame, and F. Sciarrino. "Experimental multiphase estimation on a chip." In: *Optica* 6.3 (2019), pp. 288–295 (cit. on pp. 40, 125).

[236] F. Ceccarelli, S. Atzeni, C. Pentangelo, F. Pellegatta, A. Crespi, and R. Osellame. "Low power reconfigurability and reduced crosstalk in integrated photonic circuits fabricated by femtosecond laser micromachining." In: *Laser & Photonics Reviews* 14.10 (2020), p. 2000024 (cit. on pp. 40, 49, 50, 89).

[237] I. Dyakonov, I. Pogorelov, I. Bobrov, A. Kalinkin, S. Straupe, S. Kulik, P. Dyakonov, and S. Evlashin. "Reconfigurable photonics on a glass chip." In: *Physical Review Applied* 10.4 (2018), p. 044048 (cit. on p. 40).

[238] V. A. Amorim, J. M. Maia, D. Viveiros, and P. Marques. "Inscription of surface waveguides in glass by femtosecond laser writing for enhanced evanescent wave overlap." In: *Journal of Optics* 22.8 (2020), p. 085801 (cit. on p. 40).

[239] C. Pentangelo, S. Atzeni, F. Ceccarelli, R. Osellame, and A. Crespi. "Analytical modeling of the static and dynamic response of thermally actuated optical waveguide circuits." In: *Physical Review Research* 3.2 (2021), p. 023094 (cit. on p. 40).

[240] J. Kaakkunen, M Silvennoinen, K Paivasaari, and P Vahimaa. "Water-assisted femtosecond laser pulse ablation of high aspect ratio holes." In: *Physics Procedia* 12 (2011), pp. 89–93 (cit. on p. 40).

[241] A. Killi, A. Steinmann, J. Dörring, U. Morgner, M. J. Lederer, D. Kopf, and C. Fallnich. "High-peak-power pulses from a cavity-dumped Yb: KY (WO 4) 2 oscillator." In: *Optics Letters* 30.14 (2005), pp. 1891–1893 (cit. on p. 45).

[242] W. Vogel. *Glass chemistry*. Springer Science & Business Media, 2012 (cit. on p. 48).

[243] F. Ceccarelli, S. Atzeni, A. Prencipe, R. Farinaro, and R. Osellame. "Thermal phase shifters for femtosecond laser written photonic integrated circuits." In: *Journal of Lightwave Technology* 37.17 (2019), pp. 4275–4281 (cit. on p. 51).

[244] K. Chopra, L. Bobb, and M. Francombe. "Electrical resistivity of thin single-crystal gold films." In: *Journal of Applied Physics* 34.6 (1963), pp. 1699–1702 (cit. on p. 51).

[245] P. v. Tien. "Light waves in thin films and integrated optics." In: *Applied Optics* 10.11 (1971), pp. 2395–2413 (cit. on p. 56).

[246] D Gloge. "Bending loss in multimode fibers with graded and ungraded core index." In: *Applied Optics* 11.11 (1972), pp. 2506–2513 (cit. on p. 57).

[247] G. Corrielli. "Integrated photonic circuits by femtosecond laser writing for qubit manipulation, quantum cryptography and quantum-optical analogies." In: (2015) (cit. on pp. 58, 59).

[248] A. Yariv. "Coupled-mode theory for guided-wave optics." In: *IEEE Journal of Quantum Electronics* 9.9 (1973), pp. 919–933 (cit. on p. 59).

[249] S. Piacentini, T. Vogl, G. Corrielli, P. K. Lam, and R. Osellame. "Space Qualification of Ultrafast Laser-Written Integrated Waveguide Optics." In: *Laser & Photonics Reviews* 15.2 (2021), p. 2000167 (cit. on pp. 63, 64, 66, 67, 70–74).

[250] G. Zhang, J. Y. Haw, H. Cai, F. Xu, S. Assad, J. F. Fitzsimons, X. Zhou, Y Zhang, S Yu, J Wu, et al. "An integrated silicon photonic chip platform for continuous-variable quantum key distribution." In: *Nature Photonics* 13.12 (2019), pp. 839–842 (cit. on p. 63).

[251] G. Vest, M. Rau, L. Fuchs, G. Corrielli, H. Weier, S. Nauerth, A. Crespi, R. Osellame, and H. Weinfurter. "Design and evaluation of a handheld quantum key distribution sender module." In: *IEEE journal of selected topics in quantum electronics* 21.3 (2014), pp. 131–137 (cit. on p. 63).

[252] *General Environmental Verification Standard (GEVS) for GSFC Flight Programs and Projects*. URL: `https://standards.nasa.gov/standard/gsfc/gsfc-std-7000` (visited on 06/12/2021) (cit. on p. 63).

[253] Y. C. Tan, R. Chandrasekara, C. Cheng, and A. Ling. "Silicon avalanche photodiode operation and lifetime analysis for small satellites." In: *Optics Express* 21.14 (2013), pp. 16946–16954 (cit. on p. 63).

[254] T. Vogl, K. Sripathy, A. Sharma, P. Reddy, J. Sullivan, J. R. Machacek, L. Zhang, F. Karouta, B. C. Buchler, M. W. Doherty, et al. "Radiation tolerance of two-dimensional material-based devices for space applications." In: *Nature Communications* 10.1 (2019), pp. 1–10 (cit. on p. 63).

[255] S. J. Mihailov, D. Grobnic, C. Hnatovsky, R. B. Walker, P. Lu, D. Coulas, and H. Ding. "Extreme environment sensing using femtosecond laser-inscribed fiber Bragg gratings." In: *Sensors* 17.12 (2017), p. 2909 (cit. on p. 64).

[256] N. Jovanovic, S. Armatys, S. Gross, P. G. Tuthill, J. Lawrence, and M. Withford. "Prospects for integrated photonics in space applications." In: *Conference on Lasers and Electro-Optics/Pacific Rim*. Optical Society of America. 2011, p. C1115 (cit. on p. 64).

[257] N. Y. Ganushkina, I Dandouras, Y. Shprits, and J Cao. "Locations of boundaries of outer and inner radiation belts as observed by Cluster and Double Star." In: *Journal of Geophysical Research: Space Physics* 116.A9 (2011) (cit. on p. 64).

[258] A. Dean, L. Fan, K Byard, A Goldwurm, and C. Hall. "The gamma-ray emissivity of the Earth's atmosphere." In: *Astronomy and Astrophysics* 219 (1989), pp. 358–361 (cit. on p. 65).

[259] J Kataoka, T Toizumi, T Nakamori, Y Yatsu, Y Tsubuku, Y Kuramoto, T Enomoto, R Usui, N Kawai, H Ashida, et al. "In-orbit performance of avalanche photodiode as radiation detector on board the picosatellite Cute-1.7+ APD II." In: *Journal of Geophysical Research: Space Physics* 115.A5 (2010) (cit. on p. 65).

[260] J. F. Ziegler, M. D. Ziegler, and J. P. Biersack. "SRIM–The stopping and range of ions in matter (2010)." In: *Nuclear Instruments and Methods in Physics Research Section B: Beam Interactions with Materials and Atoms* 268.11-12 (2010), pp. 1818–1823 (cit. on p. 65).

[261] *Corning Boro-Aluminosilicate Glass Products*. URL: `http://www.delta-technologies.com/products.asp?C=1` (visited on 06/12/2021) (cit. on p. 65).

[262] F. Hoch, S. Piacentini, T. Giordani, Z.-N. Tian, M. Iuliano, C. Esposito, A. Camillini, G. Carvacho, F. Ceccarelli, N. Spagnolo, A. Crespi, F. Sciarrino, and R. Osellame. "Boson Sampling in a reconfigurable continuously-coupled 3D photonic circuit." In: *arXiv preprint arXiv:2106.08260* (2021) (cit. on pp. 75, 77, 83, 85, 87, 88).

[263] A. Szameit, T. Pertsch, F. Dreisow, S. Nolte, A. Tünnermann, U. Peschel, and F. Lederer. "Light evolution in arbitrary two-dimensional waveguide arrays." In: *Physical Review A* 75.5 (2007), p. 053814 (cit. on p. 78).

[264] C. P. Dietrich, A. Fiore, M. G. Thompson, M. Kamp, and S. Höfling. "GaAs integrated quantum photonics: Towards compact and multi-functional quantum photonic integrated circuits." In: *Laser & Photonics Reviews* 10.6 (2016), pp. 870–894 (cit. on pp. 99, 100).

[265] L Goldstein, F Glas, J. Marzin, M. Charasse, and G Le Roux. "Growth by molecular beam epitaxy and characterization of InAs/GaAs strained-layer superlattices." In: *Applied Physics Letters* 47.10 (1985), pp. 1099–1101 (cit. on p. 99).

[266] P. Senellart, G. Solomon, and A. White. "High-performance semiconductor quantum-dot single-photon sources." In: *Nature Nanotechnology* 12.11 (2017), pp. 1026–1039 (cit. on pp. 99, 100, 103).

[267] A. Bennett, y. M. Pooley, n. R. Stevenson, M. Ward, R. Patel, A. B. de La Giroday, N Sköld, I Farrer, C. Nicoll, D. Ritchie, et al. "Electric-field-induced coherent coupling of the exciton states in a single quantum dot." In: *Nature Physics* 6.12 (2010), pp. 947–950 (cit. on p. 99).

[268] P. Michler. *Quantum dots for quantum information technologies*. Vol. 237. Springer, 2017 (cit. on p. 99).

[269] K. A. Fischer, K. Müller, K. G. Lagoudakis, and J. Vučković. "Dynamical modeling of pulsed two-photon interference." In: *New Journal of Physics* 18.11 (2016), p. 113053 (cit. on p. 100).

[270] M. Cosacchi, F. Ungar, M. Cygorek, A. Vagov, and V. M. Axt. "Emission-frequency separated high quality single-photon sources enabled by phonons." In: *Physical Review Letters* 123.1 (2019), p. 017403 (cit. on pp. 101, 110).

[271] S. Thomas, M Billard, N Coste, S. Wein, H Ollivier, O Krebs, L Tazaïrt, A Harouri, A Lemaitre, I Sagnes, et al. "Bright polarized single-photon source based on a linear dipole." In: *Physical Review Letters* 126.23 (2021), p. 233601 (cit. on pp. 101, 103, 110).

[272] P. Michler. *Single semiconductor quantum dots*. Vol. 28. Springer, 2009 (cit. on p. 101).

[273] V. M. Rao and S. Hughes. "Single quantum-dot Purcell factor and β factor in a photonic crystal waveguide." In: *Physical Review B* 75.20 (2007), p. 205437 (cit. on p. 101).

[274] E. M. Purcell. "Spontaneous emission probabilities at radio frequencies." In: *Confined Electrons and Photons*. Springer, 1995, pp. 839–839 (cit. on p. 102).

[275] A. Badolato, K. Hennessy, M. Atatüre, J. Dreiser, E. Hu, P. M. Petroff, and A. Imamoğlu. "Deterministic coupling of single quantum dots to single nanocavity modes." In: *Science* 308.5725 (2005), pp. 1158–1161 (cit. on p. 102).

[276] M. Lermer, N. Gregersen, F. Dunzer, S. Reitzenstein, S. Höfling, J. Mørk, L. Worschech, M. Kamp, and A. Forchel. "Bloch-wave engineering of quantum dot micropillars for cavity quantum electrodynamics experiments." In: *Physical Review Letters* 108.5 (2012), p. 057402 (cit. on p. 102).

[277] C. Schneider, P. Gold, S. Reitzenstein, S. Hoefling, and M. Kamp. "Quantum dot micropillar cavities with quality factors exceeding 250,000." In: *Applied Physics B* 122.1 (2016), p. 19 (cit. on p. 102).

[278] T. Stievater, X. Li, D. G. Steel, D Gammon, D. Katzer, D Park, C Piermarocchi, and L. Sham. "Rabi oscillations of excitons in single quantum dots." In: *Physical Review Letters* 87.13 (2001), p. 133603 (cit. on p. 105).

[279] H. Ollivier, I. Maillette de Buy Wenniger, S. Thomas, S. C. Wein, A. Harouri, G. Coppola, P. Hilaire, C. Millet, A. Lemaître, I. Sagnes, et al. "Reproducibility of high-performance quantum dot single-photon sources." In: *ACS photonics* 7.4 (2020), pp. 1050–1059 (cit. on pp. 106, 108).

[280] H Ollivier, S. Thomas, S. Wein, I. M. de Buy Wenniger, N Coste, J. Loredo, N Somaschi, A Harouri, A Lemaitre, I Sagnes, et al. "Hong-ou-mandel interference with imperfect single photon sources." In: *Physical Review Letters* 126.6 (2021), p. 063602 (cit. on pp. 109, 137).

[281] M. Spagnolo, J. Morris, S. Piacentini, M. Antesberger, F. Massa, F. Ceccarelli, A. Crespi, R. Osellame, and P. Walther. "Experimental quantum memristor." In: *arXiv preprint arXiv:2105.04867* (2021) (cit. on pp. 113, 119, 122, 123).

[282] C. Mead. "Neuromorphic electronic systems." In: *Proceedings of the IEEE* 78.10 (1990), pp. 1629–1636 (cit. on p. 113).

[283] G. Indiveri and T. K. Horiuchi. "Frontiers in neuromorphic engineering." In: *Frontiers in neuroscience* 5 (2011), p. 118 (cit. on p. 113).

[284] G. Indiveri, B. Linares-Barranco, T. J. Hamilton, A. Van Schaik, R. Etienne-Cummings, T. Delbruck, S.-C. Liu, P. Dudek, P. Häfliger, S. Renaud, et al. "Neuromorphic silicon neuron circuits." In: *Frontiers in neuroscience* 5 (2011), p. 73 (cit. on p. 114).

[285] D. B. Strukov, G. S. Snider, D. R. Stewart, and R. S. Williams. "The missing memristor found." In: *Nature* 453.7191 (2008), pp. 80–83 (cit. on p. 114).

[286] G. Indiveri, B. Linares-Barranco, R. Legenstein, G. Deligeorgis, and T. Prodromakis. "Integration of nanoscale memristor synapses in neuromorphic computing architectures." In: *Nanotechnology* 24.38 (2013), p. 384010 (cit. on p. 114).

[287] B. J. Shastri, A. N. Tait, T. F. de Lima, W. H. Pernice, H. Bhaskaran, C. D. Wright, and P. R. Prucnal. "Photonics for artificial intelligence and neuromorphic computing." In: *Nature Photonics* 15.2 (2021), pp. 102–114 (cit. on p. 114).

[288] I. Chakraborty, G. Saha, A. Sengupta, and K. Roy. "Toward fast neural computing using all-photonic phase change spiking neurons." In: *Scientific Reports* 8.1 (2018), pp. 1–9 (cit. on p. 114).

[289] A. Javadi, I Söllner, M. Arcari, S. L. Hansen, L. Midolo, S. Mahmoodian, G Kiršanskė, T. Pregnolato, E. Lee, J. Song, et al. "Single-photon non-linear optics with a quantum dot in a waveguide." In: *Nature communications* 6.1 (2015), pp. 1–5 (cit. on p. 114).

[290] L. Chua. "Memristor-the missing circuit element." In: *IEEE Transactions on circuit theory* 18.5 (1971), pp. 507–519 (cit. on p. 114).

[291] L. O. Chua and S. M. Kang. "Memristive devices and systems." In: *Proceedings of the IEEE* 64.2 (1976), pp. 209–223 (cit. on pp. 114, 124).

[292] J. J. Yang, M. D. Pickett, X. Li, D. A. Ohlberg, D. R. Stewart, and R. S. Williams. "Memristive switching mechanism for metal/oxide/metal nanodevices." In: *Nature Nanotechnology* 3.7 (2008), pp. 429–433 (cit. on p. 115).

[293] P. Pfeiffer, I. Egusquiza, M Di Ventra, M Sanz, and E Solano. "Quantum memristors." In: *Scientific Reports* 6.1 (2016), pp. 1–6 (cit. on p. 116).

[294] J. Salmilehto, F Deppe, M. Di Ventra, M Sanz, and E Solano. "Quantum memristors with superconducting circuits." In: *Scientific Reports* 7.1 (2017), pp. 1–6 (cit. on p. 116).

[295] M. Sanz, L. Lamata, and E. Solano. "Invited article: Quantum memristors in quantum photonics." In: *APL Photonics* 3.8 (2018), p. 080801 (cit. on p. 116).

[296] G. T. Reed, G Mashanovich, F. Y. Gardes, and D. Thomson. "Silicon optical modulators." In: *Nature Photonics* 4.8 (2010), pp. 518–526 (cit. on p. 124).

[297] A. Peruzzo, A. Laing, A. Politi, T. Rudolph, and J. L. O'brien. "Multimode quantum interference of photons in multiport integrated devices." In: *Nature Communications* 2.1 (2011), pp. 1–6 (cit. on p. 126).

[298] R. H. Brown and R. Q. Twiss. "Correlation between photons in two coherent beams of light." In: *Nature* 177.4497 (1956), pp. 27–29 (cit. on p. 136).

[299] C.-K. Hong, Z.-Y. Ou, and L. Mandel. "Measurement of subpicosecond time intervals between two photons by interference." In: *Physical Review Letters* 59.18 (1987), p. 2044 (cit. on p. 137).